SIMULTANEOUS MITIGATION OF SUBSYNCHRONOUS RESONANCE AND SUBSYNCHRONOUS INTERACTION USING OFFSHORE AND DOUBLY-FED INDUCTION GENERATOR-BASED WIND FARMS

A Thesis

Submitted to the College of Graduate Studies and Research

in Partial Fulfillment of the Requirements

For the Degree of Master of Science

in the Department of Electrical and Computer Engineering

University of Saskatchewan

Saskatoon, Saskatchewan

By

Emmanuel Ogemuno

PERMISSION TO USE

I agree that the Library, University of Saskatchewan, may make this thesis freely available for inspection. I further agree that permission for copying of this thesis for scholarly purpose may be granted by the professor or professors who supervised the thesis work recorded herein or, in their absence, by the Head of the Department or the Dean of the College in which the thesis work was done. It is understood that due recognition will be given to me and to the University of Saskatchewan in any use of the material in this thesis. Copying or publication or any other use of this thesis for financial gain without approval by the University of Saskatchewan and my written permission is prohibited.

Request for permission to copy or to make any other use of the material in this thesis in whole or part should be addressed to:

Head of the Department of Electrical and Computer Engineering
University of Saskatchewan
57 Campus Drive
Saskatoon, Saskatchewan S7N 5A9
Canada.

ABSTRACT

Subsynchronous resonance (SSR) is one of the major obstacles for the wide spread of high degrees (60% and higher) of series capacitor compensation. Recently, a new obstacle, namely Subsynchronous Interaction (SSI) has been added to the list after the Zorillo Gulf wind farm incident in Texas in October 2009. SSI is due to the interaction between large Doubly Fed Induction Generator (DFIG)-based wind farms and series capacitor compensated transmission systems.

In integrated power systems incorporating series capacitor compensated transmission lines and high penetration of wind energy conversion systems, especially DFIG-based wind farms, SSR and SSI could occur concurrently as a result of some system contingences. Therefore, mitigating SSR and SSI is an important area of research and development targeting at developing practical and effective countermeasures.

This thesis reports the results of digital time-domain simulation studies that are carried out to investigate the potential use of offshore and DFIG-based wind farms for simultaneous mitigation of SSR and SSI. This is achieved through introducing supplemental control signals in the reactive power control loops of the grid side converters of the DFIG wind turbines or the HVDC onshore Modular Multilevel Converter (MMC) connecting the offshore wind farm to the grid. In this context, two supplemental controls designated as Supplemental Controls I and II are examined. Supplemental Control I introduces a signal in the HVDC onshore converter to damp both SSR and SSI oscillations. On the other hand, Supplemental Control II introduces a signal in the HVDC onshore converter for damping SSR oscillations and another signal in the grid side converters of the DFIG wind turbines for damping SSI oscillations.

Time-domain simulations are conducted on a benchmark model using the ElectroMagnetic Transients program (EMTP-RV). The results of the investigations have demonstrated that the presented two supplemental controls are very effective in mitigating the SSR and SSI phenomena at different system contingencies and operating conditions.

ACKNOWLEDGEMENTS

Firstly, my sincere appreciation goes to my supervisor Dr. S.O. Faried for the opportunity to work with him during the duration of my studies. His guidance, patience, encouragement and assistance during the course of this research work are greatly appreciated.

My sincere appreciation also goes to my graduate study teachers, Dr. Rajesh Karki, Dr. N.A. Chowdhury and Dr. Daniel Chen for strengthening my knowledge on reliability, mathematics and control systems engineering. I also would like to appreciate Dr. Ulas Karaagac for providing some of the models used in this thesis.

My sincere appreciation also goes to my fellow graduate students Jipeng Zhang, Xuan Gao, Qi Zhao, Linh Pham, Wenhao Yue and Ran Long, for all their support and inputs.

Finally special thanks to my parents, Mr and Mrs Godwin Ogemuno, my siblings and all my friends for their prayers, love and encouragement throughout the duration of this program.

TABLE OF CONTENT

LIST OF FIGURES

LIST OF TABLES

LIST OF SYMBOLS

A	blade sweep area (m^2)
BPF	band pass filter
C	capacitor in compensated transmission line
C_{dc}	capacitor in dc link of the HVDC back-to-back system.
C_f	wind turbine blade design constant.
C_p	power coefficient of the blade
D_E, D_g, D_B, D_A, D_I, D_H	damping coefficients of the corresponding inertia
d	direct axis.
e_a, e_b, e_c	stator three-phase voltages
e_d, e_q	d- and q- axis components of the stator voltage
e_{fd}	field voltage
GSC	grid side converter
i_a, i_b, i_c	stator currents in phase a, b, c
i_d, i_q	d- and q- axis components of the stator current
i_{dc}	current through the dc capacitor
i_{fd}	field winding current
i_{1d}	d-axis damper winding current
i_{1q}, i_{2q}	q-axis damper winding currents
i_T	current flowing through dc terminals of the HVDC back-to-back system
K	shaft stiffness
K_{Eg}, K_{gB}, K_{BA}, K_{AI}, K_{IH}	stiffness of the connecting shafts
$K_{i,i+1}$	stiffness between i^{th} and $(i+1)^{th}$ mass-spring
K_{shaft}	speed deviation damping

K_ω	gain of the supplemental controller
k	degree of compensation
L	inductance
L_T	inductance of the converter transformer
L_{ad}, L_{aq}	d- and q-axis components of the magnetizing inductance
L_d, L_q	d and q-axis components of the stator inductance
L_{ffd}	self-inductance of the field winding
L_{ls}, L_{lr}	DFIG stator and rotor linkage inductance
L_{11d}	self-inductance of the d-axis damper winding
L_{11q}, L_{22q}	self-inductances of the q-axis damper winding
L_s, L_r	stator and rotor inductances
M_Φ	mutual inductance between rotor and stator
M_E, M_g, M_B, M_A, M_I, M_H	inertia constants of exciter, generator, two low-pressure turbines, intermediate-pressure turbine and high-pressure turbine respectively.
M_I	modulation index of VSC-HVDC converters
M_i	inertia constant of the i^{th} rotating mass
MPT	maximum power tracking point
P	real power
P_A, P_B, P_I, P_H	power of the stages of the turbine
PI	proportional integral
P_{WFA}	wind farm A real power
$P_{WFB,MMC}$	wind farm B real power
P_m	mechanical power
Pr, Pg	active power of the RSC and GSC

$P_{grid\text{-}Ref}$	real power reference for GSC
p_{ac}	ac power
p_{dc}	dc power
Q	reactive power
Q_{WFA}	wind farm A reactive power
$Q_{WFB,\ MMC}$	wind farm B reactive power
$Q_{grid\text{-}Ref}$	reactive power reference for RSC
$Q_{GSC\text{-}Ref}$	reactive power reference for GSC
q	quadrature axis
R_T	resistance of the converter transformer
R_ω	wind turbine blade length
RSC	rotor side converter
R_a	armature resistance
R_{fd}	field winding resistance
R_{1d}	d-axis damper winding resistance
R_{1q}, R_{2q}	q-axis damper winding resistances
r_s, r_r	DFIG stator and rotor resistances
s	laplace transformation operator
T_C	fault clearing time
T_e	electromagnetic torque
T_F	simulation time
T_{LB}, T_{LA}, T_{IP}, T_{HP}	input torques of two low-pressure turbines, intermediate-pressure turbine and high-pressure turbine respectively
T_{MECH}	mechanical torque
U_{SSI}	SSI supplemental control signal

U_{SSR}	SSR supplemental control signal
U_S	total supplemental control signal
V_C	voltage across the series capacitor of the compensated transmission line
V_{Cd}, V_{Cq}	voltages across the series capacitor in the d-q reference frame
V_L	voltage across the inductance of the series capacitor compensated transmission line
V_{Ld}, V_{Lq}	voltages across the inductance in the d-q reference frame
V_R	voltage across the resistance of the series capacitor compensated transmission line
V_{Rd}, V_{Rq}	voltages across the resistance in the d-q reference frame.
V_{WFA}	wind farm A terminal voltage
V_{WFB}	wind farm B terminal voltage
V_a, V_b, V_c	three phase voltages on the ac side
V_{dc}	voltage across the dc capacitor
V_{dcT}	voltage at the dc terminal of the HVDC system
V_{dc_WFA}	wind farm A dc capacitor voltage
V_{dc_WFB}	wind farm B dc capacitor voltage
V_s	ac system voltage.
V_{sh}	converter ac voltage
V_{shd}, V_{shq}	d and q-axis components of the converter ac voltage
V_t	generator terminal voltage
v_{qg}, v_{dg}	quadrature and direct axis GSC voltages
v_s, v_r	stator and rotor side voltages
v_{qs}, v_{ds}	quadrature and direct axis GSC voltages
v_{qr}, v_{dr}	quadrature and direct axis RSC voltages

V_ω	wind speed (m/s)
X_C	series capacitor reactance
X_L	transmission line reactance
X_l	synchronous generator leakage reactance
X_0	synchronous generator zero-sequence reactance
δ	load angle
δ_{sh}	phase shift between fundamental component of converter and ac voltage
δ_E, δ_B, δ_A, δ_I, δ_H	rotor angles of exciter, two low-pressure turbines, intermediate-pressure turbine and high-pressure turbine respectively
Ψ_d, Ψ_q	d- and q- axis components of the stator flux linkages
Ψ_{fd}	field winding flux linkage
Ψ_{1d}	d-axis damper winding flux linkage
Ψ_{1q}, Ψ_{2q}	q-axis damper winding flux linkages
ρ	air density (kgm^{-3})
ω	angular velocity
ω_E, ω_B, ω_A, ω_I, ω_H	angular velocity of exciter, two low-pressure turbines, intermediate-pressure turbine and high-pressure turbine respectively
ω_{gen}	turbine-generator rotating mass speeds
$\omega_e(f_e)$	subsynchronous natural frequency
ω_{ref}	reference angular velocity
ω_m	wind turbine rotational speed (rad/s)
$\omega_0(f_0)$	synchronous frequency
$\Delta\omega_m$	modal speed deviation matrix
$\Delta\omega$	speed deviation matrix of the turbine-generator rotating masses

λ	wind turbine blade tip speed ratio
λ_{dm}, λ_{qm}	d- and q- axis components of the magnetizing flux linkages
λ_{ds}, λ_{qs}	DFIG stator d- and q-axis components of the flux linkage
λ_{dr}, λ_{qr}	DFIG rotor d- and q-axis components of the flux linkage
$\Delta Y'$	output of the band filters in supplemental controller
θ	blade pitch angle
Φ_i	phase compensations

Chapter 1

INTRODUCTION

1.1 Wind Energy

The global quest for clean and renewable sources of energy, aimed at reducing pollution and greenhouse gases associated with conventional thermal power plants, has led to the growth and substantial investments in renewable energy (of recent wind energy) around the world. World wind generation more than quadrupled between 2000 and 2006, doubling about every three years. According to the World Wind Energy Association, wind powered generation accounted for 2.5% of the worldwide electricity usage in 2010 and it is expected to reach 8% by 2018 [1]. Wind energy has thus far experienced significant growth, with a worldwide installed capacity of 318,000 MW at the end of 2013, representing a 35,000 MW growth over the preceding year [1]. Examples of large wind farms around the world includes, the 1020 MW Alta Energy Center in California, the 845 MW Shepherds Flat wind farm in Oregon and the over 5000 MW Gansu wind farm in China [1].

In recent years the focus on wind energy technologies has been shifting from onshore wind farms to offshore wind farms [2]. One of the reasons is the availability of lands, as massive lands are needed for onshore wind farms projects. The second is that wind is much stronger off the coasts than wind over the continent. Offshore breeze is stronger in the afternoon which coincides with the peak electricity demand in industrialized countries or regions. Lastly, offshore wind farms can also be located in places with higher electricity demand, which eliminates the need for new overland transmission lines.

Furthermore, at the end of 2011, there were 53 European offshore wind farms off the coast of Belgium, Denmark, Finland, Germany, Ireland, Netherland, Norway, Sweden and the United Kingdom, with an operating capacity of 3,813 MW [3]. In addition, under construction across Europe are offshore wind farms with total capacity of 5,603 MW [4]. More than 100,000 MW of offshore wind farm projects are proposed across Europe. The European Wind Energy Association (EWEA) has set a target of 40 GW installed by 2020 and 150 GW installed by 2030 [4].

1.2 Transmission Line Series Capacitive Compensation

Series capacitive compensation is the injection of reactive power into electric power transmission system, to make transmission lines appear shorter than normal. Series capacitive compensation is a cheap and effective method of enhancing the power transfer capability of transmission systems and improving system stability [5]-[6]. However, one of the hindering factors for increased utilization of series capacitive compensation is the potential risk of subsynchronous resonance (SSR) and subsynchronous interaction (SSI) [7]-[9]. Figure 1.1 shows a typical time response of a turbine-generator shaft torsional torque (High-Pressure turbine to Low-Pressure turbine shaft section, (HP-LP)) during and after clearing a 3-cycle fault in a series capacitive compensated transmission system in the presence of the SSR phenomenon. On the other hand, Figure 1.2 shows a typical time response of the terminal voltage (root mean square) of a large doubly-fed induction generator-based wind farm during and after clearing a fault in a series capacitive compensated transmission system in the presence of the SSI phenomenon. As it can be seen from this figure, the wind farm terminal voltage exhibits sustained oscillations.

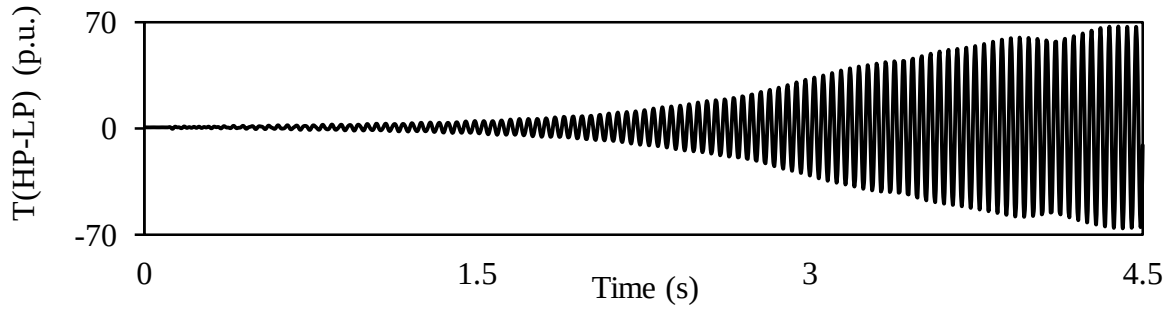

Figure 1.1: Transient time response of a turbine-generator shaft torsional torque during and after clearing a system fault on a series capacitive compensated transmission line.

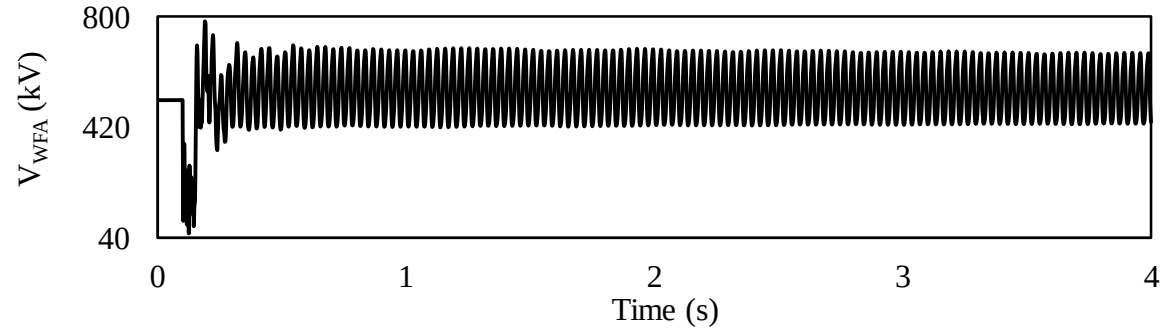

Figure 1.2: Transient time response of a large DFIG-based wind farm terminal voltage (root mean square) during and after clearing a system fault on a series capacitive compensated transmission line.

The following are some of the benefits of incorporating series capacitors in transmission systems [10], [11]:

1.2.1 Increase in power transfer

The increase in the power transfer capability as a function of the degree of compensation for a transmission line can be illustrated using the circuit and the vector diagram shown in Figure 1.3 [11]. The power transfer on the transmission line is given by:

$$P = \frac{|V_t||V_b|}{X_L - X_c}\sin\delta = \frac{|V_t||V_b|}{X_L(1-k)}\sin\delta \tag{1.1}$$

where k is the degree of compensation, the degree of compensation is usually within the range $0.2 \leq k \leq 0.7$.

$$k = \frac{X_c}{X_L}$$

The effect on the power transfer when a constant load angle difference is assumed is shown in Figure 1.4 [11]. Transmission capability increases of more than two times can be obtained in practice.

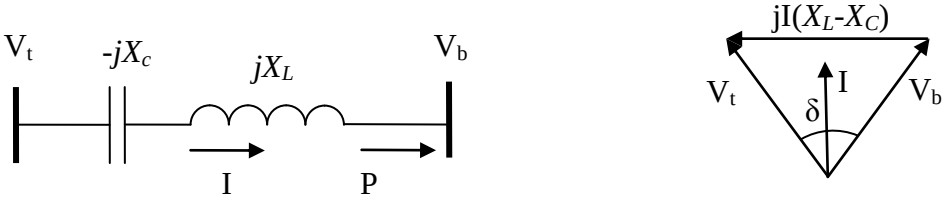

Figure 1.3: A transmission line with a series capacitor.

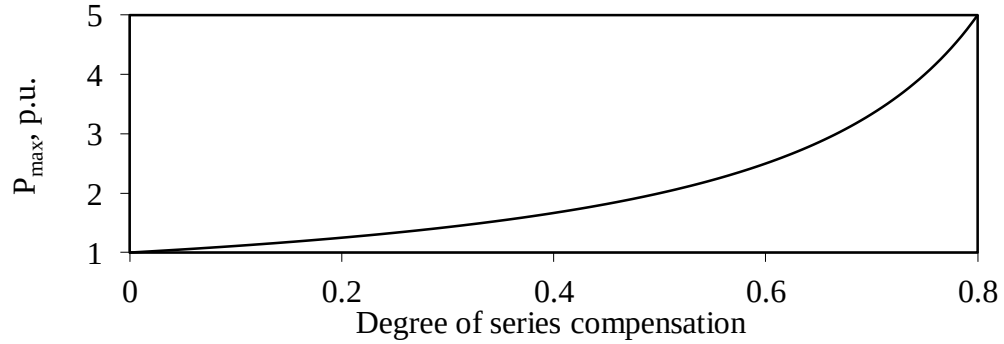

Figure 1.4: Maximum power transmitted over a transmission line as a function of the degree of series compensation ($|V_t| = |V_b| = 1$ *p.u.*, $X_L = 1$ *p.u.*).

1.2.2 Voltage stability improvement

The voltage of a transmission system is a function of both the active (P) and reactive power (Q) flow [10]:

$$V = f(P, Q) \tag{1.2}$$

However, in a transmission system incorporating series capacitors, the reactive power contribution from a capacitive element in series with the line acts to improve the reactive power balance of the transmission system [10]. According to [10], this reactive power contribution is instantaneous and of a self-regulatory nature. That is, the reactive power injected into the transmission system increases when the system load increases and vice-versa. This makes series capacitive compensation an effective means for maintaining or even increasing the voltage stability in a heavily loaded transmission line [10].

1.2.3 Increase the power transfer capability by raising the first swing stability limit

A substantial increase in the stability margin is achieved by installing a series capacitor. The series compensation will improve the situation in two ways: it will decrease the initial generator load angle corresponding to a specific power transfer and it will also shift the power-load angle (P-δ) characteristic upwards [10]. This will result in increasing the transient stability margin.

1.3 Subsynchronous Resonance (SSR)

According to the IEEE definition [12], *"SSR is defined as an electric power system phenomenon where there is an exchange of energy between a series capacitive compensated transmission system and a turbine-generator shaft system, at one or more natural frequencies of the combined system below the synchronous frequency of the system."*

SSR can also be defined as a phenomenon that occurs where there is an exchange of energy (at a frequency below the system nominal frequency) between a series capacitive compensated transmission system and a turbine-generator shaft system, either through sustained oscillations, poorly damped oscillations or transient effects [13].

This phenomenon leads to potential turbine-generator damage [7], [14]. The shaft failure cannot be accurately predicted and as such can be a source of hazard to personnel. A more likely

most-severe hazard would be crack initiation at the surface of one of the turbine-generator shafts, indicating fatigue and requiring shaft replacement, resulting in a unit outage of 90 days or more.

Figure 1.5 represents a simple power system [15]. It consists of a large generator driven by a multi-stage turbine (HP and LP), connected to an infinite-bus system through a series capacitive compensated transmission line. The natural resonance frequency for the electrical system is given by [15]:

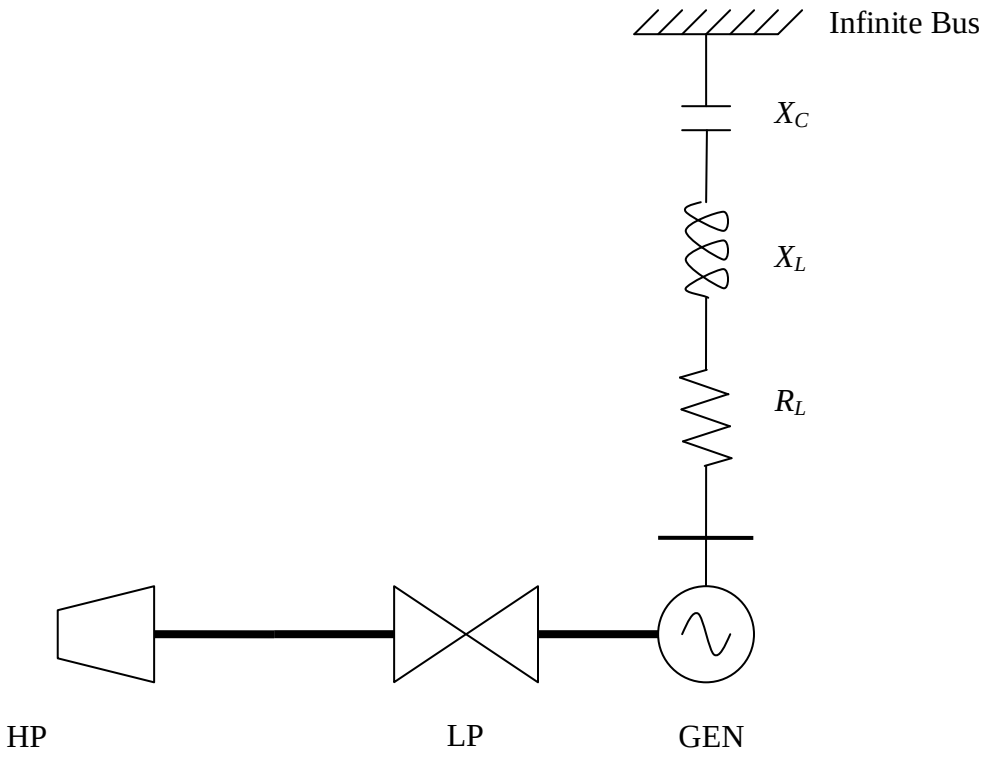

Figure 1.5: A turbine-generator connected to an infinite-bus system through a series capacitor compensated transmission line.

$$\omega_e = \frac{1}{\sqrt{LC}} = \frac{\omega_0}{\sqrt{(\omega_0 L)(\omega_0 C)}} = \omega_0\sqrt{\frac{X_C}{X_L}} \quad \text{rad/s} \tag{1.3}$$

or

$$f_e = f_0\sqrt{\frac{X_C}{X_L}} \quad \text{Hz} \tag{1.4}$$

where ω_0 is the system synchronous frequency ($\omega_0 = 2\pi f_0\ rad/s$, $f_0 = 60\ Hz$), X_C is the capacitive reactance and X_L is the total inductive reactance (generator sub-transient reactance and the transmission line inductive reactance) of the electric system.

In practice, f_e is always below the synchronous frequency f_0 since the compensation level of transmission lines are usually less than 100%. For this reason, f_e is called the sub-synchronous natural frequency of the electrical system [15]-[16].

The shaft system of a turbine-generator has (N-1) natural torsional frequencies, where N is the number of the rotating masses. These torsional frequencies are functions of the inertia of the different masses and the stiffness of the connected shafts. Due to the shaft physical properties and the mechanical design of the shaft, the torsional natural frequencies of turbine-generator shafts are below the nominal frequency of the system [15]. Therefore, the interaction between the electrical and mechanical system is due to the closeness of f_e to the natural torsional frequencies of the turbine-generator shaft system [15]. This phenomenon was first recognized in the 1970 Mohave project [17].

There are three different types of SSR according to [7], [17], [18]:

- Induction Generator Effect (IGE)
- Torsional Interaction (TI)
- Torque Amplification (TA)

Both induction generator effect and torsional interaction are classified as small disturbances at the initial stage, while torque amplification is considered as a large disturbance.

1.3.1 Induction Generator Effect (IGE)

IGE is a pure electrical phenomenon taking place at frequencies very close to the rated network frequency in power systems with high series capacitive compensation degree. IGE is caused by self-excitation of the electrical system. It occurs when the rotor resistance to subsynchronous currents, viewed from the armature terminal is negative, for the same current the network presents a positive resistance [17]. If the negative resistance of the generator is greater in magnitude than the resistance of the network, sustained subsynchronous current will be

induced [17]-[18]. IGE is experienced in induction machine based wind turbines, but rare in hydro and thermal generators [17].

1.3.2 Torsional Interaction (TI)

TI is an unstable condition that denotes the exchange of energy between transmission systems and turbine-generator shaft systems. As oscillation builds up as a result of this energy exchange, the motion will induce armature voltage components at both subsynchronous frequency (f_0-f_e) and supersynchronous frequency (f_0+f_e), if the resultant subsynchronous torque equals or exceeds the inherent mechanical damping of the rotor, the system will become self-excited [17]. Where f_0 and f_e are the system frequency and natural frequency of the turbine-generator shaft respectively.

According to [19], TI does not occur in hydro power plants, since the inertia of the hydro turbine is much smaller compared to inertia of the generator (in the range of 5%), when torsional oscillations occur in the shaft, the speed variation will be countered on the hydro turbine. Thus the speed of the generator is unaffected. As a result, the oscillation will not be recognized by the transmission system. However, TI occurs in thermal power plants with multi-stage turbine-generator shaft system such as coal fired power plants and gas turbine-generators [20].

1.3.3 Torque Amplification (TA)

TA is a phenomenon that results from system disturbances. In the case of uncompensated transmission systems, the disturbance will result in a dc offset that will decay with the sub-transient and transient time constant of the generator. However, in a series capacitive compensated system, oscillations having a frequency corresponding to the resonance frequency of the network will be experienced. If this frequency coincides with one or more of the turbine-generator shaft natural frequencies, large torques will be experienced, this may lead to shaft fatigue or severe damage [7], [17]. Unlike torsional interaction and induction generator effect, subsynchronous oscillations resulting from torque amplification might be expected to reach a damaging level within 0.1 seconds.

1.4 Subsynchronous Interaction (SSI)

SSI is the exchange of energy (at subsynchronous frequency) between large DFIG-based wind farms and series capacitive compensated transmission systems [21]-[22]. Recent findings into SSI phenomenon attributes the interaction to be between the series capacitor compensated system and the power electronic devices in the wind turbine conversion system [22]. Most wind farms are DFIG–based wind turbines. Concerns over the use of high series capacitive compensation degree (60% and above) has been extended to include the vulnerability of DFIG wind turbines to SSI [8]-[9]. This was confirmed in the Zorillo Gulf wind farm (485 MW) incident of October 2009 in Texas. This incident can be regarded as the first event of SSI between a DFIG-based wind farm and series capacitor compensated transmission system (345 kV, 80 miles and a 50% compensation degree) [9], [23].

Furthermore, the electrical resonance frequency of DFIG is largely dependent on the converter (both the rotor and grid-side converters) controller parameters, as well as on the system operating conditions. This dependency leads to a fairly wide range of frequencies meaning resonance can occur for a wide range of series compensation levels [17]. It is worthwhile to mention that subsynchronous interaction (SSI) associated with wind power plants consist of two types namely [24]:

- Subsynchronous Control Interaction (SSCI)
- Subsynchronous Torsional Interaction (SSTI)

SSCI is purely an electrical phenomenon, without the wind turbine shaft torsional dynamics being involved. As a result, SSCI oscillations tend to grow quickly compared to electromechanical interaction. It is caused by the fast action of the rotor side current controller in DFIG-based wind turbines [21]. That is, the rotor side current controller changes the rotor resistance in such a way that it is seen from the stator side as a negative resistance. It is an interaction between the wind turbine controllers and the series capacitor compensated system caused by induction generator effect [25].

SSTI is an electromechanical phenomenon where there is an exchange of energy between the series compensated transmission system and the wind turbine rotating masses [25]. It is similar to SSR, turbine-generator shaft torsional interaction. According to [25], wind turbine

drive trains have low shaft stiffness which leads to low frequency torsional modes (as low as 1 - 3 Hz). Hence in order to have SSTI, the network mode should have a frequency of 57 - 59 Hz. However, this is rarely the case, because a high level of series compensation (about 90%) is required to attain such network modes.

Furthermore, in the integration of wind power plants into transmission networks, developers of wind energy are required to conduct SSI studies to demonstrate that the possible radial connection of the wind power plant to a series capacitive compensated system does not affect the safe operation of the wind turbine or the series compensated transmission system during system contingencies. According to [26], this study involves two phases, *"The first phase corresponds to the most pessimistic operating condition, where the detailed model of the wind power plant is radially connected to a weak a.c. line. Simulation case studies have demonstrated that this configuration will give rise to excessive oscillations and eventual tripping of the wind turbine, when a DFIG wind turbine is used."* The second phase of simulation study uses the actual transmission line model of the system where the wind power plant will be integrated. If the wind turbine fails the second phase of the simulation test, mitigation actions will be necessary at both the turbine or/and transmission system level [26].

1.5 High Voltage Direct Current (HVDC) Transmission

High voltage direct current (HVDC) transmission system uses direct current for the transmission of bulk electrical power in contrast to high voltage alternating current (HVAC) transmission system. HVDC transmission has advantages over ac transmission in the following situations [15], [27]:

1. Asynchronous link between two ac systems, where ac ties will not be feasible because of system stability problems or a difference in nominal frequencies of the two systems. Example is the interconnection of two systems where the nominal frequencies are 50 Hz and 60 Hz.
2. Transmission of large amounts of power over long distance by overhead lines. HVDC transmission is a competitive alternative to ac transmission for distance in excess of about 600 km.

3. Underwater cables longer than 30 km, ac transmission is impractical for such distances because of the high capacitance of the cable requiring intermediate compensation stations.

There are two types of HVDC technologies available in the market [28]:

- Line commutated converter (LCC)-based HVDC system.
- Voltage source converter (VSC)-based HVDC system.

The LCC-based HVDC is characterised by very high transmission voltage and power and most importantly low transmission losses when compared to the VSC-based HVDC system. The LCC disadvantages are [28]:

- Weak network cannot be connected to this system.
- Low degree of controllability and converter's reactive power consumption.

The voltage source converter (VSC)-based HVDC uses self-commutating valves (such as IGBTs, GTOs and IGCTs) and it is only available for low voltage and power rating. It has high transmission losses and more capital intensive when compared to the LCC [28]. However, the new soft switching of topologies of VSC-based HVDC can significantly reduce converter losses and make transmission more economical and reliable [29].

Figure 1.6 shows the schematic diagram of a VSC-HVDC back-to-back system. The rectifier converter is used to control active and reactive powers between ac and dc transmission, while the inverter converter controls the dc voltage and reactive power.

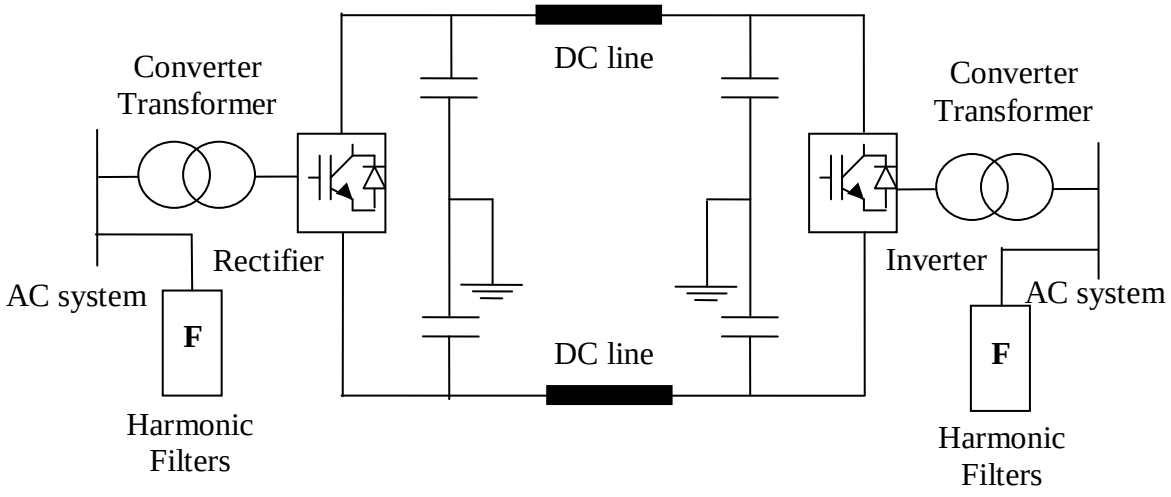

Figure 1.6: Schematic diagram of a VSC-HVDC back-to-back system.

The VSC-based HVDC system has some advantages and this makes it suitable for connecting offshore wind farms to the grid [27]-[28]. These include;

i. Independent and fast control of active and reactive powers.
ii. Contribution to voltage stability and transient stability of the connected ac network through ac voltage control.
iii. Connection to weak and passive network is possible.
iv. The sizes of converter stations are small.
v. Power flow direction can be changed instantly.
vi. Black start capability in case of total grid collapse.

The modular multilevel converter (MMC) HVDC system is a type of voltage source converter HVDC system. The recent trend in power electronic technologies and controllable devices in power system have led to the growth of multilevel converters for HVDC systems. The use of MMC for HVDC applications is expected to supersede two and three-level VSC-based technologies, because of its recognized advantages in terms of efficiency, reliability performance and scalability [30].

1.6 Research Objective and Scope of the Thesis

Series capacitive compensation is the most economical way for increasing the transmission capacity and improving power system transient stability. However, subsynchronous resonance (SSR) is one of the major obstacles for the wide spread of high degrees (60% and higher) of series capacitor compensation. Recently, a new obstacle, namely subsynchronous interaction (SSI) has been added to the list after the Zorillo Gulf wind farm incident in Texas in October 2009. SSI is due to the interaction between large doubly-fed induction generator (DFIG)-based wind farms and series capacitor compensated transmission systems. In an integrated power system where series capacitive compensation (60% and higher) and high wind energy penetration exists, SSR and SSI could occur concurrently during some system contingencies and operating conditions. Therefore, mitigating SSR and SSI is an important area of research and development targeted at developing practical and effective countermeasures.

The main objective of this research work is to investigate the potential use of an offshore DFIG-based wind farm for simultaneous mitigation of SSR and SSI. This is achieved through

introducing supplemental control signals in the reactive power control loops of the grid side converters of DFIG wind turbines and the HVDC onshore converter connecting offshore wind farm to the grid. In this context, two supplemental controls designated as Supplemental controls I and II are examined. Supplemental control I introduces a signal in the HVDC onshore converter to damp both SSR and SSI oscillations. On the other hand, Supplemental control II introduces a signal in the HVDC onshore converter for damping SSR oscillations and another signal in the grid side converters of DFIG wind turbines for damping SSI oscillations. The effectiveness of Supplemental controls I and II in mitigating the two phenomena is demonstrated on a test benchmark through time-domain simulation studies using the ElectroMagnetic Transients program (EMTP-RV).

The thesis is organized in four chapters, a reference section and two appendices. Chapter 1 introduces a brief review of wind energy generation and benefits of series capacitive compensation on power systems. Brief introductions to SSR and SSI are also presented, as well as, HVDC transmission system. The objective of the research is also presented in this chapter.

In Chapter 2, the system used for the investigations conducted in this thesis is described and the detailed dynamic models of its individual components are also presented in this chapter. The results of the digital time-domain simulations of a case study for the system during a three-phase fault are presented at the end of this chapter.

Chapter 3 demonstrates the effectiveness of supplemental controls I and II in damping SSR and SSI oscillations through time-domain simulation studies. Supplemental controls I and II performance at different system contingencies and operating conditions are also investigated.

Chapter 4 summarizes the research described in this thesis and presents some conclusions.

The data of the systems under investigations are given in Appendix A. Supplemental controls I and II output SSR and SSI signals for the case studies reported in Chapter 3 are given in Appendix B.

Chapter 2

MATHEMATICAL MODELING OF POWER SYSTEMS INCORPORATING OFFSHORE AND DFIG-BASED WIND FARMS FOR LARGE DISTURBANCE STUDIES

2.1 Introduction

In this chapter, the system used for the studies reported in this thesis is described and the mathematical models of its various components are presented. A digital time-domain simulation of a case study of the system during a three-phase fault is presented at the end of this chapter.

2.2 Description of the System under Study

The system used in the investigations of this thesis is shown in Figure 2.1. It consists of a generating station and two wind farms designated as wind farms A and B. The generating station and wind farm A are connected to each other through two transmission lines (Lines 3 and 4) as well as to an infinite-bus system through two series capacitor compensated transmission lines (Lines 1 and 2, each with a 60% compensation degree except for the sample case study in Section 2.4 where the compensation degree in both lines is 40%). Wind farm B is connected to the generating station and wind farm A through Lines 3, 4 respectively and to the infinite-bus system through two transmission lines (Lines 5 and 6). The generating station comprises two turbine-generators, G1 (600 MVA, 22 kV) and G2 (700 MVA, 22 kV). The shaft system of G1 comprises high and low-pressure turbines (HP1, LP1), the generator rotor and an exciter (EXC). The shaft system of G2 comprises high and low-pressure turbines (HP2, LP2) and the generator rotor. The frequencies of the natural torsional modes of oscillations of G1 and G2 shaft systems are 24.65 Hz, 32.39 Hz, 51.1 Hz and 24.65 Hz, 44.99 Hz respectively. The data of G1 and G2 are taken from the IEEE second benchmark model for computer simulation of SSR [8]. Wind farm A comprises 300 × 1.5 MW DFIG wind turbines. Wind farm B is an offshore wind farm (OWF) comprising 140 x 1.5 MW DFIG wind turbines and connected to the onshore ac grid through a modular multilevel converter (MMC) topology based voltage source converter (VSC) HVDC system.

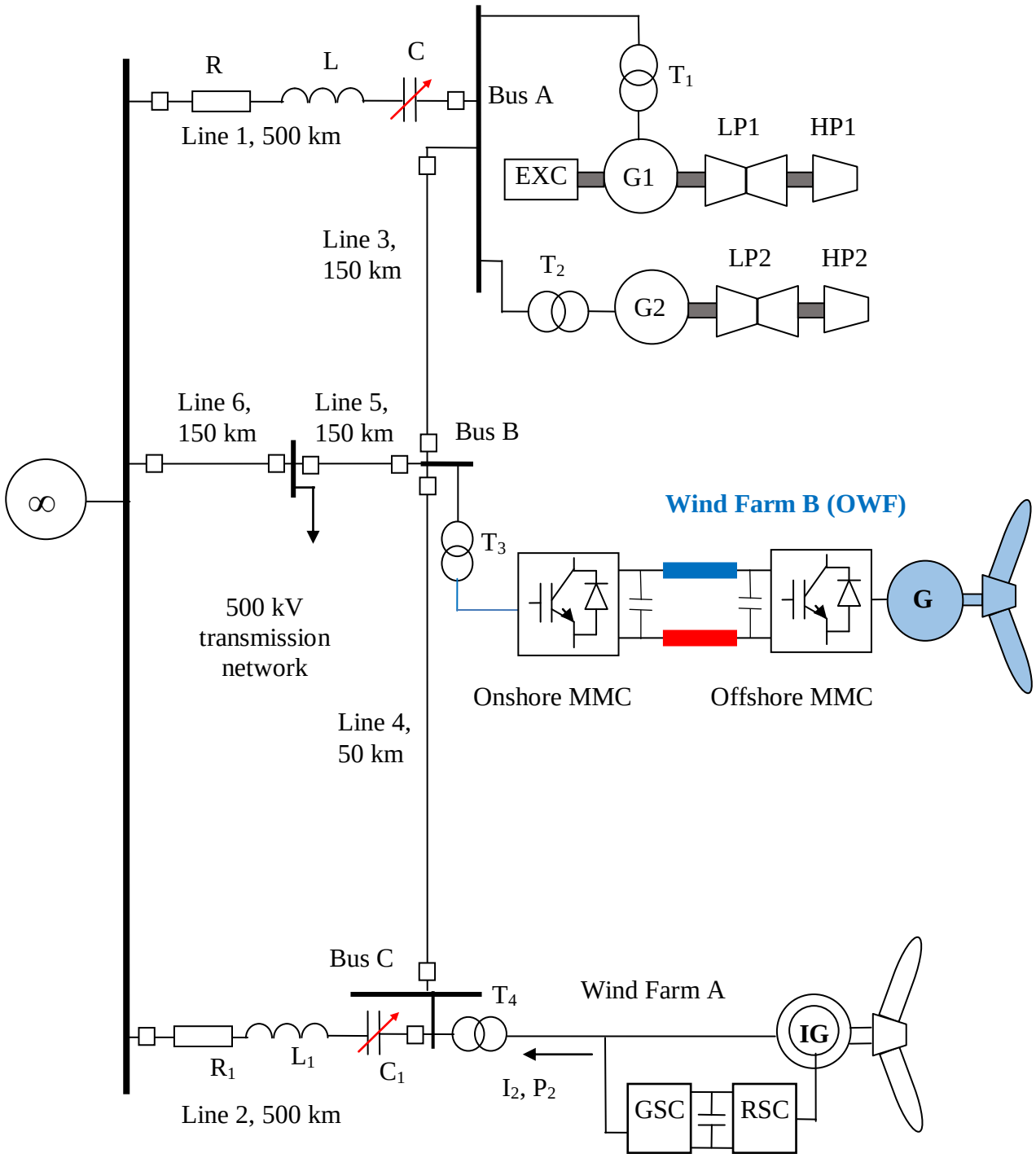

Figure 2.1: System under study.

The VSC-HVDC system consists of two 20-level MMC terminals (± 110 kV, 150 MW) and a single core 100 km submarine cable. The operating wind speeds and power outputs of the two wind farms are given in Table 2.1. The medium voltage collector grid is represented with its equivalent PI circuit model [32]. Faults are assumed to occur on Lines 4 and 5 and to be cleared by circuit breaker operations at both ends of the line.

Table 2.1: Wind speeds and wind farm outputs.

Wind farm	Operating speed and output power
A (DFIG-based wind farm)	Wind Speed = 11 m/s , ≈ 427.50 MW
B (Offshore wind farm (OWF))	Wind Speed = 11 m/s, ≈ 186 MW

2.3 Power System Modeling

The nonlinear differential equations of the system under study are derived by developing individually the mathematical models which represent the various components of the system, namely the synchronous machine, the transmission line, the turbine-generator mechanical system, the DFIG-based wind turbine and its conversion system, the wind turbine aerodynamic model and the VSC-HVDC transmission system. Knowing the mutual interaction among these models, the system of differential equations can be formed.

2.3.1 Modeling of the synchronous machine

In a conventional synchronous machine, the stator circuit consisting of a three-phase winding produces a sinusoidally space distributed magnetomotive force. The rotor of the machine carries the field (excitation) winding which is excited by a dc voltage. The electrical damping due to the eddy currents in the solid rotor and, if present, the damper winding is represented by three equivalent damper circuits; one on the direct axis (d-axis) and the other two on the quadrature axis (q-axis). The performance of the synchronous machine can be described by the equations given below in the d-q reference frame (Figure 2.2) [33]. In these equations, the convention adopted for the signs of the voltages and currents is that v is the impressed voltage at the terminals and that the direction of positive current i corresponds to generation. The sign of

the currents in the equivalent damper windings is taken positive when they flow in a direction similar to that of the positive field current.

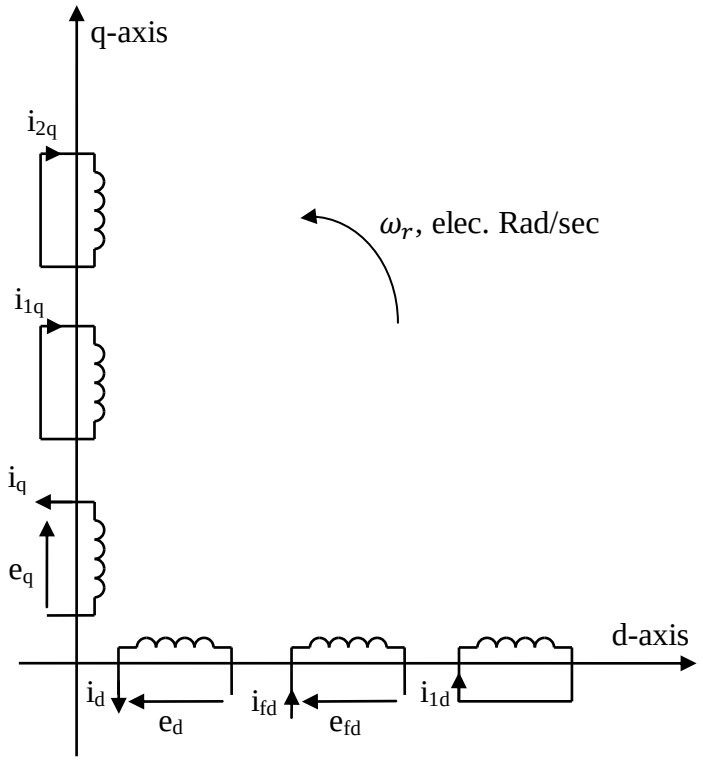

Figure 2.2: Modeling of the synchronous machine in the d-q reference frame.

With time *t* expressed in seconds, the angular velocity ω expressed in rad/s（ω_0 = 377 rad/sec） and the other quantities expressed in per unit, the stator equations become:

$$e_d = \frac{1}{\omega_0}\frac{d\Psi_d}{dt} - \frac{\omega}{\omega_0}\Psi_q - R_a i_d \tag{2.1}$$

$$e_q = \frac{1}{\omega_0}\frac{d\Psi_q}{dt} + \frac{\omega}{\omega_0}\Psi_d - R_a i_q \tag{2.2}$$

The rotor equations:

$$e_{fd} = \frac{1}{\omega_0}\frac{d\Psi_{fd}}{dt} + R_{fd} i_{fd} \tag{2.3}$$

$$0 = \frac{1}{\omega_0}\frac{d\Psi_{1d}}{dt} + R_{1d} i_{1d} \tag{2.4}$$

$$0 = \frac{1}{\omega_0}\frac{d\Psi_{1q}}{dt} + R_{1q} i_{1q} \tag{2.5}$$

$$0 = \frac{1}{\omega_0}\frac{d\Psi_{2q}}{dt} + R_{2q}i_{2q} \tag{2.6}$$

The stator flux linkage equations:

$$\Psi_d = -L_d i_d + L_{ad} i_{fd} + L_{ad} i_{1d} \tag{2.7}$$

$$\Psi_q = -L_q i_q + L_{aq} i_{1q} + L_{aq} i_{2q} \tag{2.8}$$

The rotor flux linkage equations:

$$\Psi_{fd} = L_{ffd} i_{fd} + L_{ad} i_{1d} - L_{ad} i_d \tag{2.9}$$

$$\Psi_{1d} = L_{ad} i_{fd} + L_{11d} i_{1d} - L_{ad} i_d \tag{2.10}$$

$$\Psi_{1q} = L_{11q} i_{1q} + L_{aq} i_{2q} - L_{aq} i_q \tag{2.11}$$

$$\Psi_{2q} = L_{aq} i_{1q} + L_{22q} i_{2q} - L_{aq} i_q \tag{2.12}$$

The electromagnetic torque equation:

$$T_e = \Psi_d i_q - \Psi_q i_d \tag{2.13}$$

The overall differential equations which describe the transient performance of the synchronous machine are given by the following matrix equation [11], [15]:

$$\left[\frac{dX_{syn}}{dt}\right] = [At_{syn}][X_{syn}] + [Bt_{syn}]\begin{bmatrix} V_{td} \\ V_{tq} \\ e_{fd} \end{bmatrix} \tag{2.14}$$

where,

$$[X_{syn}] = [i_d \quad i_q \quad i_{fd} \quad i_{1q} \quad i_{1d} \quad i_{2q}]^T$$

$$[At_{syn}] = [L]^{-1}[Qt]$$

$$[Bt_{syn}] = [L]^{-1}[Rt]$$

$$[L] = \begin{bmatrix} -L_d & 0 & L_{ad} & 0 & L_{ad} & 0 \\ 0 & -L_q & 0 & L_{aq} & 0 & L_{aq} \\ -L_{ad} & 0 & L_{ffd} & 0 & L_{ad} & 0 \\ 0 & -L_{aq} & 0 & L_{11q} & 0 & L_{aq} \\ -L_{aq} & 0 & L_{ad} & 0 & L_{11d} & 0 \\ 0 & -L_{aq} & 0 & L_{aq} & 0 & L_{22q} \end{bmatrix} \tag{2.15}$$

$$[Qt] = \begin{bmatrix} \omega_0 R_a & -\omega L_q & 0 & \omega L_{aq} & 0 & \omega L_{aq} \\ \omega L_d & \omega_0 R_a & -\omega L_{ad} & 0 & -\omega L_{ad} & 0 \\ 0 & 0 & -\omega_0 R_{fd} & 0 & 0 & 0 \\ 0 & 0 & 0 & -\omega_0 R_{1q} & 0 & 0 \\ 0 & 0 & 0 & 0 & -\omega_0 R_{1d} & 0 \\ 0 & 0 & 0 & 0 & 0 & -\omega_0 R_{2q} \end{bmatrix}$$

$$[Rt] = \begin{bmatrix} \omega_0 & 0 & 0 \\ 0 & \omega_0 & 0 \\ 0 & 0 & \omega_0 \\ 0 & 0 & 0 \\ 0 & 0 & 0 \\ 0 & 0 & 0 \end{bmatrix}$$

Here, the superscript ^{T} means matrix transpose.

The synchronous machine swing equation can be written as:

$$\frac{M}{\omega_0}\frac{d\omega}{dt} = T_{MECH} - T_e \tag{2.16}$$

$$\frac{d\delta}{dt} = \omega - \omega_0 \tag{2.17}$$

In the above two equations (2.16 and 2.17), ω is in radians per second, the inertia constant M is in seconds, and the load angle δ is in radians, ω_0 is the synchronous frequency (377 rad/sec) and the mechanical and electrical torques T_{MECH} and T_e are in per unit.

In developing the equations of multi-machine systems, the equations of each synchronous machine expressed in its own d-q reference frame which rotates with its rotor must be expressed in a common reference frame. Usually, a reference frame rotating at synchronous speed is used as the common reference. Axis transformation equations are used to transform between the individual machine (d-q) reference frames and the common (R-I) reference frame [33].

2.3.2 Modeling of the transmission line

A series capacitor-compensated transmission line may be represented by the *RLC* circuit shown in Figure 2.3 [11], [15]. In the voltage phasor diagram shown in Figure 2.4 [15], the rotor angle δ is the angle (in elec. *rad*) by which the q-axis leads the infinite-bus (reference) voltage

V_b. The differential equations for the circuit elements, after applying Park's transformation, can be expressed in the d-q reference frame by the following matrix expressions [15], [33].

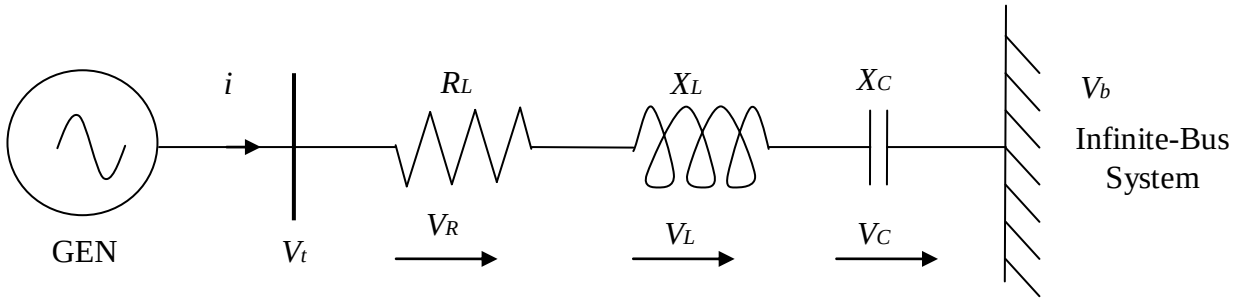

Figure 2.3: A series capacitor compensated transmission line.

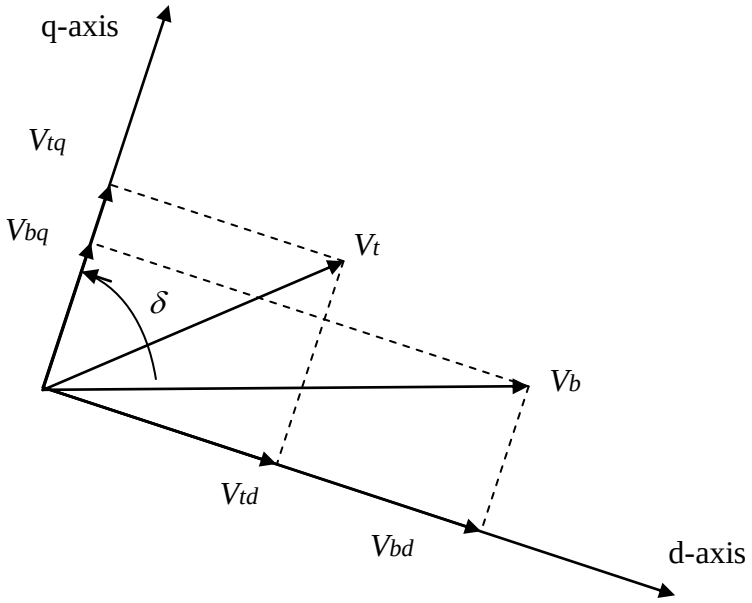

Figure 2.4: Voltage phasor diagram.

The voltage across the resistance:

$$\begin{bmatrix} V_{Rd} \\ V_{Rq} \end{bmatrix} = \begin{bmatrix} R_L & 0 \\ 0 & R_L \end{bmatrix} \begin{bmatrix} i_d \\ i_q \end{bmatrix} \tag{2.18}$$

The voltage across the inductance:

$$\begin{bmatrix} V_{Ld} \\ V_{Lq} \end{bmatrix} = \begin{bmatrix} 0 & -\frac{\omega}{\omega_0} X_L \\ \frac{\omega}{\omega_0} X_L & 0 \end{bmatrix} \begin{bmatrix} i_d \\ i_q \end{bmatrix} + \begin{bmatrix} \frac{X_L}{\omega_0} & 0 \\ 0 & \frac{X_L}{\omega_0} \end{bmatrix} \begin{bmatrix} \frac{di_d}{dt} \\ \frac{di_q}{dt} \end{bmatrix} \tag{2.19}$$

The voltage across the capacitor:

$$\begin{bmatrix} \frac{dV_{Cd}}{dt} \\ \frac{dV_{Cq}}{dt} \end{bmatrix} = \begin{bmatrix} \omega_0 X_C & 0 \\ 0 & \omega_0 X_C \end{bmatrix} \begin{bmatrix} i_d \\ i_q \end{bmatrix} + \begin{bmatrix} 0 & \omega \\ -\omega & 0 \end{bmatrix} \begin{bmatrix} V_{Cd} \\ V_{Cq} \end{bmatrix} \tag{2.20}$$

The overall equations of the transmission line can be written as:

$$\begin{bmatrix} \frac{dV_{Cd}}{dt} \\ \frac{dV_{Cq}}{dt} \\ V_{td} \\ V_{tq} \end{bmatrix} = [Att] \begin{bmatrix} V_{Cd} \\ V_{Cq} \end{bmatrix} + [Rt1] \begin{bmatrix} \frac{di_d}{dt} \\ \frac{di_q}{dt} \end{bmatrix} + [Rt2] \begin{bmatrix} i_d \\ i_q \end{bmatrix} + [Btt][V_b] \tag{2.21}$$

where

$$[Att] = \begin{bmatrix} 0 & \omega \\ -\omega & 0 \\ 1 & 0 \\ 0 & 1 \end{bmatrix}$$

$$[Rt1] = \begin{bmatrix} 0 & 0 \\ 0 & 0 \\ \frac{X_L}{\omega_0} & 0 \\ 0 & \frac{X_L}{\omega_0} \end{bmatrix}$$

$$[Rt2] = \begin{bmatrix} \omega_0 X_C & 0 \\ 0 & \omega_0 X_C \\ R_L & -\frac{\omega}{\omega_0} X_L \\ \frac{\omega}{\omega_0} X_L & R_L \end{bmatrix} \tag{2.22}$$

$$[Btt] = \begin{bmatrix} 0 \\ 0 \\ \sin\delta \\ \cos\delta \end{bmatrix}$$

2.3.3 Modeling of the turbine-generator mechanical system

Figure 2.5 illustrates a typical representation of the mechanical system of a large turbine-generator which consists of a high-pressure turbine (HP), an intermediate-pressure turbine (IP), two low-pressure turbines (LPA & LPB), the generator rotor (GEN) and the exciter (EXC). Such a system can be modeled by a six-mass-spring system [15].

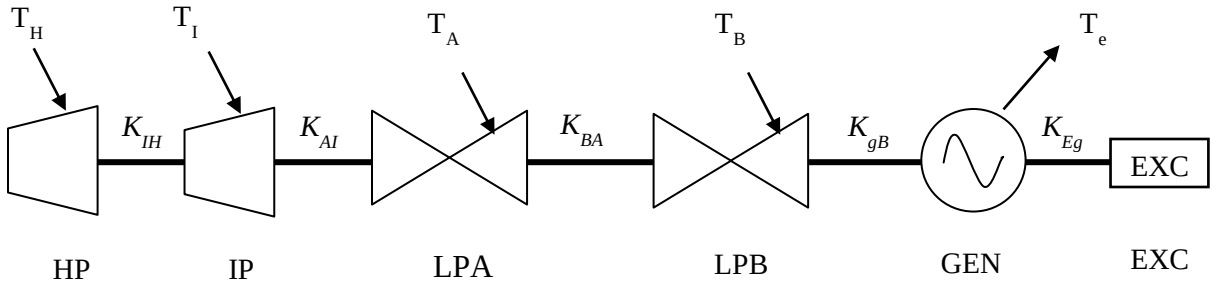

Figure 2.5: Representation of a typical turbine-generator shaft system.

Assuming that M is the inertia constant in seconds, D is the damping coefficient in p.u. torque/p.u. speed for each rotating mass and K is the stiffness in p.u. torque/rad for each shaft section, the equations of the i^{th} mass of an N-mass spring system shown in Figure 2.6 are given by [15]:

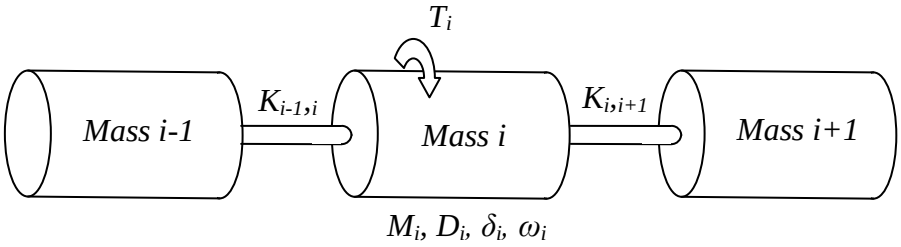

Figure 2.6: The ith mass of an N-mass spring system.

$$\frac{M_i}{\omega_0}\frac{d\omega_i}{dt} = T_i + K_{i-1,i}(\delta_{i-1} - \delta_i) - K_{i,i+1}(\delta_i - \delta_{i+1}) - \frac{D_i}{\omega_0}(\omega_i - \omega_0) \tag{2.23}$$

$$\frac{d\delta_i}{dt} = \omega_i - \omega_0 \tag{2.24}$$

where

$$K_{i-1,i}|_{i=1} = 0, \qquad K_{i,i+1}|_{i=N} = 0 \tag{2.25}$$

The two shaft torsional torques of the three-mass system in Figure 2.6 are the two terms $K_{i-1,i}(\delta_{i-1} - \delta_i)$ and $K_{i,i+1}(\delta_i - \delta_{i+1})$.

As an example, when Equations (2.23) to (2.25) are applied to the linear six-mass-spring system of Figure 2.5, the shaft system equations are written as:

$$\frac{M_E}{\omega_0}\frac{d\omega_E}{dt} = K_{Eg}(\delta - \delta_E) - \frac{D_E}{\omega_0}(\omega_E - \omega_0)$$

$$\frac{d\delta_E}{dt} = \omega_E - \omega_0$$

$$\frac{M_g}{\omega_0}\frac{d\omega}{dt} = -T_e + K_{gB}(\delta_B - \delta) - K_{Eg}(\delta - \delta_E) - \frac{D_g}{\omega_0}(\omega - \omega_0)$$

$$\frac{d\delta}{dt} = \omega - \omega_0$$

$$\frac{M_B}{\omega_0}\frac{d\omega_B}{dt} = \frac{\omega_0}{\omega_B}P_B + K_{BA}(\delta_A - \delta_B) - K_{gB}(\delta_B - \delta) - \frac{D_B}{\omega_0}(\omega_B - \omega_0)$$

$$\frac{d\delta_B}{dt} = \omega_B - \omega_0 \qquad (2.26)$$

$$\frac{M_A}{\omega_0}\frac{d\omega_A}{dt} = \frac{\omega_0}{\omega_A}P_A + K_{AI}(\delta_I - \delta_A) - K_{BA}(\delta_A - \delta_B) - \frac{D_A}{\omega_0}(\omega_A - \omega_0)$$

$$\frac{d\delta_A}{dt} = \omega_A - \omega_0$$

$$\frac{M_I}{\omega_0}\frac{d\omega_I}{dt} = \frac{\omega_0}{\omega_I}P_I + K_{IH}(\delta_H - \delta_I) - K_{AI}(\delta_I - \delta_A) - \frac{D_I}{\omega_0}(\omega_I - \omega_0)$$

$$\frac{d\delta_I}{dt} = \omega_I - \omega_0$$

$$\frac{M_H}{\omega_0}\frac{d\omega_H}{dt} = \frac{\omega_0}{\omega_H}P_H - K_{IH}(\delta_H - \delta_I) - \frac{D_H}{\omega_0}(\omega_H - \omega_0)$$

$$\frac{d\delta_H}{dt} = \omega_H - \omega_0$$

The overall shaft equations are given by the following matrix equation:

$$\left[\frac{dX_{ms}}{dt}\right] = [At_{ms}][X_{ms}] + [Bt_{ms}][U_{tms}] \qquad (2.27)$$

where

$$[X_{ms}] = [\delta_E \quad \delta \quad \delta_B \quad \delta_A \quad \delta_I \quad \delta_H \quad \omega_E \quad \omega \quad \omega_B \quad \omega_A \quad \omega_I \quad \omega_H]^T$$

$$[U_{tms}] = [\omega_0 \quad P_H \quad P_I \quad P_A \quad P_B \quad T_e]^T \qquad (2.28)$$

$$[At_{ms}] = \begin{bmatrix} 0_{6\times6} & I_{6\times6} \\ As1 & As2 \end{bmatrix}$$

$$[As1] = \omega_0 \begin{bmatrix} -\frac{K_{Eg}}{M_E} & \frac{K_{Eg}}{M_E} & 0 & 0 & 0 & 0 \\ \frac{K_{Eg}}{M_g} & -\frac{K_{gB}+K_{Eg}}{M_g} & \frac{K_{gB}}{M_g} & 0 & 0 & 0 \\ 0 & \frac{K_{gB}}{M_B} & -\frac{K_{BA}+K_{gB}}{M_B} & \frac{K_{gB}}{M_B} & 0 & 0 \\ 0 & 0 & \frac{K_{BA}}{M_A} & -\frac{K_{AI}+K_{BA}}{M_A} & \frac{K_{AI}}{M_A} & 0 \\ 0 & 0 & 0 & \frac{K_{AI}}{M_I} & -\frac{K_{HI}+K_{AI}}{M_I} & \frac{K_{HI}}{M_I} \\ 0 & 0 & 0 & 0 & \frac{K_{HI}}{M_H} & -\frac{K_{HI}}{M_H} \end{bmatrix}$$

$$[As2] = \begin{bmatrix} -\frac{D_E}{M_E} & 0 & 0 & 0 & 0 & 0 \\ 0 & -\frac{D_g}{M_g} & 0 & 0 & 0 & 0 \\ 0 & 0 & -\frac{D_B}{M_B} & 0 & 0 & 0 \\ 0 & 0 & 0 & -\frac{D_A}{M_A} & 0 & 0 \\ 0 & 0 & 0 & 0 & -\frac{D_I}{M_I} & 0 \\ 0 & 0 & 0 & 0 & 0 & -\frac{D_H}{M_H} \end{bmatrix} \quad (2.29)$$

$$[Bt_{ms}] = \begin{bmatrix} -1_{6\times1} & 0_{6\times1} & 0_{6\times1} & 0_{6\times1} & 0_{6\times1} & 0_{6\times1} \\ \frac{D_E}{M_E} & 0 & 0 & 0 & 0 & 0 \\ \frac{D_g}{M_g} & 0 & 0 & 0 & 0 & -\frac{\omega_0}{M_g} \\ \frac{D_B}{M_B} & 0 & 0 & 0 & \frac{\omega_0^2}{\omega_B M_B} & 0 \\ \frac{D_A}{M_A} & 0 & 0 & \frac{\omega_0^2}{\omega_B M_B} & 0 & 0 \\ \frac{D_I}{M_I} & 0 & \frac{\omega_0^2}{\omega_I M_I} & 0 & 0 & 0 \\ \frac{D_H}{M_H} & \frac{\omega_0^2}{\omega_H M_H} & 0 & 0 & 0 & 0 \end{bmatrix}$$

Here, the $[\boldsymbol{I}_{nxn}]$ is an *n* by *n* identity matrix, 0_{mxn} is an *m* by *n* matrix with all elements zero, and -1_{6x1} is a 6 by 1 matrix with all elements -1. The natural torsional frequencies of oscillations of the turbine-generator shaft system are the eigenvalues of the matrix [AS1] [7].

2.3.4 Doubly-fed induction generator (DFIG) wind turbine

The basic structure of a doubly-fed induction generator (DFIG) wind turbine is shown in Figure 2.7. The stator of the induction machine is directly connected to the grid and the wound rotor windings are connected to the grid through slip rings and an indirect ac-ac converter system which controls both the rotor and the grid currents. The ac-ac converter system consists of two three-phase pulse-width modulated (PWM) Voltage-Sourced Converters (VSC) (Rotor-Side Converter (RSC) and Grid-Side Converter (GSC)) connected by a dc bus. A line inductor and an ac filter are used at the GSC to improve the power quality. A crowbar is also used to protect the RSC against over-current and the dc capacitor against over-voltage [34].

The control of the DFIG is realized by controlling the RSC and GSC using vector control techniques. The function of the RSC is to control the active and reactive powers delivered to the grid, and to follow a tracking characteristic to adjust the generator speed for optimal power generation depending on the wind speed. On the other hand, the function of the GSC is to keep the dc bus voltage constant and to support the grid with reactive power during system faults [34].

The main advantage of the DFIG is the low cost of its converters as their rating is typically 25% to 30% of the DFIG rated power. As a result, the cost of the converters and electromagnetic interference (EMI) filters is also reduced.

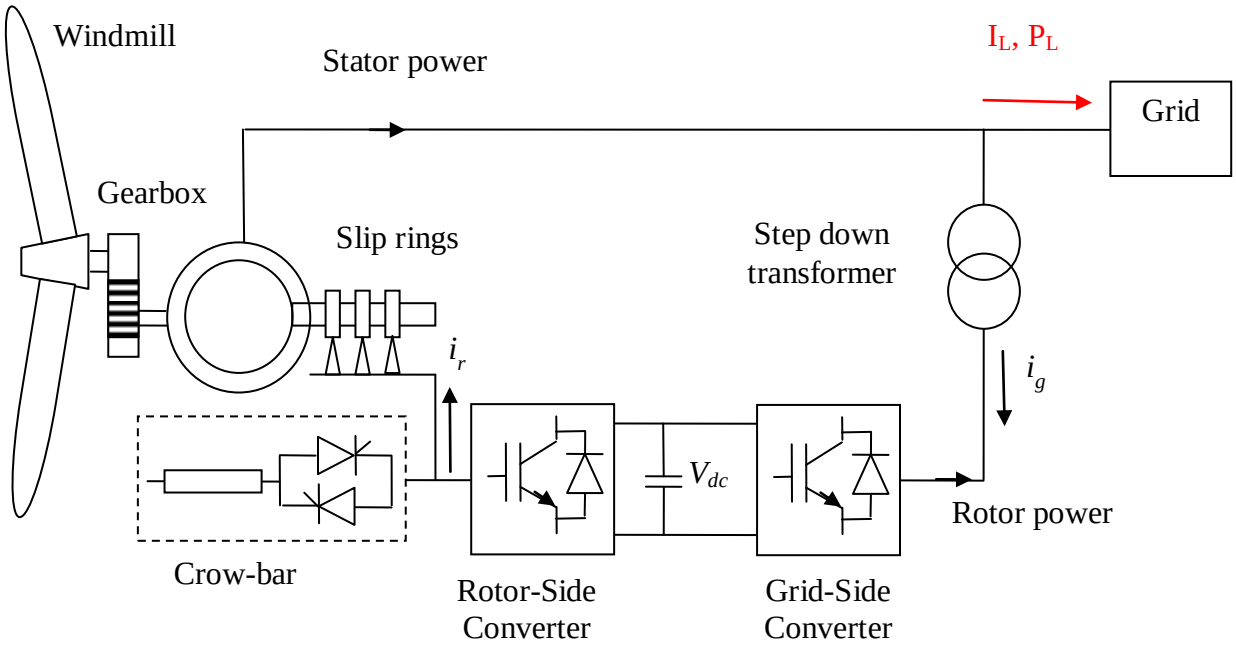

Figure 2.7: A basic configuration of a DFIG wind turbine.

2.3.5 Wind Turbine Aerodynamic Model

The dynamic output mechanical torque of the wind turbine is expressed as [8, 31]:

$$T_{MECH} = \frac{1}{2}\rho A R_\omega C_P V_\omega^2/\lambda \tag{2.30}$$

where ρ is the air density (kgm^{-3}), A is the blade sweep area (m^2), R_ω is the blade length (m), and V_ω is the wind speed (m/s), C_P is the power coefficient of the blade which is a function of the blade pitch angle θ and the tip speed ratio λ according to the following equation:

$$C_P = \frac{1}{2}\left(\frac{R_\omega C_f}{\lambda} - 0.022\theta - 2\right) e^{-0.255\frac{R_\omega C_f}{\lambda}} \tag{2.31}$$

where; C_f = wind turbine blade design constant and the tip speed ratio

λ = tip speed ratio of the wind turbine, given by [31]:

$$\lambda = \frac{\omega_m R_\omega}{V_\omega} \tag{2.32}$$

where, ω_m, is the wind turbine rotational speed in rad/s.

The mechanical power, wind turbine rotor speed and wind speed relationships are illustrated in Figure 2.8 [8].

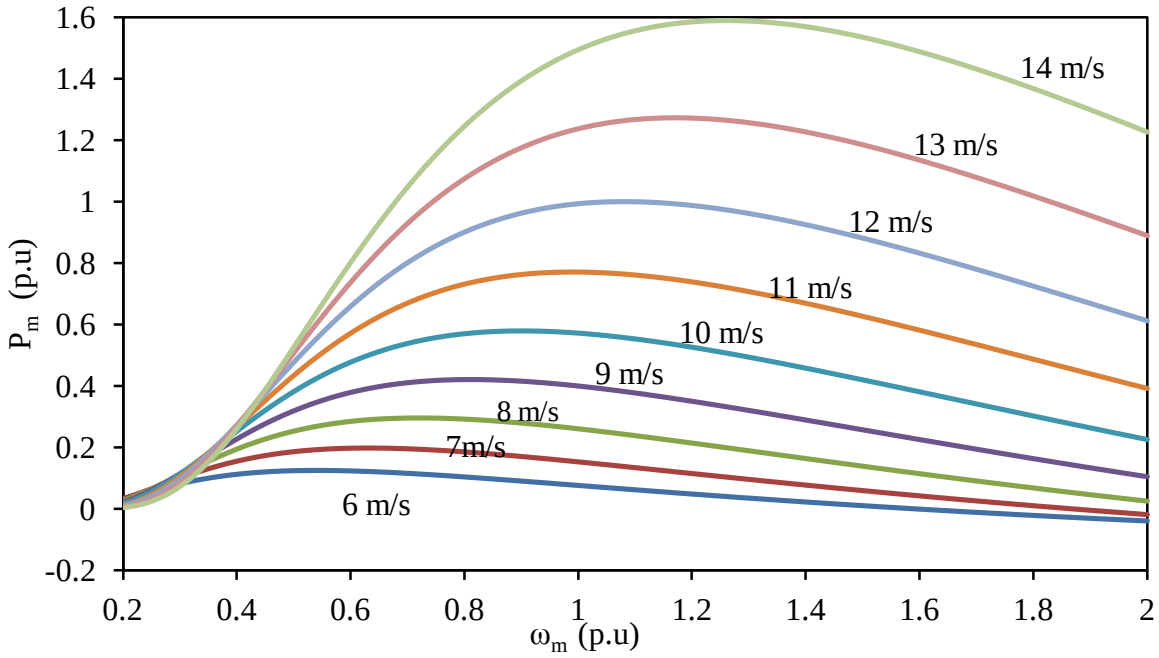

Figure 2.8: Mechanical power, rotor speed and wind speed relationships.

2.3.6 Modeling of the DFIG

Figure 2.9 shows the equivalent circuit of a DFIG in the synchronous q-d reference frame, where the q-axis leads the d-axis by 90˚ [11].

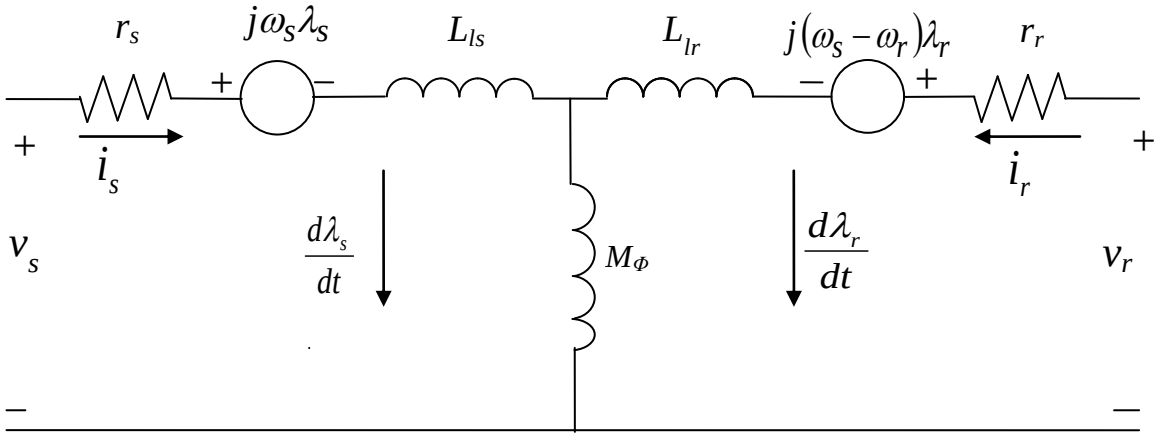

Figure 2.9: Equivalent circuit of a DFIG.

The stator and rotor voltage equations in the q-d reference frame can be written as:

$$\begin{cases} v_s = r_s i_s + j\omega_s \lambda_s + \frac{d\lambda_s}{dt} \\ v_r = r_r i_r + j(\omega_S - \omega_r)\lambda_r + \frac{d\lambda_r}{dt} \end{cases} \quad (2.33)$$

where $v_s = v_{qs} - jv_{ds}$; $v_r = v_{qr} - jv_{dr}$

The flux linkage expressions are given as follows:

$$\begin{cases} \lambda_s = L_s i_s + M_\Phi i_r \\ \lambda_r = L_r i_r + M_\Phi i_s \end{cases} \quad (2.34)$$

where $L_s = L_{ls} + M_\Phi$; $L_r = L_{lr} + M_\Phi$; $\lambda_s = \lambda_{qs} - j\lambda_{ds}$

$\lambda_r = \lambda_{qr} - j\lambda_{dr}$; $i_s = i_{qs} - ji_{ds}$; $i_r = i_{qr} - ji_{dr}$

From Equations 2.33 and 2.34, a set of differential equations with the stator and rotor currents are state variables and the stator and rotor voltage as inputs can be established. While the rotor voltages are determined by the RSC control scheme, the stator voltages are determined by the network interface.

The electromagnetic torque, T_e, can be expressed as follows:

$$T_e = \lambda_{qm} i_{dr} - \lambda_{dm} i_{qr} \quad (2.35)$$

where λ_{qm} and λ_{dm} are, respectively, the q- and d-axes magnetizing flux linkages defined as:

$$\begin{cases} \lambda_{qm} = \lambda_{qs} - i_{qs} L_{ls} \\ \lambda_{dm} = \lambda_{ds} - i_{ds} L_{ls} \end{cases} \quad (2.36)$$

2.3.7 Modeling of the BtB dc capacitor link

The dynamics of the BtB dc capacitor link can be described using the equivalent circuit shown in Figure 2.10 as [8]:

$$C v_{dc} \frac{dv_{dc}}{dt} = P_r - P_g \quad (2.37)$$

where $$\begin{cases} P_r = K_1 (v_{qr} i_{qr} + v_{dr} i_{dr}) \\ P_g = K_2 (v_{qg} i_{qg} + v_{dg} i_{dg}) \end{cases} \quad (2.38)$$

In Equation 2.38, K_1 and K_2 are constants, P_r, P_g are the active powers of the RSC and the GSC respectively, v_{qr}, v_{dr} are the quadrature- and direct- axes RSC voltage respectively and v_{qg}, v_{dg} are the quadrature- and direct- axes GSC voltage respectively.

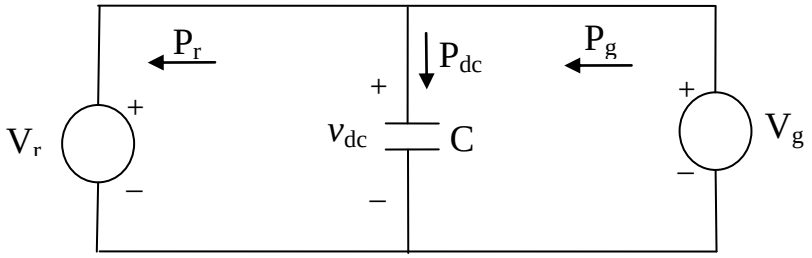

Figure 2.10: Equivalent circuit for the BtB dc capacitor link.

2.3.8 Control of the DFIG BtB converters

The control of the DFIG wind turbine is achieved by controlling the RSC and GSC utilizing vector control techniques. Vector control allows decoupled control of both the real and reactive power. The idea is to use a rotating reference frame based on an AC flux or voltage and then to project the currents on this rotating frame. Such projections are usually referred to as the d- and q- components of their respective currents. For flux-based rotating frames, changes in the q- component leads to real power changes, while changes in the d- component leads to reactive power changes. In voltage-based rotating frames (90˚ ahead of flux-based frames), the effect is the opposite.

Figure 2.11 shows a general control scheme for the DFIG BtB converters [35]. In such a scheme, the RSC operates in the stator flux reference while the GSC operates in the stator voltage reference frame. The q-axis current of the RSC is used to control the real power while the d-axis current is used for reactive power control. On the other hand, the d-axis current for the GSC is used to control the dc link voltage to a constant level while the q-axis current is used for reactive power control.

As illustrated in Figure 2.11, both RSC and GSC are controlled by a two-stage controller. The first stage consists of very fast current controllers regulating the rotor currents to reference values that are specified by slower power controllers (Stage-2). In normal operation, the aim of the RSC is to control independently the real and reactive power on the grid while the GSC has to

maintain the dc link capacitor at a set value regardless of the magnitude and direction of the rotor power and to guarantee converter operation with unity power factor (zero reactive power) [35].

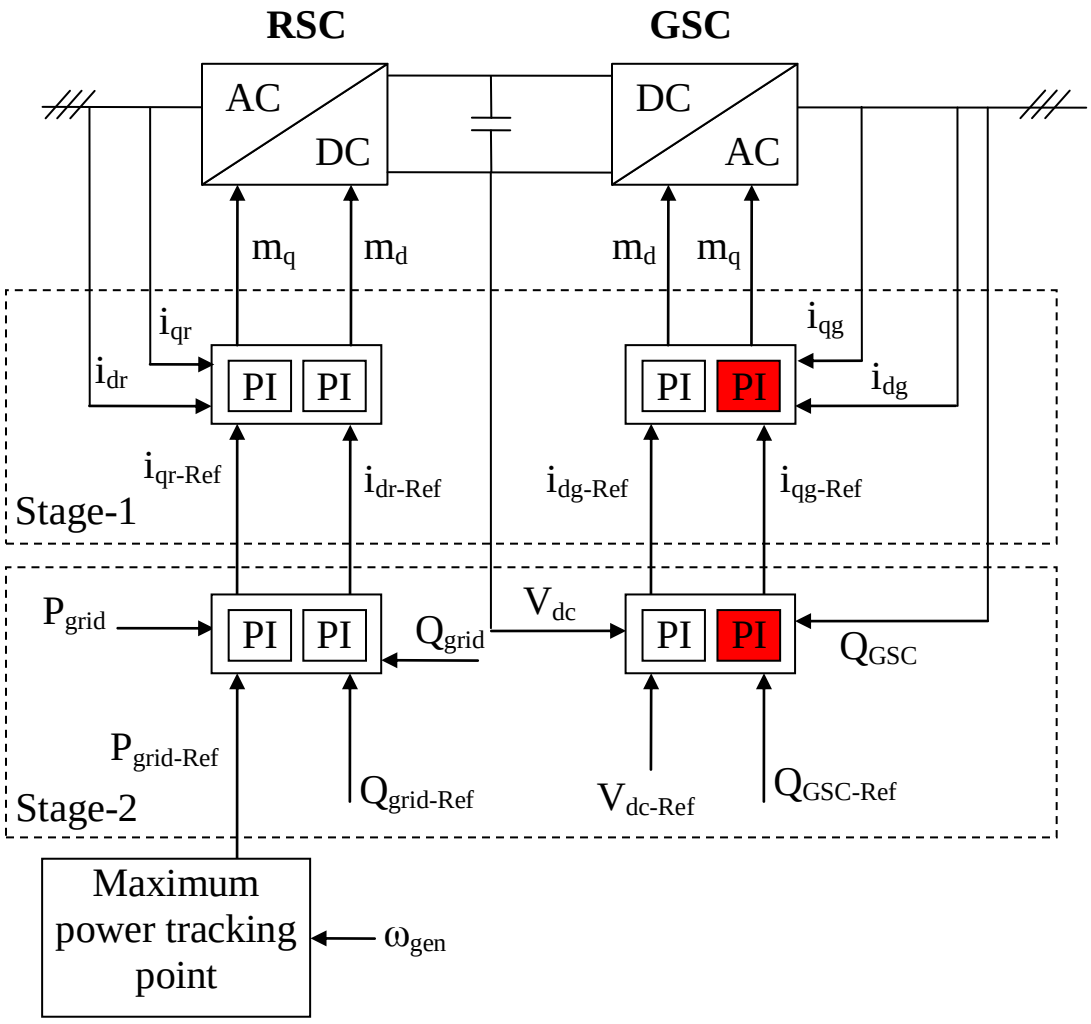

Figure 2.11: Schematic diagram of a general control scheme of DFIG BtB converters.

The reference $P_{grid-Ref}$ for the real power is given by the maximum power tracking point (MPT) lookup table as a function of the optimal generator speed. The reference $Q_{grid-Ref}$ for the reactive power of the RSC can be set to a certain value or to zero according to whether or not the DFIG is required to contribute with reactive power. The reactive power reference for the GSC, $Q_{GSC-Ref}$ is "usually" set to zero. This means that the GSC exchanges only real power with the grid and, therefore, the transmission of reactive power controllability of the GSC can be useful during the process of voltage reestablishment after clearing a system fault. The reference signal

V_{dc-Ref} is set to a constant value that depends on the size of the converter, the stator/rotor voltage ratio and the modulation factor of the power converter [35].

2.3.9 Modeling of voltage source converter (VSC)-HVDC system

The VSC-HVDC system has the capability to precisely control both active and reactive power flow to maintain voltage stability, using vector control strategy [36]. This makes it suitable for connecting offshore wind farms to the grid.

Figure 2.12 shows a representation of a VSC connected to an ac system [36]. From the figure, the system ac voltage is $V_S\angle 0°$ and the converter ac voltage is $V_{Sh}\angle\delta_{sh}$. Applying Kirchhoff's Voltage Law (KVL) to the circuit in Figure 2.12 obtains [36]:

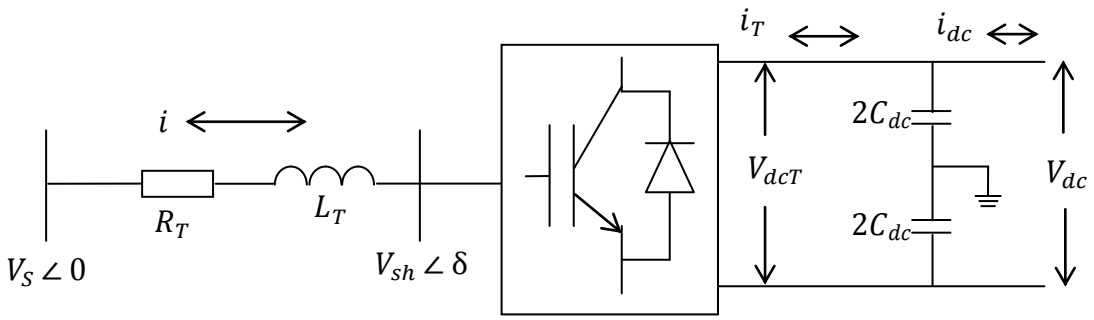

Figure 2.12: A representation of a VSC connected to an ac system.

$$Vs_{abc} = R_T i_{abc} + L_T \frac{d}{dt} i_{abc} + Vsh_{abc} \tag{2.39}$$

where, Vs_{abc} is the ac system voltage, Vsh_{abc} is the converter ac output voltage and i_{abc} is the three phase current. R_T and L_T are resistance and inductance of the converter transformer respectively. Equation 2.39 is converted into the d-q reference frame by applying Park's transformation and expressed as follows [36]:

$$Vs_{dq} = R_T i_{dq} + L_T \frac{d}{dt} i_{dq} + Vsh_{dq} \tag{2.40}$$

$$\frac{di_d}{dt} = \omega i_q + \frac{Vs_d - Vsh_d}{L_T} - \frac{R_T}{L_T} i_d \tag{2.41}$$

$$\frac{di_q}{dt} = -\omega i_d + \frac{Vs_q - Vsh_q}{L_T} - \frac{R_T}{L_T} i_q \tag{2.42}$$

Equations 2.41 and 2.42 are obtained by separating Equation 2.40 into the d-q reference frame. The converter ac voltage and dc voltage relationship in Figure 2.12 can be expressed as follows [36]:

$$V_{\mathrm{sh}}(t) = \frac{1}{2} V_{dc} M_I sin(\omega t + \delta_{sh}) \tag{2.43}$$

where, M_I is modulation index, δ_{sh} is phase shift between fundamental component of converter ac voltage and ac system voltage and V_{dc} is dc voltage. Transforming Equation 2.43 into the d-q reference frame yields [36]:

$$Vsh_d = \frac{1}{2} M_I V_{dc} cos\delta_{sh} \;\; ; \;\; Vsh_q = \frac{1}{2} M_I V_{dc} sin\delta_{sh} \tag{2.44}$$

The modulation index M_I and the angle δ_{sh} can be derived as follows using Equation 2.44:

$$M_I = \frac{2\sqrt{Vsh_d^2 + Vsh_q^2}}{V_{dc}}; \; \delta_{sh} = \; tan^{-1}\left(\frac{Vsh_q}{Vsh_d}\right) \tag{2.45}$$

where, Vsh_d and Vsh_q are d-axis and q-axis component of the converter ac voltage, V_{dc} is the dc voltage. The value of instantaneous active and reactive powers in d-q reference frame can be expressed as [36]:

$$P = \frac{3}{2}(Vs_d i_d + \; Vs_q i_q) \tag{2.46}$$

$$Q = \frac{3}{2}(-Vs_d i_q + \; Vs_q i_d) \tag{2.47}$$

The power on dc side is given by [36]:

$$P_{dc} = \; i_T Vdc_T \tag{2.48}$$

where, i_T is the current flowing through the dc terminal and Vdc_T is voltage at the dc terminals. The current i_T is given by:

$$i_T = \; C_{dc} \frac{dVdc_T}{dt} + \; i_{dc} \tag{2.49}$$

where, i_{dc} is the current flowing through dc cables and C_{dc} is the capacitor at dc side. Neglecting converter and transformer losses and applying the principle of power balance using Equations 2.46 and 2.48, the following equation is obtained [36]:

$$\frac{3}{2}\left(Vs_d i_d + \; Vs_q i_q\right) = \; i_T Vdc_T \tag{2.50}$$

Equation 2.51 is derived from Equations 2.48 and 2.49.

$$\frac{dVdc_T}{dt} = \frac{3}{2}\frac{Vs_d i_d}{Vdc_T C_{dc}} + \frac{3}{2}\frac{Vs_q i_q}{Vdc_T C_{dc}} - \frac{i_{dc}}{C_{dc}} \tag{2.51}$$

The mathematical model of the VSC in the synchronously rotating reference frame is represented by Equations 2.41, 2.42 and 2.51 [36].

2.3.10 Control of VSC-HVDC System

The VSC-HVDC system in EMTP-RV is modeled using vector control strategy which enables independent control of both active and reactive powers. Figure 2.13 shows the schematic diagram of a general control scheme of a VSC-HVDC system [36].

The VSC converter as shown Figure 2.13 is controlled by two-stage controllers, consisting of an outer power controller and an inner current controller. The inner stage (inner current control loop) consists of a very fast current controller regulating currents to reference values that are specified by slower power controllers (outer power control loop). Equation 2.45 forms the basis for the inner current controller, which controls the voltage drop in the transformer impedance and thus controls the converter ac voltage [36]. The VSC control scheme uses a phase-locked loop (PLL) block for synchronization of d-q reference frame vectors. This is done in such a way that the d-axis is in phase with phase A voltage vector, hence Vs_d = Vs and Vs_q = 0, substituting these values in Equations 2.46 and 2.47 yields Equation 2.52 [36]:

$$P = \frac{3}{2}(Vsi_d), Q = -\frac{3}{2}(Vsi_q) \tag{2.52}$$

Equation 2.52 shows that both active and reactive powers are controlled independently by i_d and i_q respectively, by assuming a constant voltage source. This forms the basis for the outer controller loop, Equation 2.52 can be re-written in terms of i_d and i_q as [36]:

$$i_{d-Ref} = \frac{2}{3}\left(\frac{P_{Ref}}{V_S}\right), i_{q-Ref} = -\frac{2}{3}\left(\frac{Q_{Ref}}{V_S}\right) \tag{2.53}$$

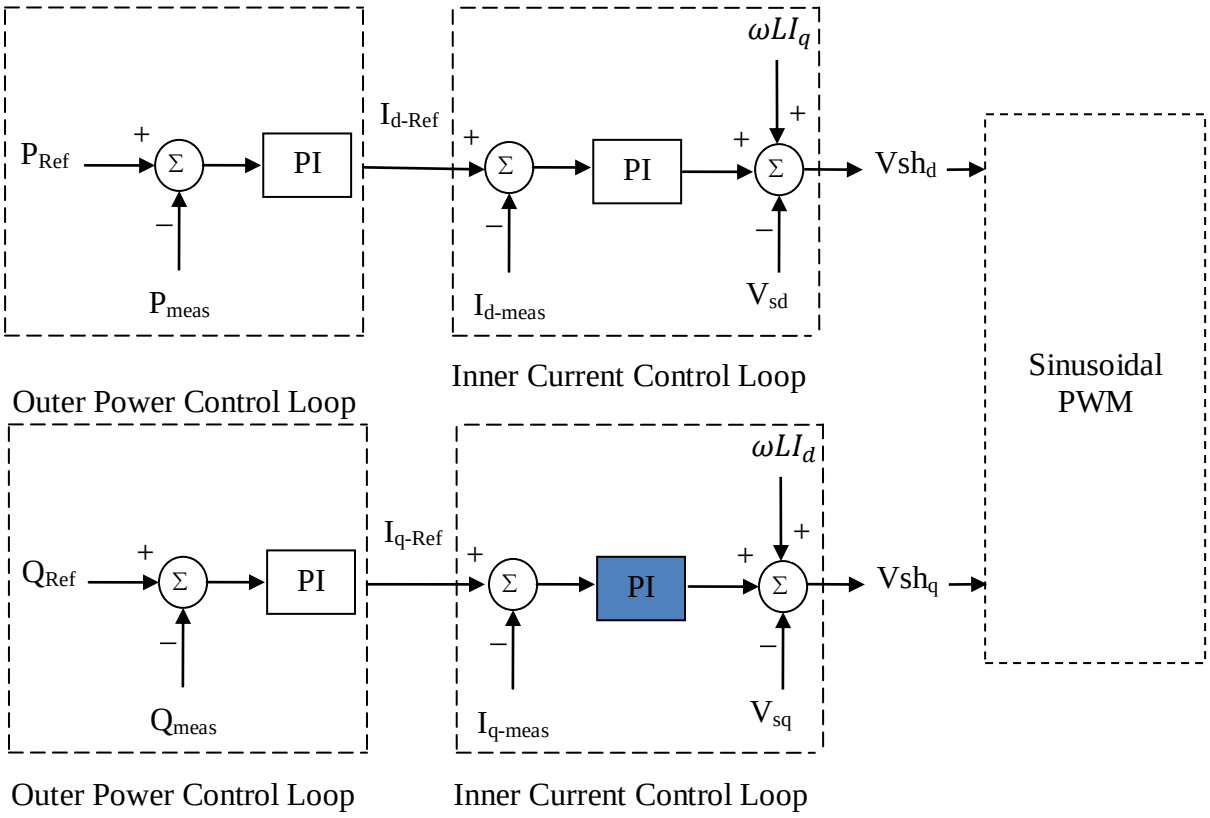

Figure 2.13: Schematic diagram of a general control scheme of a VSC-HVDC converter.

2.4 A Sample Case Study: 40% Compensation Degree in Lines 1 and 2

In the studies conducted in this thesis, the ElectroMagnetic Transient Program (EMTP-RV) is used for modeling the various system components and producing the time-domain simulation results. Moreover, faults are assumed to occur at t = 0.3 seconds.

Figure 2.14 shows the power flow results for the system bus voltages and transmission line real power flows. The turbine-generator electrical powers and shaft torsional torques during and after clearing the same fault are shown in Figure 2.15. The real and reactive powers, terminal voltages and dc capacitor voltages of wind farms A and B during and after clearing a 3-cycle, three-phase fault on Line 5 are shown in Figures 2.16 and 2.17 respectively. Moreover, the frequency spectrums (obtained by using Fast Fourier Transform (FFT) analysis) of the turbine-generator shaft torsional torques and the stator current of the DFIG wind turbine are illustrated in Figure 2.18.

The following observations can be made from examining these figures:

- The system is stable after fault clearing as the low-frequency oscillations in the turbine-generator electrical powers (PG1 and PG2, Figure 2.15) are damped.

- The Turbine-generator shaft torsional torques are not sinusodial with a single frequency component, but contain contributions from all the shaft section torsional modes. It is worth noting here that such contributions are obtained from the eigen-vectors of the matrix [AS1] given in Equation 2.29 [7]. Moreover, the shaft section between the generator rotor and the low-pressure stage turbine is subjected to the highest stresses as shown in Figure 2.15.

- The frequency spectrums of the turbine-generator shaft torsional torques, shown in Figure 2.18, identify the four natural torsional modes of oscillations of G1 and G2 shaft systems with frequencies 24.65 Hz, 32.39 Hz, 44.99 Hz and 51.1 Hz.
- At this compensation degree, wind farm A does not exhibit subsynchronous interaction as the oscillations in its real output power and terminal voltages are damped after fault clearing as shown in Figure 2.16.
- Except for the (GEN1-EXC) and (LP2-GEN2) shaft torsional torques which exhibit slowly growing oscillations, the other turbine-generator shaft torsional torques are either slightly damped or exhibit sustained oscillations as shown in Figure 2.15.
- Whereas the turbine-generator electrical powers (PG1 and PG2, Figure 2.15) decay quickly, the turbine-generator shaft torsional torques, shown in the same figure, persist for a relatively longer period. This is attributed to the greater damping which is inherent in the electrical system and the relatively low damping level in the turbine-generator shaft systems.

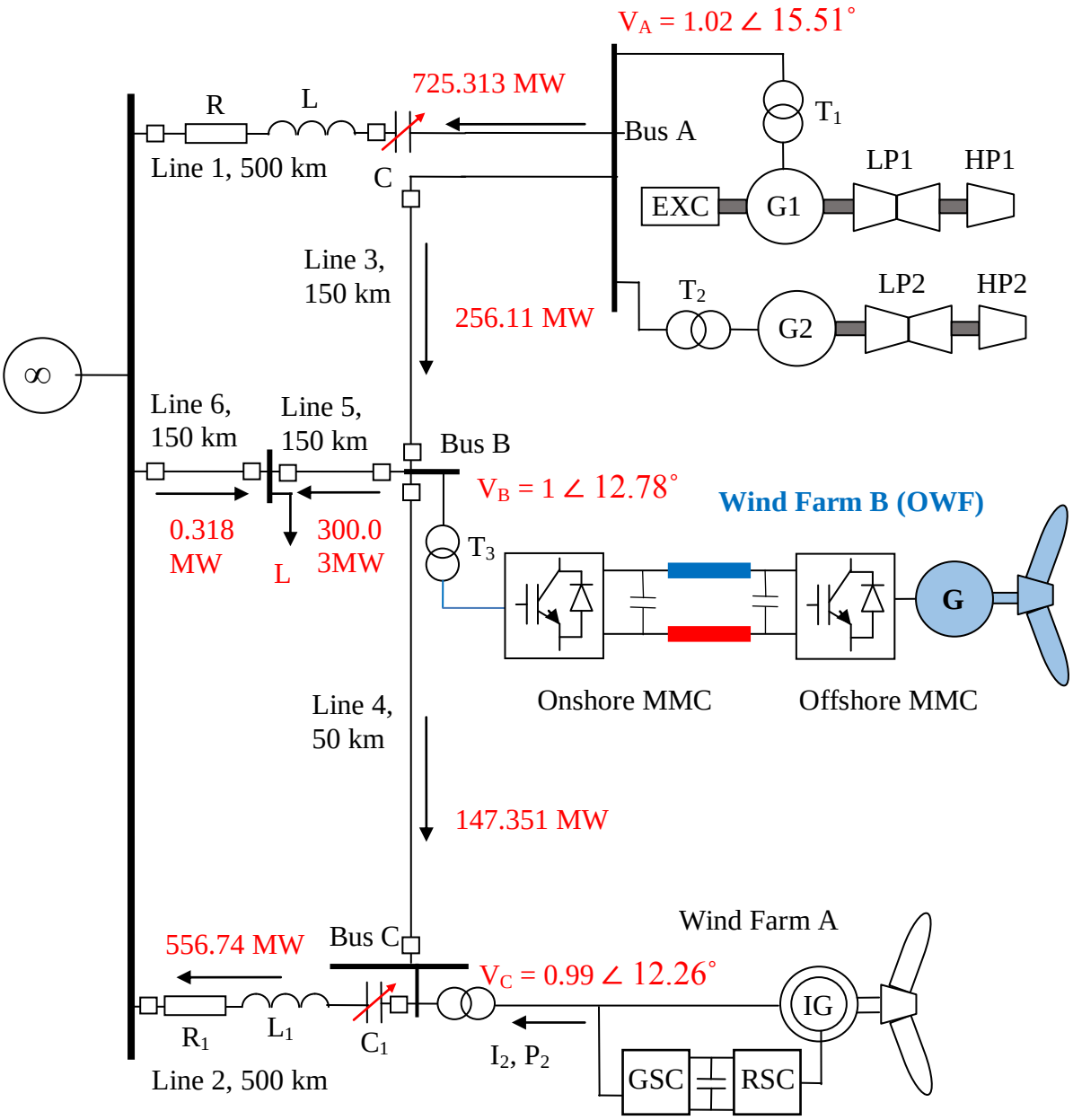

Load (L) = 300 MW + 150 MVAR

Figure 2.14: Power flow results of bus voltages and transmission line real power flows of the system under study.

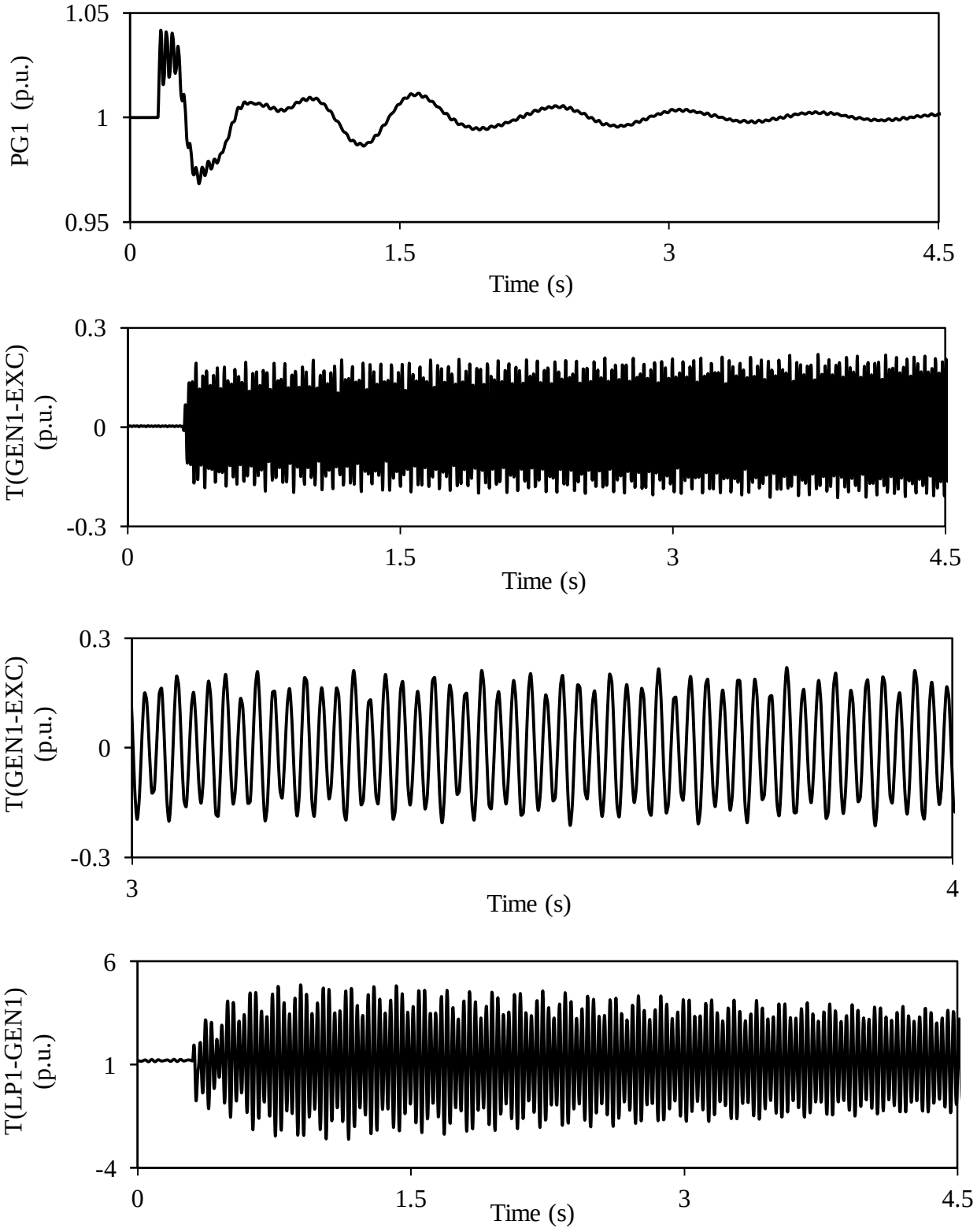

Figure 2.15: Turbine-generator electrical powers and shaft torsional torques during and after clearing a 3-cycle, three-phase fault on Line 5 (40% compensation degree).

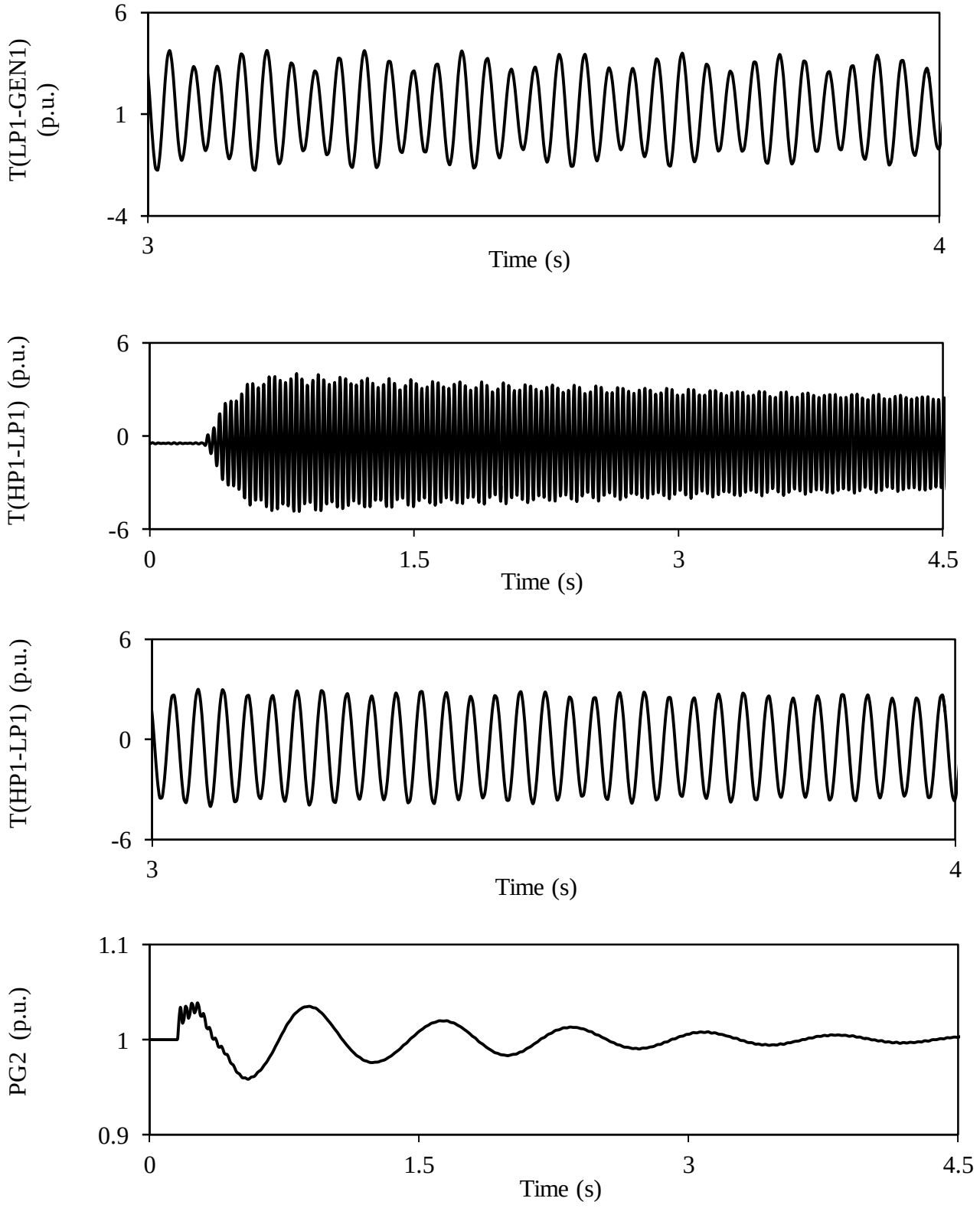

Figure 2.15: continued.

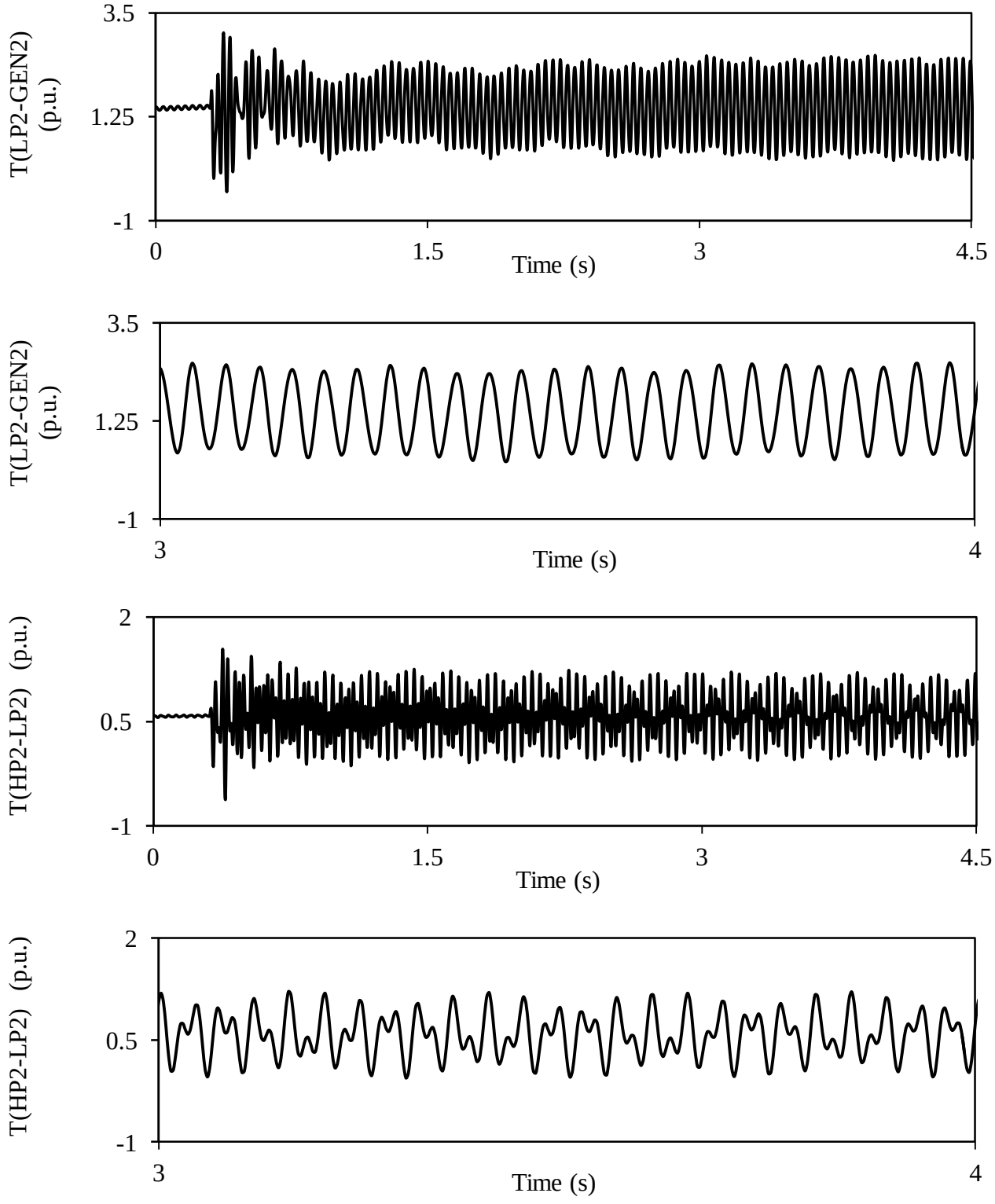

Figure 2.15: continued.

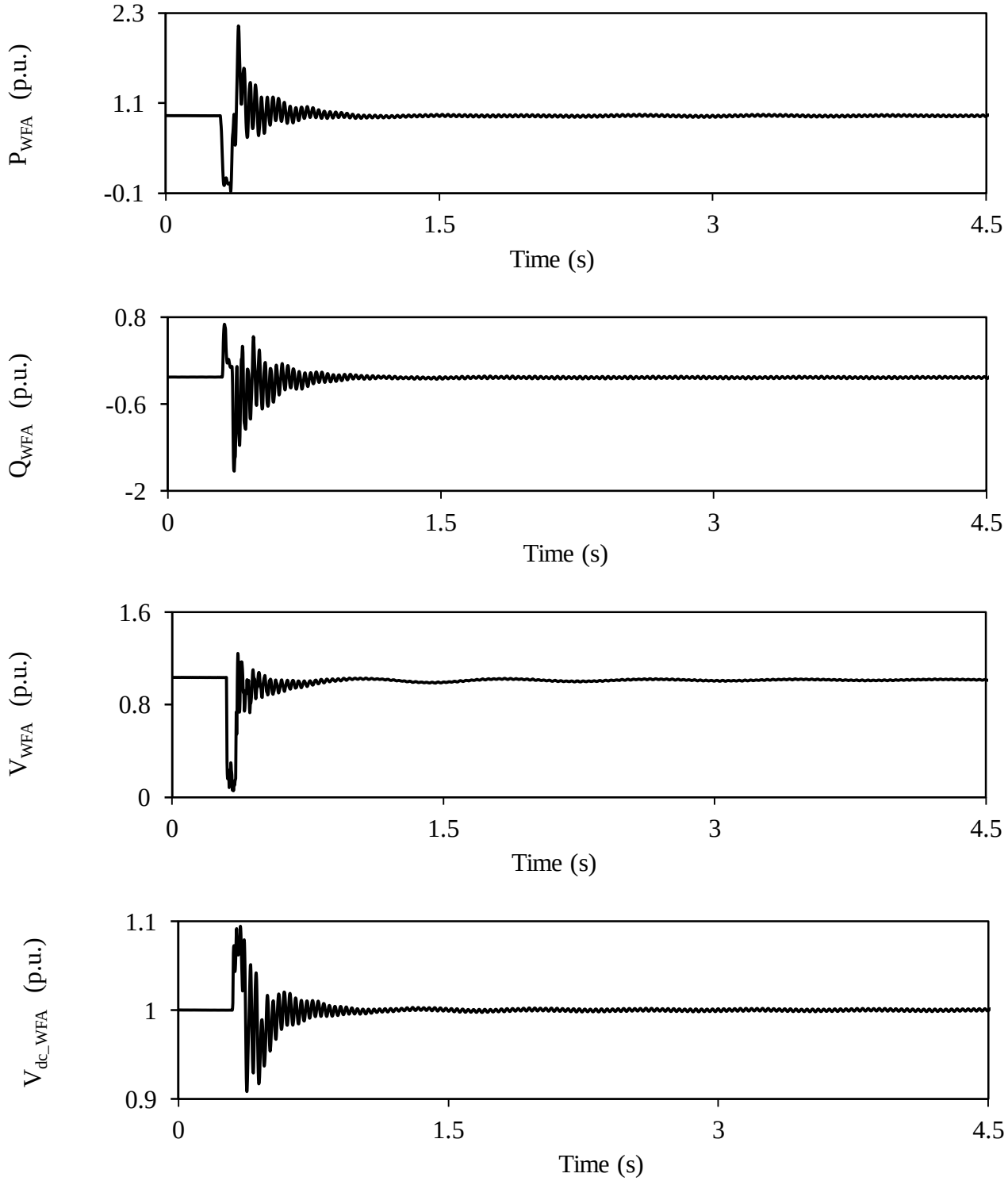

Figure 2.16: Wind farm A real and reactive powers, terminal voltage and dc capacitor voltage during and after clearing a 3-cycle, three-phase fault on Line 5 (40% compensation degree).

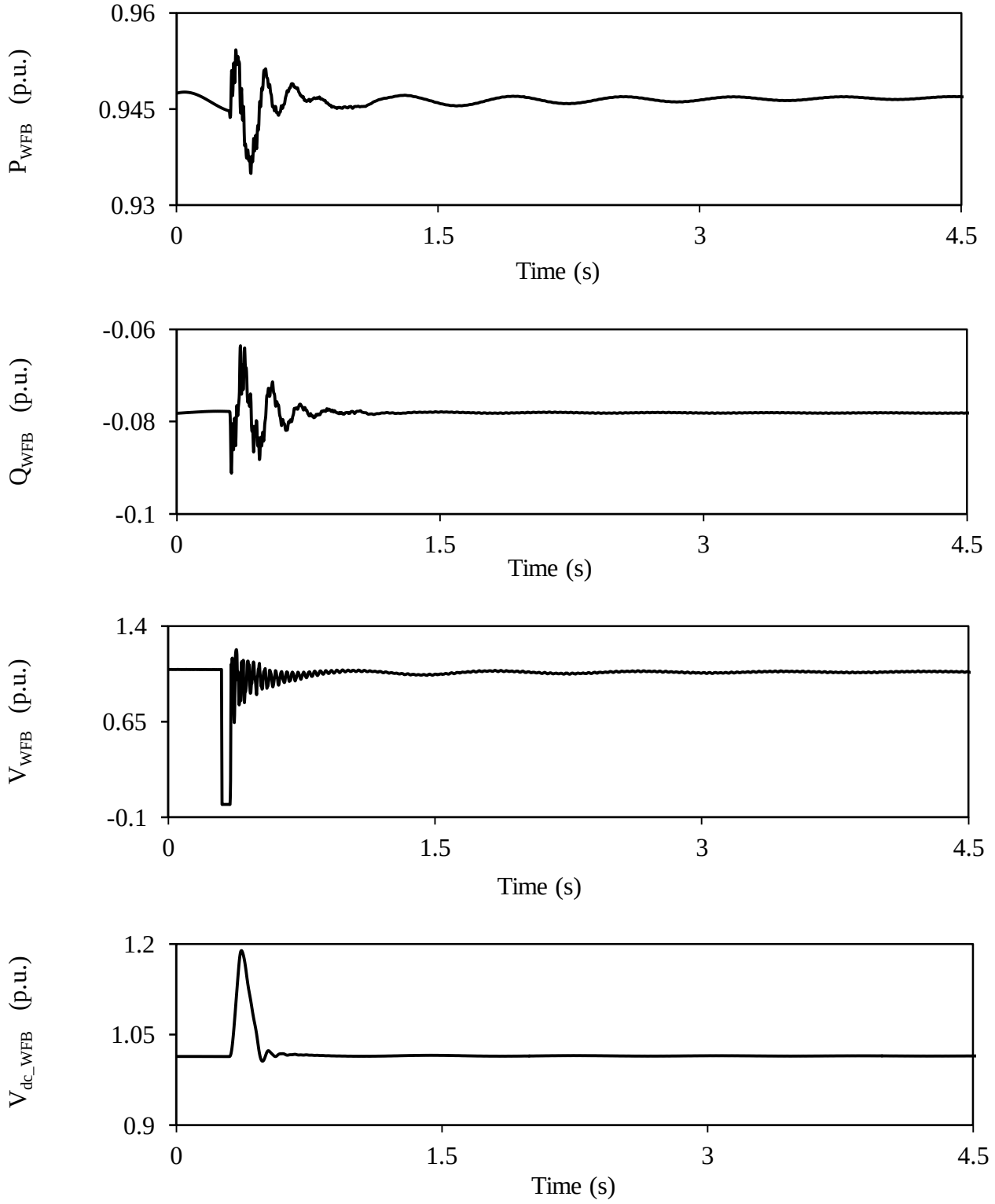

Figure 2.17: Wind farm B real and reactive powers, terminal voltage and dc capacitor voltage during and after clearing a 3-cycle, three-phase fault on Line 5 (40% compensation degree).

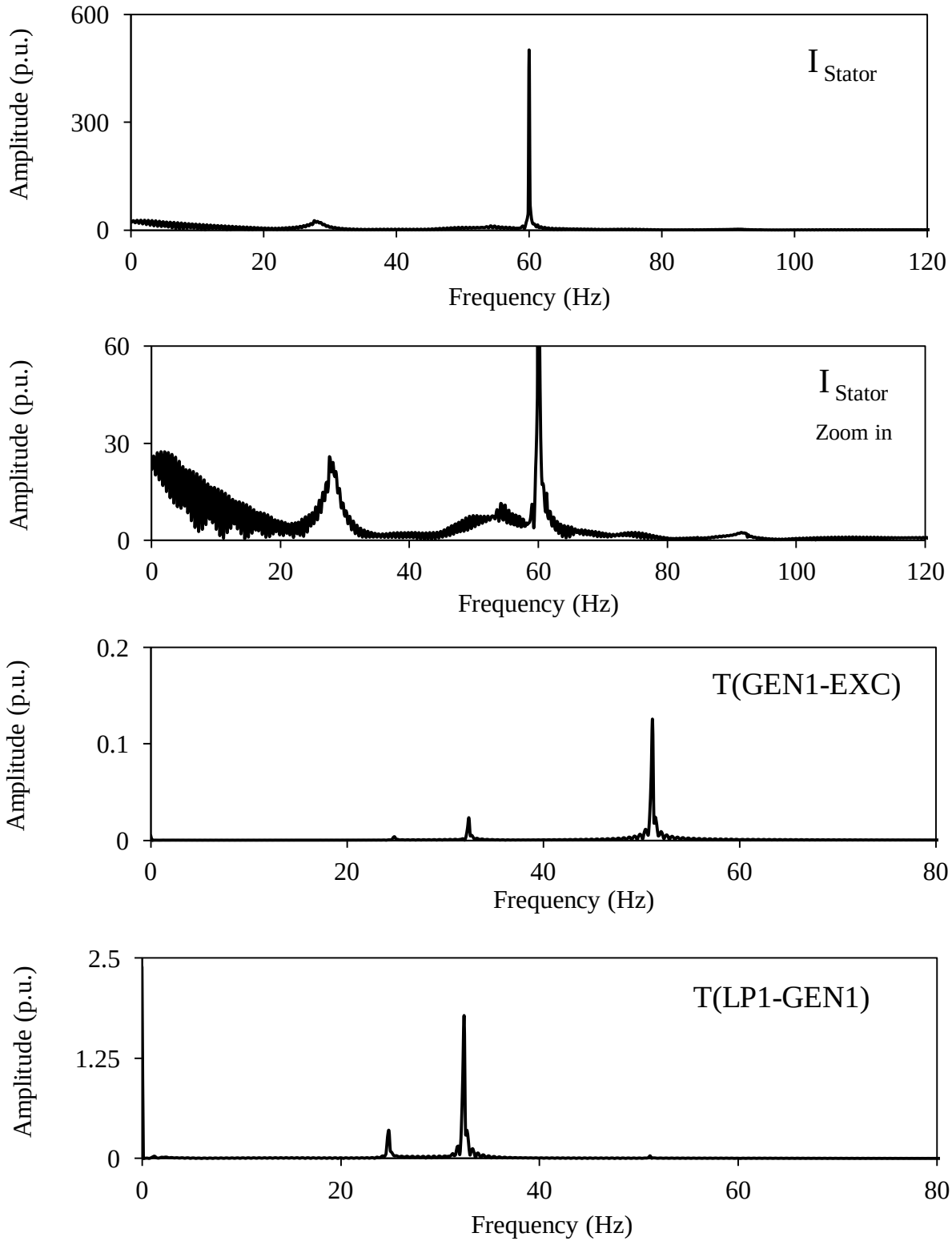

Figure 2.18: Frequency spectrums of the stator current of the DFIG wind turbine and the turbine-generator shaft torsional torques during and after clearing a 3-cycle, three-phase fault on Line 5 (40% compensation degree).

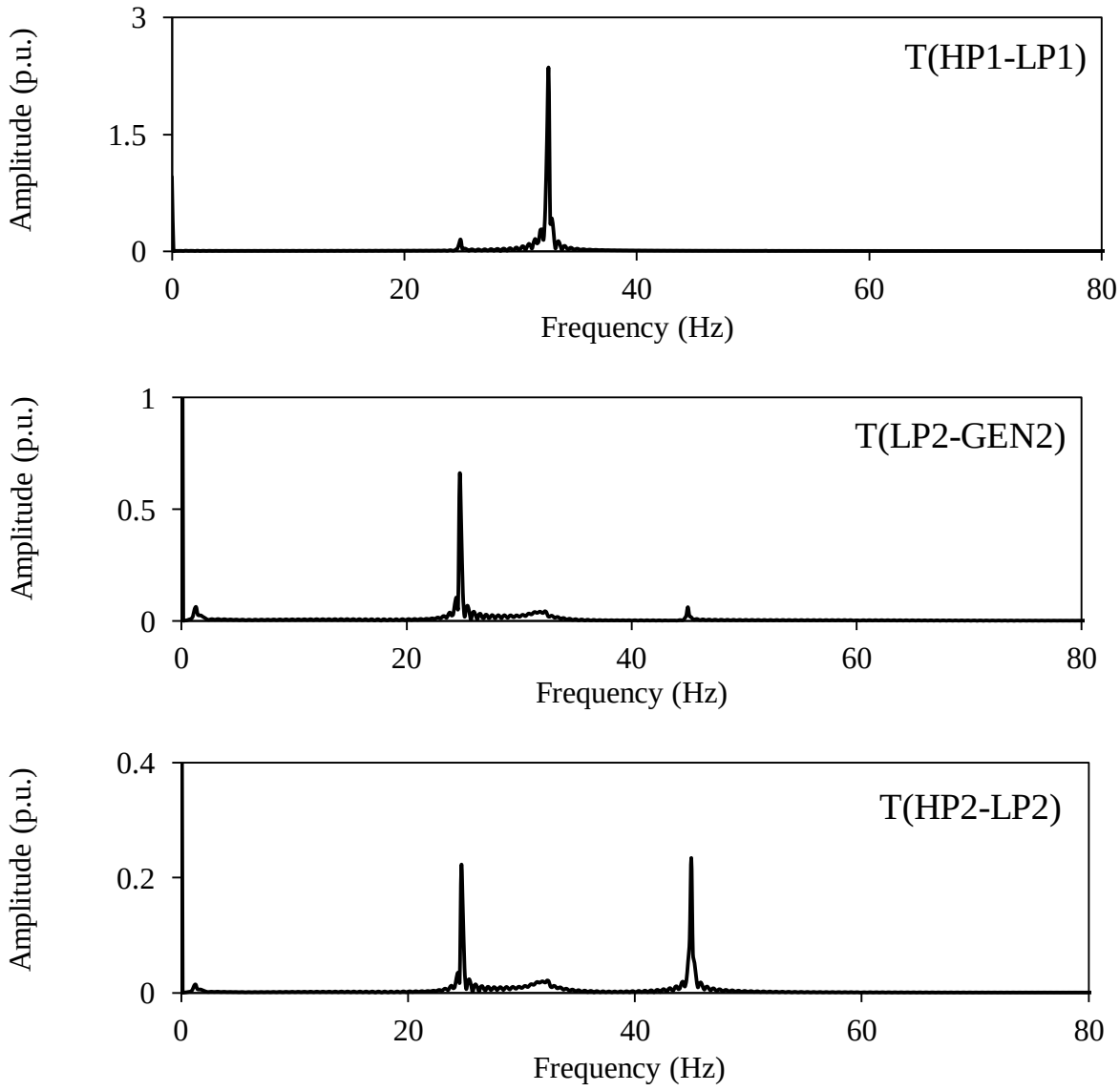

Figure 2.18: continued.

2.5 Summary

This chapter introduces the system used for the studies reported in this thesis and presents the mathematical models of its various components. A digital time-domain simulation of a case study of the system during a three-phase fault is also presented. The results of this case study show the existence of subsynchronous resonance and the absence of subsynchronous interaction. In the next chapter, supplemental controls are presented for simultaneous mitigation of the two phenomena.

Chapter 3

SUPPLEMENTAL CONTROLS OF OFFSHORE AND DFIG-BASED WIND FARMS FOR SIMULTANEOUS MITIGATION OF SUBSYNCHRONOUS RESONANCE AND SUBSYNCHRONOUS INTERACTION

3.1 Introduction

In this chapter, two supplemental controls of offshore and DFIG-based wind farms for simultaneous mitigation of SSR and SSI are introduced. The effectiveness of the two presented controllers in mitigating both phenomena is investigated through several time-domain simulation case studies for different wind farm ratings and system contingencies.

3.2 Supplemental Controls of Offshore and DFIG-Based Wind Farms

SSR and SSI damping is achieved through the modulation of the reactive powers of the HVDC onshore converter and DFIG wind turbines. This is attained by introducing supplemental control signals, U_S, in the reactive power control loops of the grid side converters of the DFIG wind turbines and the HVDC onshore converter connecting the offshore wind farm to the grid as shown in Figures 3.1 and 3.2 respectively. In this context, two supplemental controls designated as Supplemental controls I and II are proposed.

In Supplemental control I, shown in Figure 3.3, SSR and SSI damping is attained by adding the supplementary control signal $U_S = U_{SSR} + U_{SSI}$ in the reactive power control loop of the onshore HVDC converter before the PI regulator of the inner control loop as shown in Figure 3.1. On the other hand, in Supplemental control II, shown in Figure 3.4, SSR and SSI damping is attained by adding supplementary control signals $U_S = U_{SSR}$ and $U_S = U_{SSI}$ in the reactive power control loops of the onshore HVDC converter and the GSC of DFIG wind turbines respectively before the PI regulator of the inner control loop as shown in Figures 3.1 and 3.2.

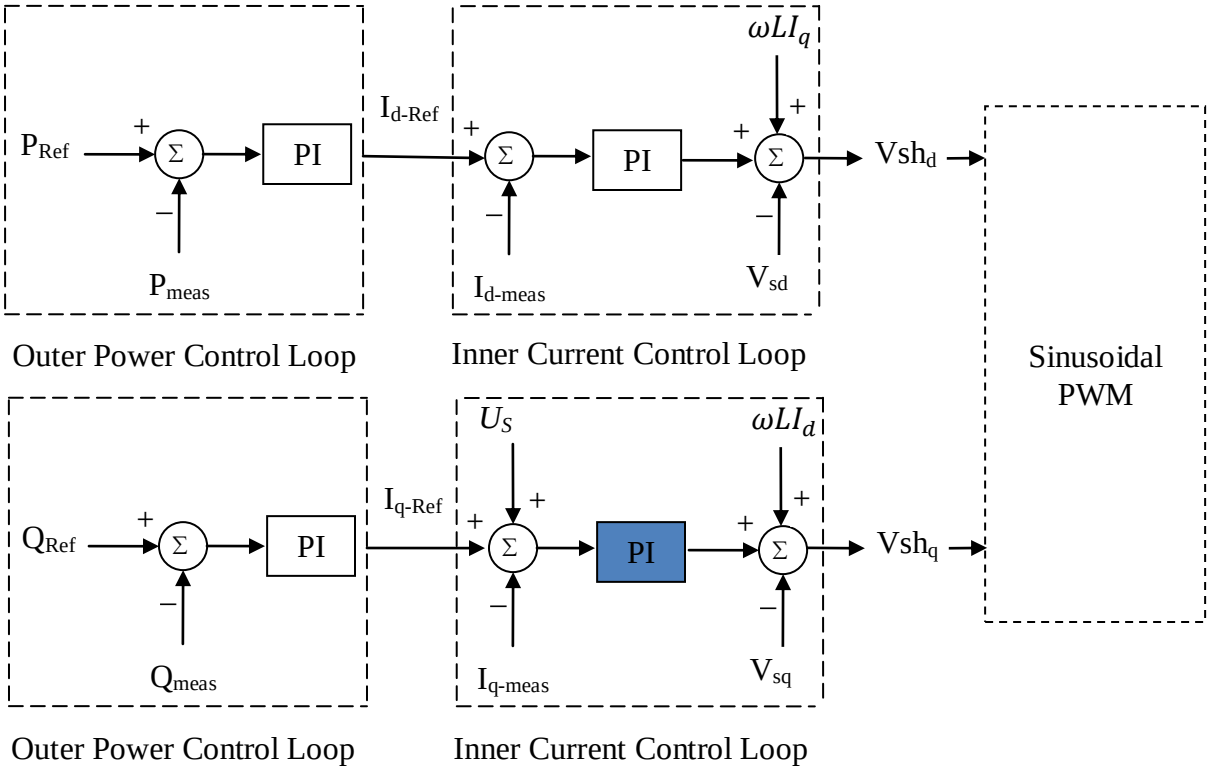

Figure 3.1: Incorporating a supplemental control signal, U_S, in the reactive power control loop of the onshore HVDC converter.

The SSR supplemental control, shown in Figures 3.3 and 3.4 has N-channels (N is the number of turbine-generator shaft system rotating masses) that employ the modal speeds as control signals. These modal speeds are derived from the turbine-generator rotating mass speeds as [37], [38]:

$$[\Delta\omega_m] = [Q]^{-1}[\Delta\omega] \tag{3.1}$$

where, $\Delta\omega_m$ is the modal speed deviation matrix, Q is the eigenvector matrix and $\Delta\omega$ is the speed deviation matrix of the turbine-generator rotating masses. The rotating mass speeds can be obtained using a torsional monitor. Each modal speed as presented is separately phase and gain adjusted to provide damping for its corresponding torsional mode. The phase compensations are provided as:

$$\emptyset_i = \frac{1+sT_{ai}}{1+sT_{bi}}, \quad \mathrm{i} = 0,1,\ldots,\mathrm{N}-1 \tag{3.2}$$

The values of the matrices Q for the two turbine-generator shaft systems are given in Appendix A. On the other hand, the SSI supplemental control, shown in Figures 3.3 and 3.4, is an m-stage lead-lag compensation controller incorporating wash-out (high-pass) and band-pass (BPF) filters and utilizes Line 2 real power flow as a control signal.

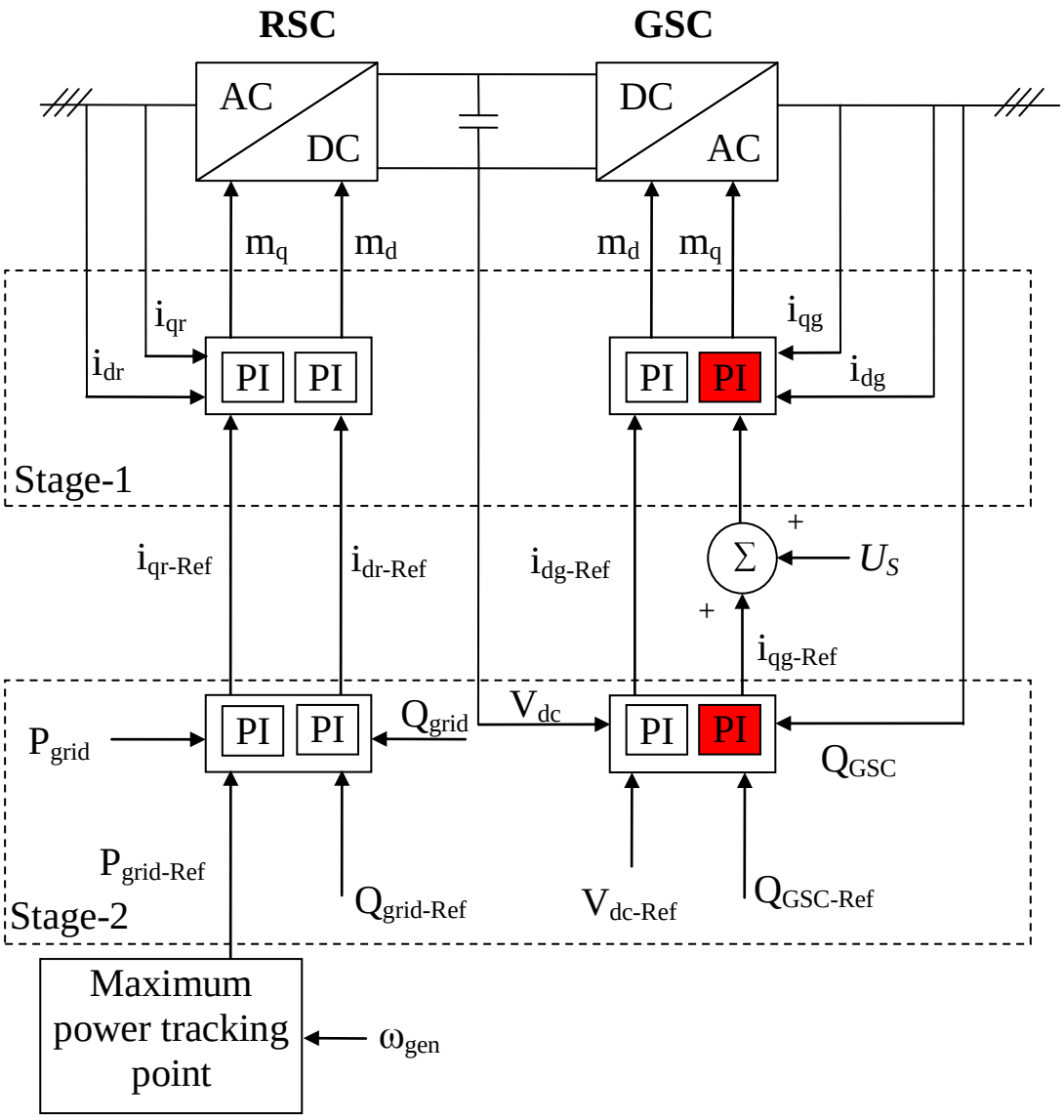

Figure 3.2: Incorporating a supplemental control signal, U_S, in the reactive power control loop of the GSC of DFIG wind turbine.

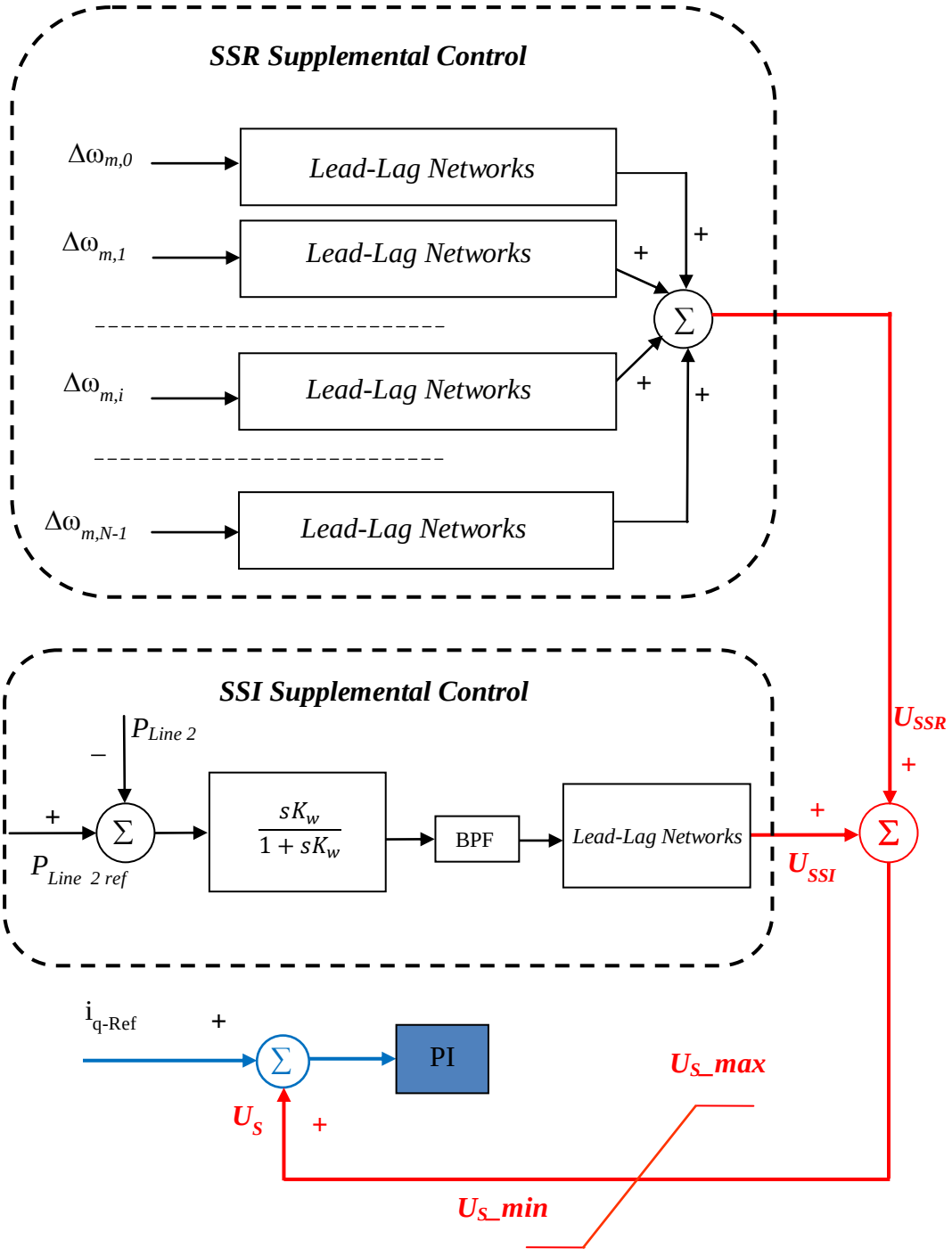

Figure 3.3: Supplemental control I.

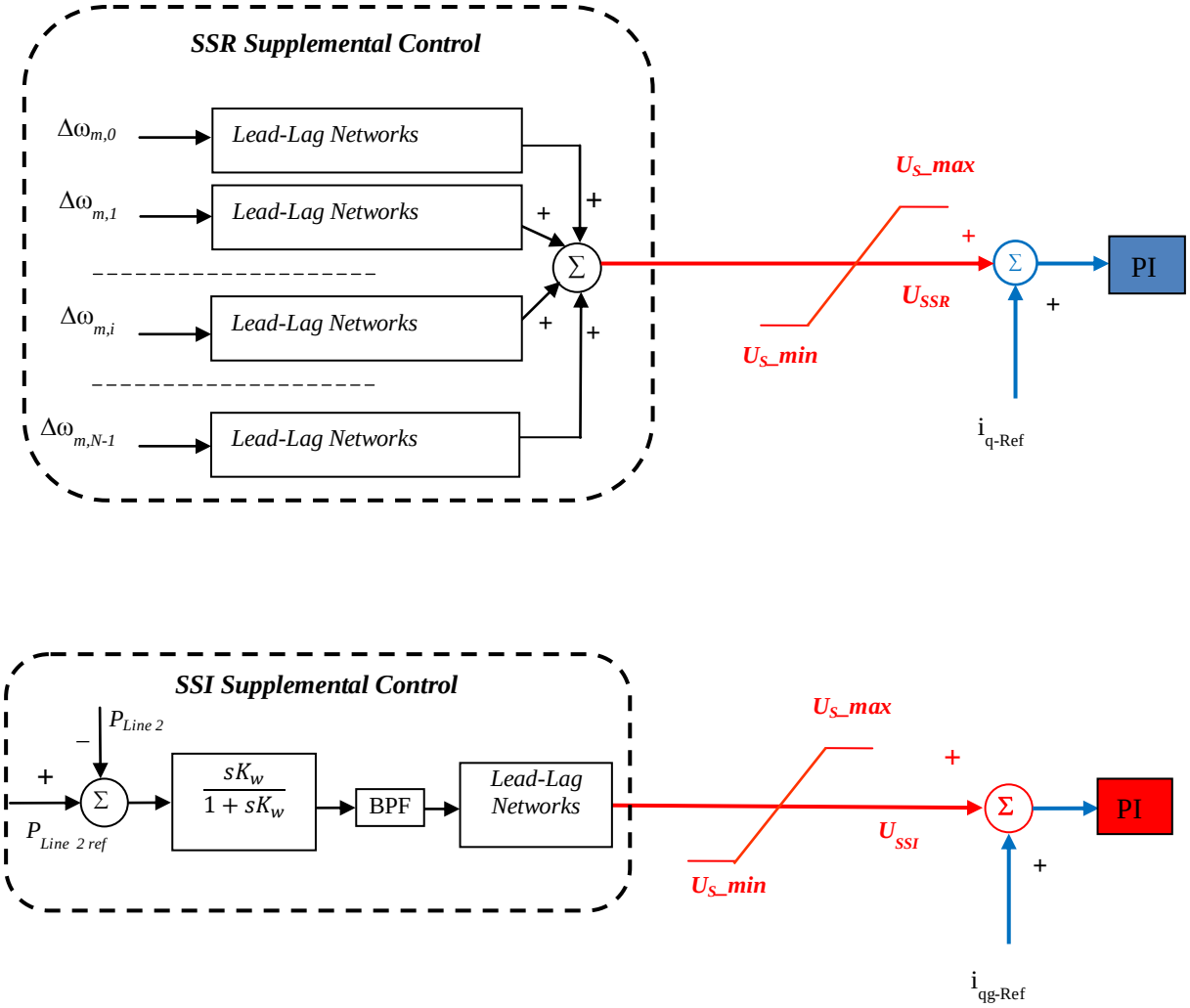

Figure 3.4: Supplemental control II.

In Supplemental control I, a central controller located in wind farm B accepts the remote input signals and sends an output signal U_S to the onshore HVDC converter. On the other hand, in Supplemental control II, there are two central controllers located in wind farms A and B. The central controller in wind farm A accepts a local input signal (Line 2 real power flow) and sends output signal $U_S = U_{SSI}$ to each DFIG wind turbine for SSI damping. The other central controller accepts the remote signals (turbine-generator shaft rotating mass speeds) and sends an output signal $U_S = U_{SSR}$ to the onshore HVDC converter for SSR damping. In the investigations reported in this thesis, it is presumed the accessibility of a wide-area network of synchronized phasor measurement units where the supplemental control input signals can be downloaded at the controller in real time without delay. Nevertheless, incorporating the effect of the time delay

in computing the phasor quantities and the variable communication network latency for a controller that uses remote synchrophasor data is achievable [39].

A trial-and-error approach is adopted in the investigations conducted in this thesis for finding appropriate controller gains and time constants that result in an acceptable oscillations damping. The fine-tuning of the controller parameters is achieved by performing repetitive time-domain simulations to minimize the objective functions

$$\mathrm{C_{SSI}} = \int_{T_C}^{T_F} (\Delta \mathrm{Y}')^2 \mathrm{dt} \tag{3.3}$$

and

$$C_{SSR} = \int_{T_C}^{T_F} \sum_{i=0}^{N-1} \left(\Delta\omega_{m,i}\right)^2 dt \tag{3.4}$$

where T_C is the fault clearing time, T_F is the total simulation time and $\Delta Y'$ is the output of the band pass filters in the controller. The design of optimal supplemental controls using nonlinear control techniques, such as indirect adaptive control, is out of scope of this thesis.

3.3 Performance of Supplemental Control I in damping SSR and SSI Oscillations

Figure 3.5 shows the turbine-generator shaft torsional torque time responses during and after clearing a ***3-cycle, three-phase fault on Line 5*** for the case when the supplemental control is not activated. Figures 3.6 and 3.7 illustrate respectively the time responses of wind farms A and B active and reactive powers, terminal voltage and the BtB dc voltage for the same case. It can be seen from Figure 3.5 that, at the 60% compensation degree of Lines 1 and 2, the turbine-generator shaft torsional torques exhibit severe torsional instability (fast growing oscillations). It can also be seen from Figures 3.6 and 3.7 that SSI, which is due to the induction generator effect, is clearly present in wind farm A and that the adverse effects of the simultaneous existence of SSR and SSI extend their impact to the OWF (wind farm B) performance.

For a clear insight of the excited SSR and SSI mode components and the effectiveness of the supplemental controllers in decreasing these components, Figure 3.8 shows the frequency spectrums of the stator current of the DFIG wind turbines and the turbine-generator shaft torsional torques. It can be seen from Figure 3.8 that the stator current contains frequency components (electrical modes) of 10.37 Hz, 14.8 Hz, 35.09 Hz, 53.96 Hz, and 60 Hz. The complements (60 – 10.37 = 49.625 Hz, 60 – 14.8 = 45.2 Hz, 60 – 35.09 =24.91 Hz) of the three

electrical modes excite SSI mode (24.5 Hz) as well as the three shaft torsional modes (24.65 Hz, 44.99 Hz, 51.1 Hz).

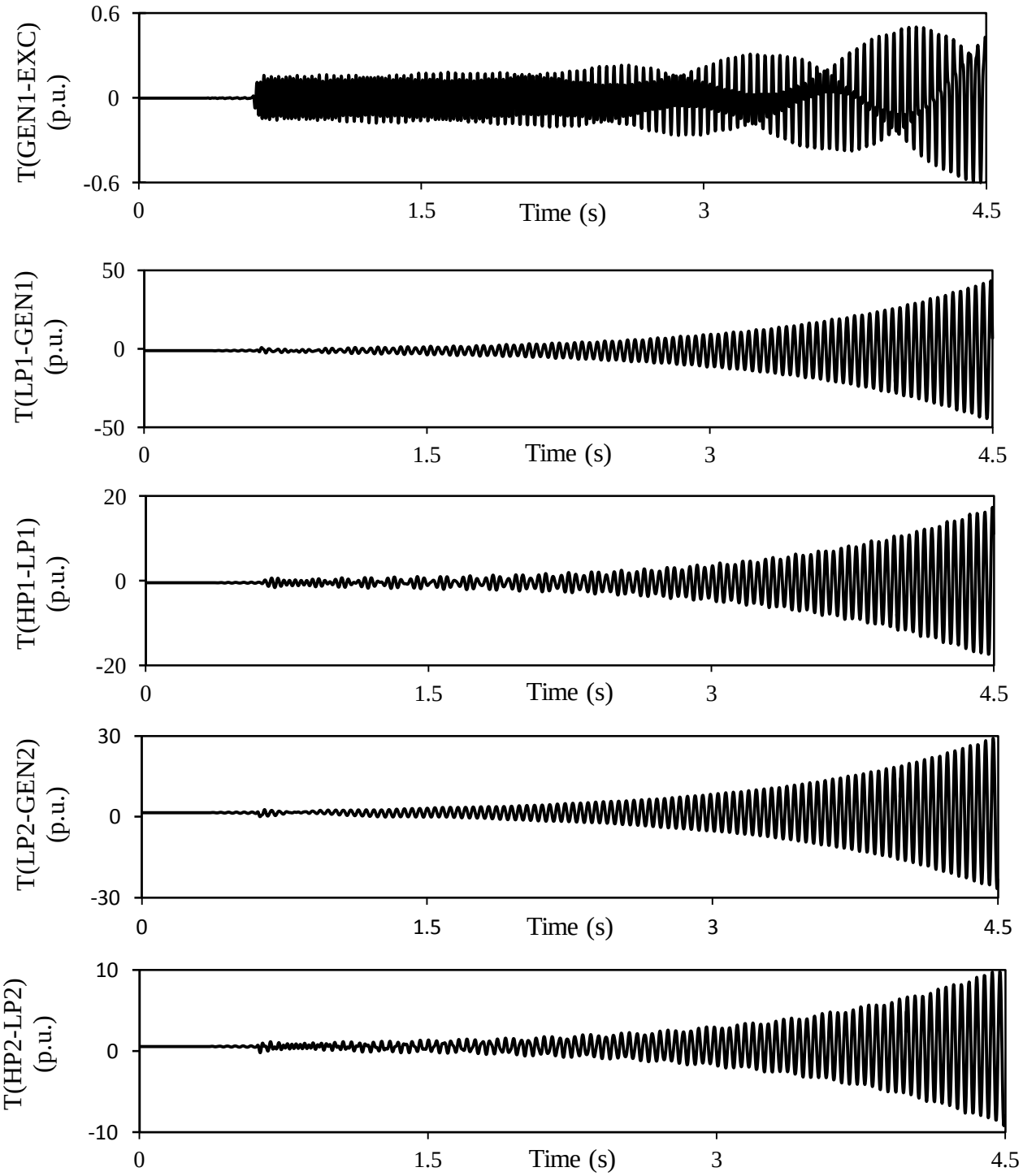

Figure 3.5: Turbine-generator shaft torsional torques during and after clearing a 3-cycle, three-phase fault on Line 5 (60% compensation degree, supplemental control I is not activated, wind farm B rating = 210 MW).

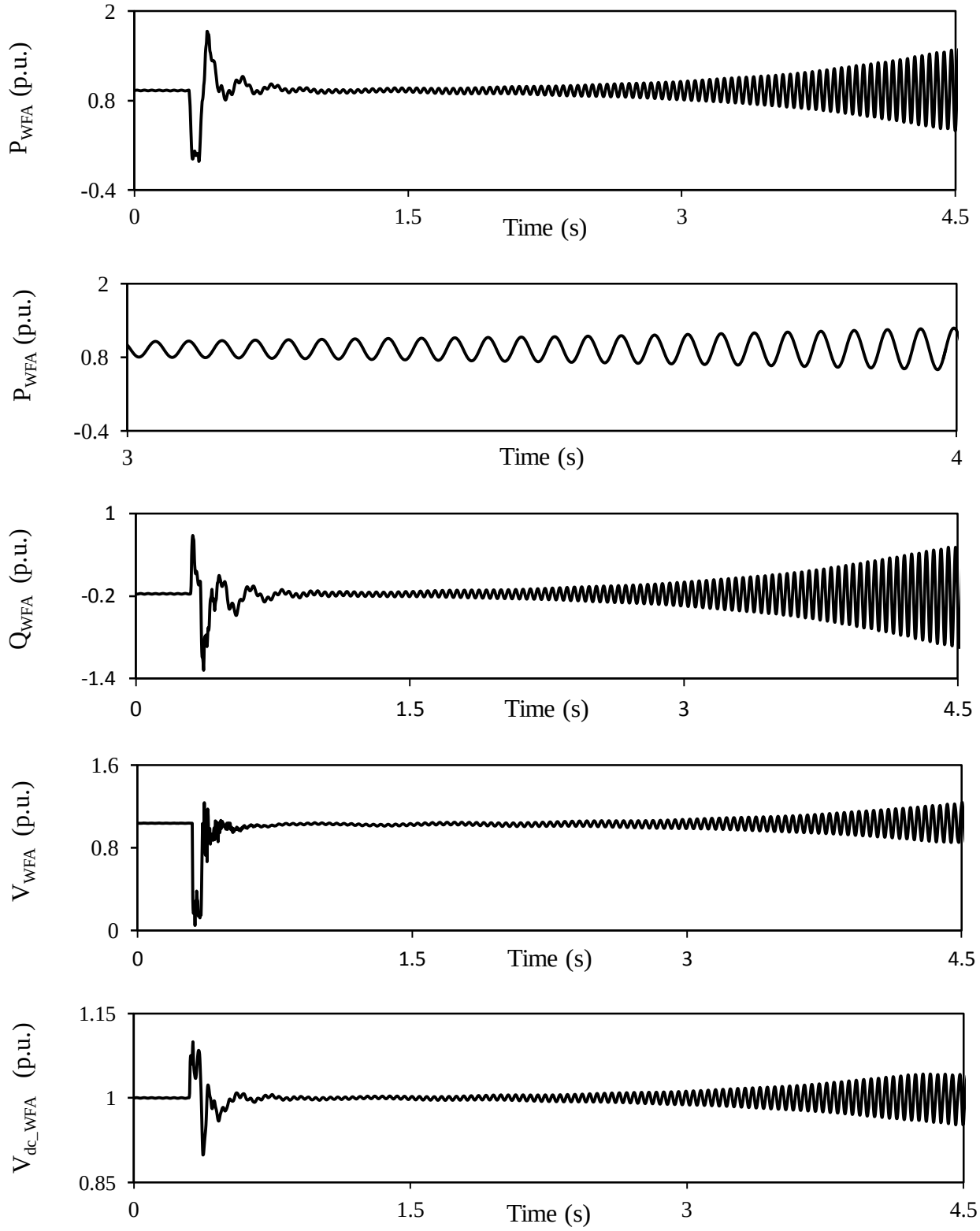

Figure 3.6: Wind farm A real and reactive powers, terminal voltage and dc capacitor voltage during and after clearing a 3-cycle, three-phase fault on Line 5 (60% compensation degree, supplemental control I is not activated, wind farm B rating = 210 MW).

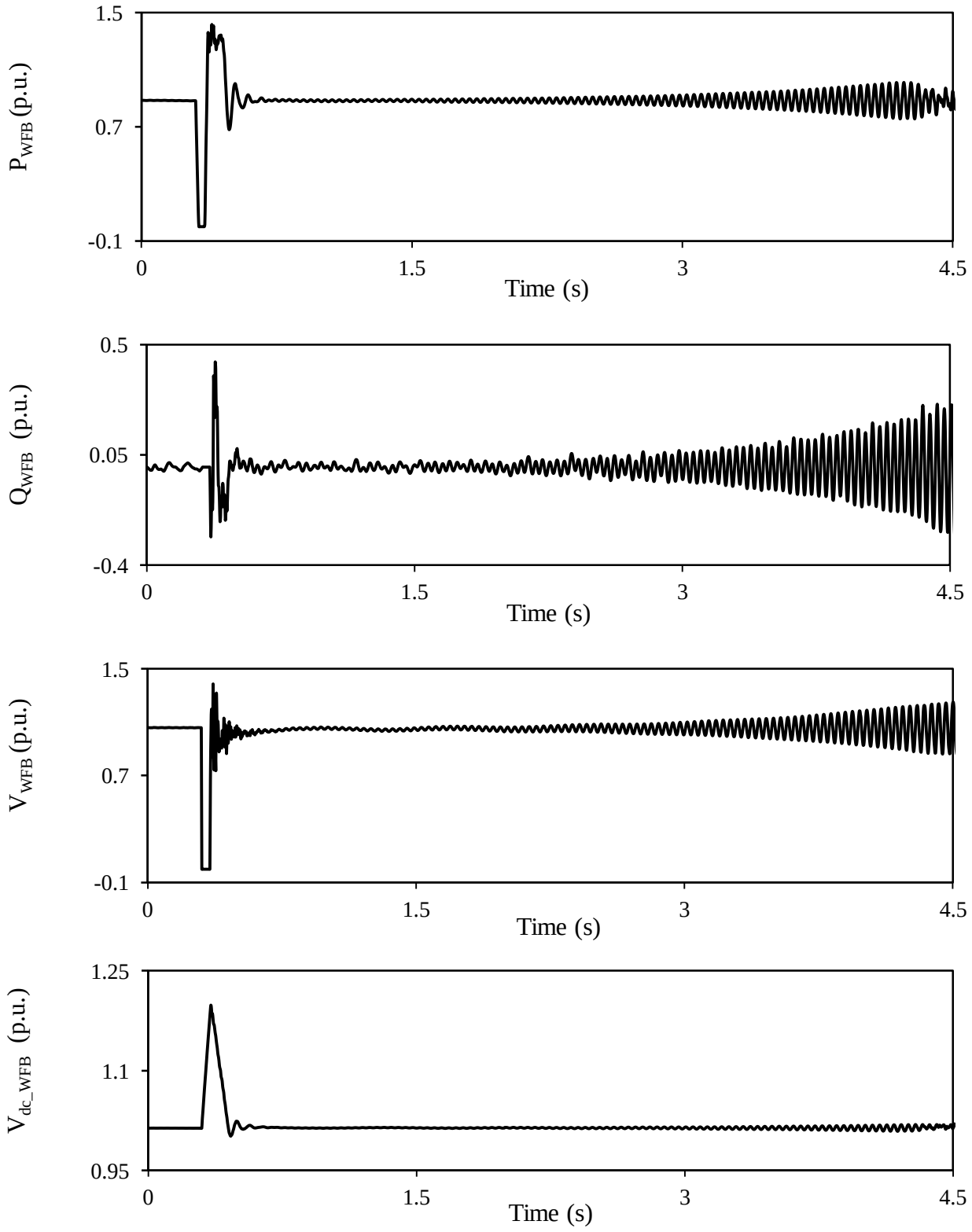

Figure 3.7: Wind farm B real and reactive powers, terminal voltage and dc capacitor voltage during and after clearing a 3-cycle, three-phase fault on Line 5 (60% compensation degree, supplemental control I is not activated, wind farm B rating = 210 MW).

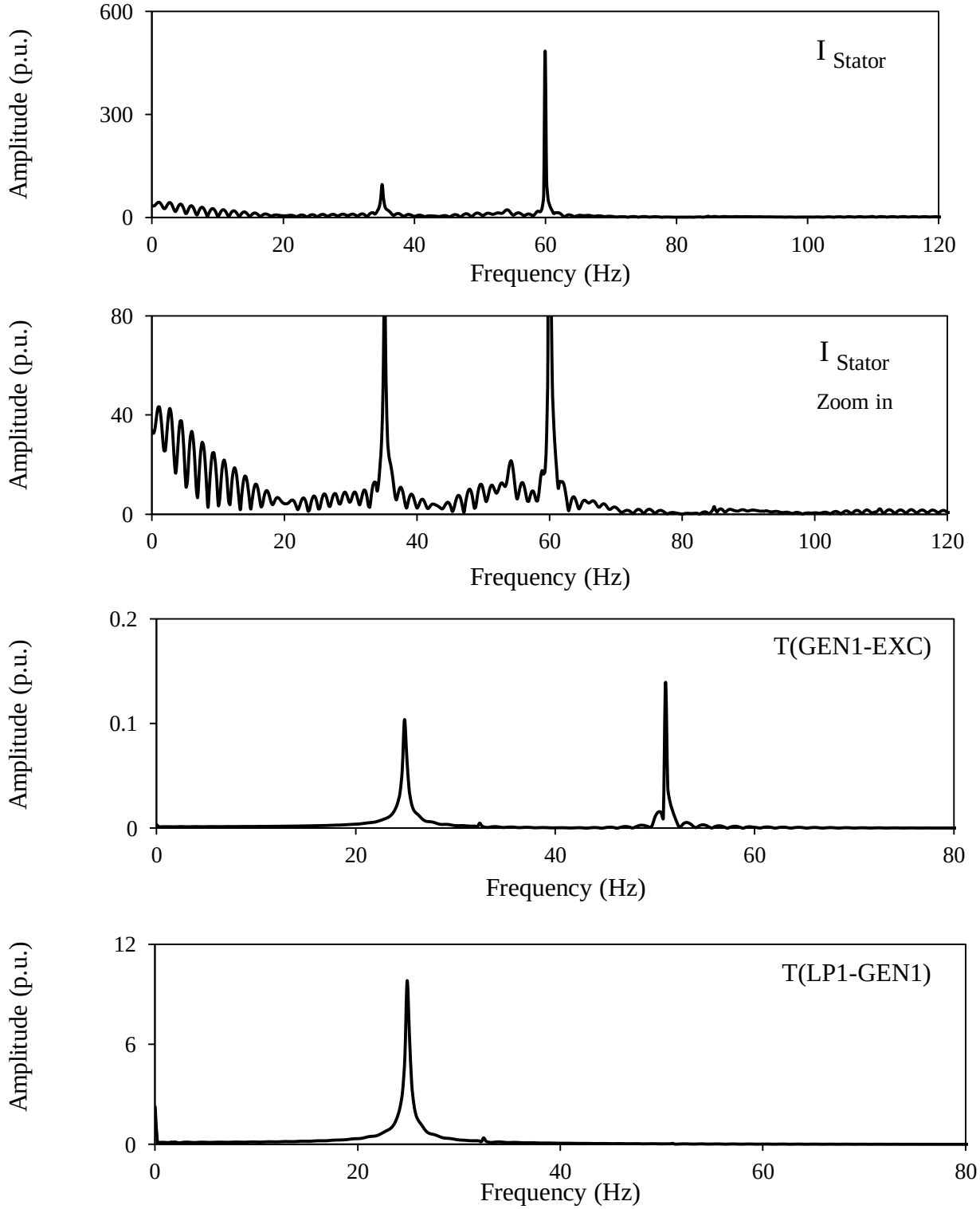

Figure 3.8: Frequency spectrums of the stator current of the DFIG wind turbine and the turbine-generator shaft torsional torques during and after clearing a 3-cycle, three-phase fault on Line 5 (60% compensation degree, supplemental control I is not activated, wind farm B rating = 210 MW).

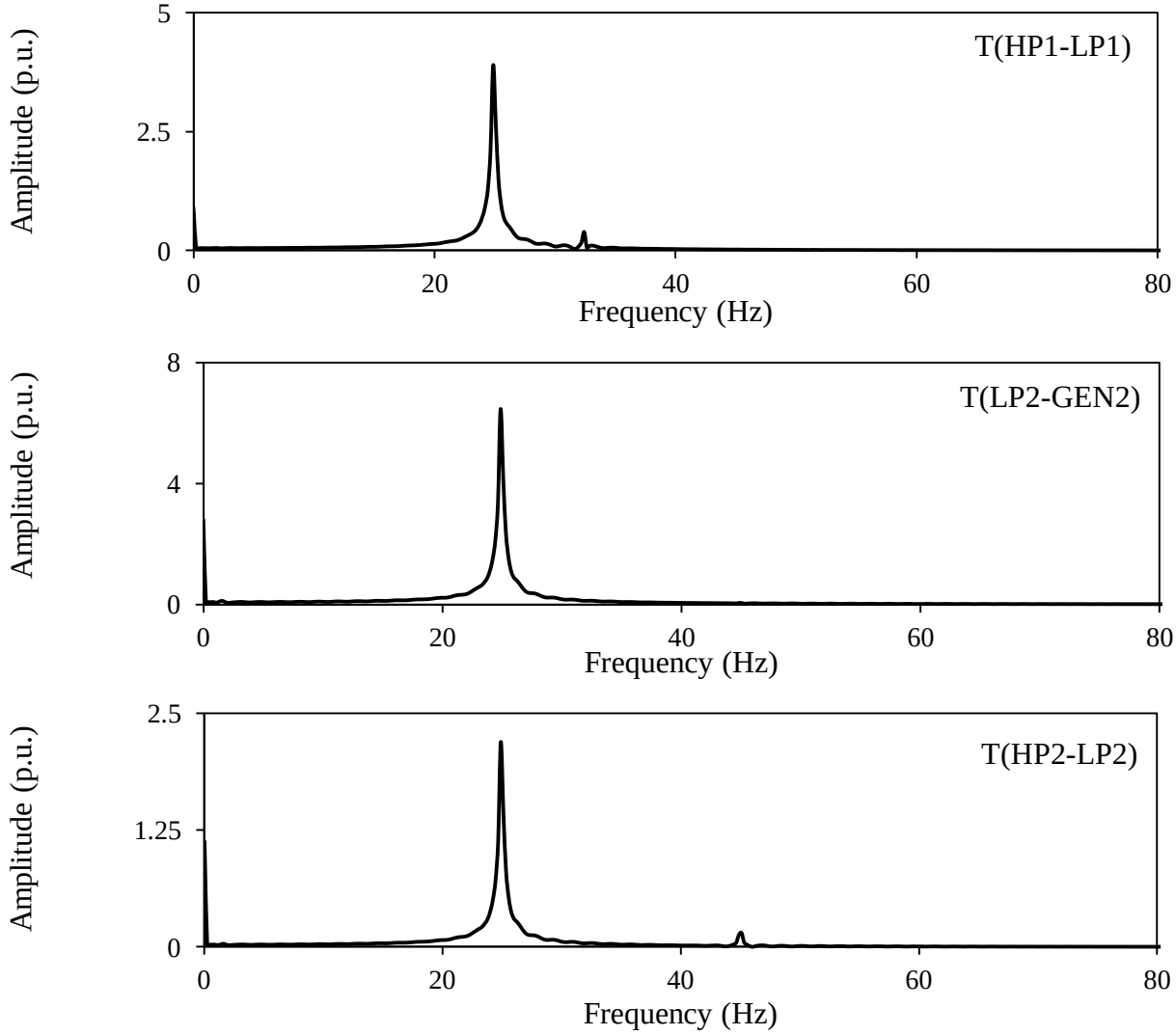

Figure 3.8: continued.

Figure 3.9 shows the turbine-generator shaft torsional torque time responses during and after clearing the same fault for the case when Supplemental control I is activated. Figures 3.10 and 3.11 illustrate respectively the time responses of wind farms A and B active and reactive powers, terminal voltage and the BtB dc voltage for the same case. Moreover, Figure 3.12 shows the frequency spectrums of the stator current of the DFIG wind turbines and the turbine-generator shaft torsional torques for the same study case. Furthermore, the transfer functions of Supplemental control I are given in Table 3.1. It is worth noting here that the negative signs in some of the transfer functions in Table 3.1 indicate that the modal speeds of the turbine-generator shaft system are not in phase.

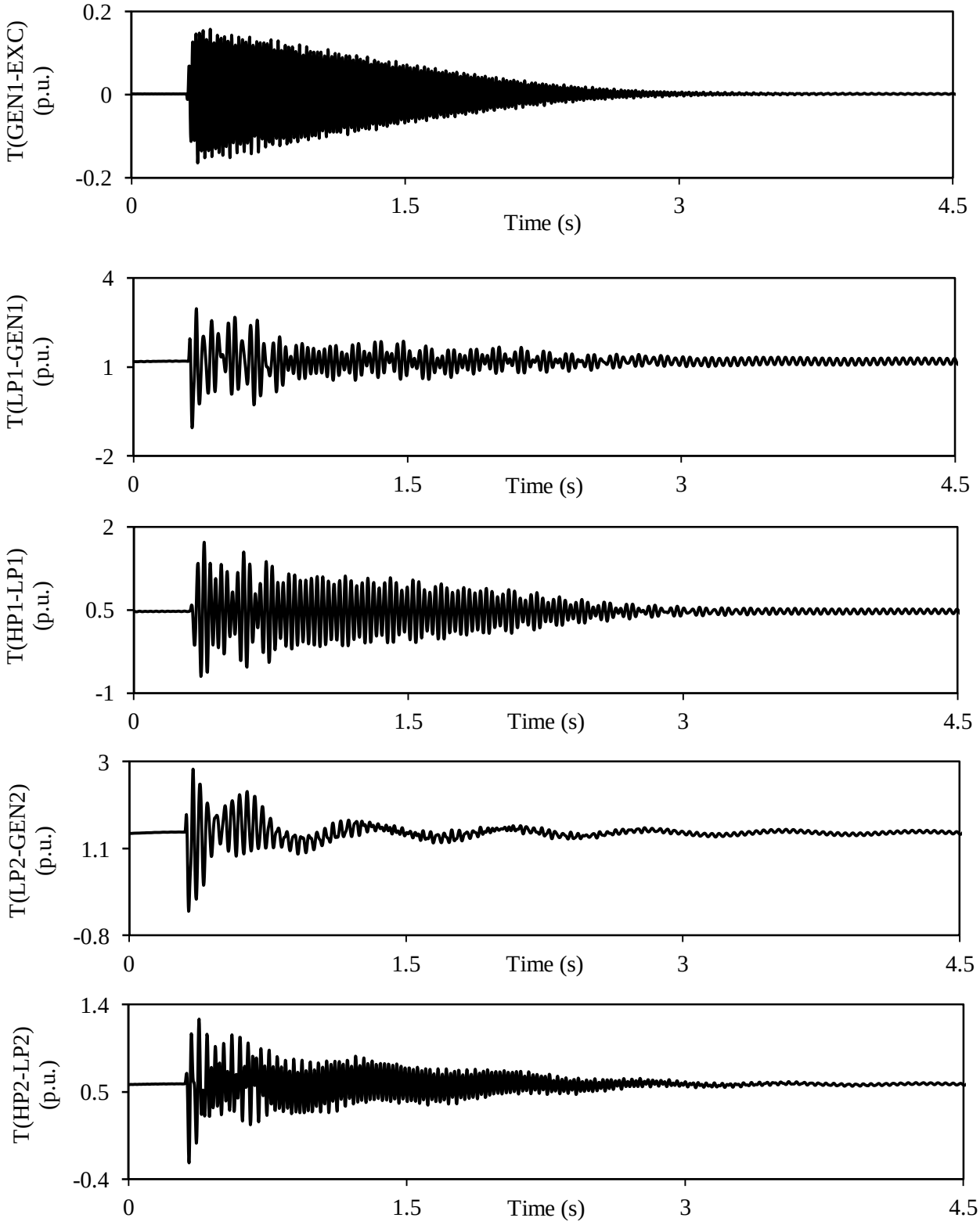

Figure 3.9: Turbine-generator shaft torsional torques during and after clearing a 3-cycle, three-phase fault on Line 5 (60% compensation degree, supplemental control I is activated, wind farm B rating = 210 MW).

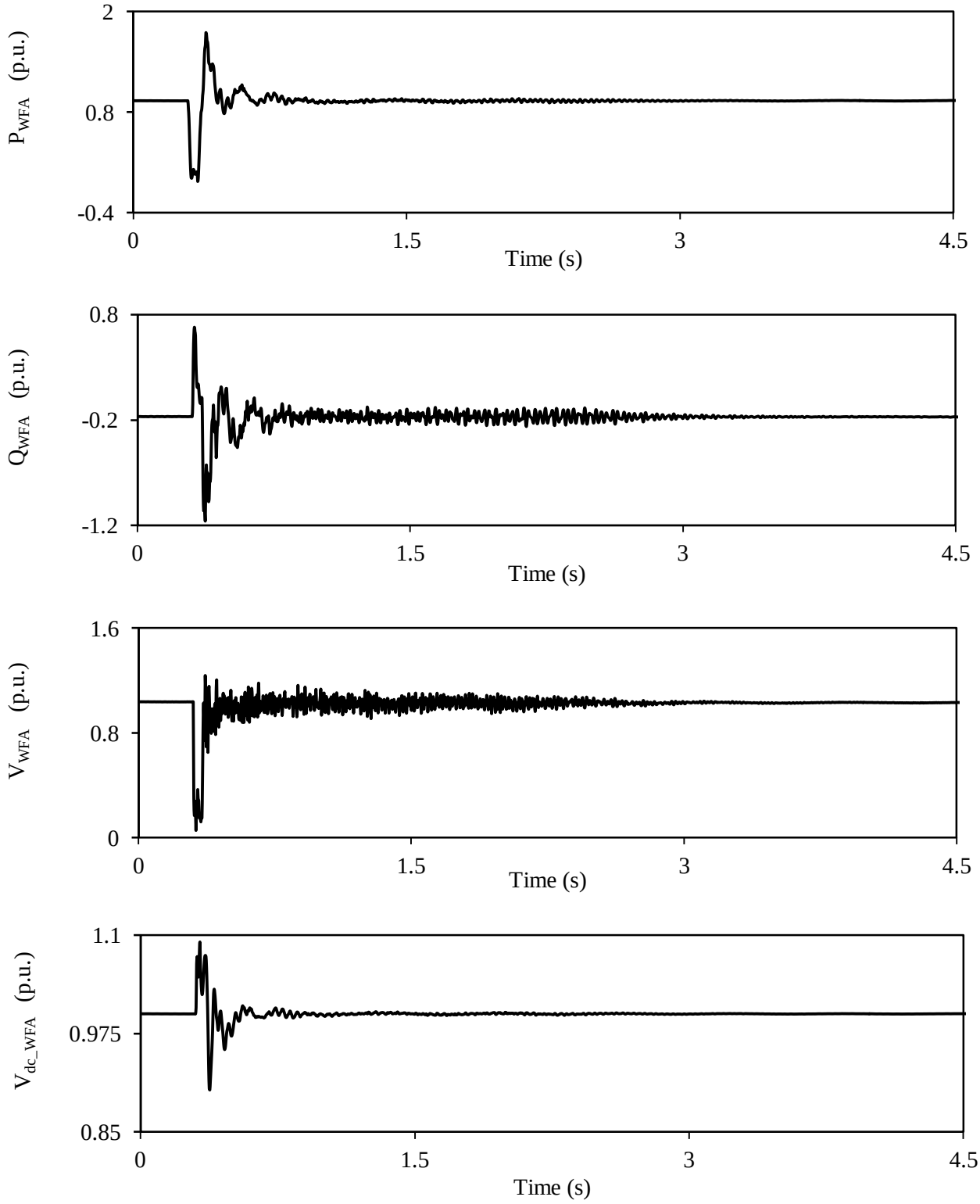

Figure 3.10: Wind farm A real and reactive powers, terminal voltage and dc capacitor voltage during and after clearing a 3-cycle, three-phase fault on Line 5 (60% compensation degree, supplemental control I is activated, wind farm B rating = 210 MW).

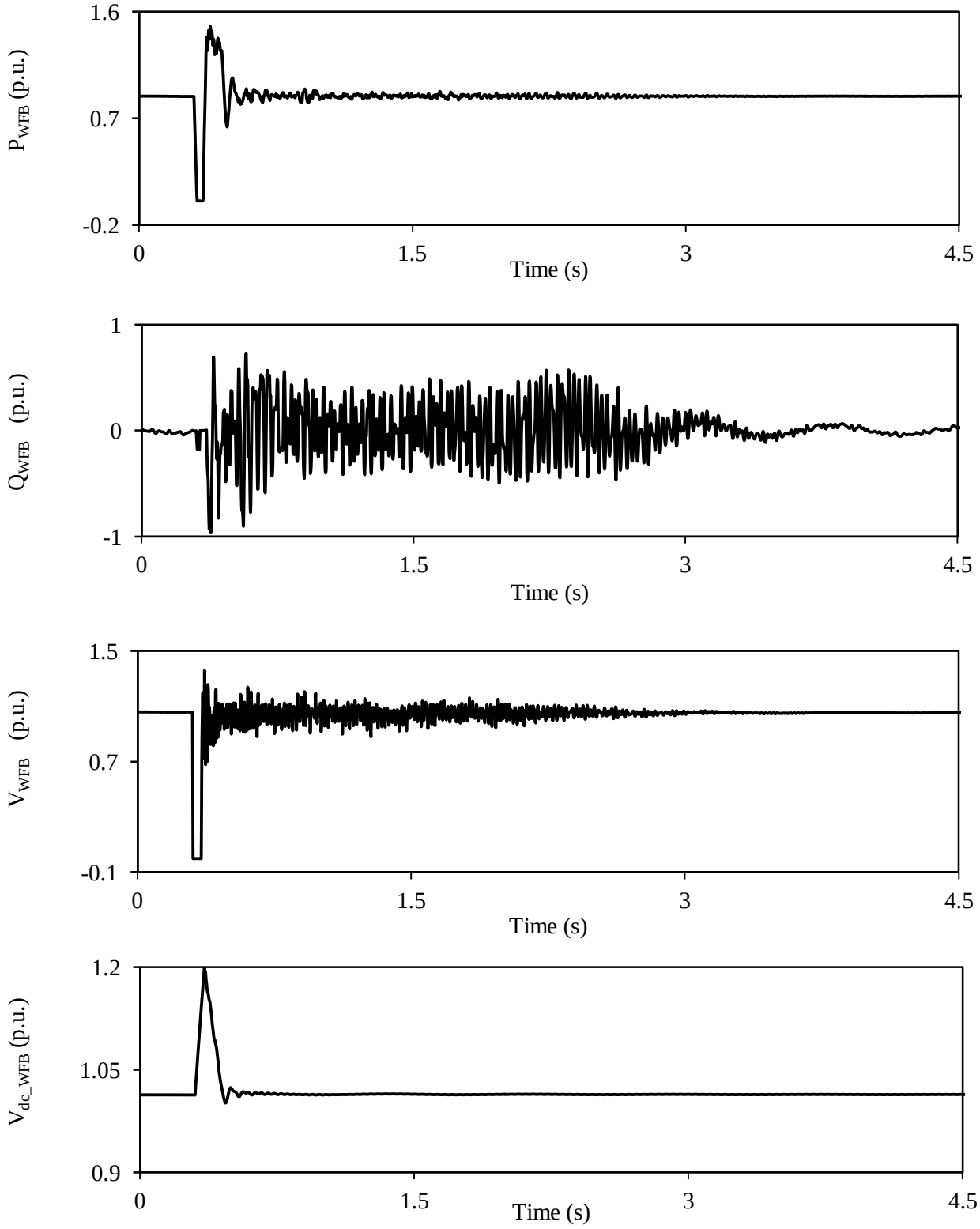

Figure 3.11: Wind farm B real and reactive powers, terminal voltage and dc capacitor voltage during and after clearing a 3-cycle, three-phase fault on Line 5 (60% compensation degree, supplemental control I is activated, wind farm B rating = 210 MW).

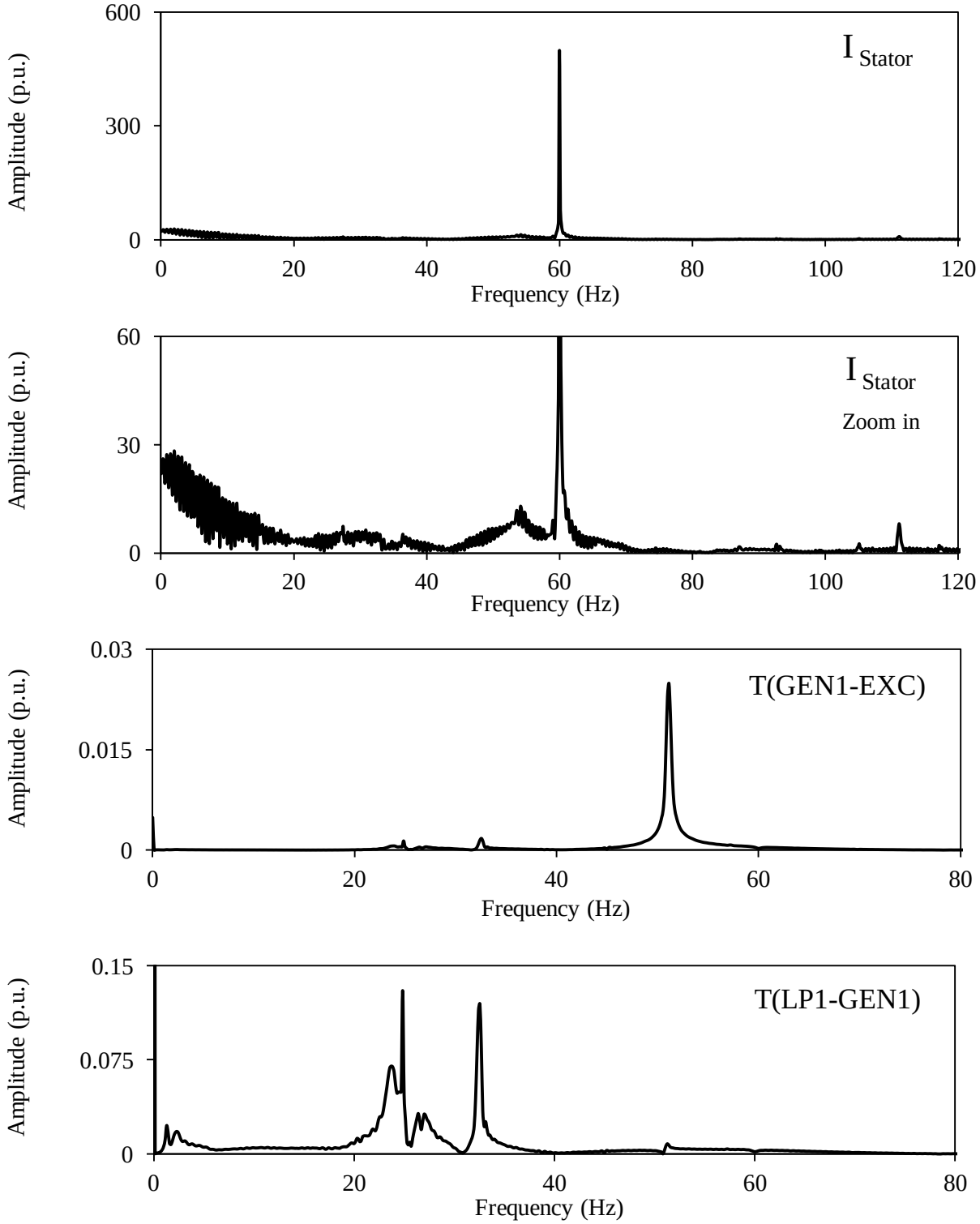

Figure 3.12: Frequency spectrums of the stator current of the DFIG wind turbine and the turbine-generator shaft torsional torques during and after clearing a 3-cycle, three-phase fault on Line 5 (60% compensation degree, supplemental control I is activated, wind farm B rating = 210 MW).

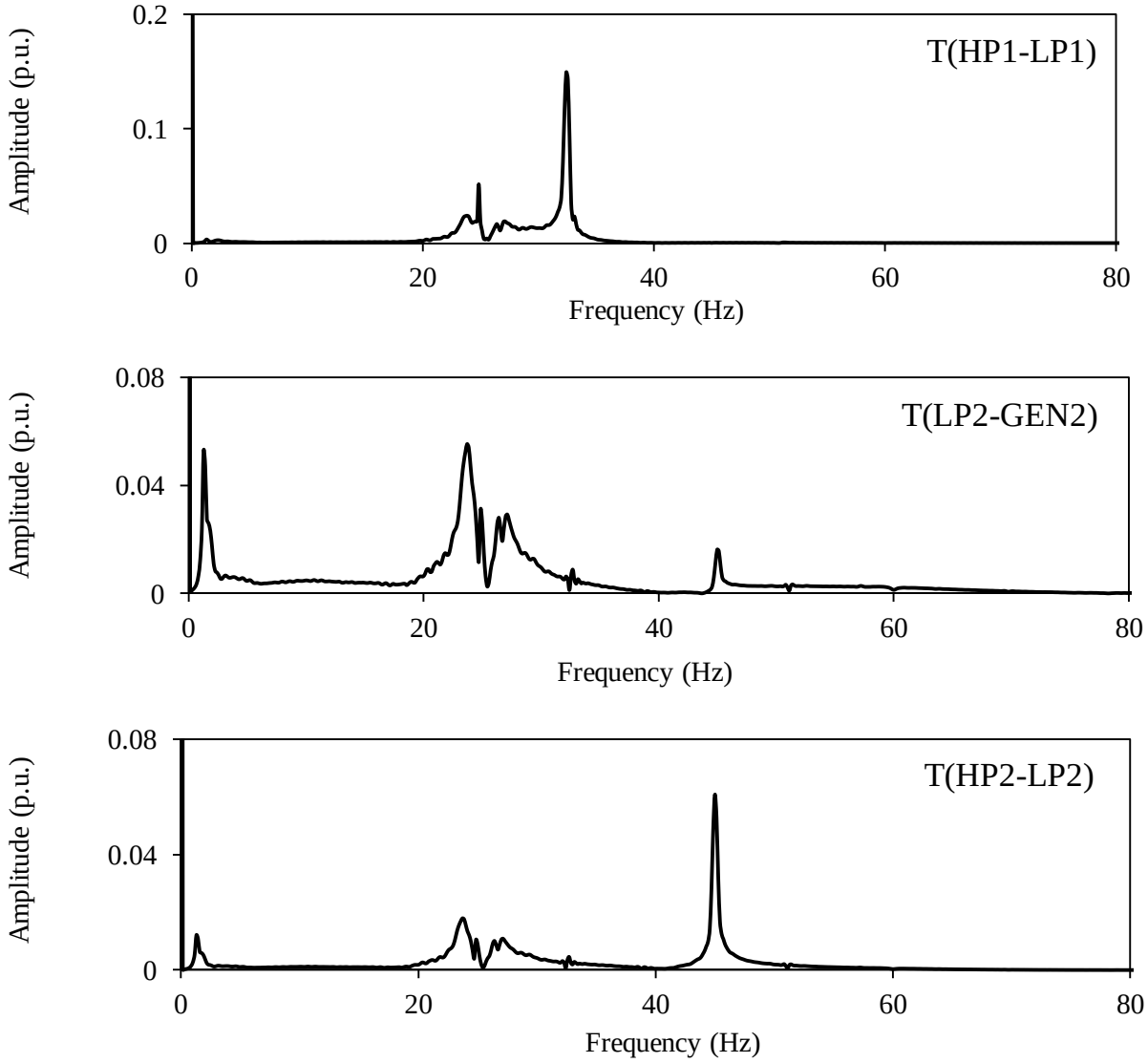

Figure 3.12: continued.

The comparison between the two groups of figures (Figures 3.5, 3.6, 3.7, 3.8) and (Figures 3.9, 3.10, 3.11, 3.12) establishes the effectiveness of Supplemental control I in damping the torsional torques in all turbine-generator shaft sections as well as in mitigating SSI in wind farm A. The contribution of wind farm B reactive power (Q_{WFB}) to SSR and SSI oscillations damping is clearly shown in Figure 3.11. It can also be seen from Figure 3.10 that the dc chopper protection of DFIG wind turbines in wind farm A limits the dc bus voltage at 1.1 p.u.

Table 3.1: Transfer functions of Supplemental control I (Wind **f**arm B rating = 210 MW, three-phase fault on Line 5).

Modal Speeds	Transfer Function
G1, $\Delta_{\omega m0}$	0
G1, $\Delta_{\omega m1}$	$G_{\omega 1}(s) = 25\dfrac{s+300}{s+1}$
G1, $\Delta_{\omega m2}$	$G_{\omega 2}(s) = 50\dfrac{s+2}{s+1}$
G1, $\Delta_{\omega m3}$	$G_{\omega 3}(s) = -50\dfrac{s+2}{s+1}$
G2, $\Delta_{\omega m0}$	0
G2, $\Delta_{\omega m1}$	$G_{\omega 1}(s) = 500\dfrac{s+2}{s+1}$
G2, $\Delta_{\omega m2}$	$G_{\omega 2}(s) = -500\dfrac{s+2}{s+1}$
Washout filter	$G(s) = \dfrac{s}{s+10}$
Band-Pass filter	$G(s) = \dfrac{62.83s}{s^2+62.83s+35500}$
Lead-Lag compensator	$G(s) = \dfrac{s+250}{s+1}$
U_{S_max}, U_{S_min}	0.5, - 0.5

3.3.1 Effect of the distance between wind farm B and the turbine-generators

The effect of the distance between wind farm B and the turbine-generators on the performance of Supplemental control I, especially in mitigating SSR, is examined by changing the length of transmission Line 3. The results of this study are presented in the following three groups of figures:

Group A: Line 3 = 50 km, (Figures 3.13, 3.14, 3.15, 3.16, 3.17, 3.18, 3.19, 3.20)

Group B: Line 3 = 100 km, (Figures 3.21, 3.22, 3.23, 3.24, 3.25, 3.26, 3.27, 3.28)

Group C: Line 3 = 200 km, (Figures 3.29, 3.30, 3.31, 3.32, 3.33, 3.34, 3.35, 3.36)

In each group, the turbine-generator shaft torsional torques, wind farms A and B active and reactive powers, terminal voltage and the BtB dc voltage as well as the frequency spectrums of the stator current of the DFIG wind turbines and the turbine-generator shaft torsional torques are shown for the cases when Supplemental control I is disabled and activated respectively. Moreover, the transfer functions of Supplemental control I in Groups A, B and C are the same as those given in Table 3.1.

The comparisons between the two sets of figures in Groups A, B and C (Set 1: Supplemental control I is disabled and Set 2: Supplemental control I is activated; e.g. Figures 3.13, 3.14, 3.15, 3.16 and Figures 3.17, 3.18, 3.19 and 3.20 in Group A) demonstrate the effectiveness of supplemental control in mitigating SSR and SSI when it is located at different distances from the turbine-generators and wind farm A.

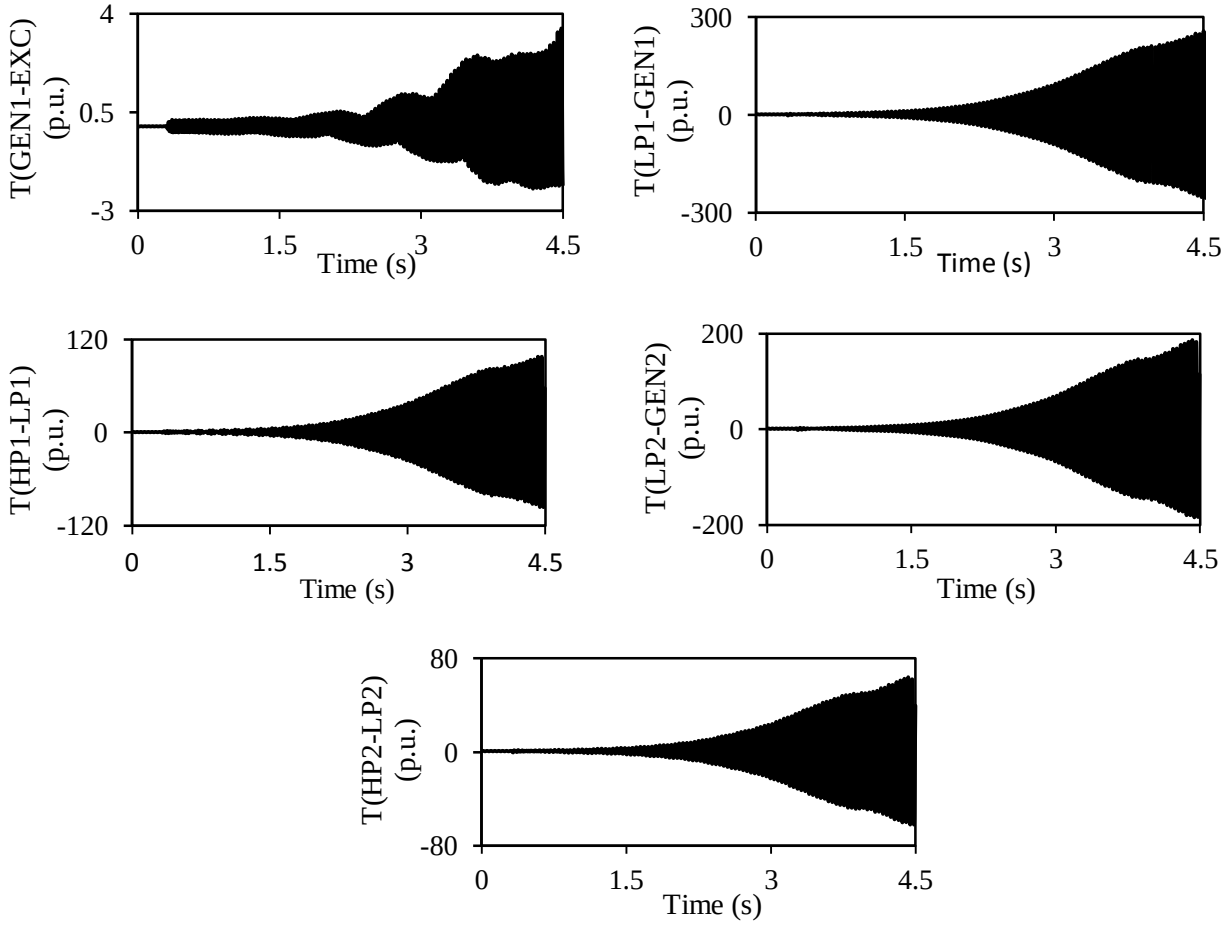

Figure 3.13: Turbine-generator shaft torsional torques during and after clearing a 3-cycle, three-phase fault on Line 5 (60% compensation degree, supplemental control I is not activated, Line 3 length = 50 km).

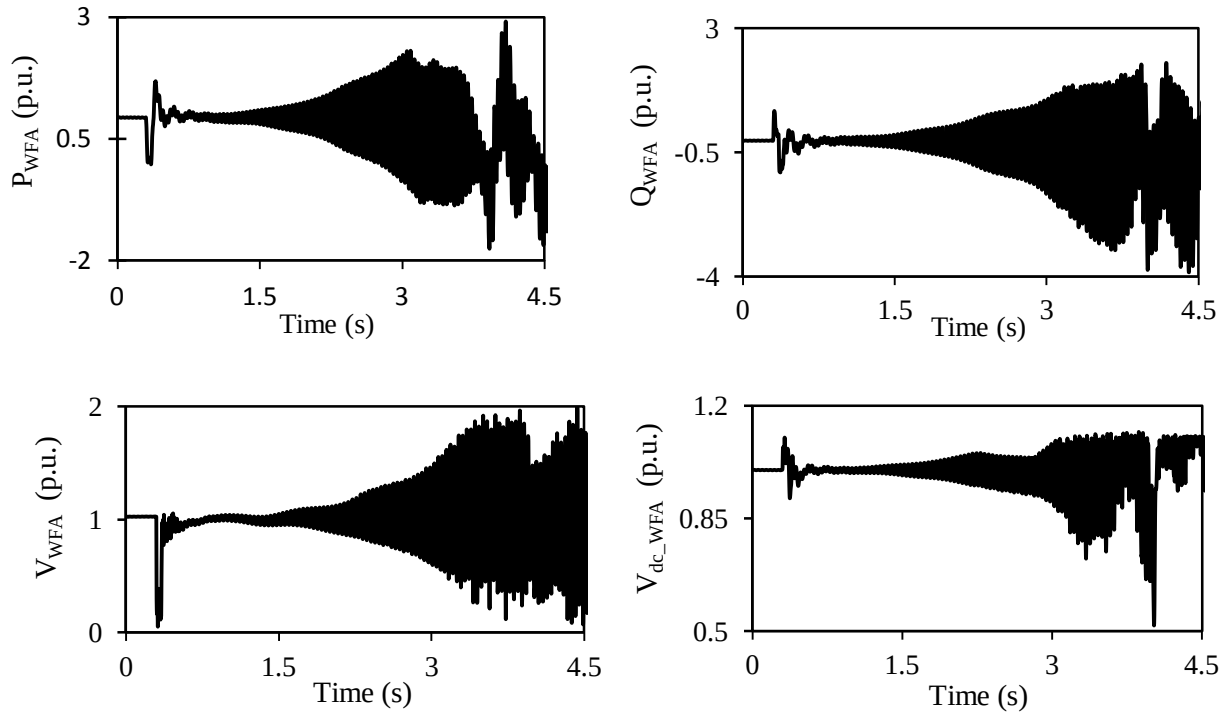

Figure 3.14: Wind farm A real and reactive powers, terminal voltage and dc capacitor voltage during and after clearing a 3-cycle, three-phase fault on Line 5 (60% compensation degree, supplemental control I is not activated, Line 3 length = 50 km).

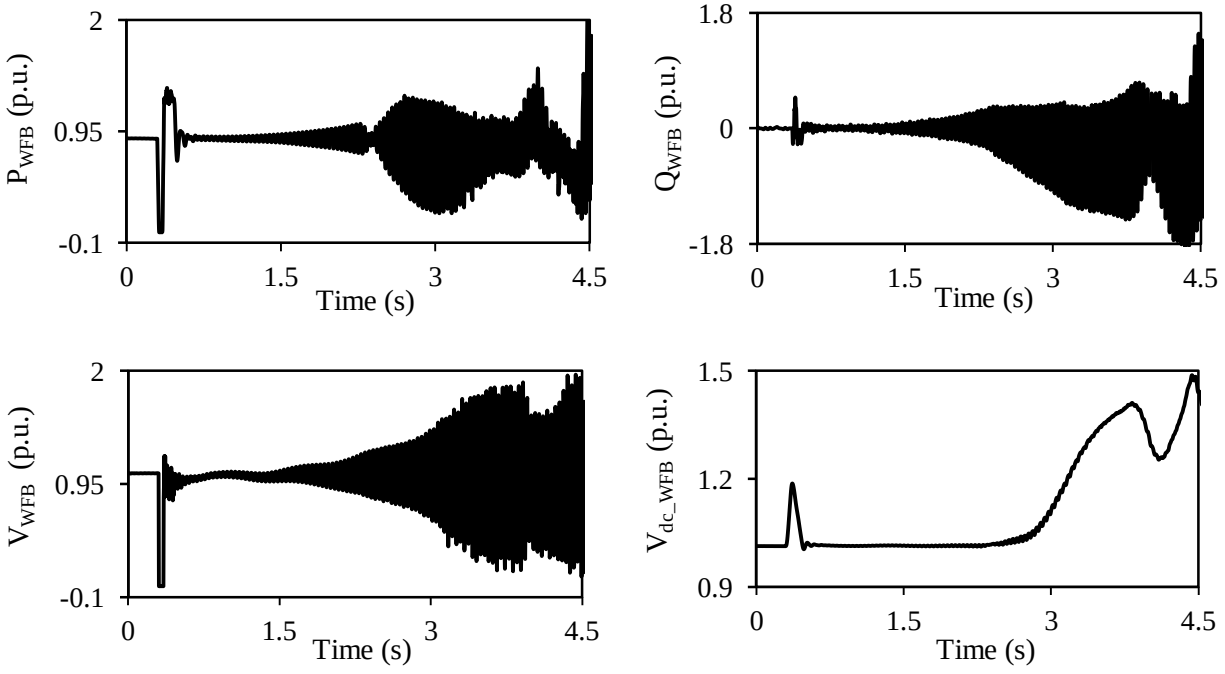

Figure 3.15: Wind farm B real and reactive powers, terminal voltage and dc capacitor voltage during and after clearing a 3-cycle, three-phase fault on Line 5 (60% compensation degree, supplemental control I is not activated, Line 3 length = 50 km).

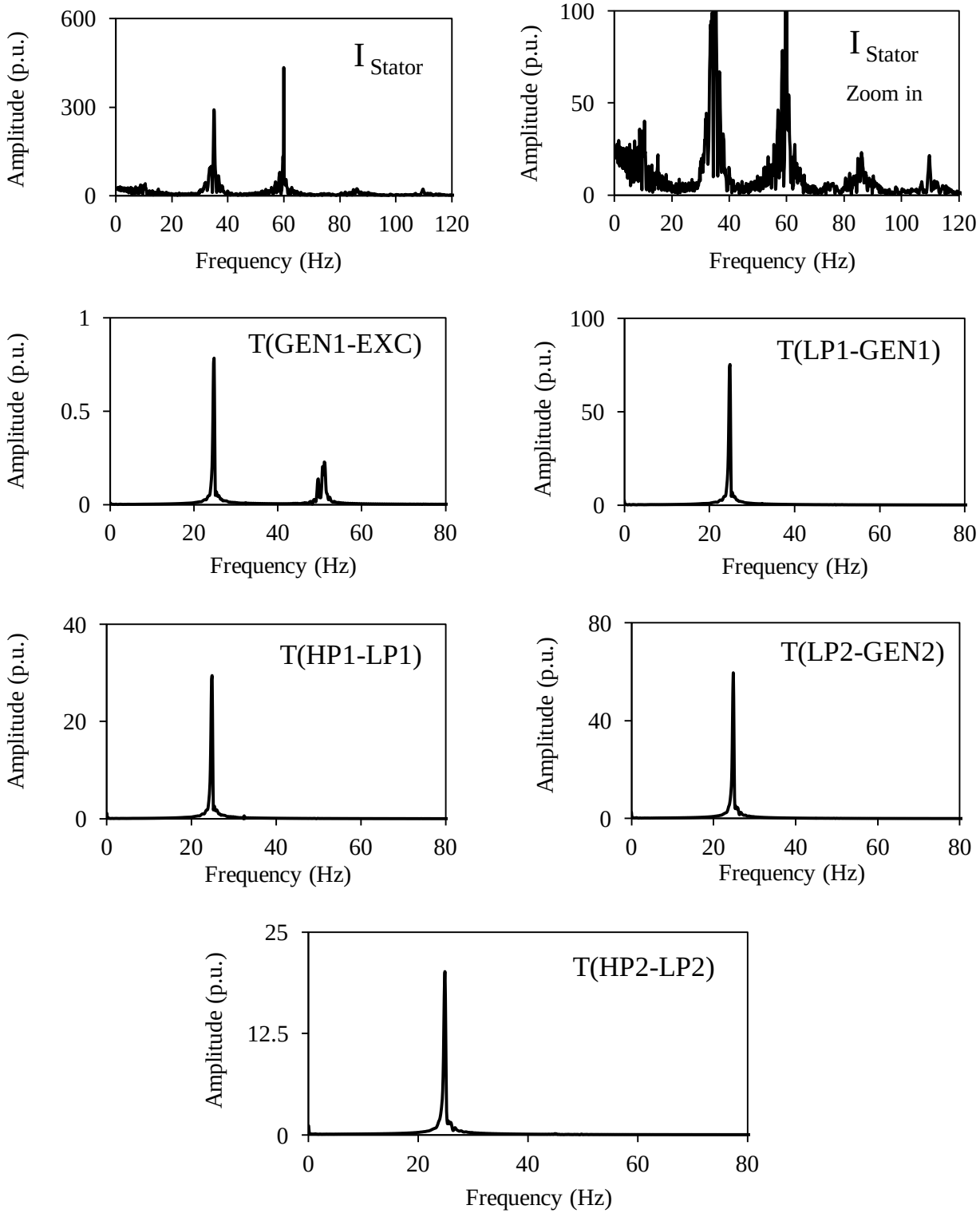

Figure 3.16: Frequency spectrums of the stator current of the DFIG wind turbine and the turbine-generator shaft torsional torques during and after clearing a 3-cycle, three-phase fault on Line 5 (60% compensation degree, supplemental control I is not activated, Line 3 length = 50 km).

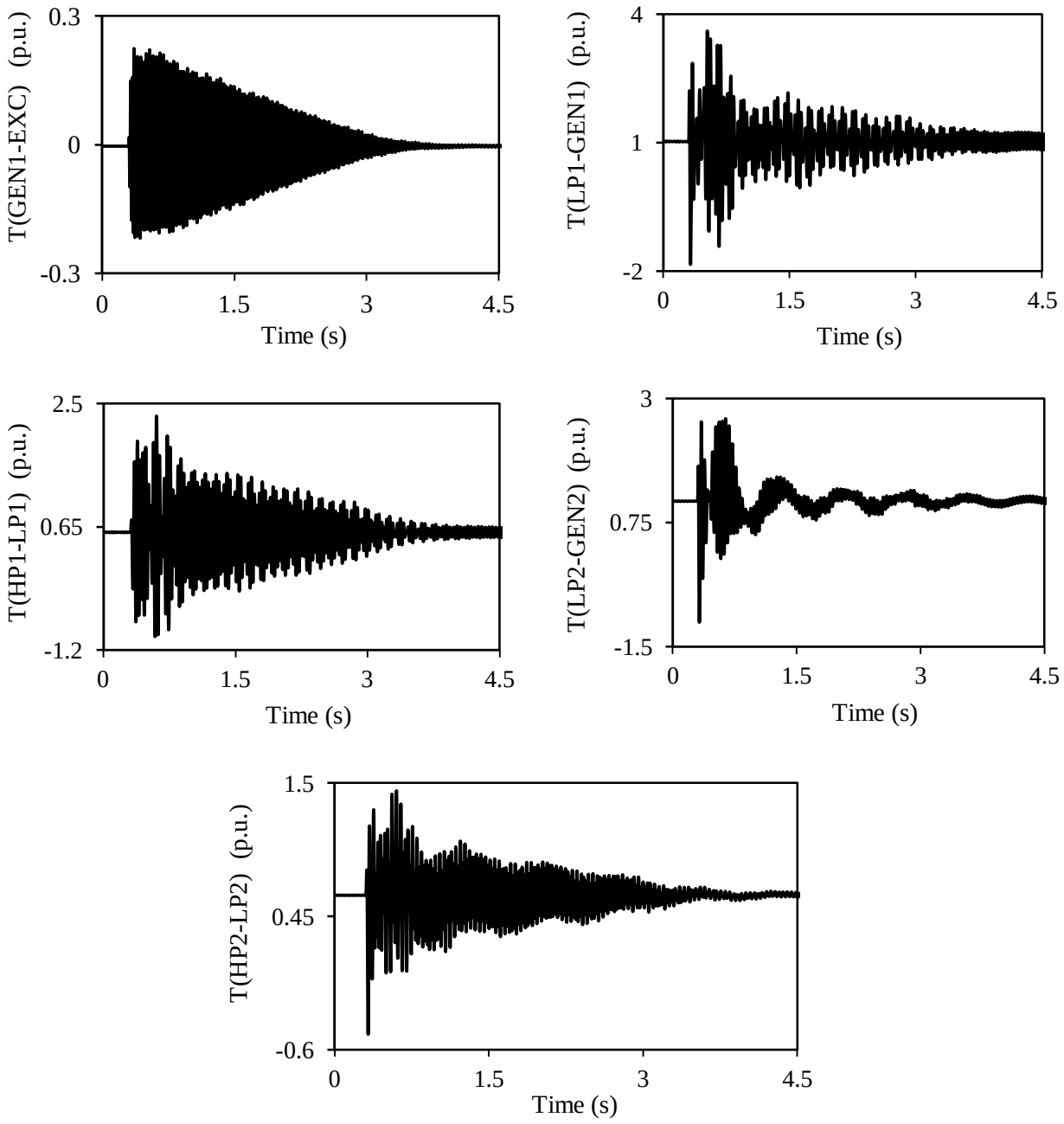

Figure 3.17: Turbine-generator shaft torsional torques during and after clearing a 3-cycle, three-phase fault on Line 5 (60% compensation degree, supplemental control I is activated, Line 3 length = 50 km).

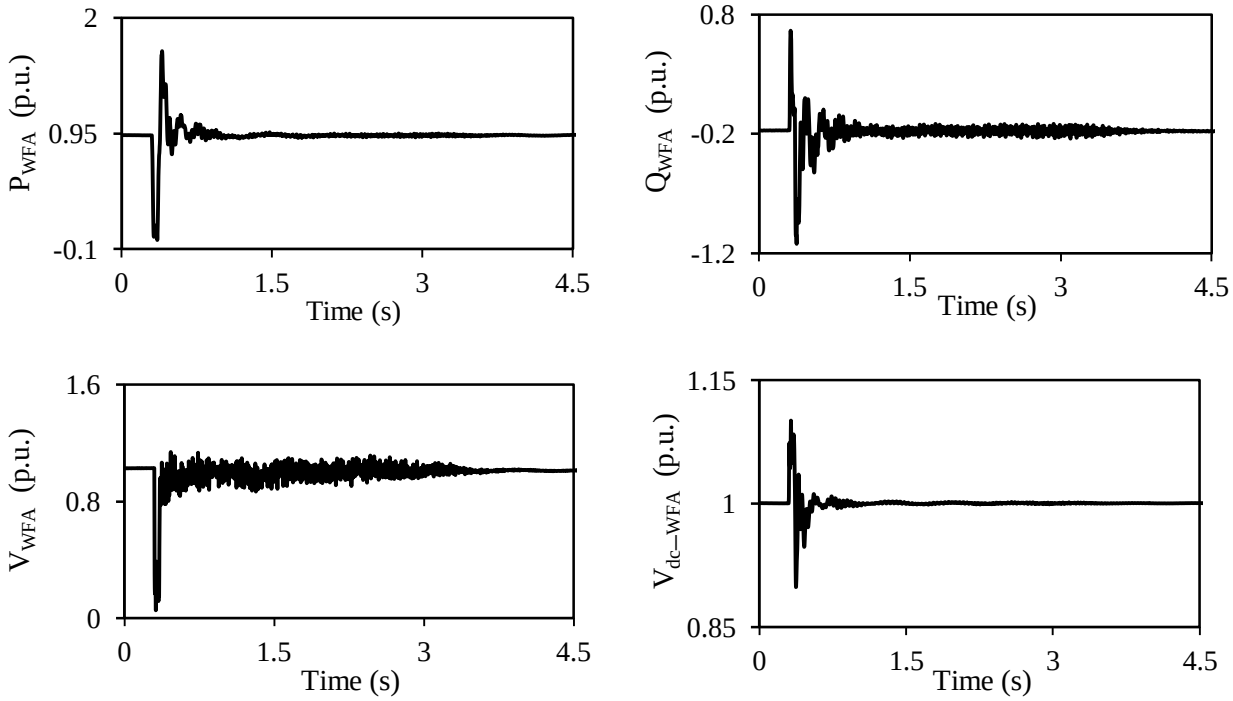

Figure 3.18: Wind farm A real and reactive powers, terminal voltage and dc capacitor voltage during and after clearing a 3-cycle, three-phase fault on Line 5 (60% compensation degree, supplemental control I is activated, Line 3 length = 50 km).

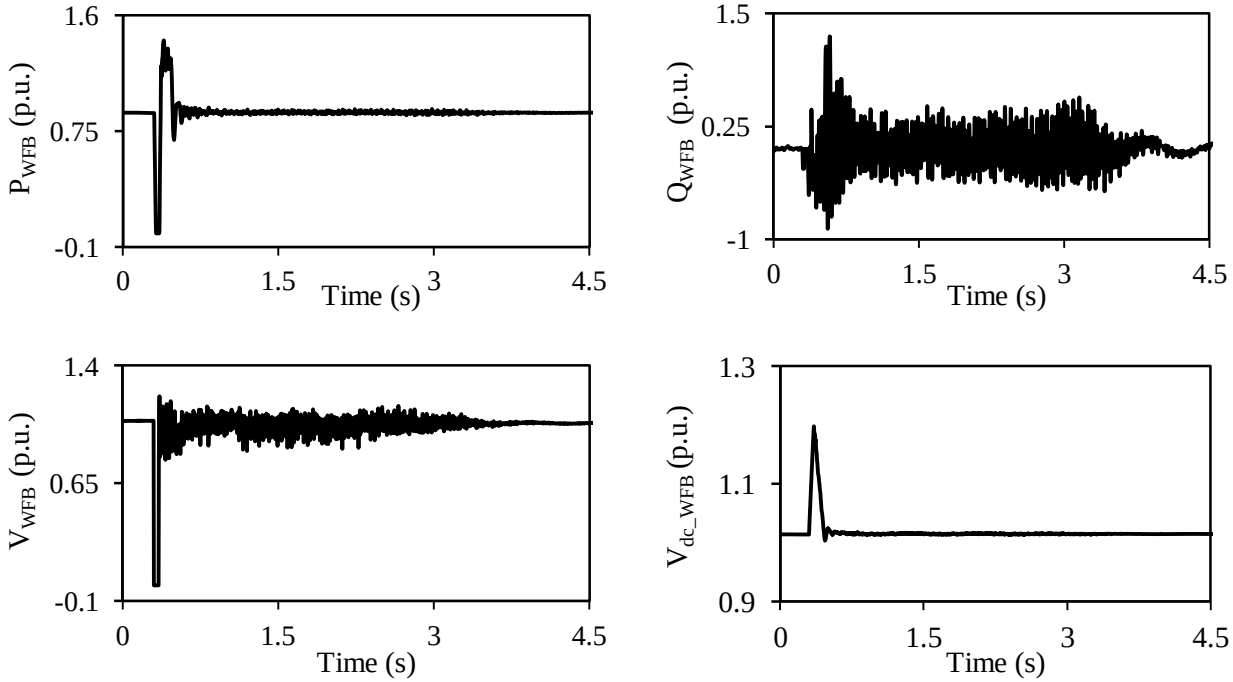

Figure 3.19: Wind farm B real and reactive powers, terminal voltage and dc capacitor voltage during and after clearing a 3-cycle, three-phase fault on Line 5 (60% compensation degree, supplemental control I is activated, Line 3 length = 50 km).

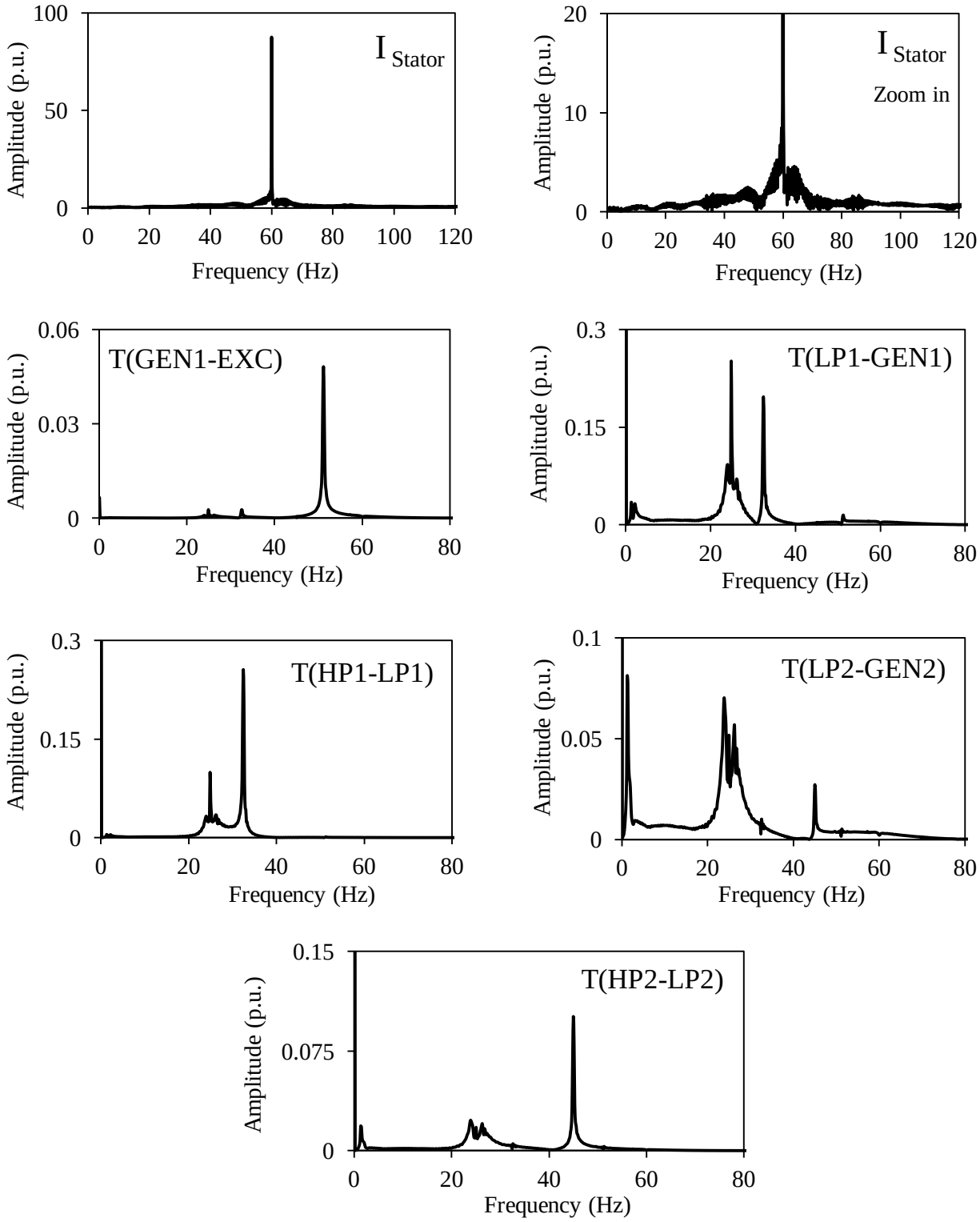

Figure 3.20: Frequency spectrums of the stator current of the DFIG wind turbine and the turbine-generator shaft torsional torques during and after clearing a 3-cycle, three-phase fault on Line 5 (60% compensation degree, supplemental control I is activated, Line 3 length = 50 km).

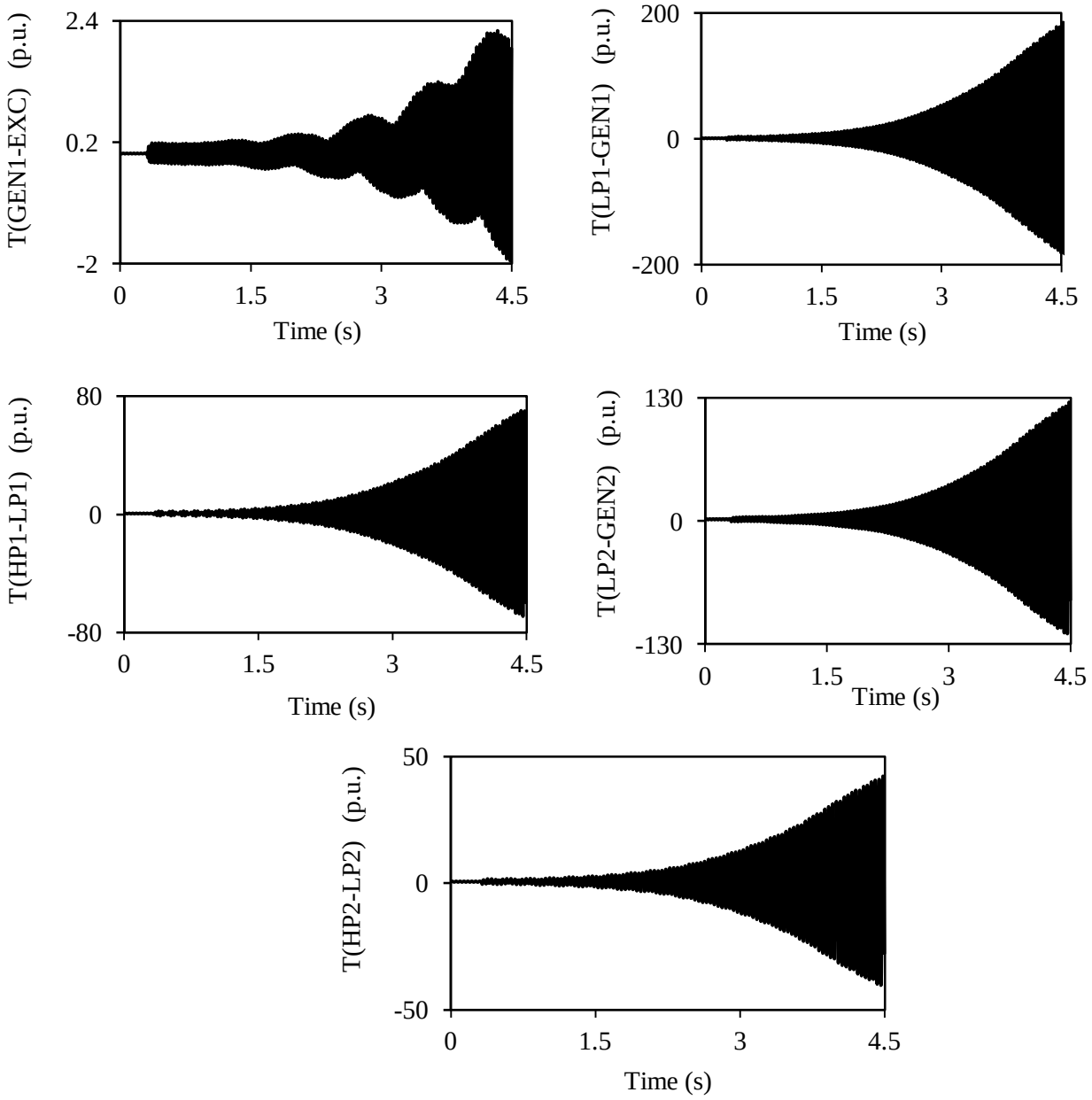

Figure 3.21: Turbine-generator shaft torsional torques during and after clearing a 3-cycle, three-phase fault on Line 5 (60% compensation degree, supplemental control I is not activated, Line 3 length = 100 km).

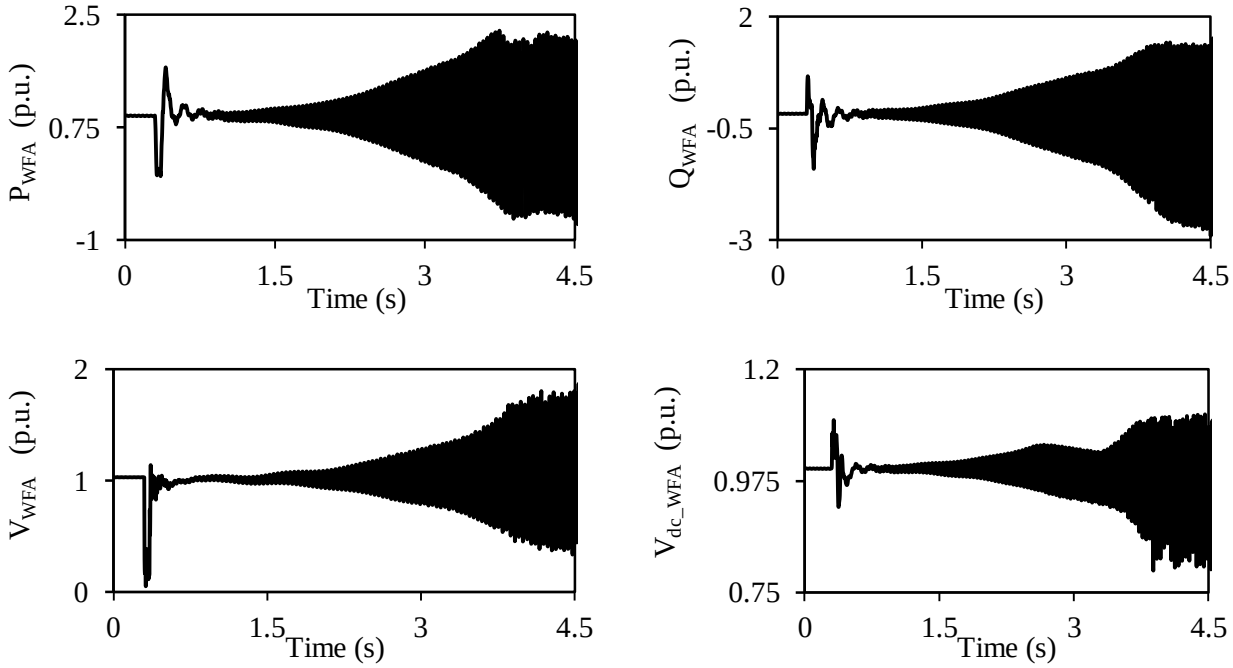

Figure 3.22: Wind farm A real and reactive powers, terminal voltage and dc capacitor voltage during and after clearing a 3-cycle, three-phase fault on Line 5 (60% compensation degree, supplemental control I is not activated, Line 3 length = 100 km).

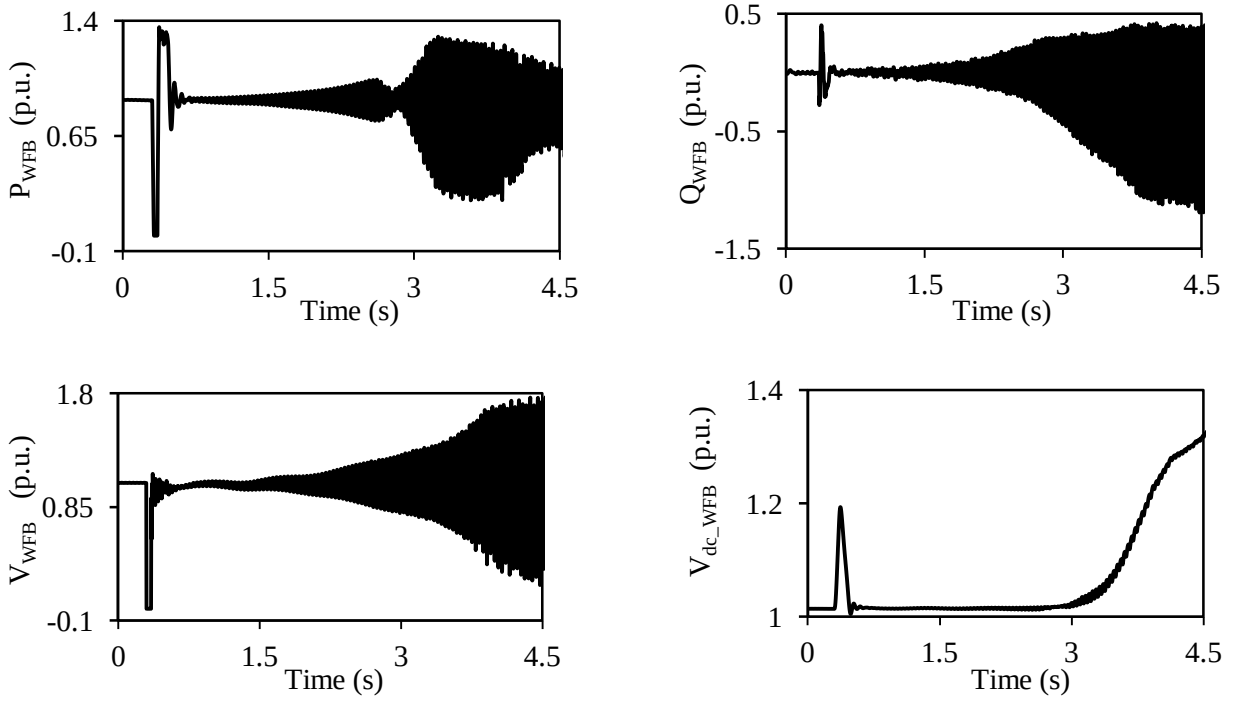

Figure 3.23: Wind farm B real and reactive powers, terminal voltage and dc capacitor voltage during and after clearing a 3-cycle, three-phase fault on Line 5 (60% compensation degree, supplemental control I is not activated, Line 3 length = 100 km).

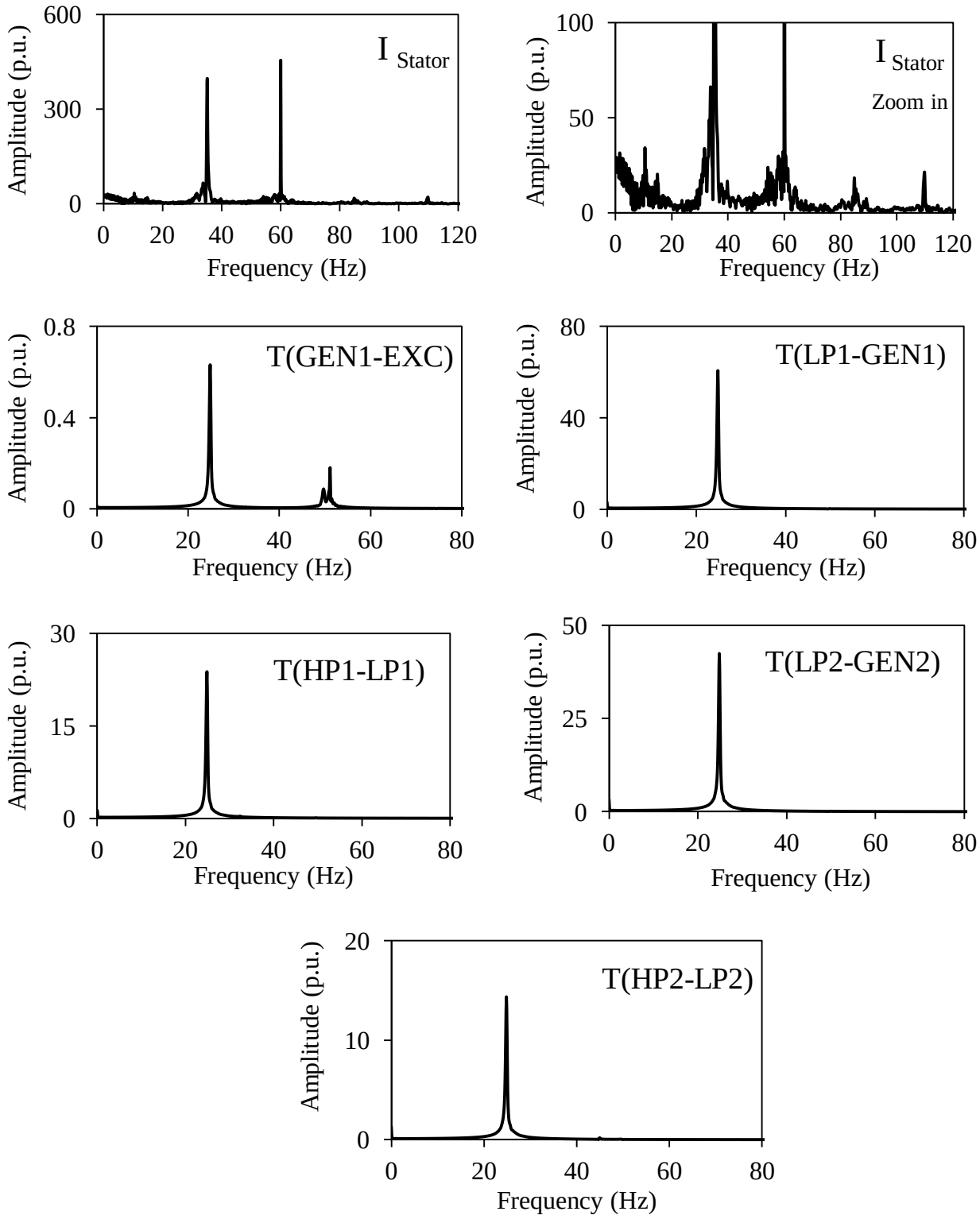

Figure 3.24: Frequency spectrums of the stator current of the DFIG wind turbine and the turbine-generator shaft torsional torques during and after clearing a 3-cycle, three-phase fault on Line 5 (60% compensation degree, supplemental control I is not activated, Line 3 length = 100 km).

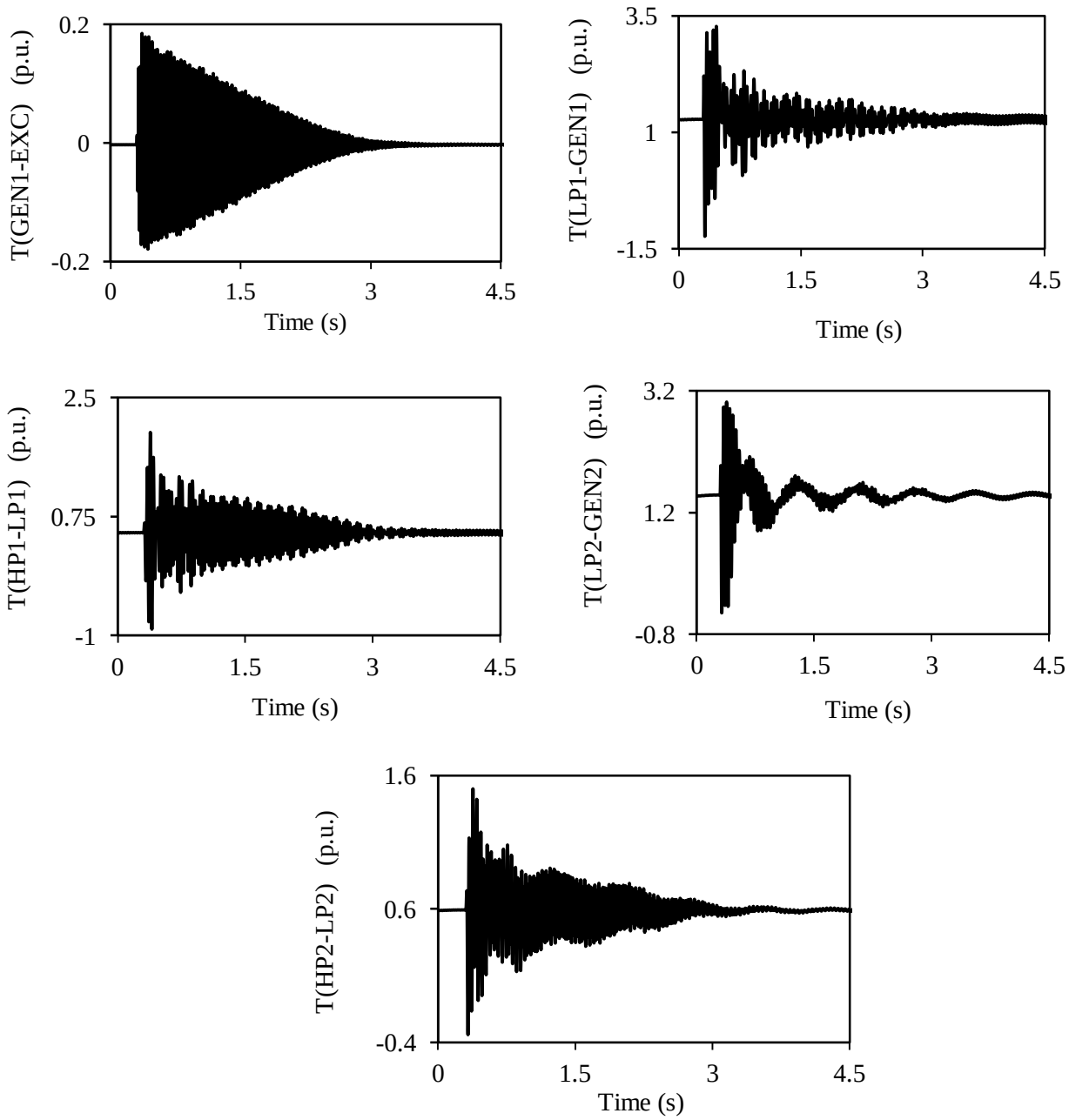

Figure 3.25: Turbine-generator shaft torsional torques during and after clearing a 3-cycle, three-phase fault on Line 5 (60% compensation degree, supplemental control I is activated, Line 3 length = 100 km).

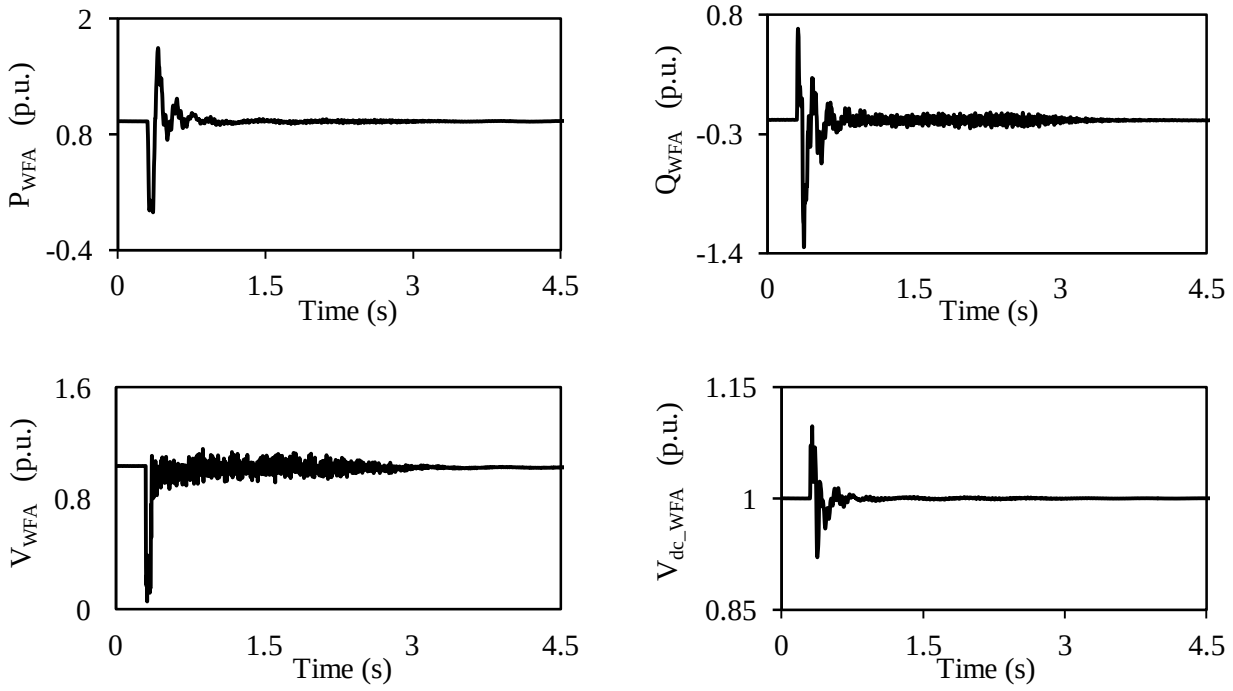

Figure 3.26: Wind farm A real and reactive powers, terminal voltage and dc capacitor voltage during and after clearing a 3-cycle, three-phase fault on Line 5 (60% compensation degree, supplemental control I is activated, Line 3 length = 100 km).

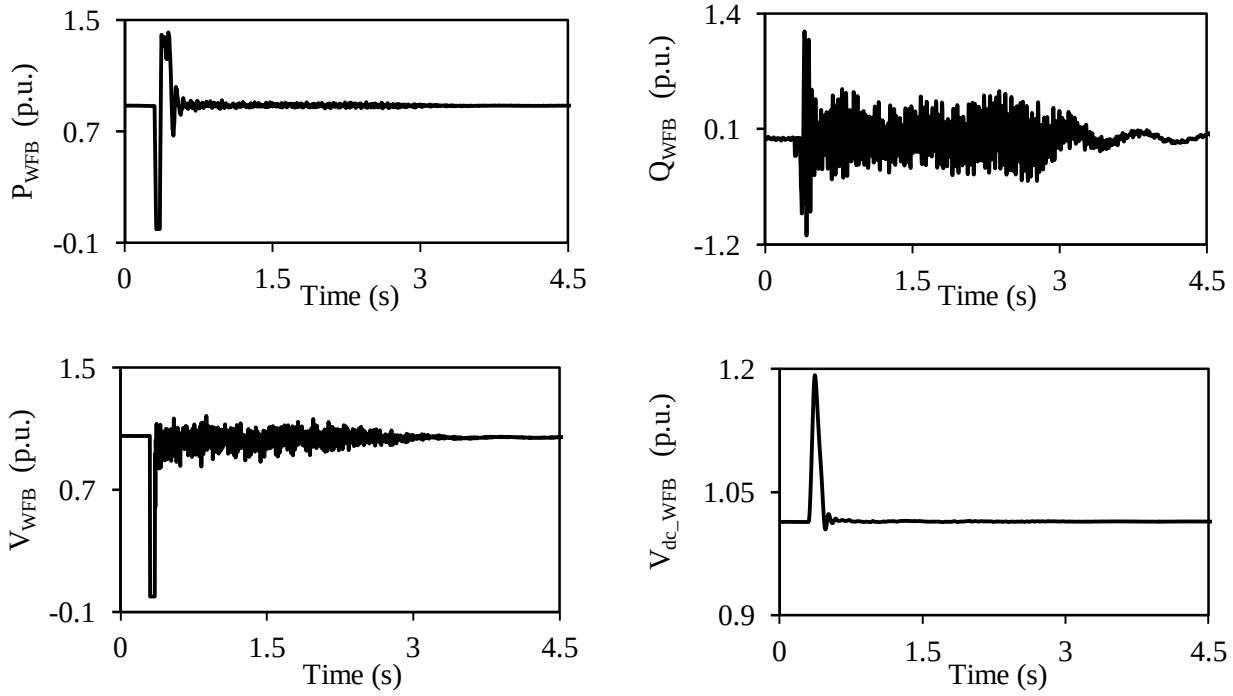

Figure 3.27: Wind farm B real and reactive powers, terminal voltage and dc capacitor voltage during and after clearing a 3-cycle, three-phase fault on Line 5 (60% compensation degree, supplemental control I is activated, Line 3 length = 100 km).

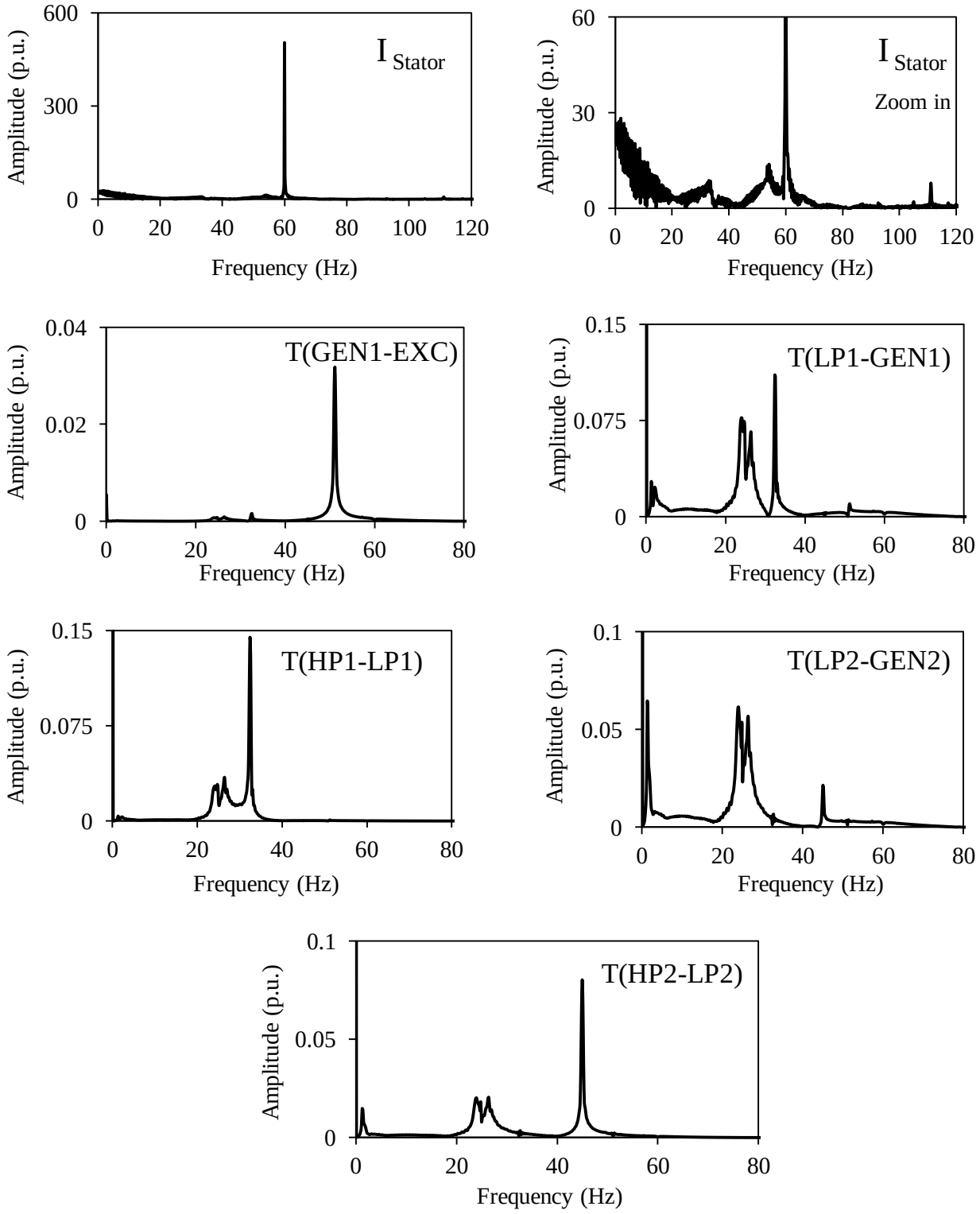

Figure 3.28: Frequency spectrums of the stator current of the DFIG wind turbine and the turbine-generator shaft torsional torques during and after clearing a 3-cycle, three-phase fault on Line 5 (60% compensation degree, supplemental control I is activated, Line 3 length = 100 km).

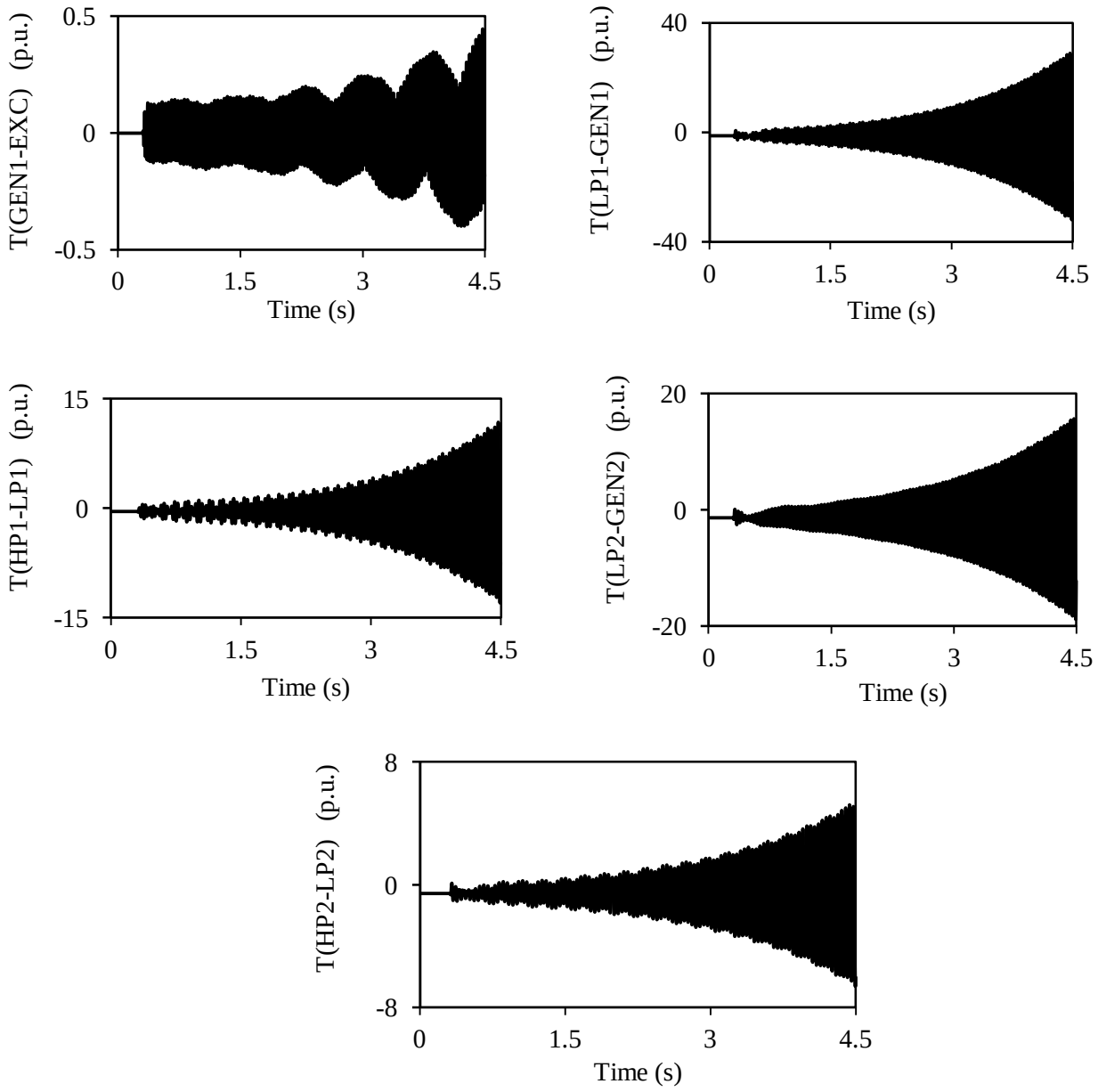

Figure 3.29: Turbine-generator shaft torsional torques during and after clearing a 3-cycle, three-phase fault on Line 5 (60% compensation degree, supplemental control I is not activated, Line 3 length = 200 km).

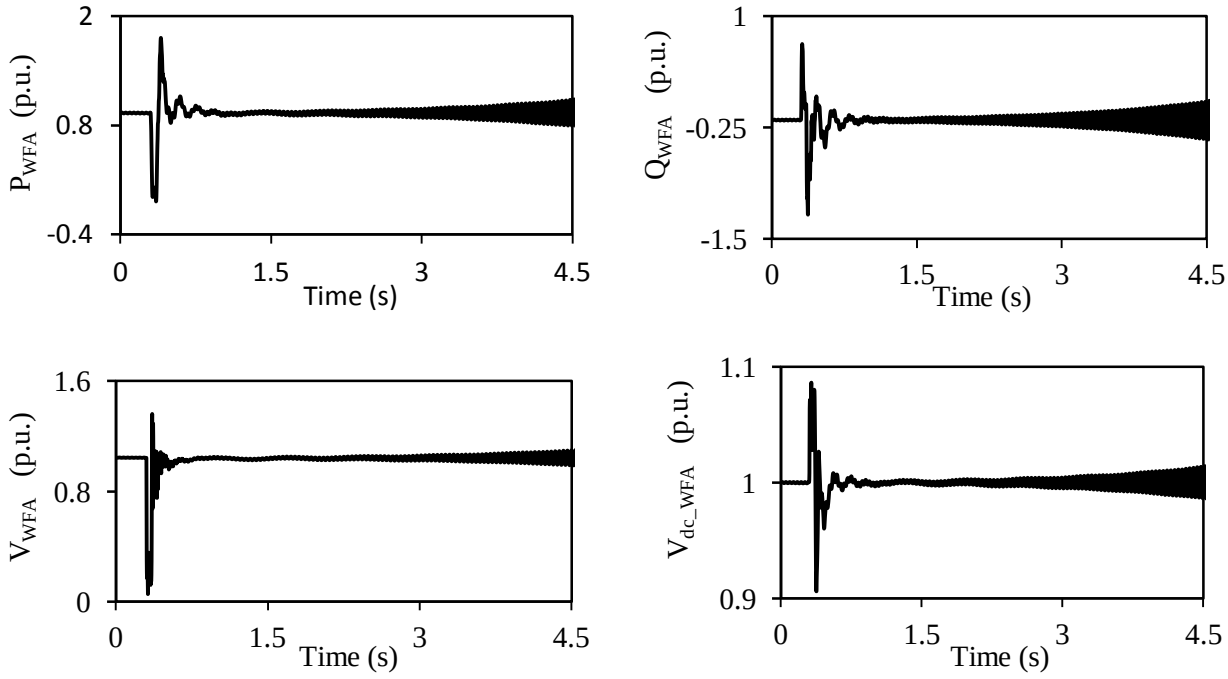

Figure 3.30: Wind farm A real and reactive powers, terminal voltage and dc capacitor voltage during and after clearing a 3-cycle, three-phase fault on Line 5 (60% compensation degree, supplemental control I is not activated, Line 3 length = 200 km).

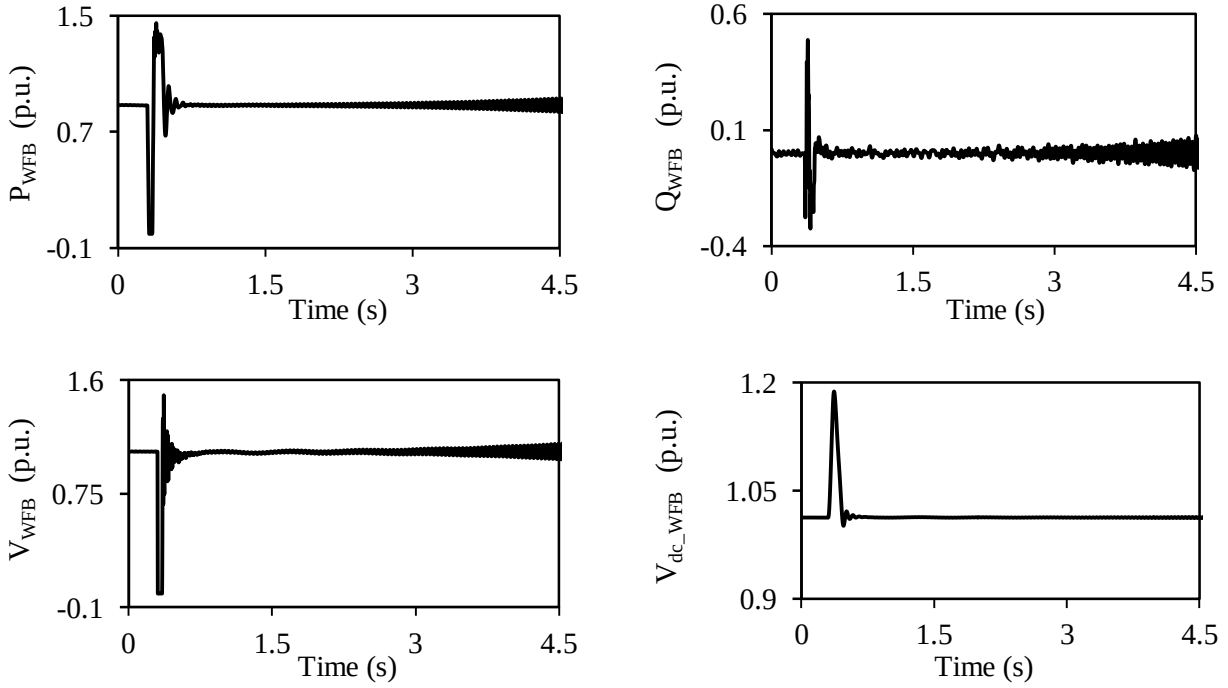

Figure 3.31: Wind farm B real and reactive powers, terminal voltage and dc capacitor voltage during and after clearing a 3-cycle, three-phase fault on Line 5 (60% compensation degree, supplemental control I is not activated, Line 3 length = 200 km).

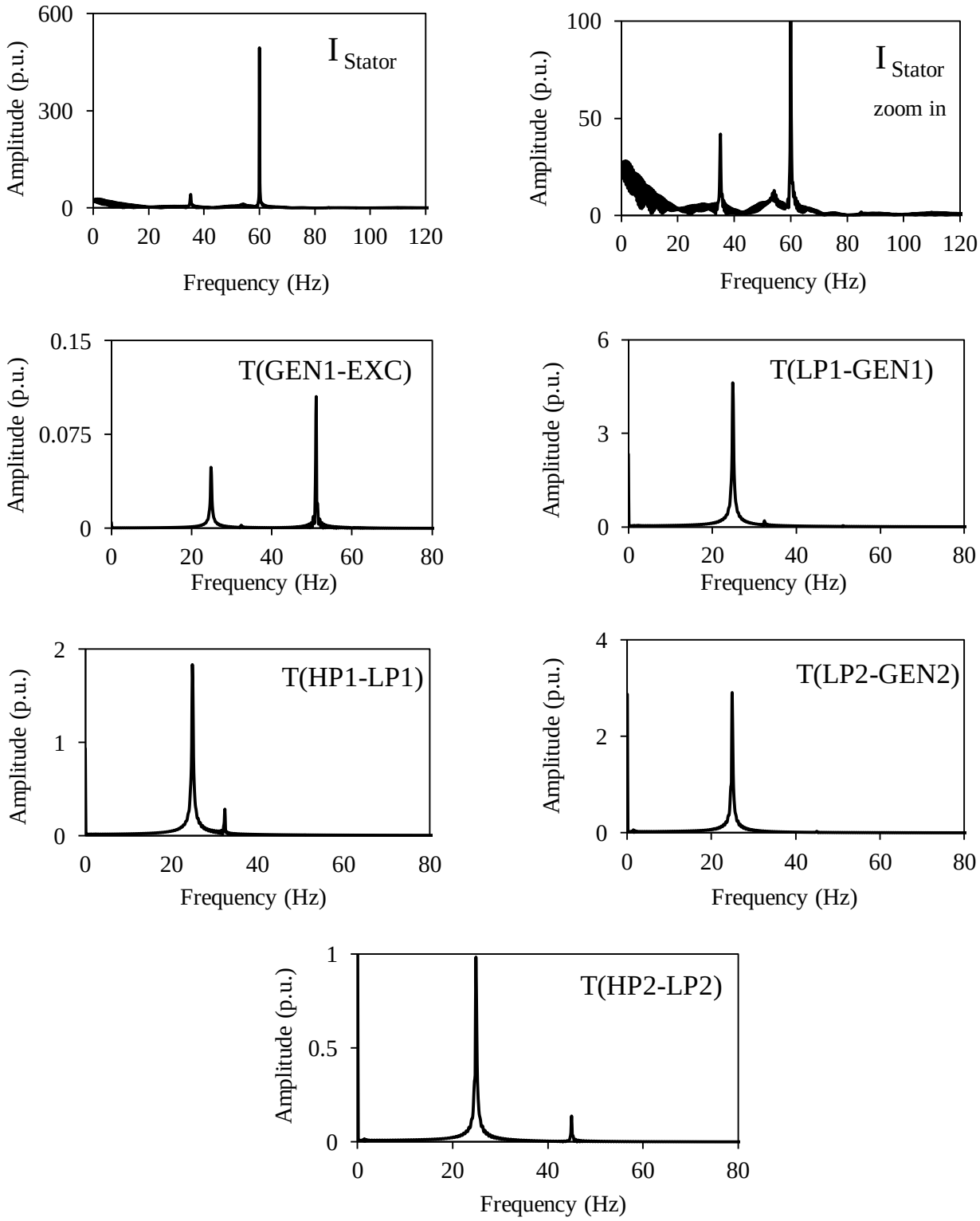

Figure 3.32: Frequency spectrums of the stator current of the DFIG wind turbine and the turbine-generator shaft torsional torques during and after clearing a 3-cycle, three-phase fault on Line 5 (60% compensation degree, supplemental control I is not activated, Line 3 length = 200 km).

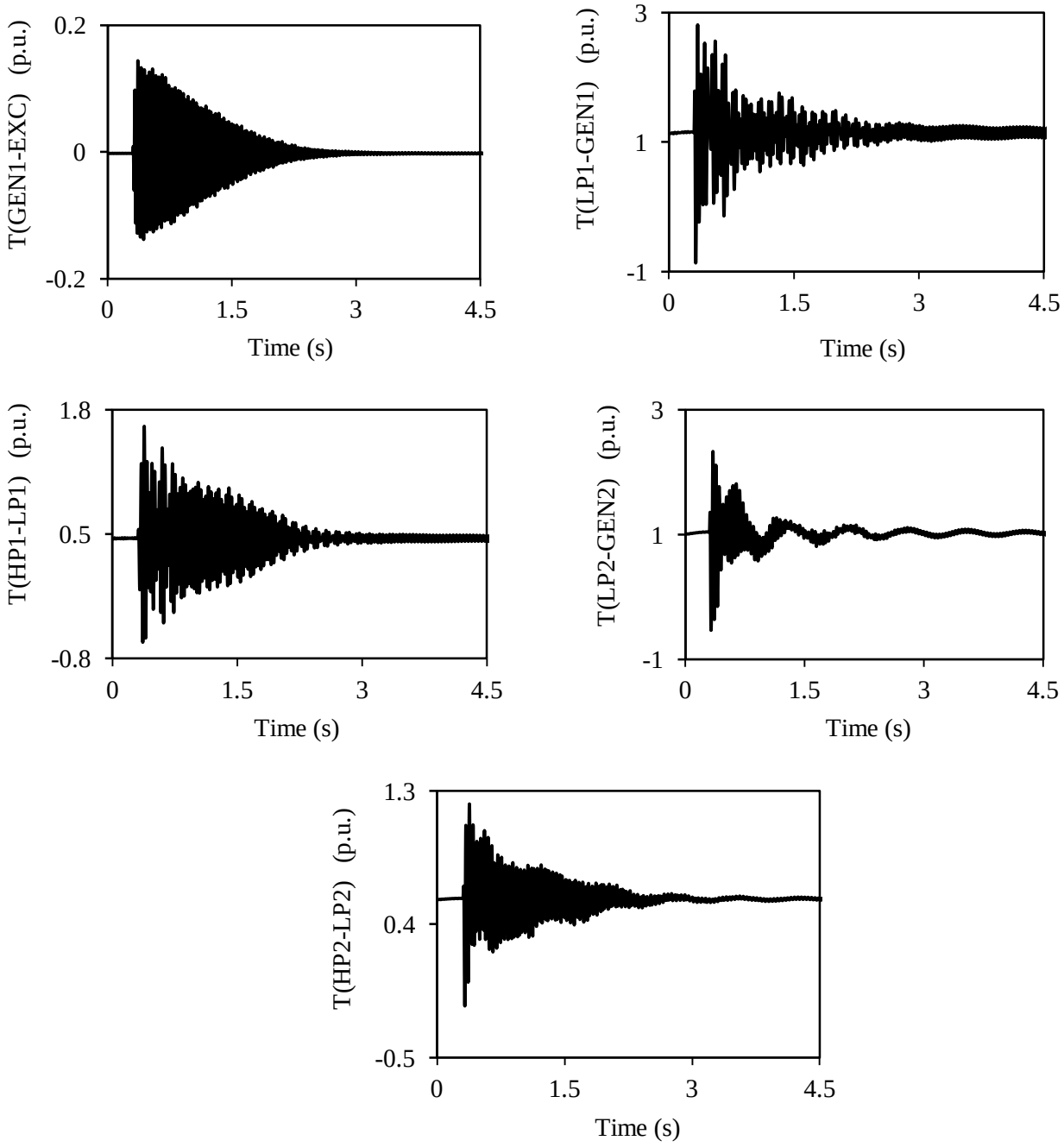

Figure 3.33: Turbine-generator shaft torsional torques during and after clearing a 3-cycle, three-phase fault on Line 5 (60% compensation degree, supplemental control I is activated, Line 3 length = 200 km).

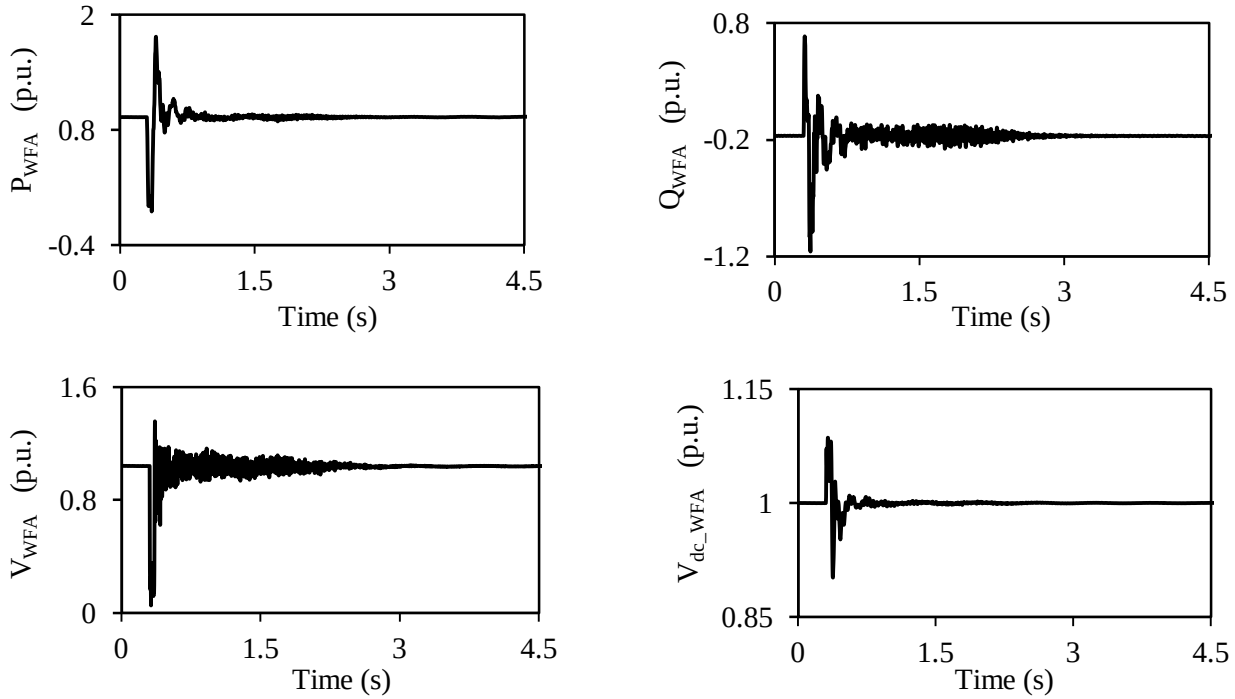

Figure 3.34: Wind farm A real and reactive powers, terminal voltage and dc capacitor voltage during and after clearing a 3-cycle, three-phase fault on Line 5 (60% compensation degree, supplemental control I is activated, Line 3 length = 200 km).

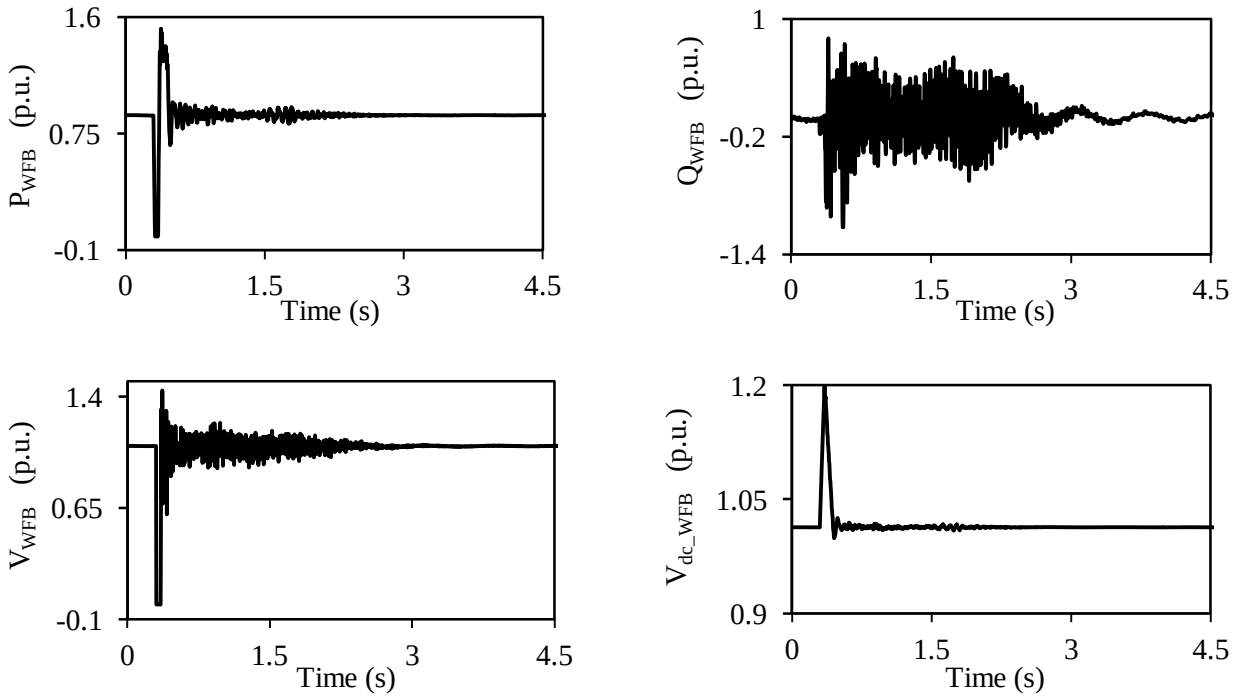

Figure 3.35: Wind farm B real and reactive powers, terminal voltage and dc capacitor voltage during and after clearing a 3-cycle, three-phase fault on Line 5 (60% compensation degree, supplemental control I is activated, Line 3 length = 200 km).

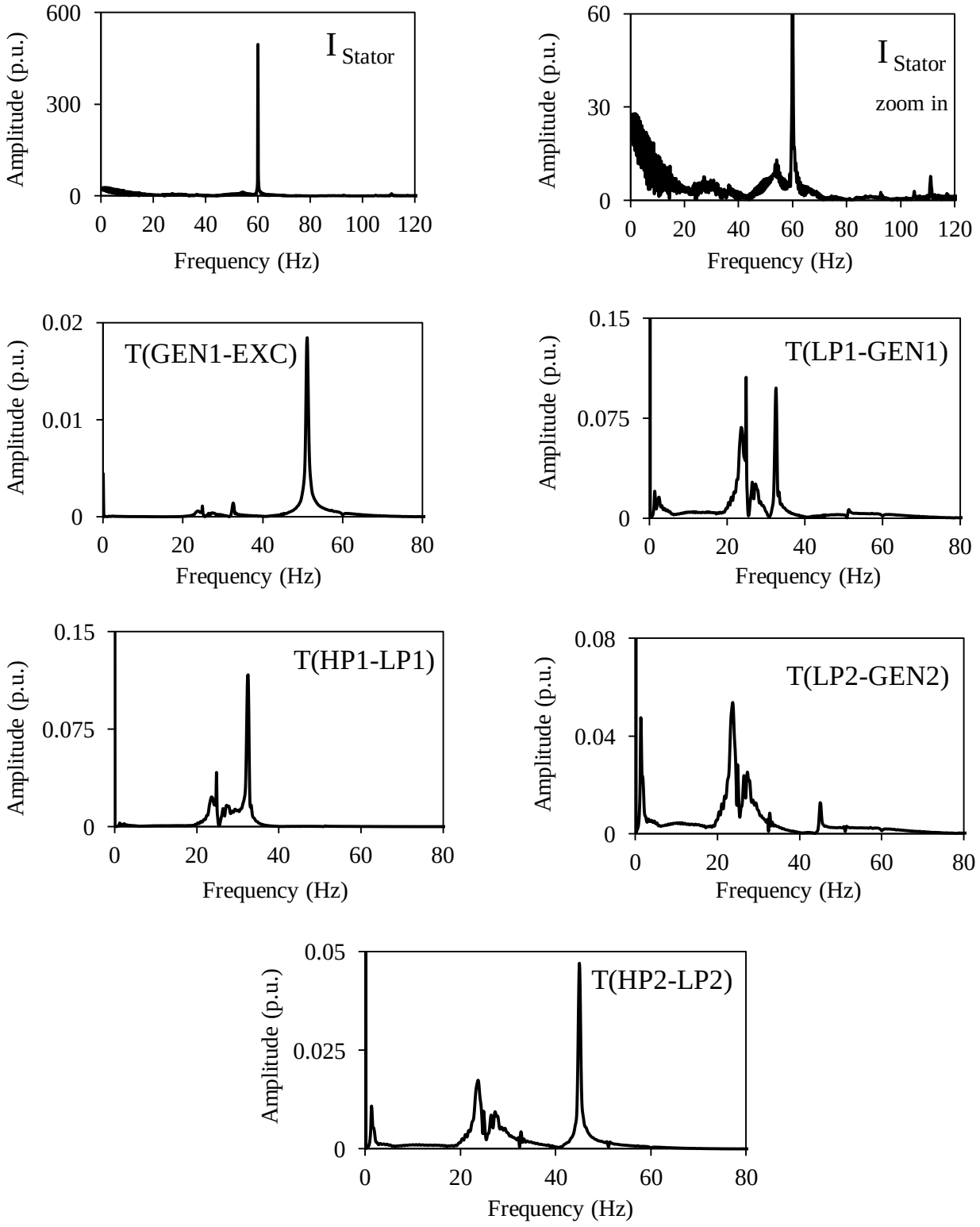

Figure 3.36: Frequency spectrums of the stator current of the DFIG wind turbine and the turbine-generator shaft torsional torques during and after clearing a 3-cycle, three-phase fault on Line 5 (60% compensation degree, supplemental control I is activated, Line 3 length = 200 km).

3.3.2 Effect of wind farm B rating

The effect of wind farm B rating on the performance of Supplemental control I, is explored at two different ratings, namely 150 MW and 300 MW. The results of this study are presented in the following two groups of figures:

Group A: Wind farm B rating = 150 MW, (Figures 3.37, 3.38, 3.39, 3.40, 3.41, 3.42, 3.43, 3.44)

Group B: Wind farm B rating = 300 MW, (Figures 3.45, 3.46, 3.47, 3.48, 3.49, 3.50, 3.51, 3.52).

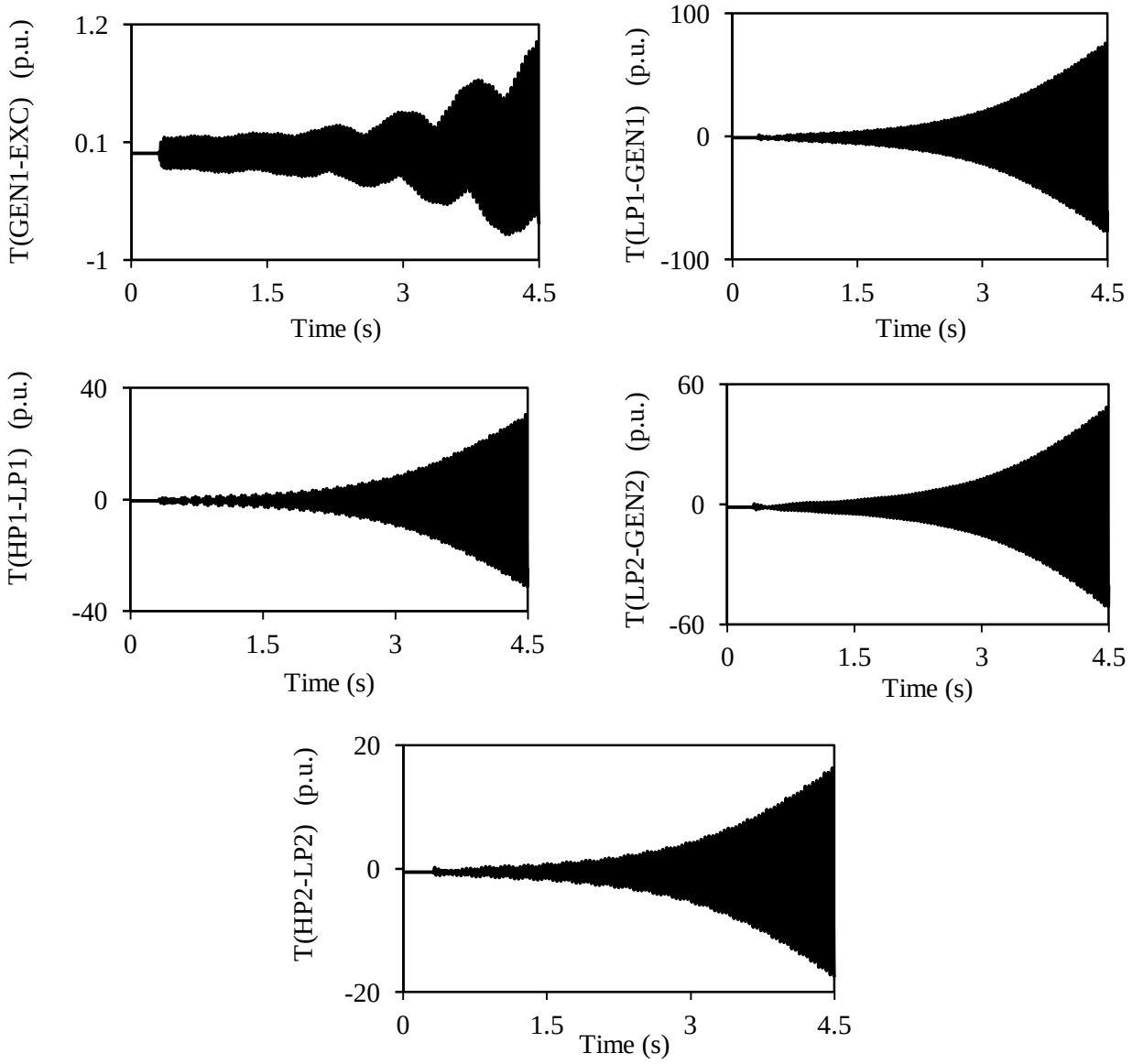

Figure 3.37: Turbine-generator shaft torsional torques during and after clearing a 3-cycle, three-phase fault on Line 5 (60% compensation degree, supplemental control I is not activated, wind farm B rating = 150 MW).

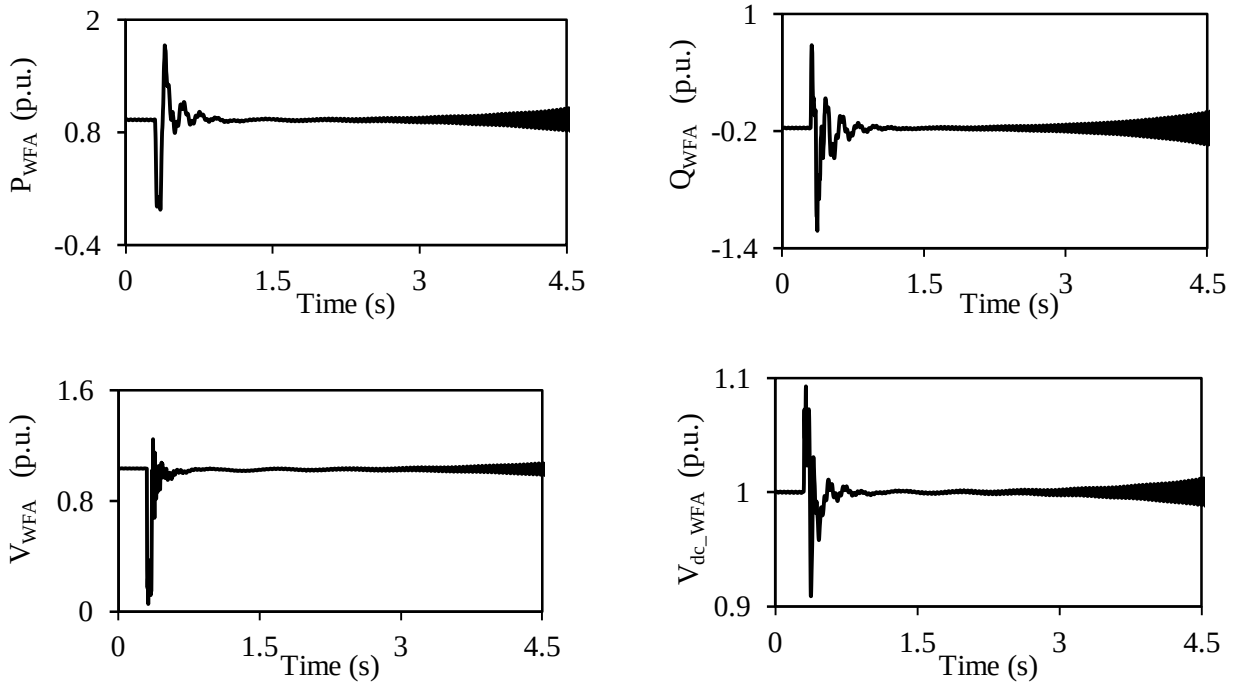

Figure 3.38: Wind farm A real and reactive powers, terminal voltage and dc capacitor voltage during and after clearing a 3-cycle, three-phase fault on Line 5 (60% compensation degree, supplemental control I is not activated, wind farm B rating = 150 MW).

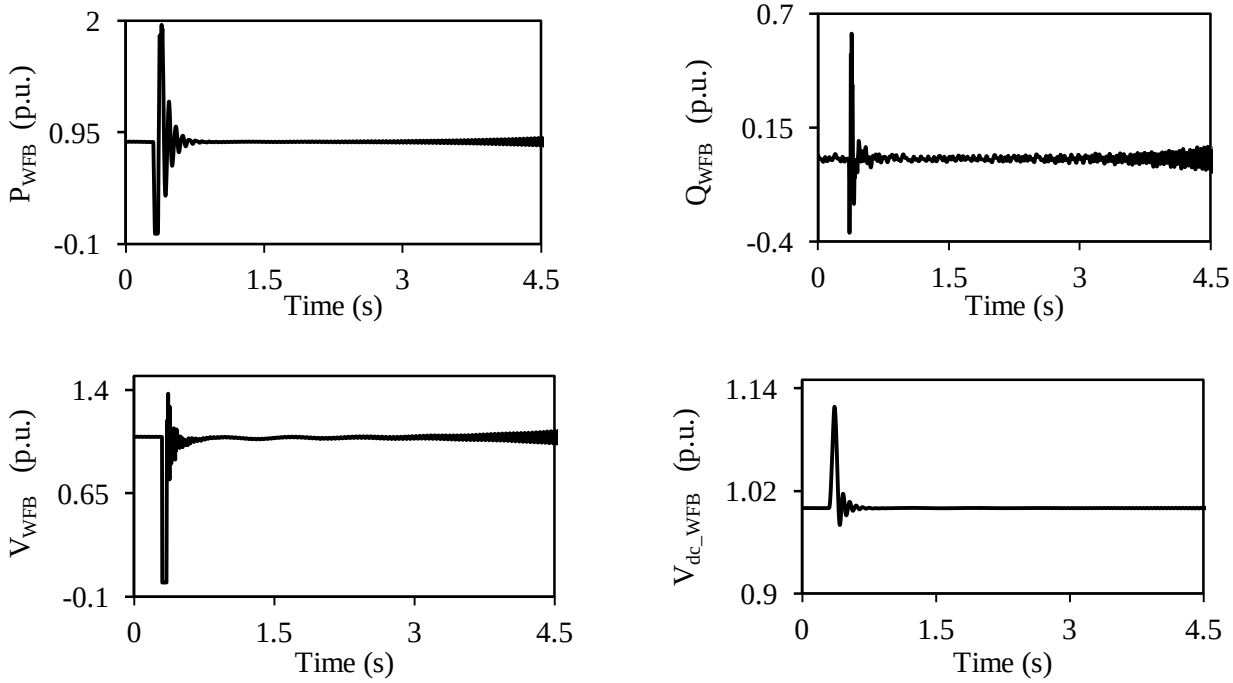

Figure 3.39: Wind farm B real and reactive powers, terminal voltage and dc capacitor voltage during and after clearing a 3-cycle, three-phase fault on Line 5 (60% compensation degree, supplemental control I is not activated, wind farm B rating = 150 MW).

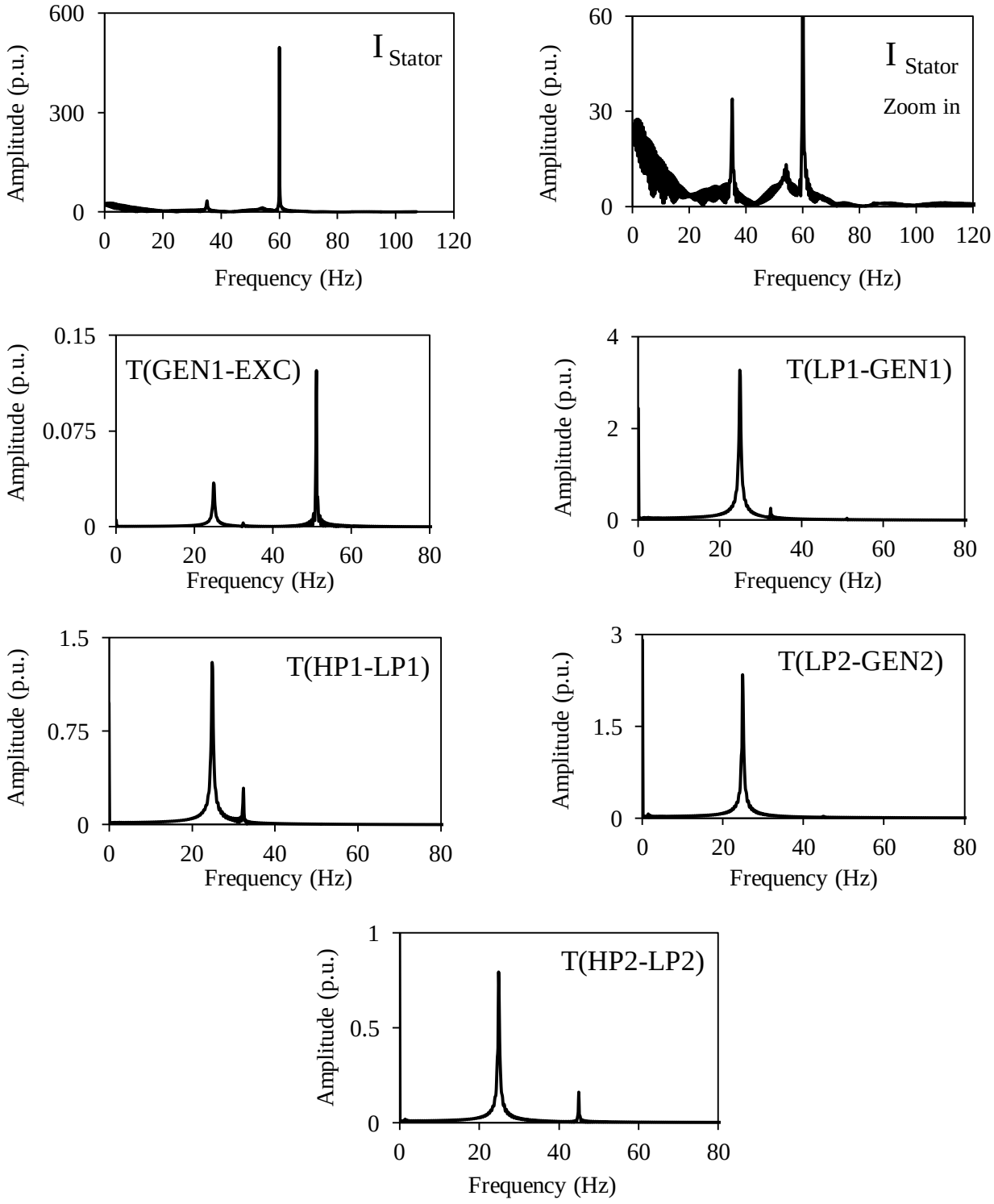

Figure 3.40: Frequency spectrums of the stator current of the DFIG wind turbine and the turbine-generator shaft torsional torques during and after clearing a 3-cycle, three-phase fault on Line 5 (60% compensation degree, supplemental control I is not activated, wind farm B rating = 150 MW).

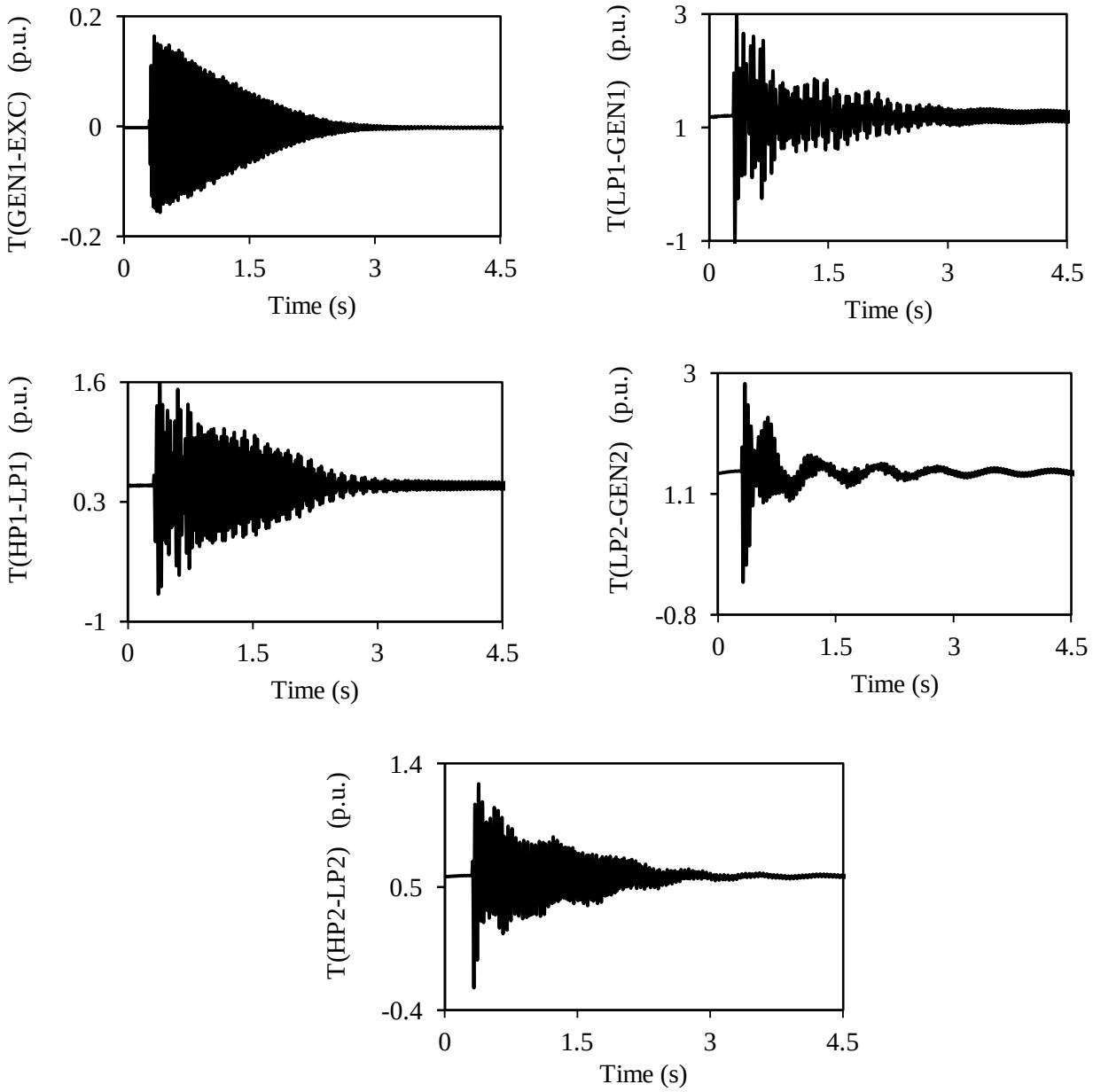

Figure 3.41: Turbine-generator shaft torsional torques during and after clearing a 3-cycle, three-phase fault on Line 5 (60% compensation degree, supplemental control I is activated, wind farm B rating = 150 MW).

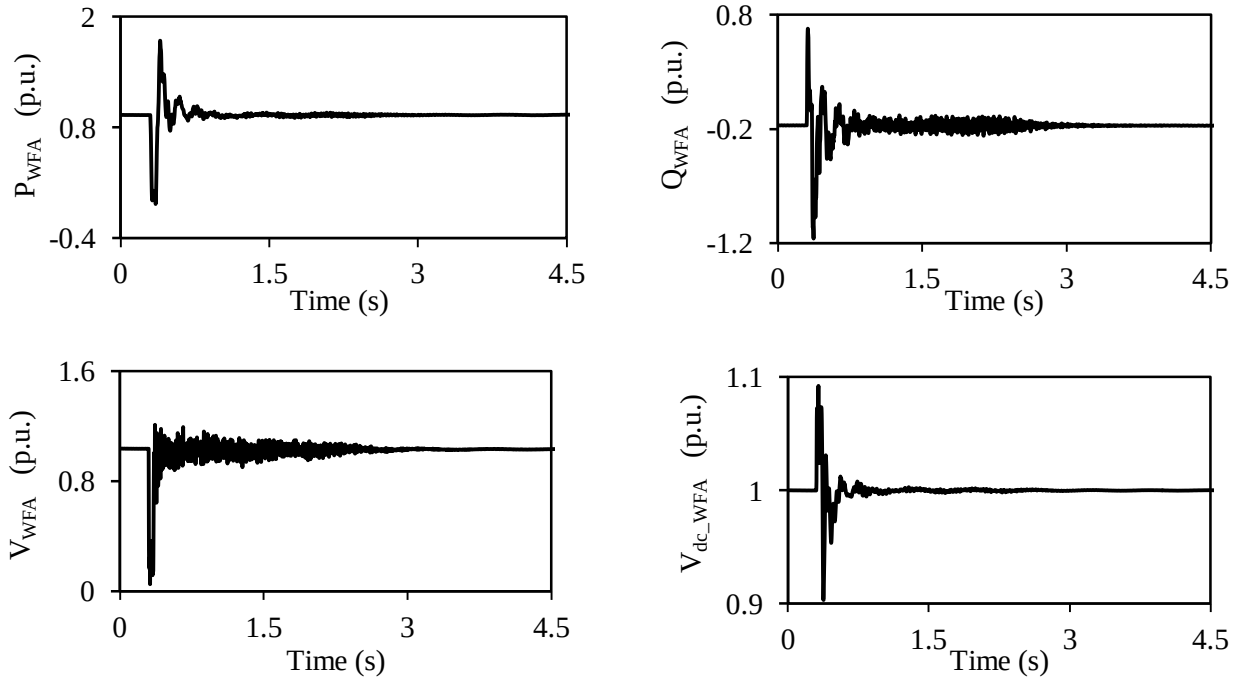

Figure 3.42: Wind farm A real and reactive powers, terminal voltage and dc capacitor voltage during and after clearing a 3-cycle, three-phase fault on Line 5 (60% compensation degree, supplemental control I is activated, wind farm B rating = 150 MW).

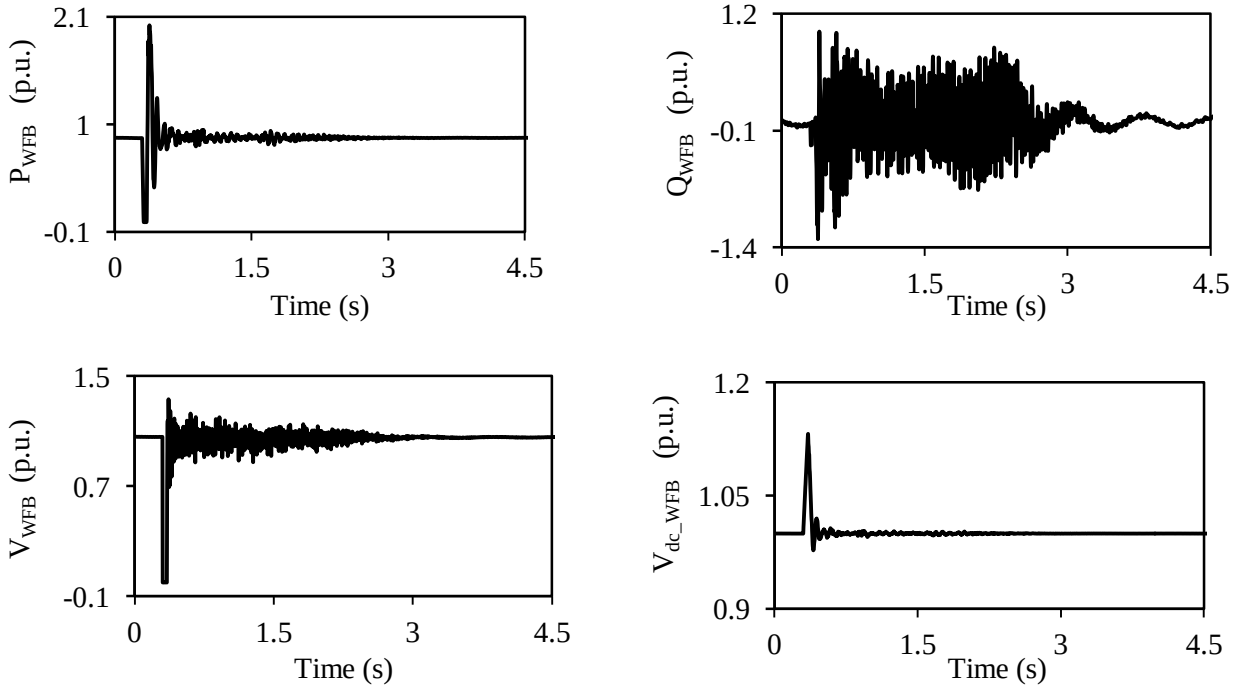

Figure 3.43: Wind farm B real and reactive powers, terminal voltage and dc capacitor voltage during and after clearing a 3-cycle, three-phase fault on Line 5 (60% compensation degree, supplemental control I is activated, wind farm B rating = 150 MW).

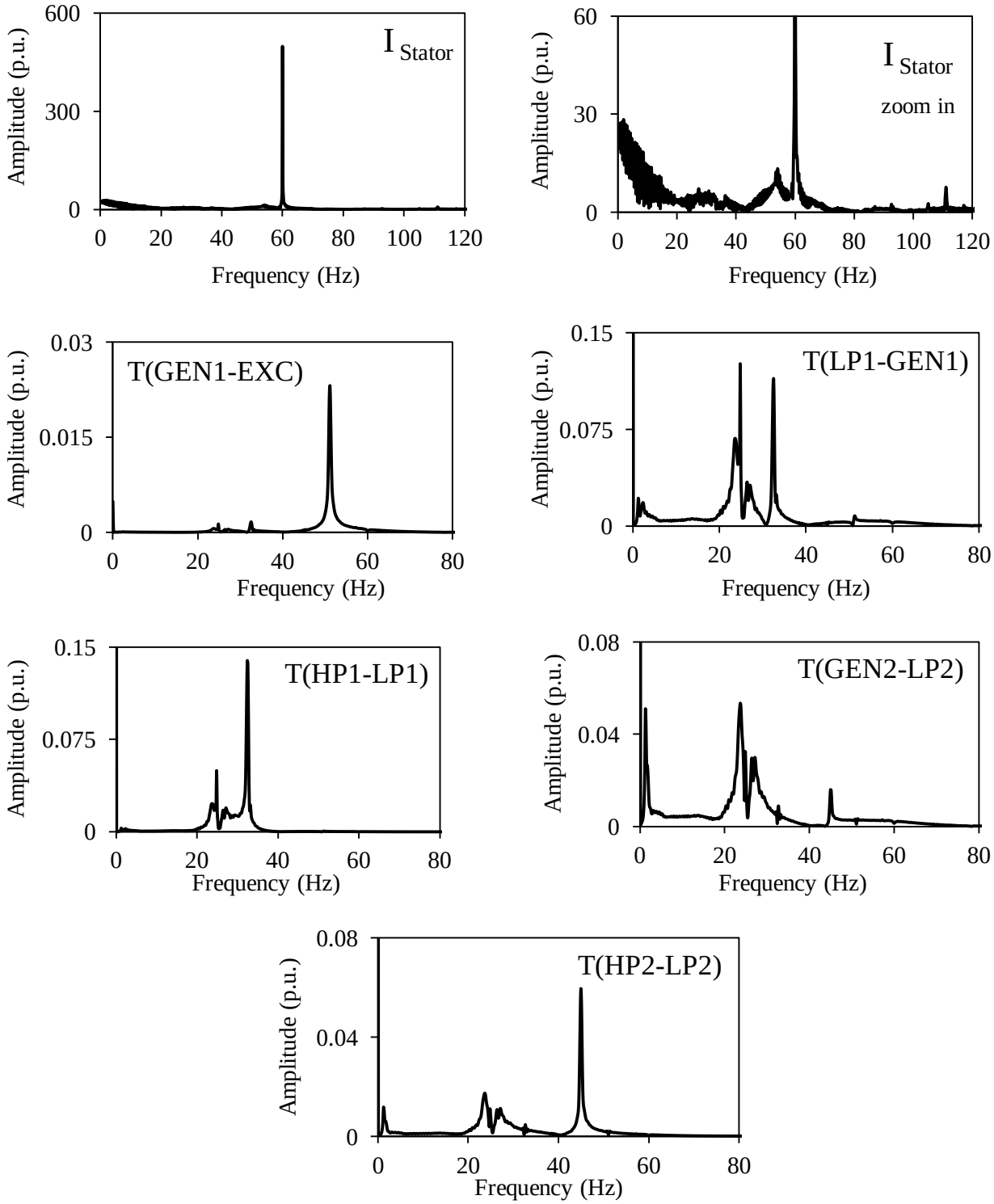

Figure 3.44: Frequency spectrums of the stator current of the DFIG wind turbine and the turbine-generator shaft torsional torques during and after clearing a 3-cycle, three-phase fault on Line 5 (60% compensation degree, supplemental control I is activated, wind farm B rating = 150 MW).

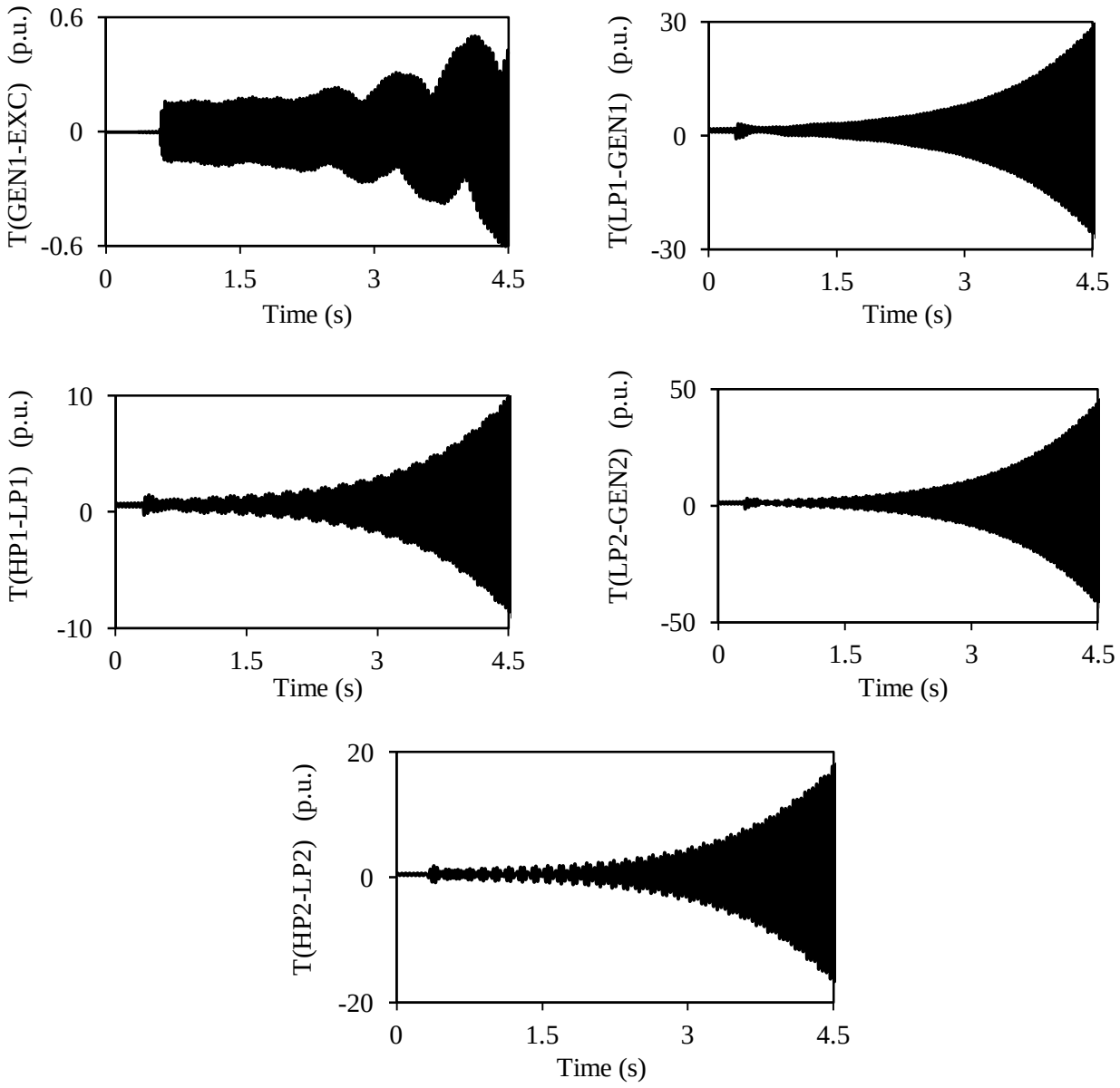

Figure 3.45: Turbine-generator shaft torsional torques during and after clearing a 3-cycle, three-phase fault on Line 5 (60% compensation degree, supplemental control I is not activated, wind farm B rating = 300 MW).

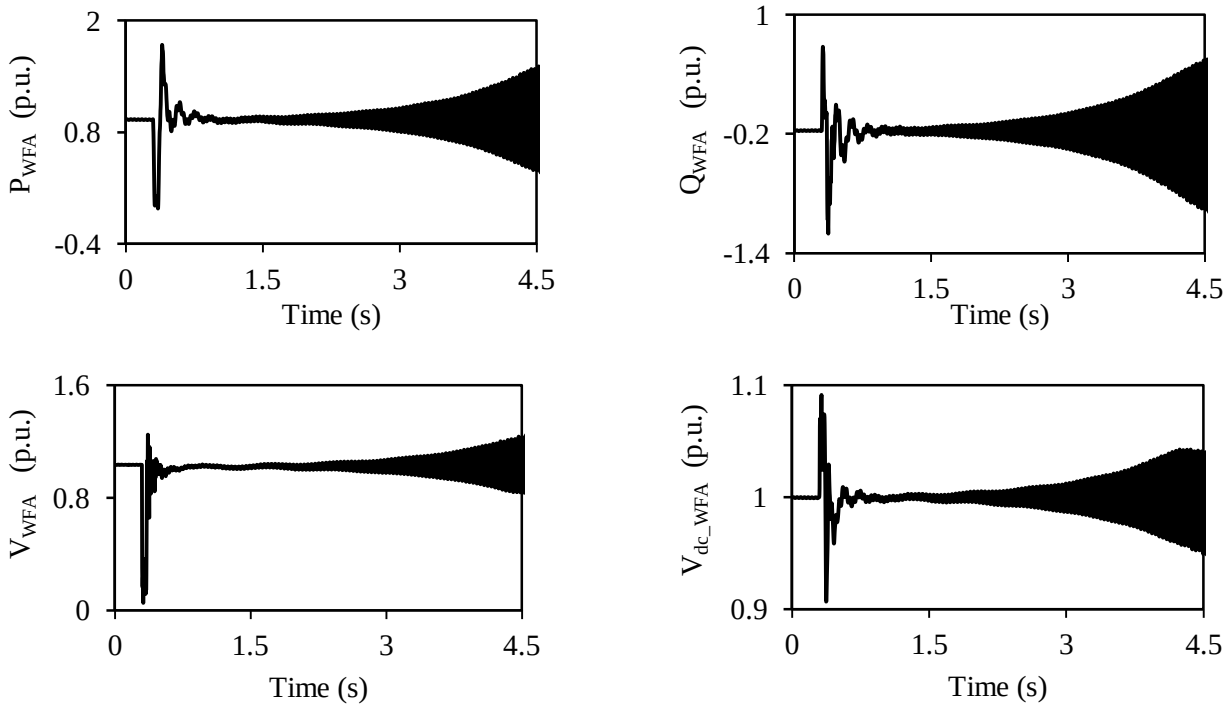

Figure 3.46: Wind farm A real and reactive powers, terminal voltage and dc capacitor voltage during and after clearing a 3-cycle, three-phase fault on Line 5 (60% compensation degree, supplemental control I is not activated, wind farm B rating = 300 MW).

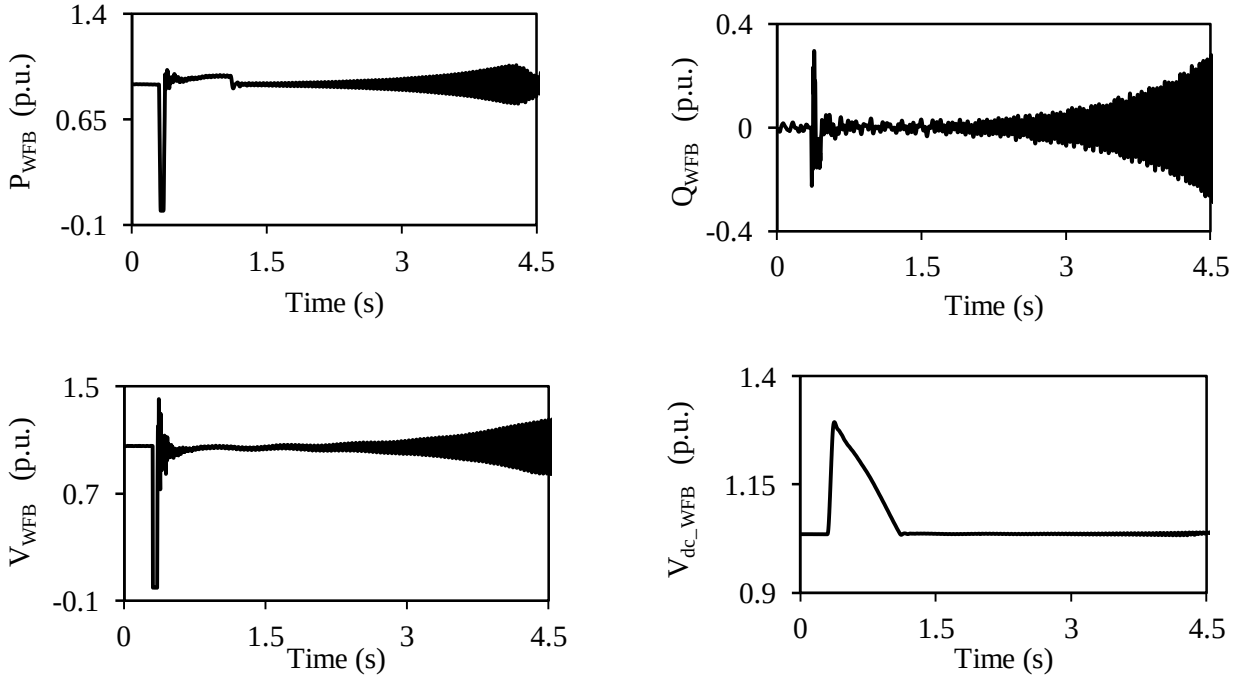

Figure 3.47: Wind farm B real and reactive powers, terminal voltage and dc capacitor voltage during and after clearing a 3-cycle, three-phase fault on Line 5 (60% compensation degree, supplemental control I is not activated, wind farm B rating = 300 MW).

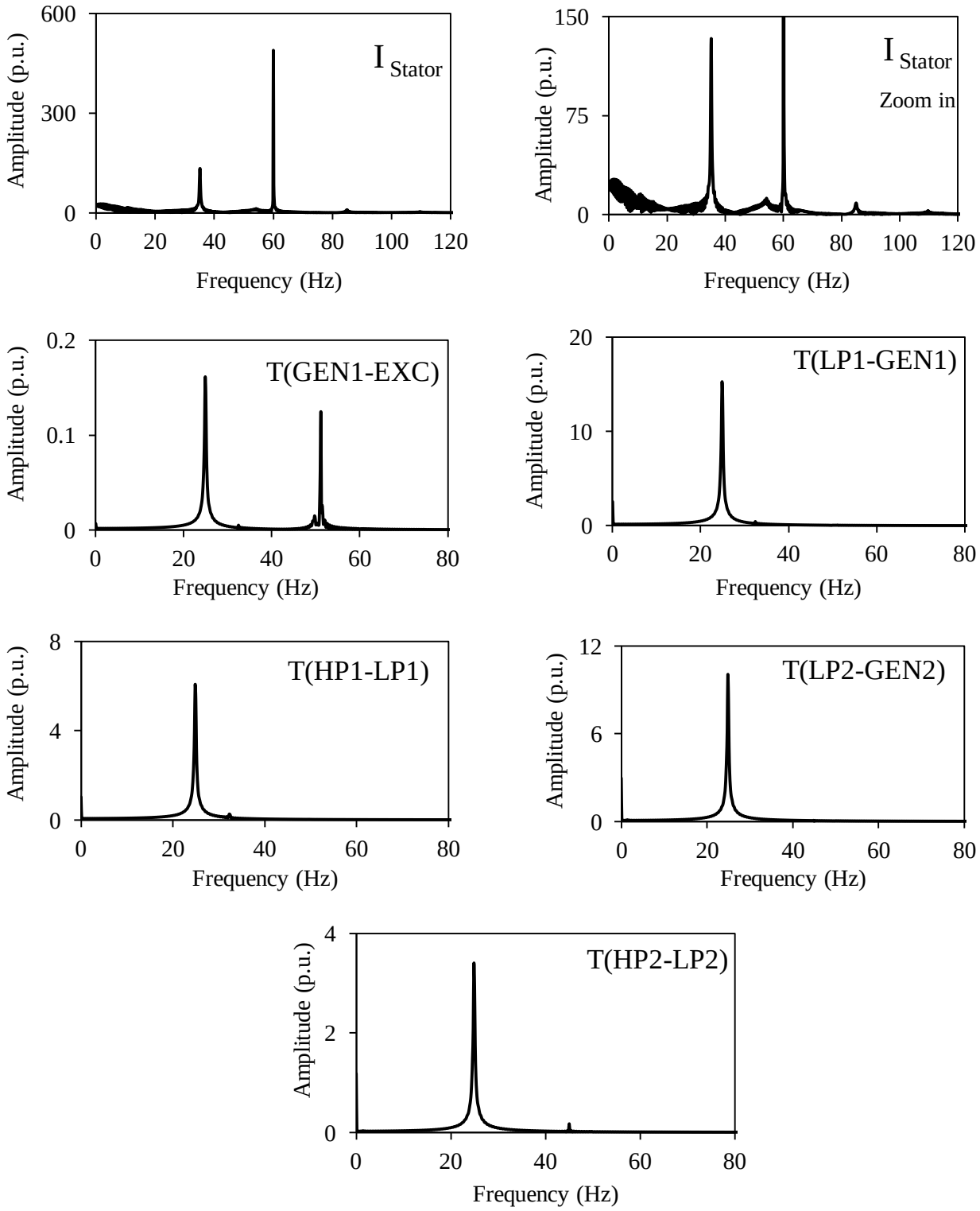

Figure 3.48: Frequency spectrums of the stator current of the DFIG wind turbine and the turbine-generator shaft torsional torques during and after clearing a 3-cycle, three-phase fault on Line 5 (60% compensation degree, supplemental control I is not activated, wind farm B rating = 300 MW).

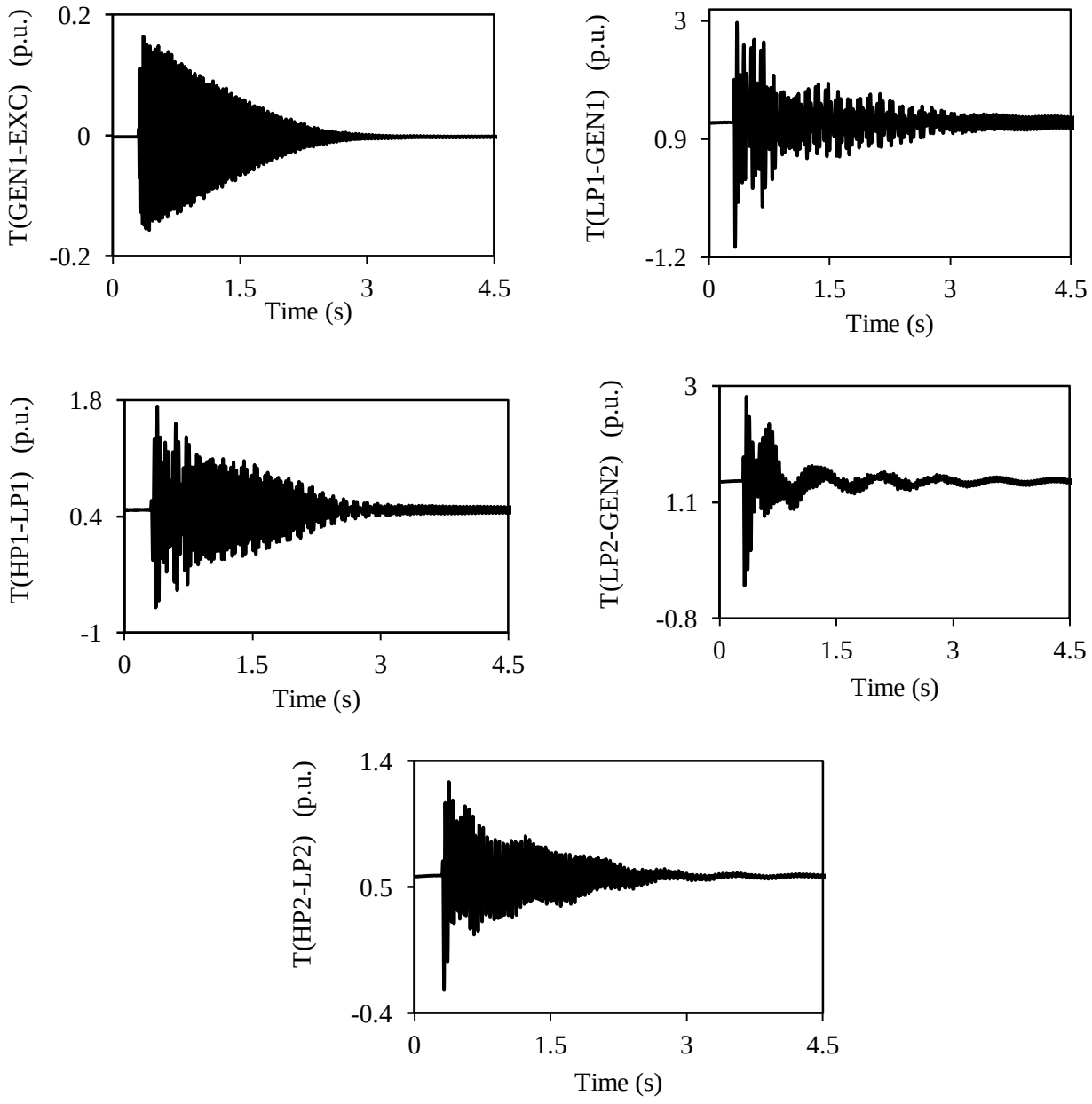

Figure 3.49: Turbine-generator shaft torsional torques during and after clearing a 3-cycle, three-phase fault on Line 5 (60% compensation degree, supplemental control I is activated, wind farm B rating = 300 MW).

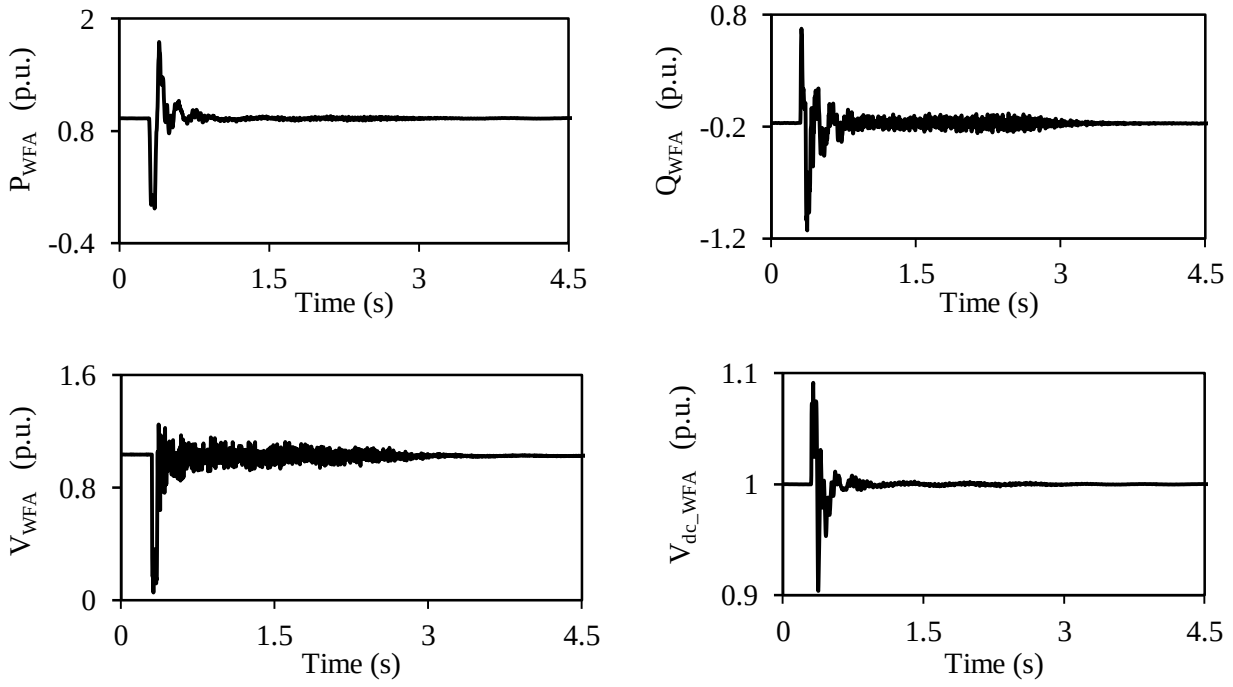

Figure 3.50: Wind farm A real and reactive powers, terminal voltage and dc capacitor voltage during and after clearing a 3-cycle, three-phase fault on Line 5 (60% compensation degree, supplemental control I is activated, wind farm B rating = 300 MW).

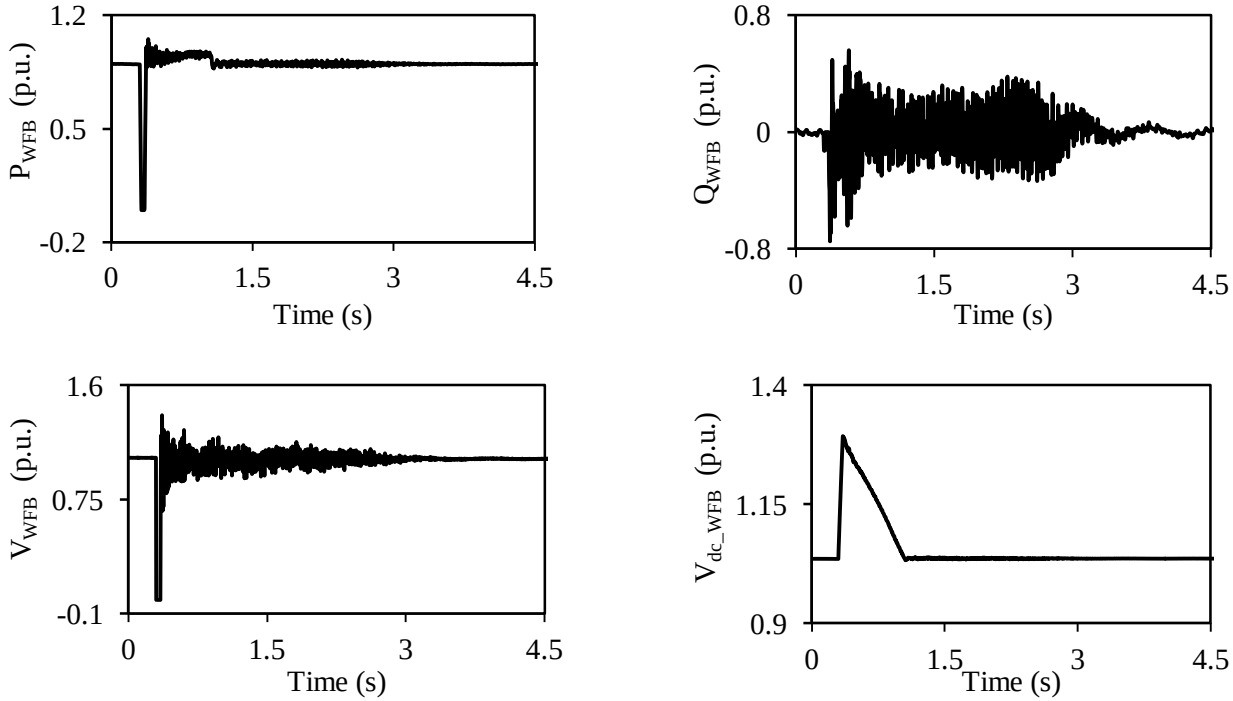

Figure 3.51: Wind farm B real and reactive powers, terminal voltage and dc capacitor voltage during and after clearing a 3-cycle, three-phase fault on Line 5 (60% compensation degree, supplemental control I is activated, wind farm B rating = 300 MW).

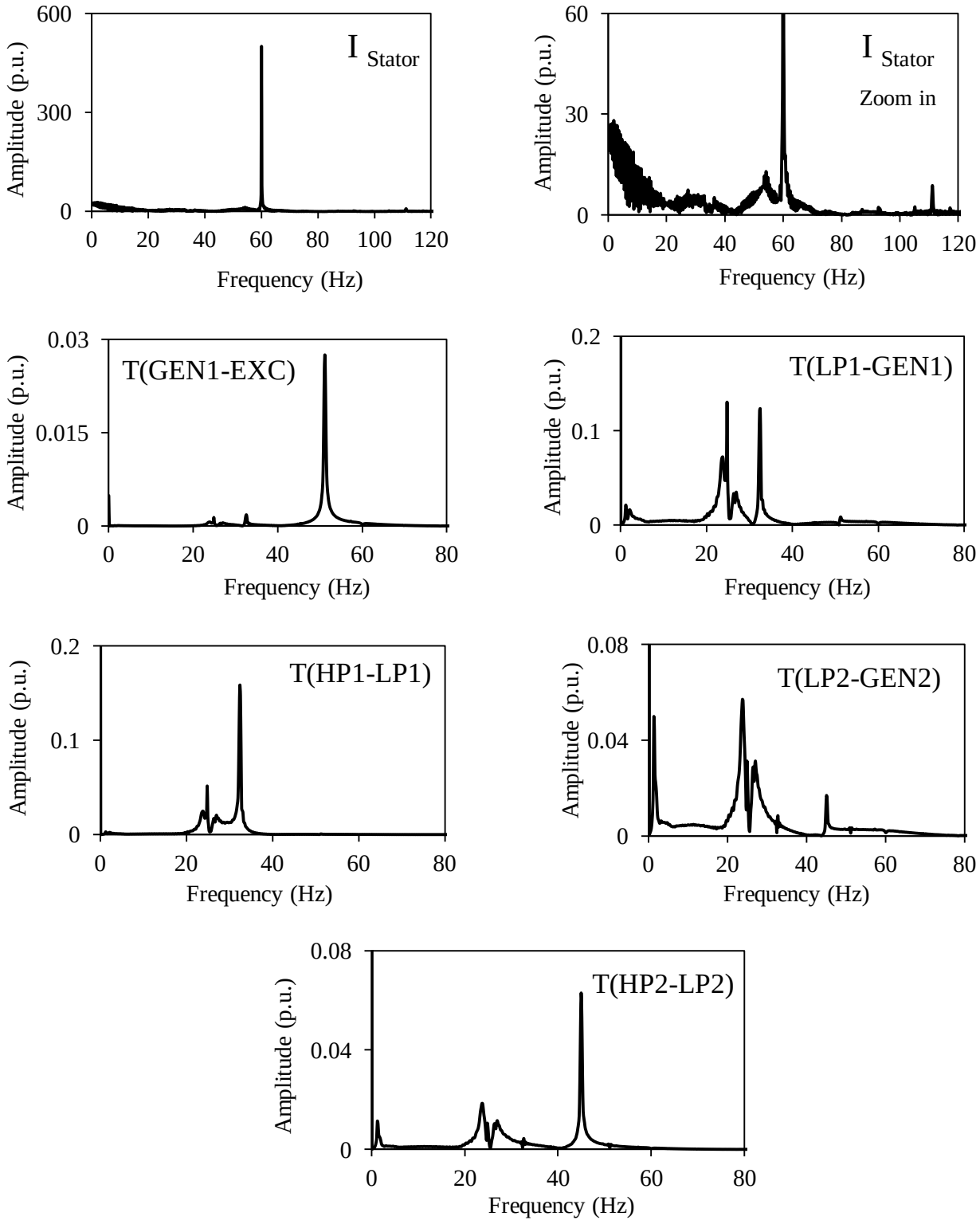

Figure 3.52: Frequency spectrums of the stator current of the DFIG wind turbine and the turbine-generator shaft torsional torques during and after clearing a 3-cycle, three-phase fault on Line 5 (60% compensation degree, supplemental control I is activated, wind farm B rating = 300 MW).

In each group, the turbine-generator shaft torsional torques, wind farms A and B active and reactive powers, terminal voltage and the BtB dc voltage as well as the frequency spectrums of the stator current of the DFIG wind turbines and the turbine-generator shaft torsional torques are shown for the cases when Supplemental control I is disabled and activated respectively. Moreover, the transfer functions of Supplemental control I in Groups A and B are the same as those given in Table 3.1.

The comparisons between the two sets of figures (Set 1: Supplemental control I is disabled and Set 2: Supplemental control I is activated) in Groups A and B show the effectiveness of the supplemental control in mitigating SSR and SSI at different ratings of wind farm B.

3.3.3 Effect of the fault type

The effect of the fault type on the performance of Supplemental control I is examined by applying a ***double line-to-ground fault (L-L-G)*** at the same fault location (Line 5). The results of this study are presented in the following two groups of figures:

Group A: Supplemental control I is disabled, (Figures 3.53, 3.54, 3.55, 3.56)

Group B: Supplemental control I is activated, (Figures 3.57, 3.58, 3.59, 3.60)

In each group, the turbine-generator shaft torsional torques, wind farms A and B active and reactive powers, terminal voltage and the BtB dc voltage as well as the frequency spectrums of the stator current of the DFIG wind turbines and the turbine-generator shaft torsional torques are shown. Moreover, the transfer functions of Supplemental control I in Group B are the same as those given in Table 3.1.

The comparison between the two sets of figures in Groups A and B (Set 1: Supplemental control I is disabled and Set 2: Supplemental control I is activated) demonstrates the effectiveness of the supplemental control in mitigating SSR and SSI during and after clearing an unsymmetrical fault. It is worth noting here that the results of the other case studies that are not reported in this thesis have shown the effectiveness of Supplemental control I in mitigating SSR and SSI during and after clearing line-to-line and single line-to-ground faults.

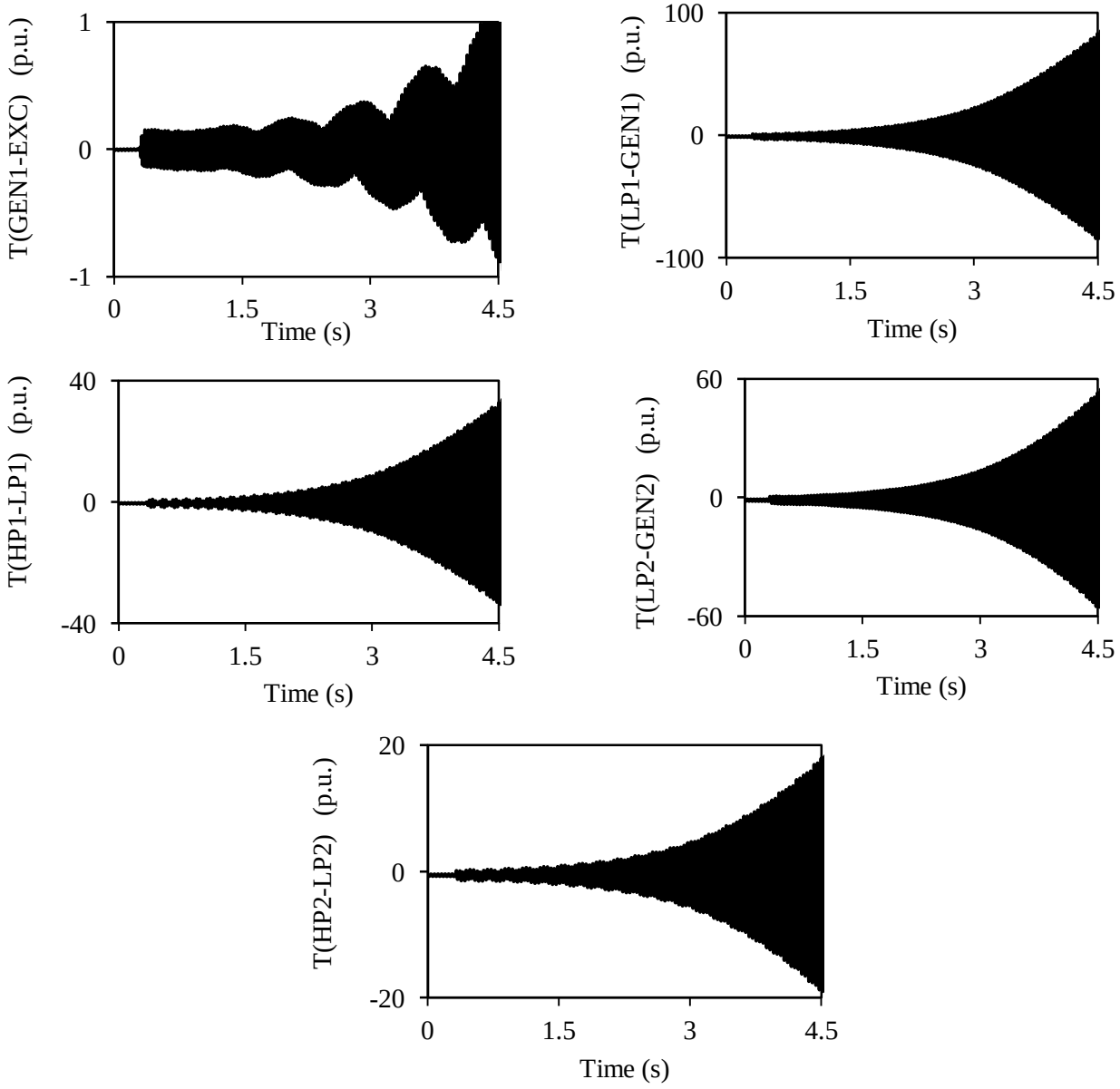

Figure 3.53: Turbine-generator shaft torsional torques during and after clearing a 3-cycle, L-L-G fault on Line 5 (60% compensation degree, supplemental control I is not activated).

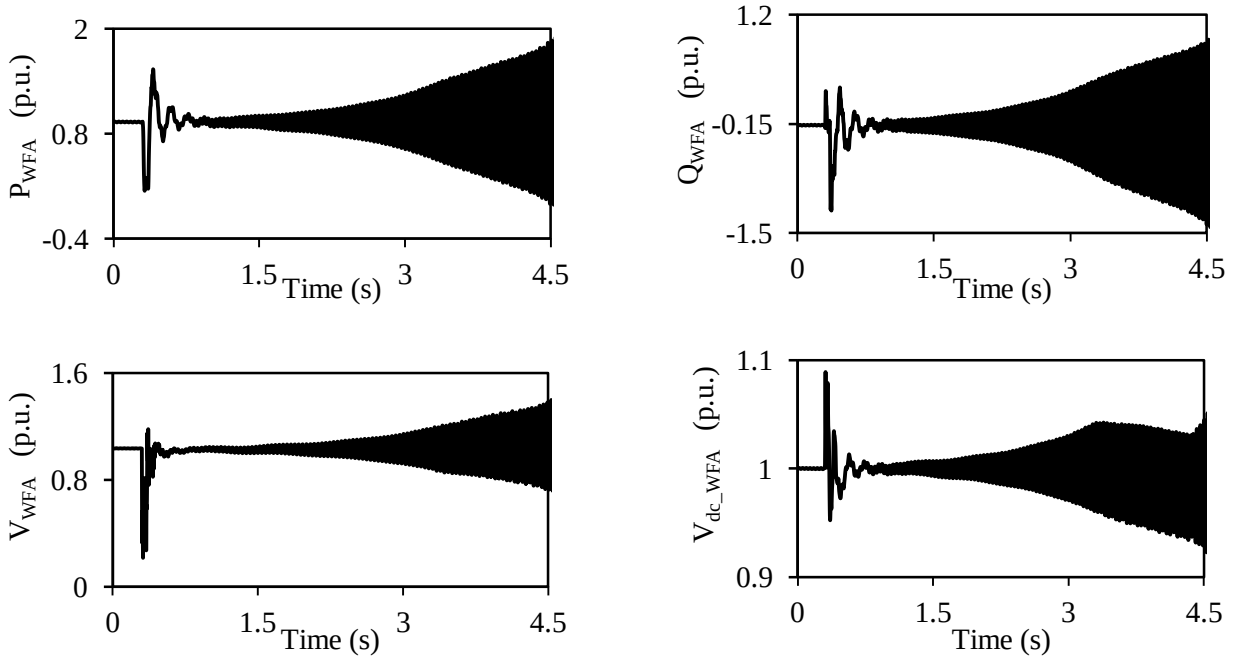

Figure 3.54: Wind farm A real and reactive powers, terminal voltage and dc capacitor voltage during and after clearing a 3-cycle, L-L-G fault on Line 5 (60% compensation degree, supplemental control I is not activated).

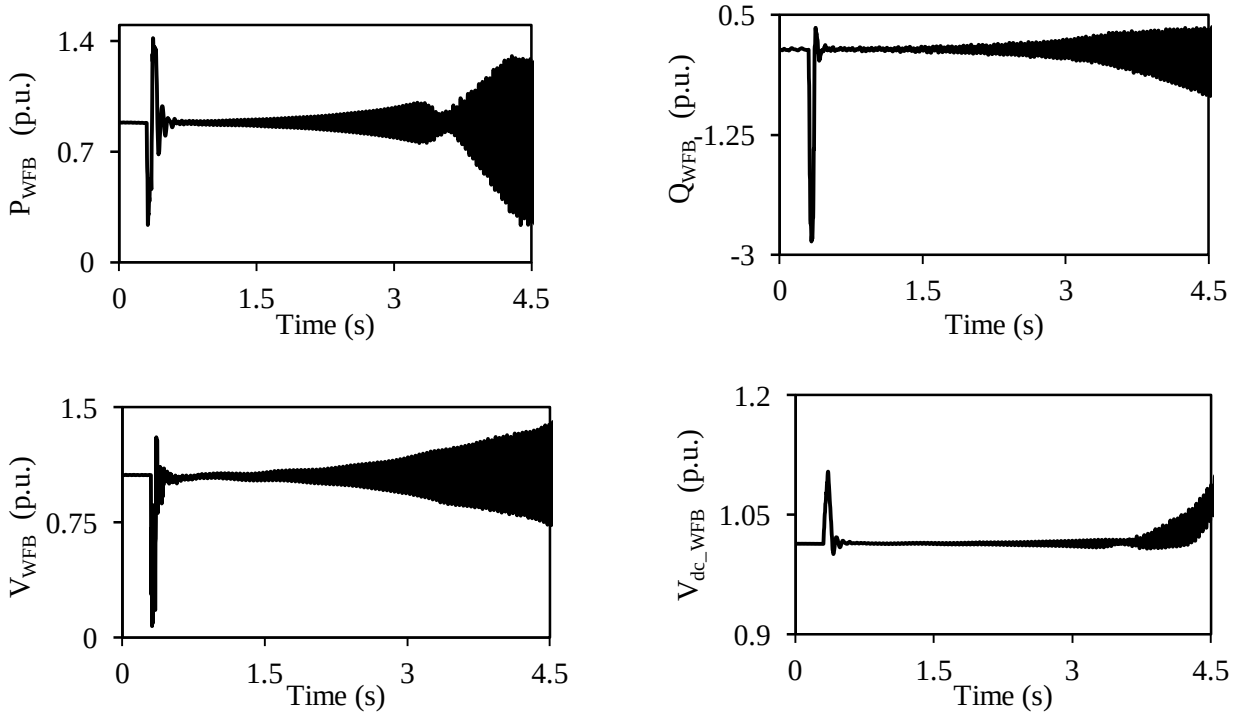

Figure 3.55: Wind farm B real and reactive powers, terminal voltage and dc capacitor voltage during and after clearing a 3-cycle, L-L-G fault on Line 5 (60% compensation degree, supplemental control I is not activated).

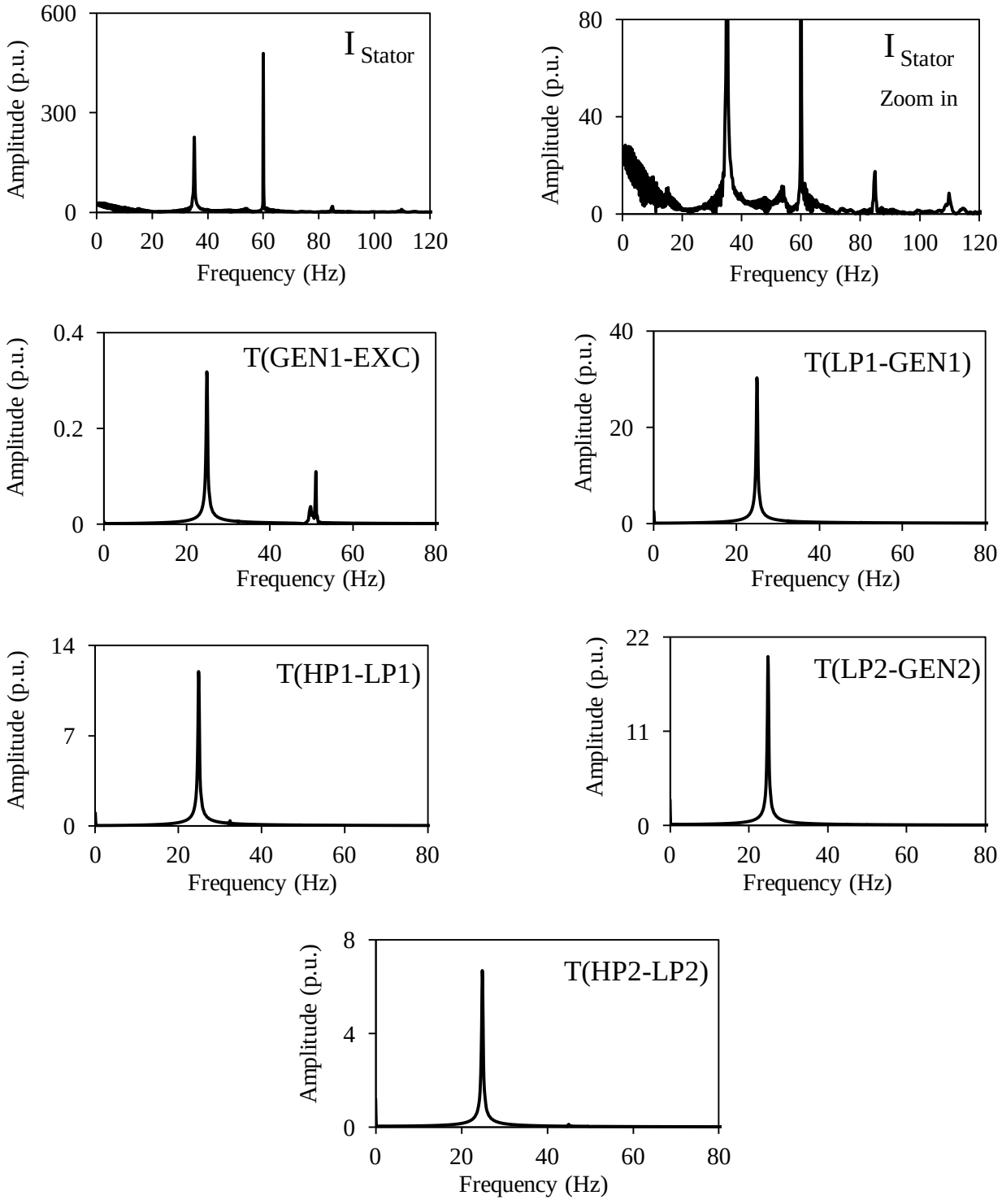

Figure 3.56: Frequency spectrums of the stator current of the DFIG wind turbine and the turbine-generator shaft torsional torques during and after clearing a 3-cycle, L-L-G fault on Line 5 (60% compensation degree, supplemental control I is not activated).

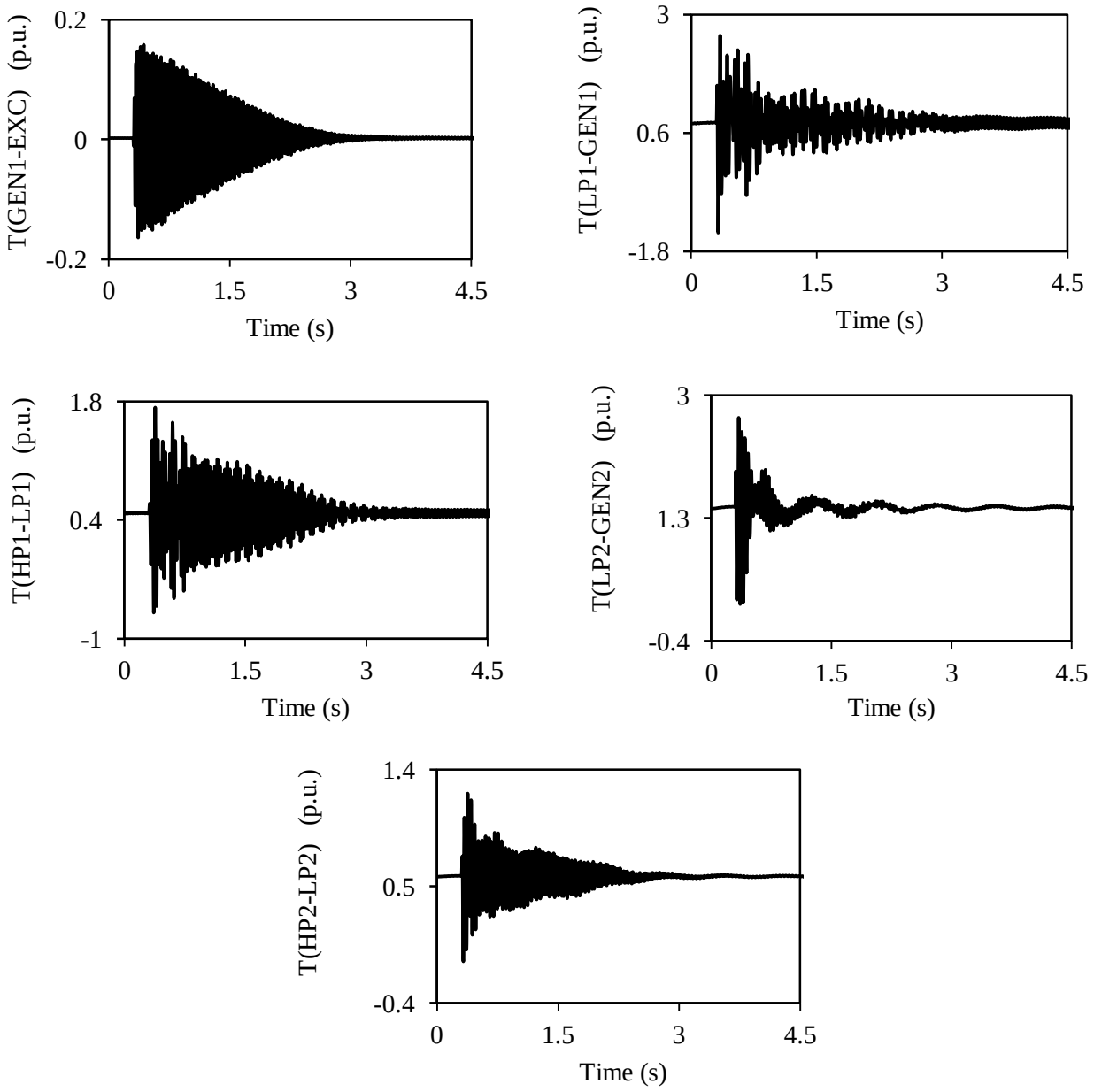

Figure 3.57: Turbine-generator shaft torsional torques during and after clearing a 3-cycle, L-L-G fault on Line 5 (60% compensation degree, supplemental control I is activated).

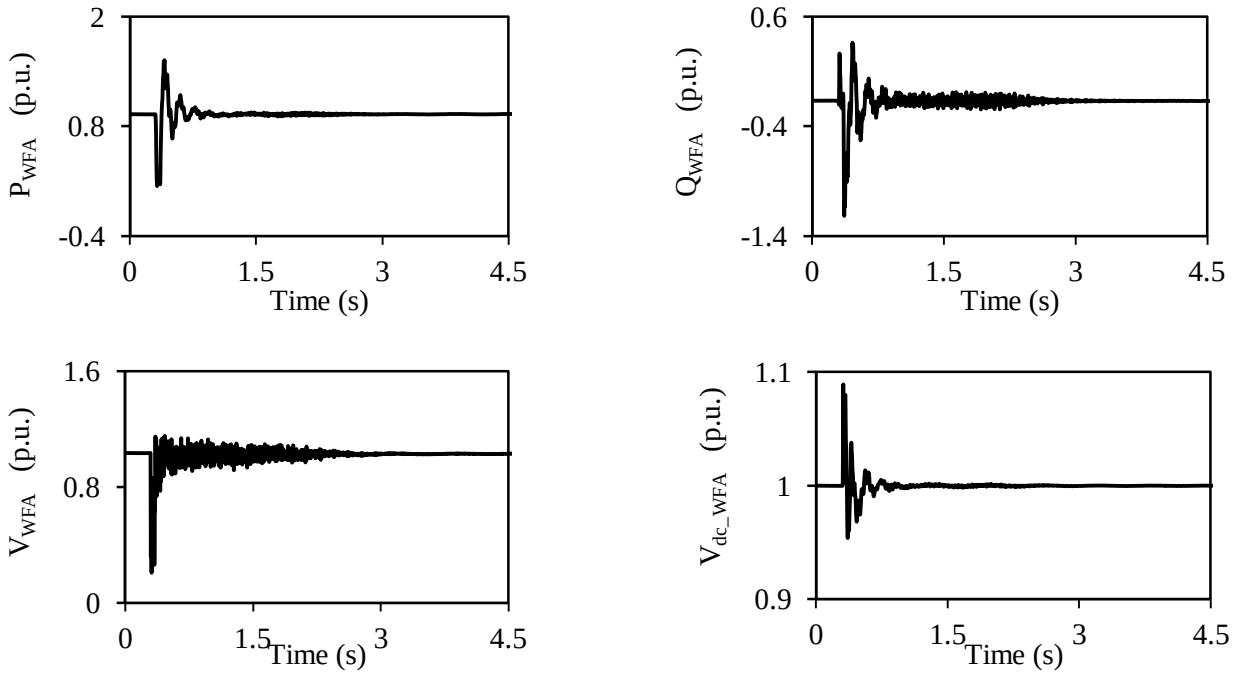

Figure 3.58: Wind farm A real and reactive powers, terminal voltage and dc capacitor voltage during and after clearing a 3-cycle, L-L-G fault on Line 5 (60% compensation degree, supplemental control I is activated).

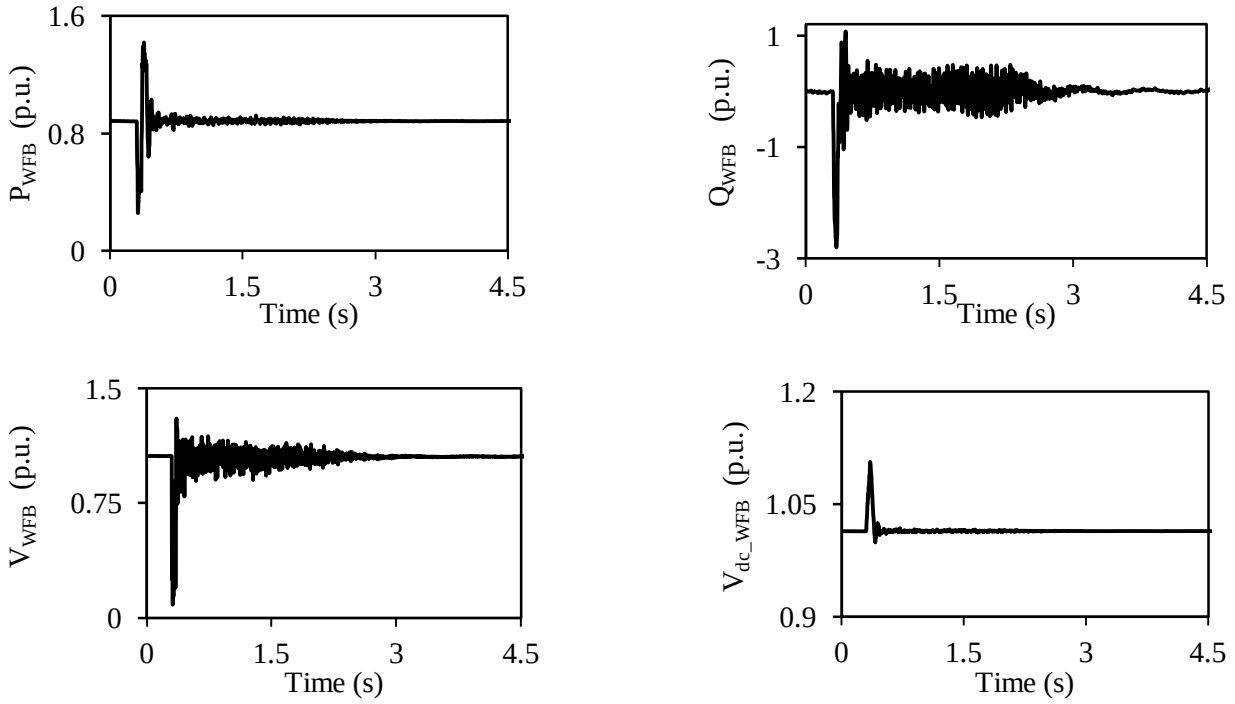

Figure 3.59: Wind farm B real and reactive powers, terminal voltage and dc capacitor voltage during and after clearing a 3-cycle, L-L-G fault on Line 5 (60% compensation degree, supplemental control I is activated).

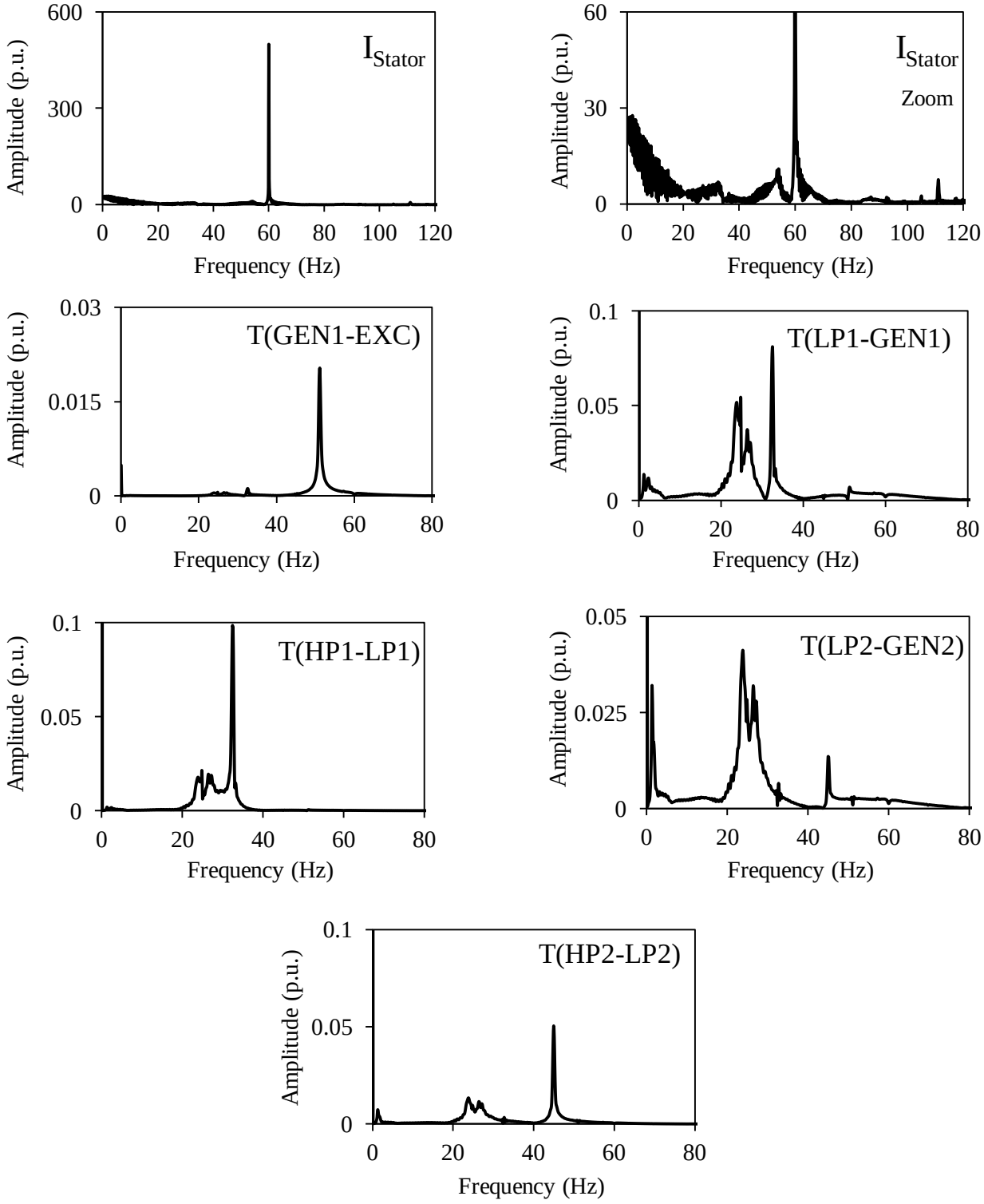

Figure 3.60: Frequency spectrums of the stator current of the DFIG wind turbine and the turbine-generator shaft torsional torques during and after clearing a three-cycle, L-L-G fault on Line 5 (60% compensation degree, supplemental control I is activated).

3.4 Performance of Supplemental Control II in damping SSR and SSI Oscillations

Figure 3.61 shows the turbine-generator shaft torsional torque time responses during and after clearing a ***3-cycle, three-phase fault on Line 5*** for the case when Supplemental control II is activated. Figures 3.62 and 3.63 illustrate respectively the time responses of wind farms A and B active and reactive powers, terminal voltage and the BtB dc voltage for the same case. Moreover, Figure 3.64 shows the frequency spectrums of the stator current of the DFIG wind turbines and the turbine-generator shaft torsional torques for the same study case. Furthermore, the transfer functions of Supplemental control II are given in Table 3.2.

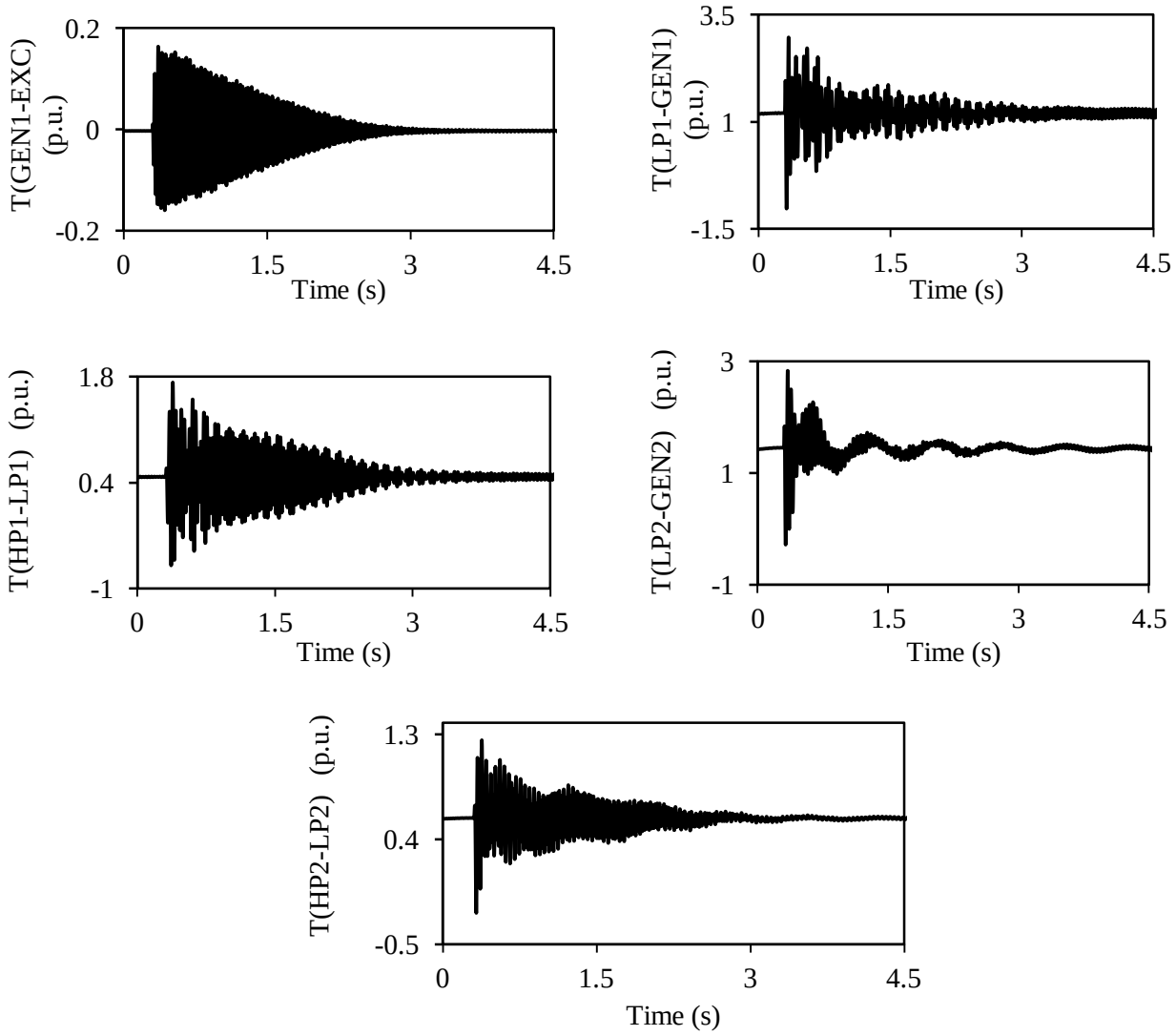

Figure 3.61: Turbine-generator shaft torsional torques during and after clearing a 3-cycle, three-phase fault on Line 5 (60% compensation degree, supplemental control II is activated).

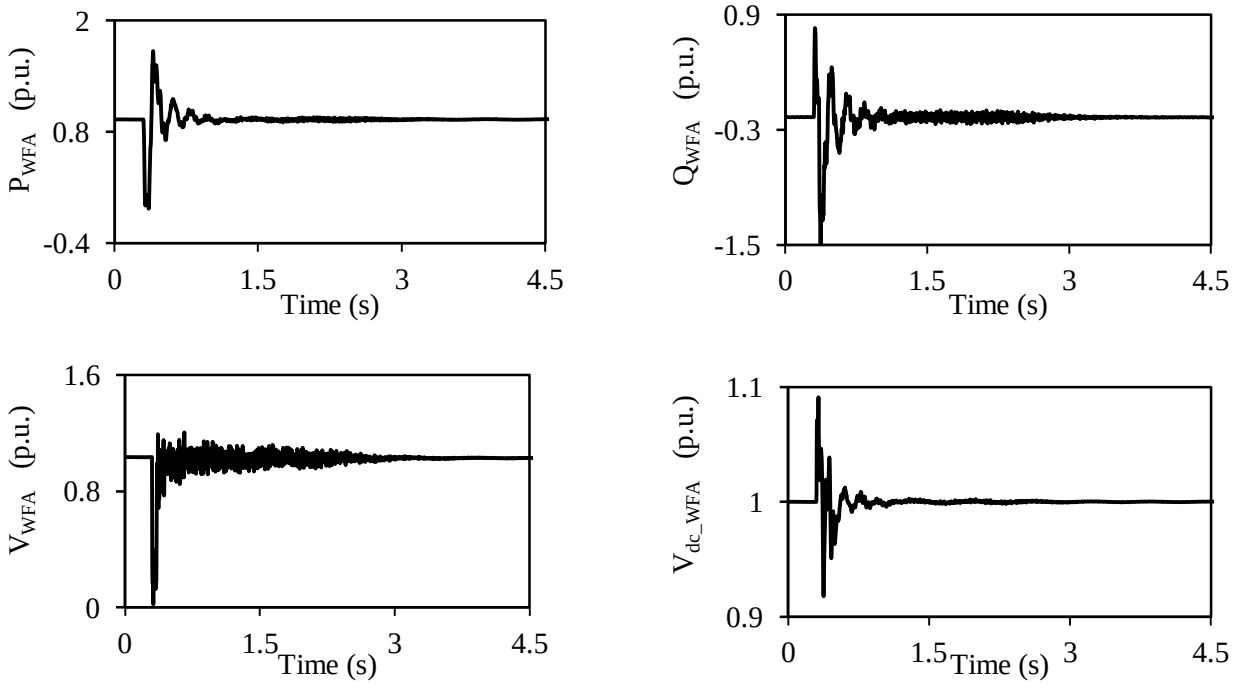

Figure 3.62: Wind farm A real and reactive powers, terminal voltage and dc capacitor voltage during and after clearing a 3-cycle, three-phase fault on Line 5 (60% compensation degree, supplemental control II is activated).

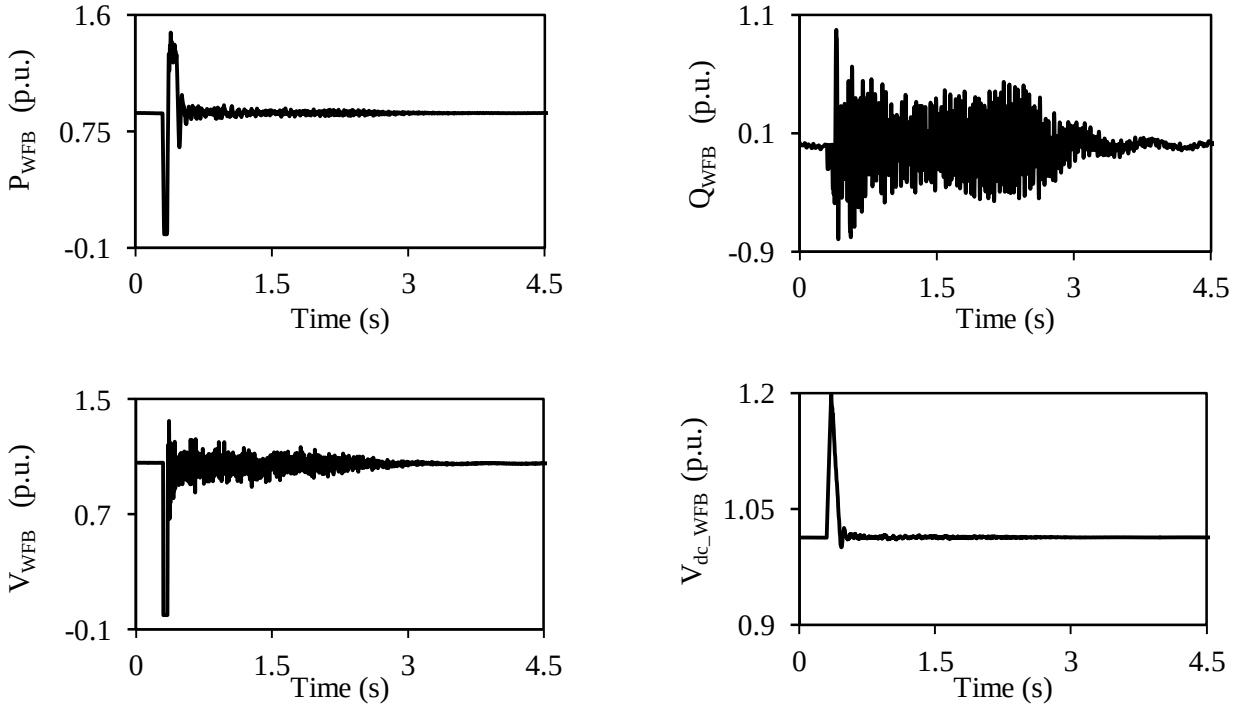

Figure 3.63: Wind farm B real and reactive powers, terminal voltage and dc capacitor voltage during and after clearing a 3-cycle, three-phase fault on Line 5 (60% compensation degree, supplemental control II is activated).

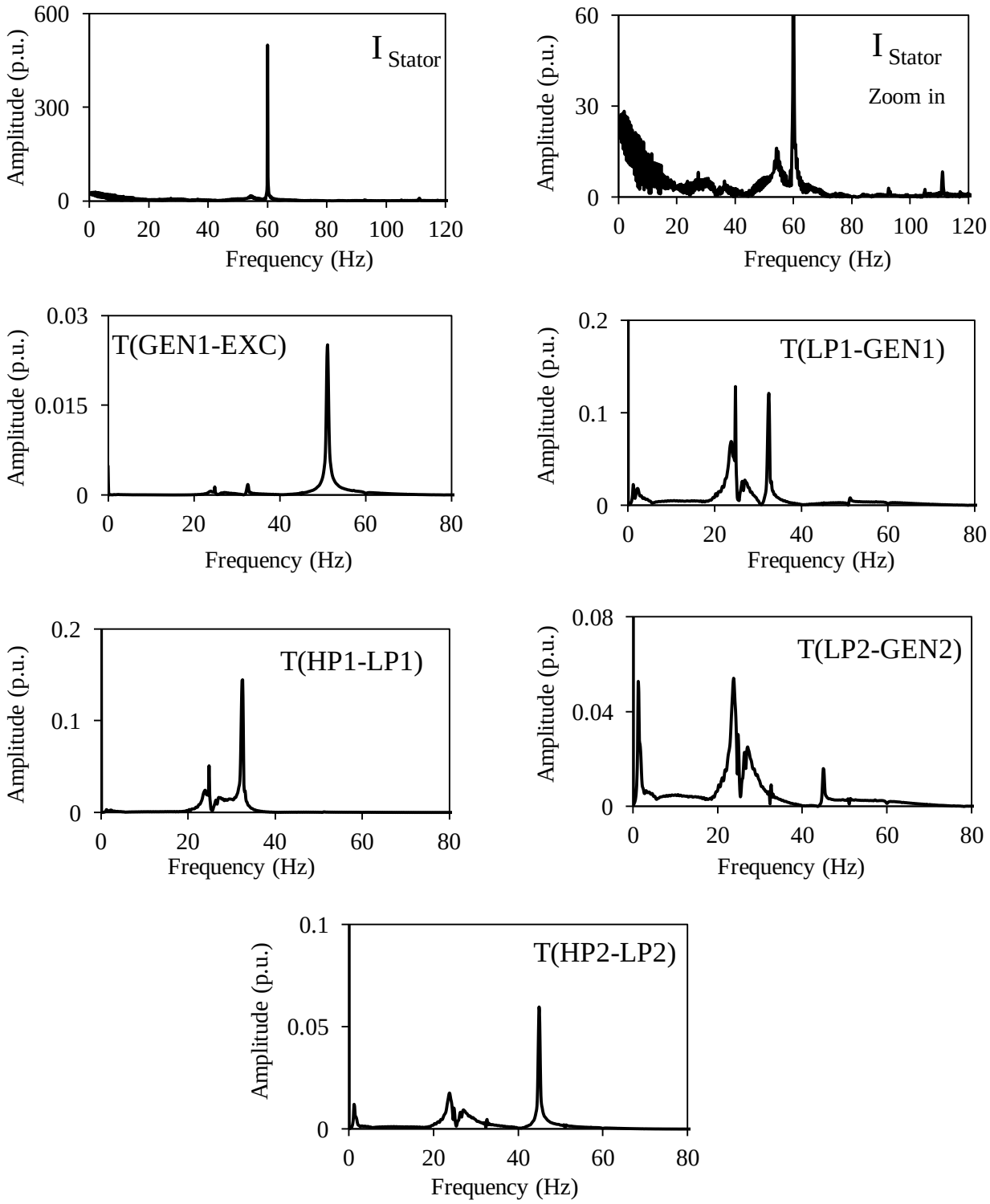

Figure 3.64: Frequency spectrums of the stator current of the DFIG wind turbine and the turbine-generator shaft torsional torques during and after clearing a 3-cycle, three-phase fault on Line 5 (60% compensation degree, supplemental control II is activated).

The comparison between the two groups of figures (Figures 3.5, 3.6, 3.7, 3.8) and (Figures 3.61, 3.62, 3.63, 3.64) establishes the effectiveness of Supplemental control II in damping the torsional torques in all turbine-generator shaft sections as well as in mitigating SSI in wind farm A.

Table 3.2: Transfer functions of Supplemental control II (Wind farm B rating = 210 MW, three-phase fault on Line 5).

Modal Speeds	Transfer Function
G1, $\Delta_{\omega m0}$	0
G1, $\Delta_{\omega m1}$	$G_{\omega 1}(s) = 25\frac{s+300}{s+1}$
G1, $\Delta_{\omega m2}$	$G_{\omega 2}(s) = 50\frac{s+2}{s+1}$
G1, $\Delta_{\omega m3}$	$G_{\omega 3}(s) = -50\frac{s+2}{s+1}$
G2, $\Delta_{\omega m0}$	0
G2, $\Delta_{\omega m1}$	$G_{\omega 1}(s) = 500\frac{s+2}{s+1}$
G2, $\Delta_{\omega m2}$	$G_{\omega 2}(s) = -500\frac{s+2}{s+1}$
Washout Filter	$G(s) = \frac{s}{s+10}$
Band Pass Filter	$G(s) = \frac{62.83s}{s^2+62.83s+35500}$
Lead-Lag Network	$G(s) = \frac{s+250}{s+1}$
U_{SSR_max}, U_{SSR_min}	0.5, - 0.5
U_{SSI_max}, U_{SSI_min}	0.25, - 0.25

3.4.1 Effect of the fault location

The effect of the fault location on the performance of Supplemental control II is examined by applying a three-cycle, three-phase fault on Line 4. The results of this study are presented in the following two groups of figures:

Group A: Supplemental control II is disabled, (Figures 3.65, 3.66, 3.67, 3.68)

Group B: Supplemental control II is activated, (Figures 3.69, 3.70, 3.71, 3.72).

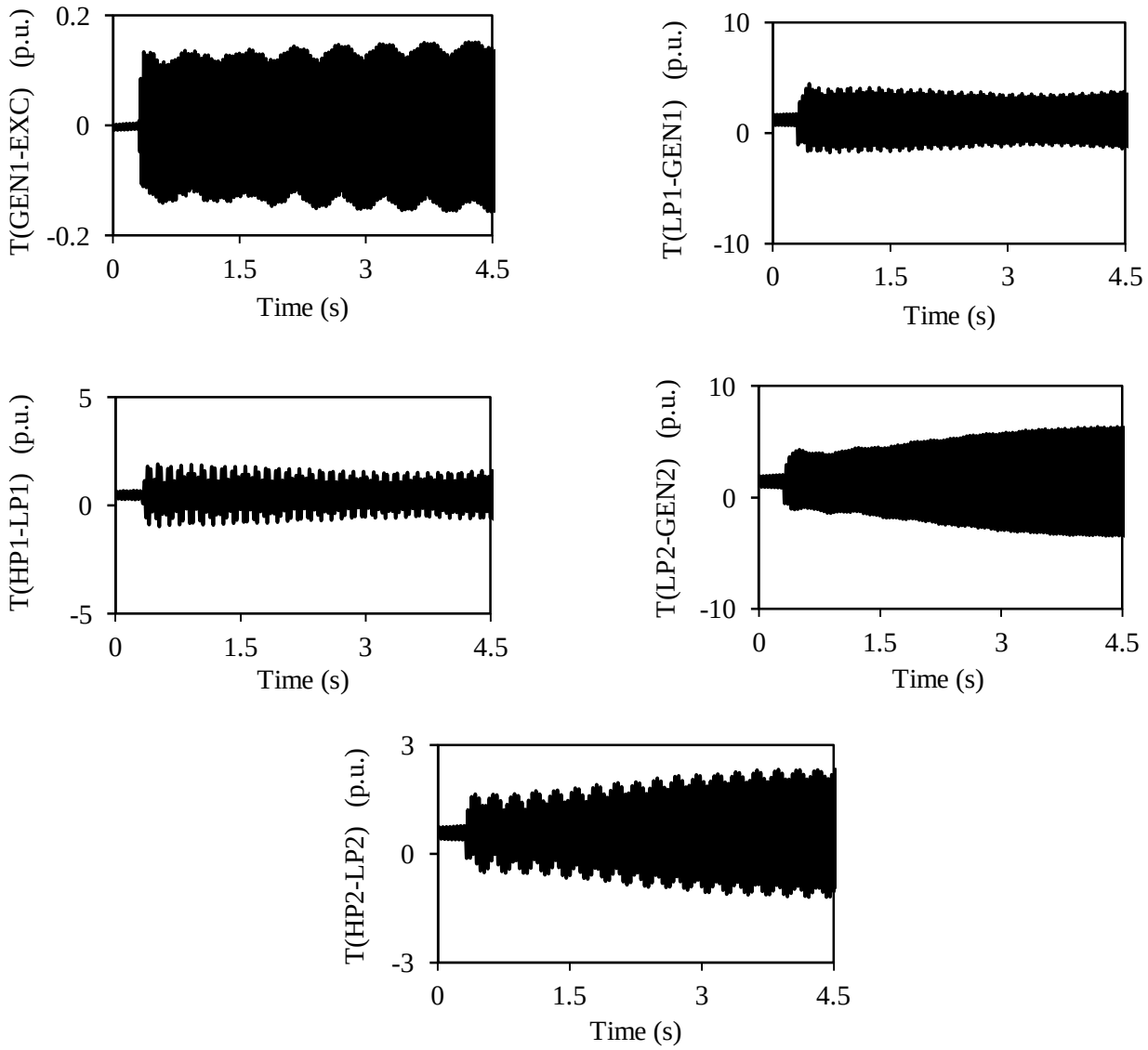

Figure 3.65: Turbine-generator shaft torsional torques during and after clearing a 3-cycle, three-phase fault on Line 4 (60% compensation degree, supplemental control II is not activated).

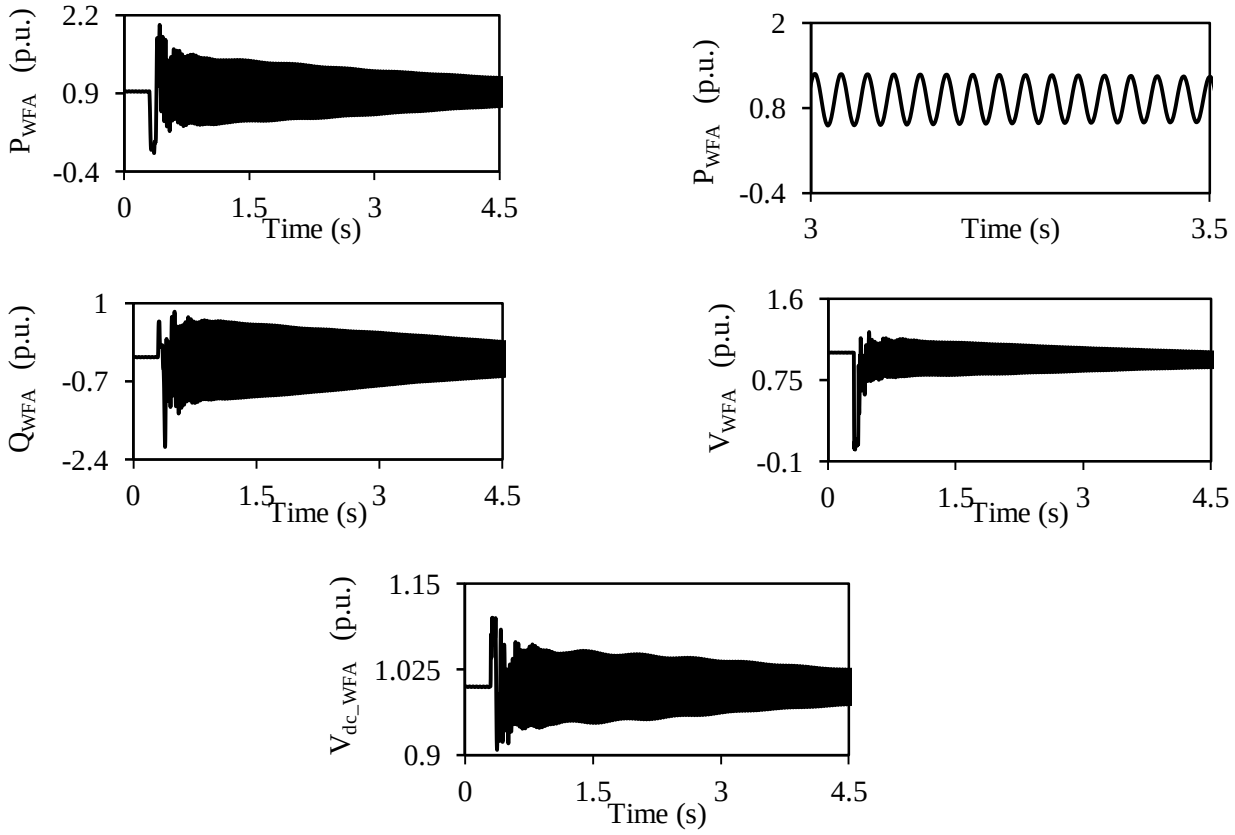

Figure 3.66: Wind farm A real and reactive powers, terminal voltage and dc capacitor voltage during and after clearing a 3-cycle, three-phase fault on Line 4 (60% compensation degree, supplemental control II is not activated).

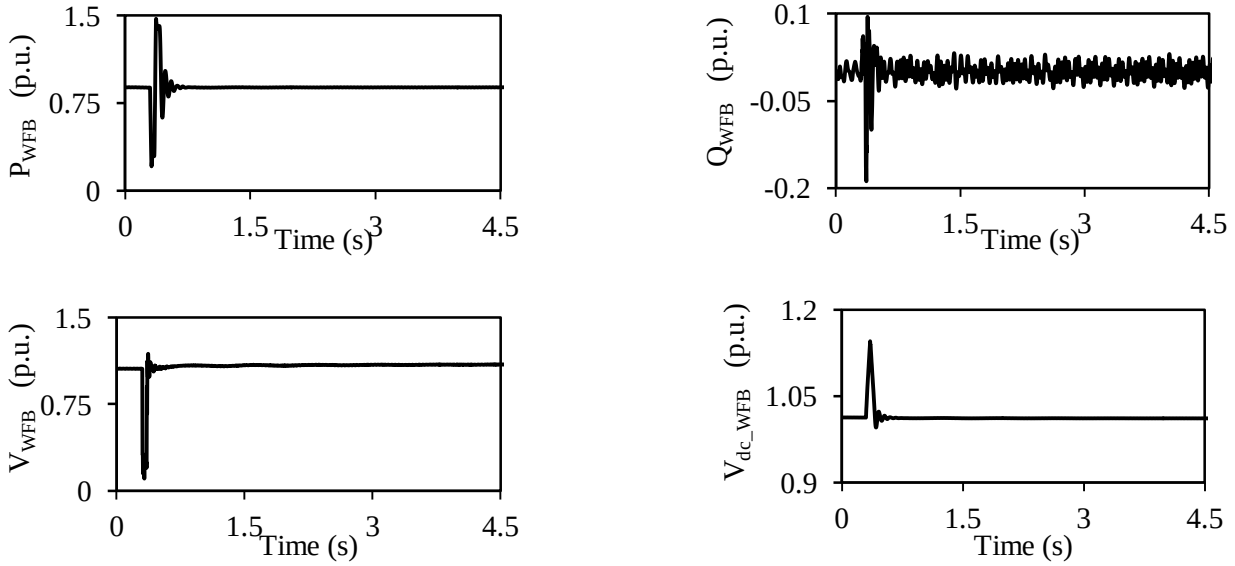

Figure 3.67: Wind farm B real and reactive powers, terminal voltage and dc capacitor voltage during and after clearing a 3-cycle, three-phase fault on Line 4 (60% compensation degree, supplemental control II is not activated).

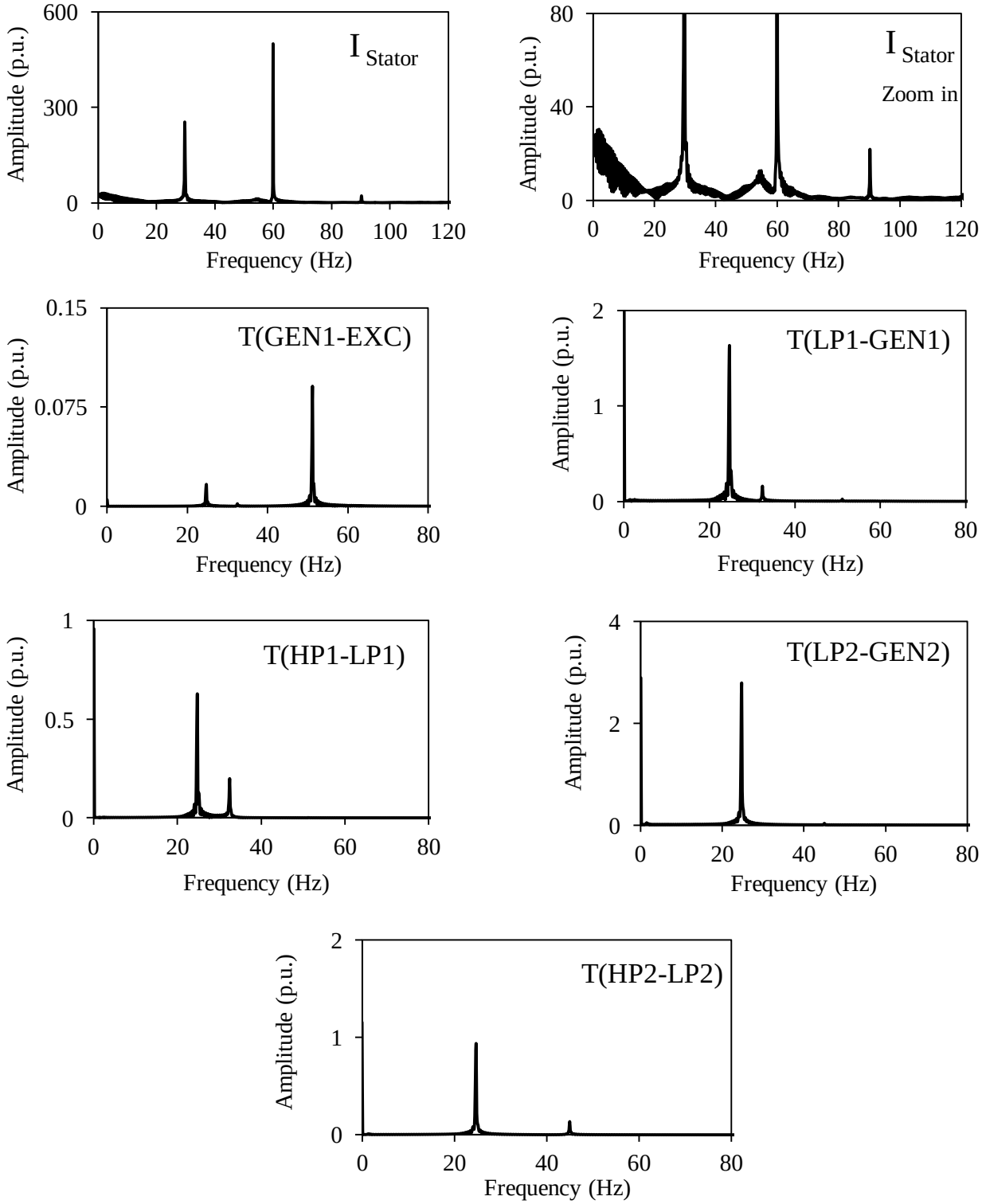

Figure 3.68: Frequency spectrums of the stator current of the DFIG wind turbine and the turbine-generator shaft torsional torques during and after clearing a 3-cycle, three-phase fault on Line 4 (60% compensation degree, supplemental control II is not activated).

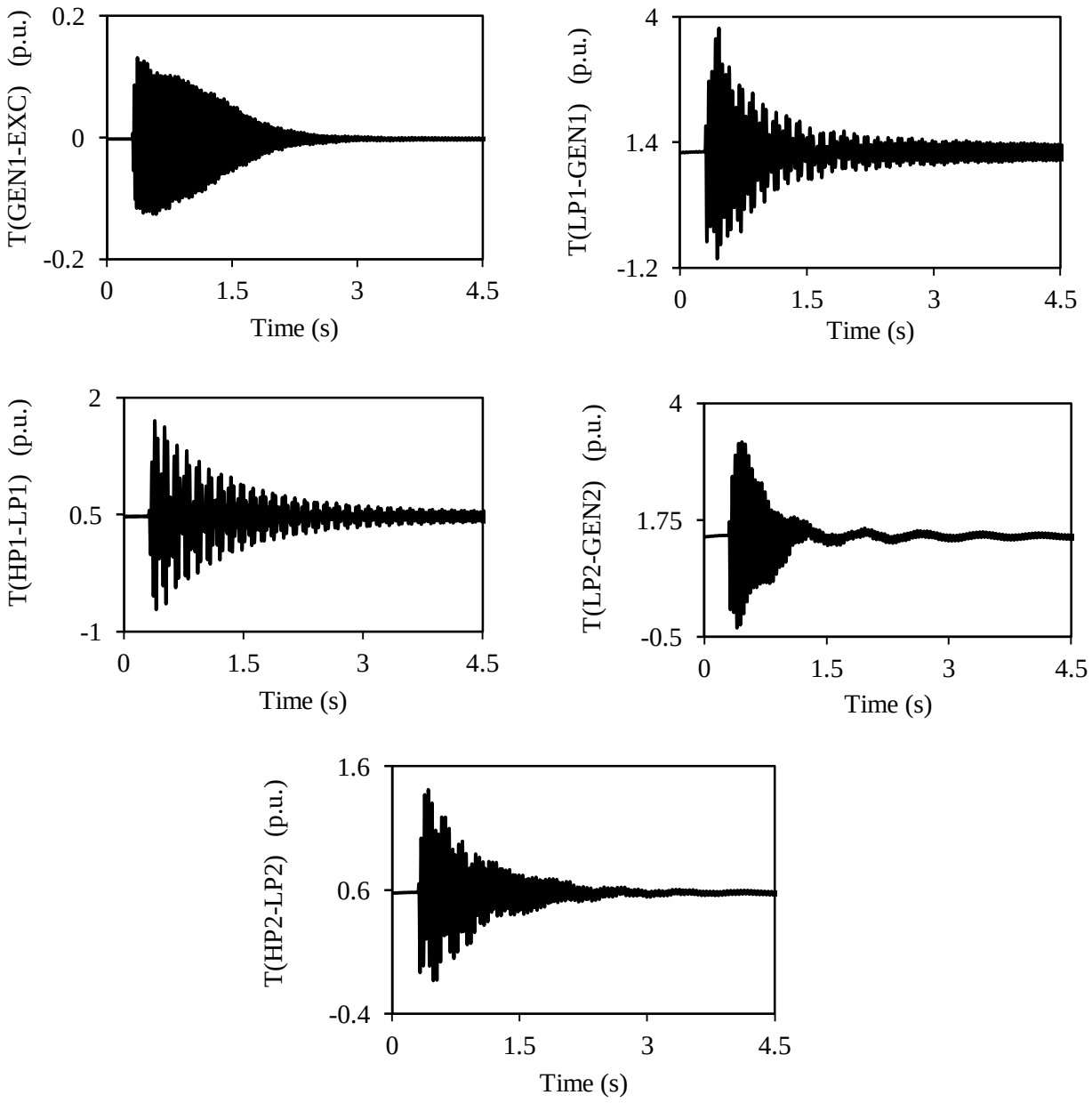

Figure 3.69: Turbine-generator shaft torsional torques during and after clearing a 3-cycle, three-phase fault on Line 4 (60% compensation degree, supplemental control II is activated).

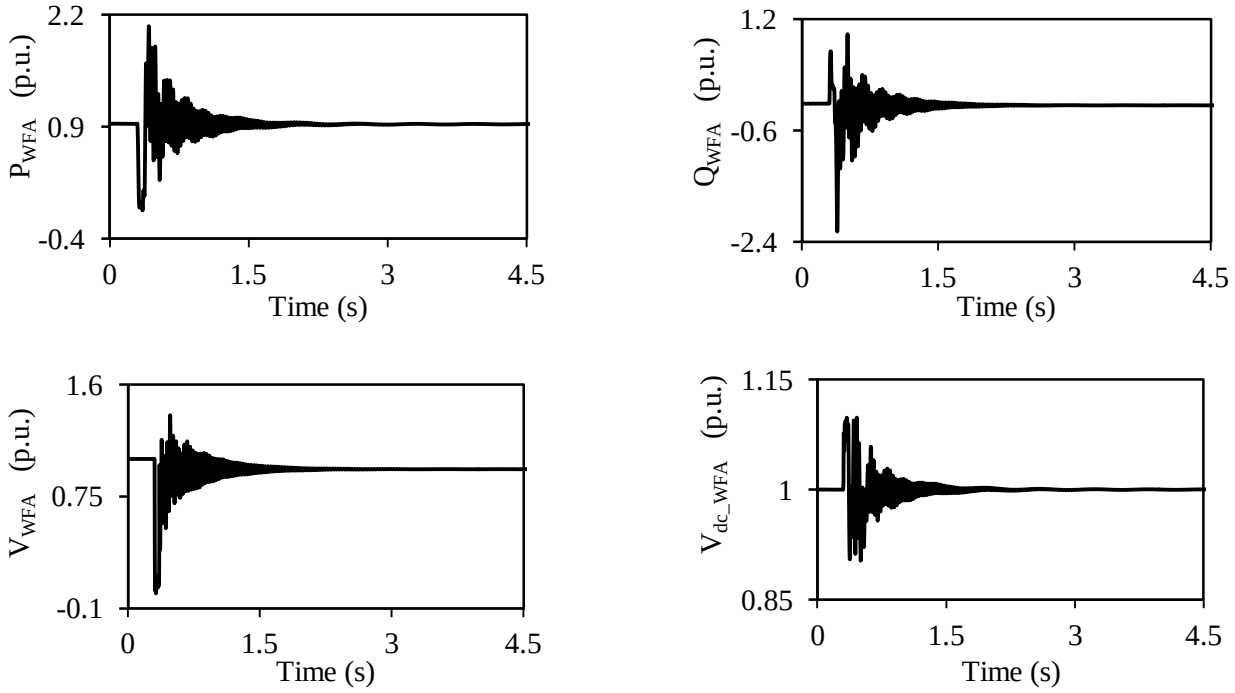

Figure 3.70: Wind farm A real and reactive powers, terminal voltage and dc capacitor voltage during and after clearing a 3-cycle, three-phase fault on Line 4 (60% compensation degree, supplemental control II is activated).

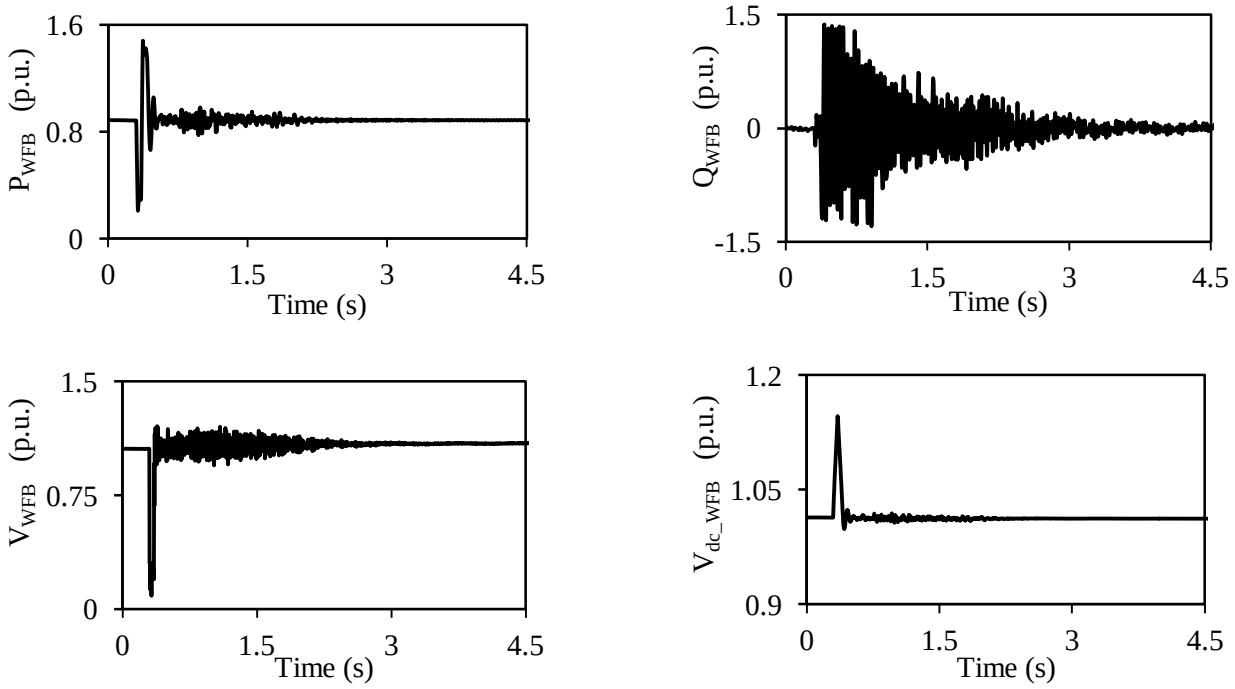

Figure 3.71: Wind farm B real and reactive powers, terminal voltage and dc capacitor voltage during and after clearing a 3-cycle, three-phase fault on Line 4 (60% compensation degree, supplemental control II is activated).

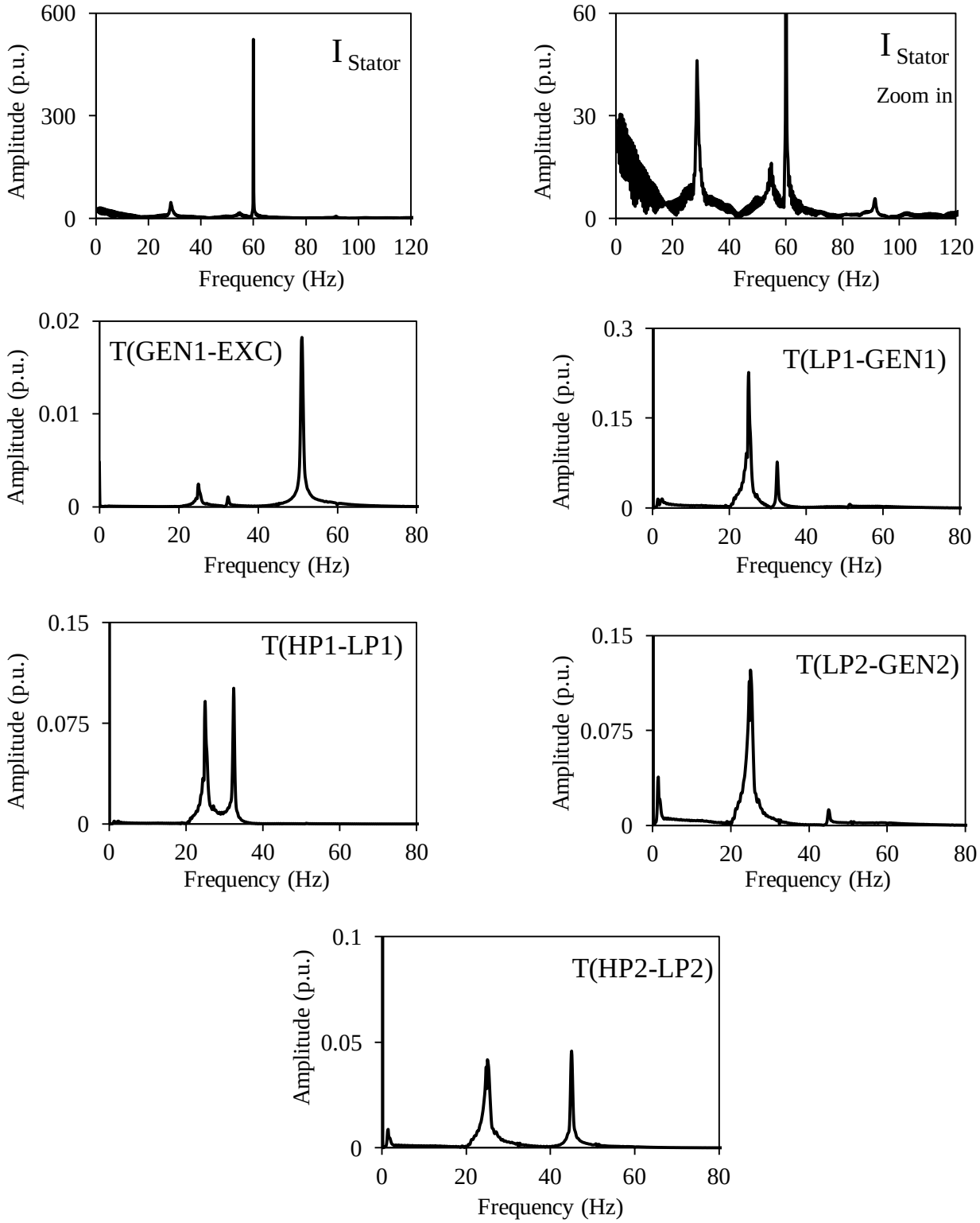

Figure 3.72: Frequency spectrums of the stator current of the DFIG wind turbine and the turbine-generator shaft torsional torques during and after clearing a 3-cycle, three-phase fault on Line 4 (60% compensation degree, supplemental control II is activated).

In each group, the turbine-generator shaft torsional torques, wind farms A and B active and reactive powers, terminal voltage and the BtB dc voltage as well as the frequency spectrums of the stator current of the DFIG wind turbines and the turbine-generator shaft torsional torques are shown. Moreover, the transfer functions of Supplemental control II in Group B are the same as those given in Table 3.2.

As it can be seen from Figure 2.1, clearing a system fault on Line 4 "virtually" isolates wind farm A from wind farm B and the turbine-generators. Wind farm A is now radially connected to the infinite-bus system through a series capacitor compensated transmission line (Line 2). This is a favorable condition for the occurrence of SSI. Figure 3.66 shows that SSI mode (30.5 Hz) is excited in wind farm A (as shown in the zoom-in plot of the wind farm real power, P_{WFA}), as a result of the radial connection to the infinite-bus system after the interruption of Line 4.

Regarding the turbine-generator shaft torsional torques, Figure 3.65 shows that these torques exhibit either decaying, sustained or growing oscillations. These oscillations, however, have an adverse impact on the performance of wind farm B (notice the sustained oscillations in the wind farm output reactive power i.e. Q_{WFB}, shown in Figure 3.67).

The comparison between the figures in Groups A and B demonstrates the effectiveness of Supplemental control II in mitigating SSR and SSI after clearing a three-phase fault at a different location.

3.4.2 Effect of the Compensation Degree

The effect of the compensation degree of transmission Lines 1 and 2 on the performance of Supplemental control II is examined by changing it from 60% to 50%. Moreover, the disturbance is a three-cycle, three-phase fault on Line 5. The results of this study are presented in the following two groups of figures:

Group A: Supplemental control II is disabled, (Figures 3.73, 3.74, 3.75, 3.76)

Group B: Supplemental control II is activated, (Figures 3.77, 3.78, 3.79, 3.80)

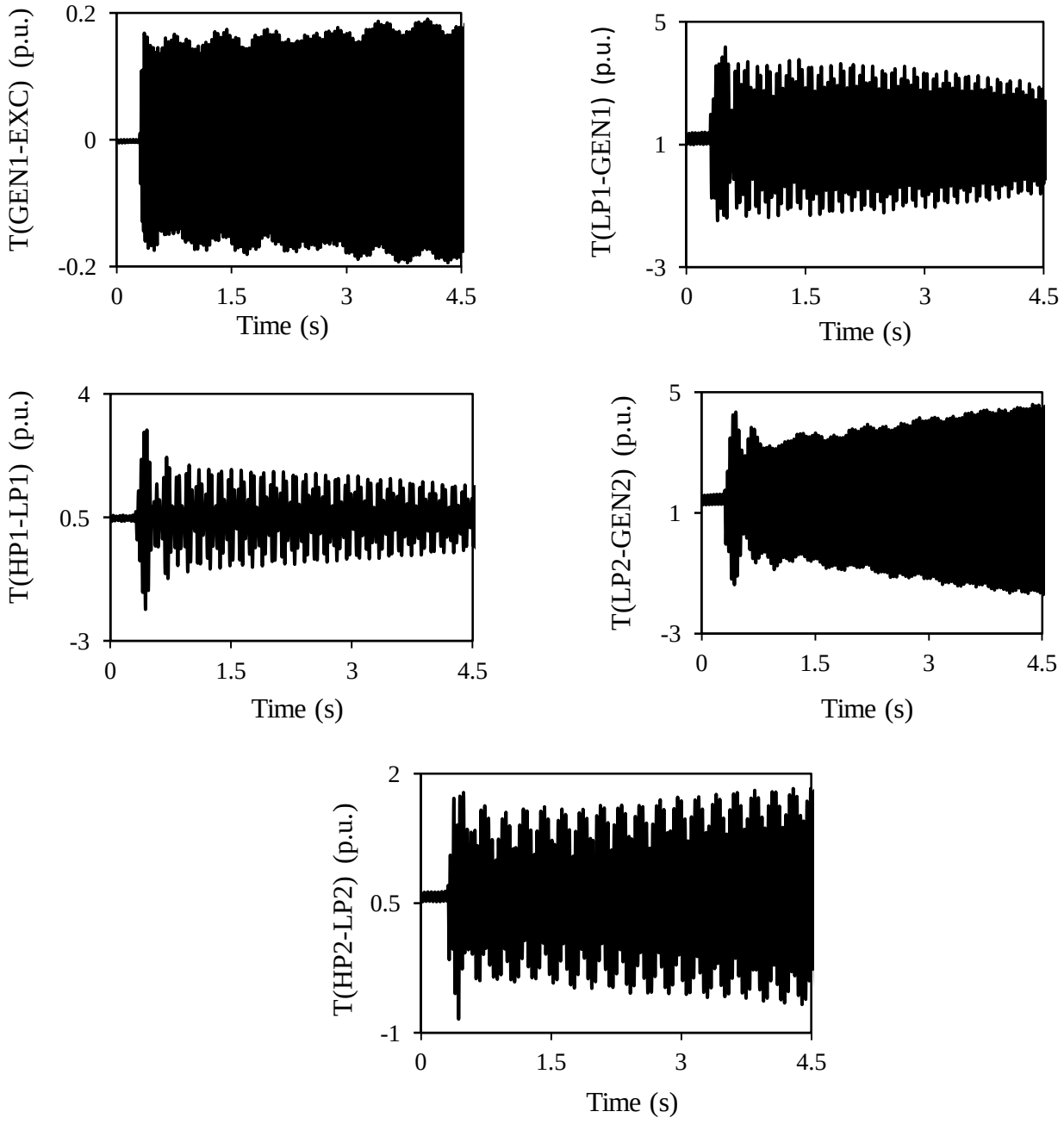

Figure 3.73: Turbine-generator shaft torsional torques during and after clearing a 3-cycle, three-phase fault on Line 5 (50% compensation degree, supplemental control II is not activated).

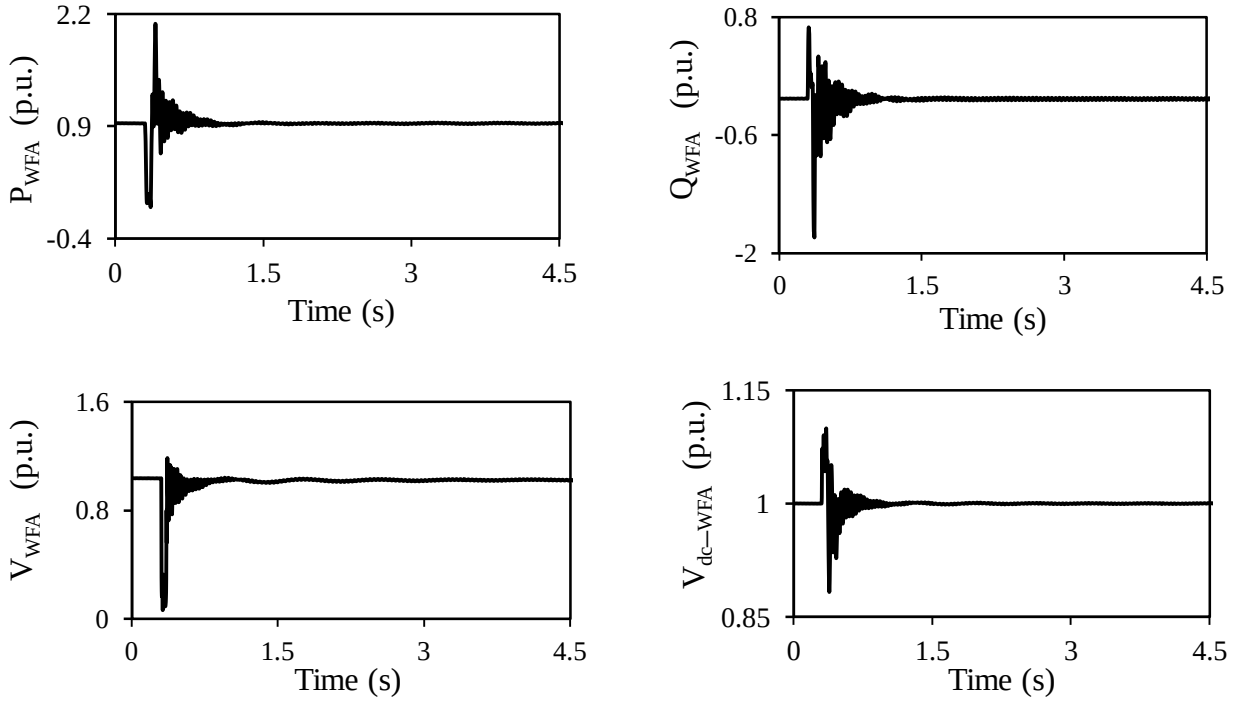

Figure 3.74: Wind farm A real and reactive powers, terminal voltage and dc capacitor voltage during and after clearing a 3-cycle, three-phase fault on Line 5 (50% compensation degree, supplemental control II is not activated).

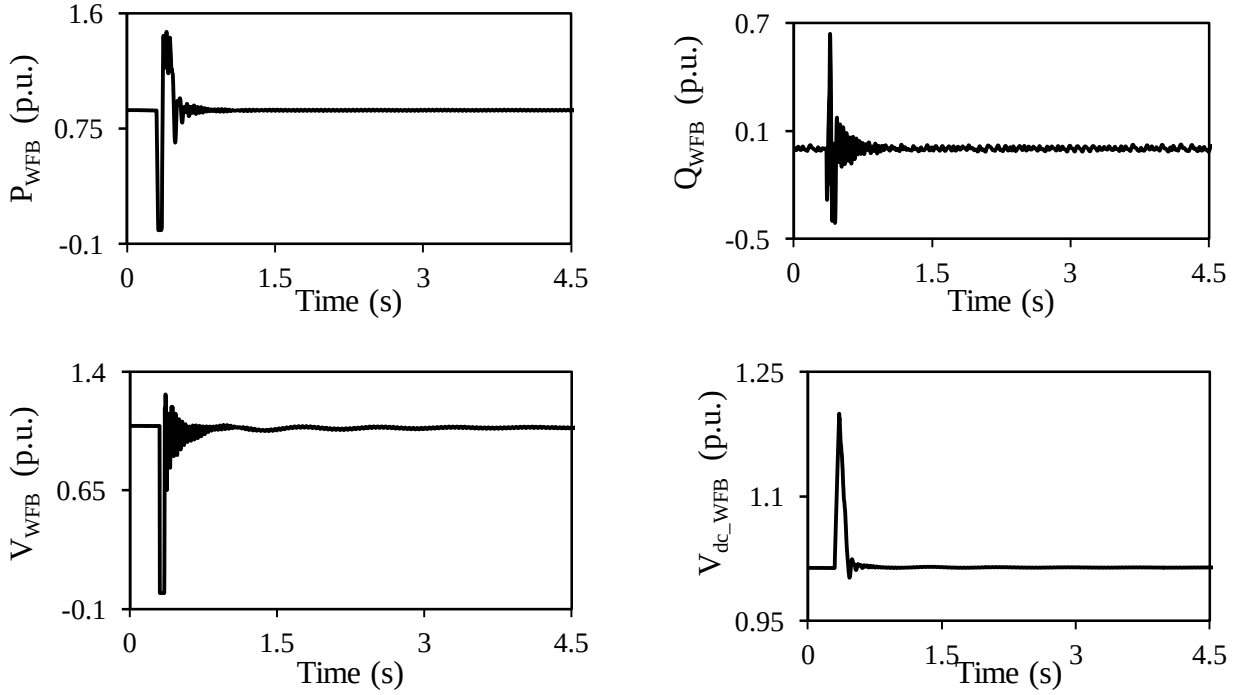

Figure 3.75: Wind farm B real and reactive powers, terminal voltage and dc capacitor voltage during and after clearing a 3-cycle, three-phase fault on Line 5 (50% compensation degree, supplemental control II is not activated).

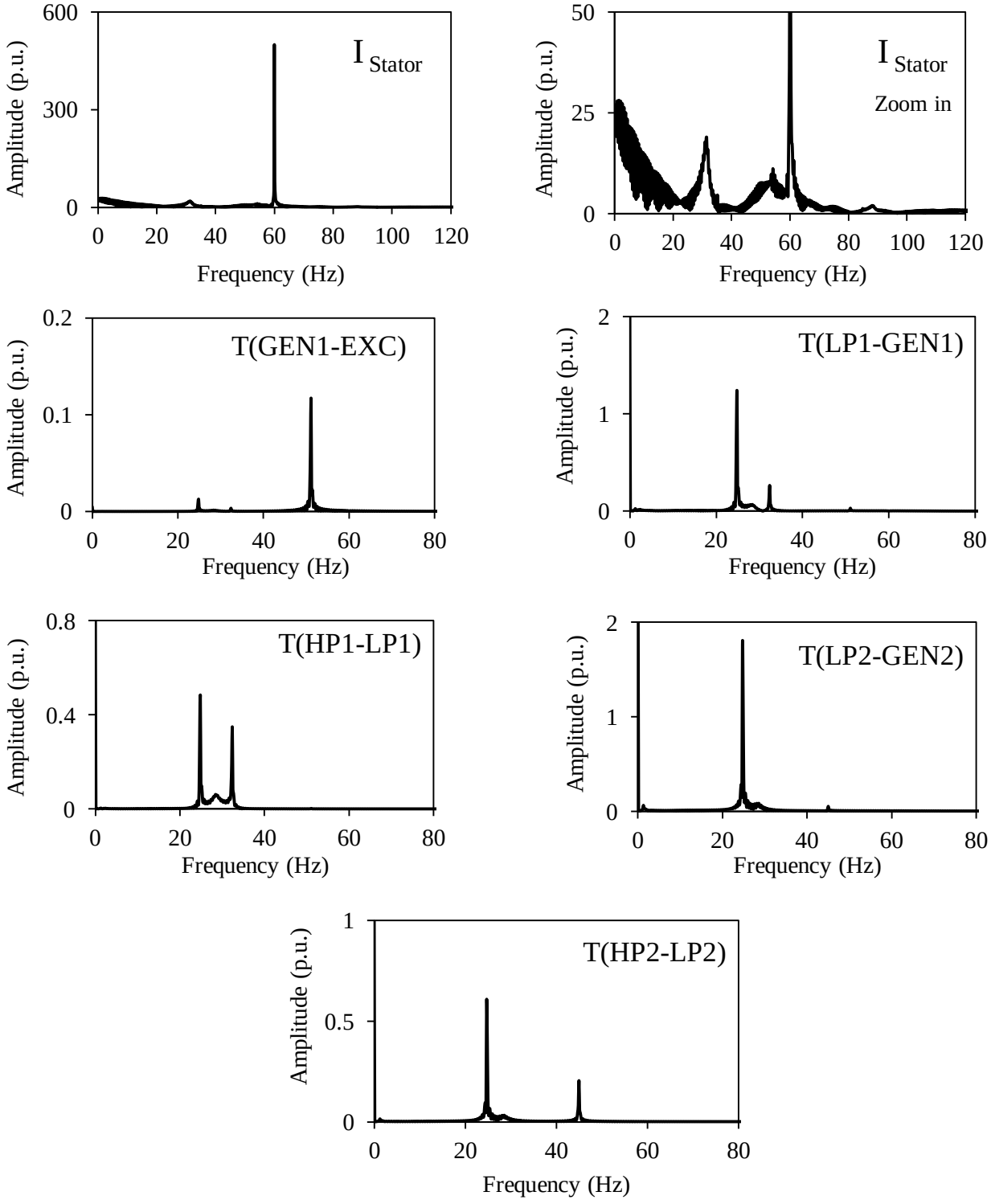

Figure 3.76: Frequency spectrums of the stator current of the DFIG wind turbine and the turbine-generator shaft torsional torques during and after clearing a 3-cycle, three-phase fault on Line 5 (50% compensation degree, supplemental control II is not activated).

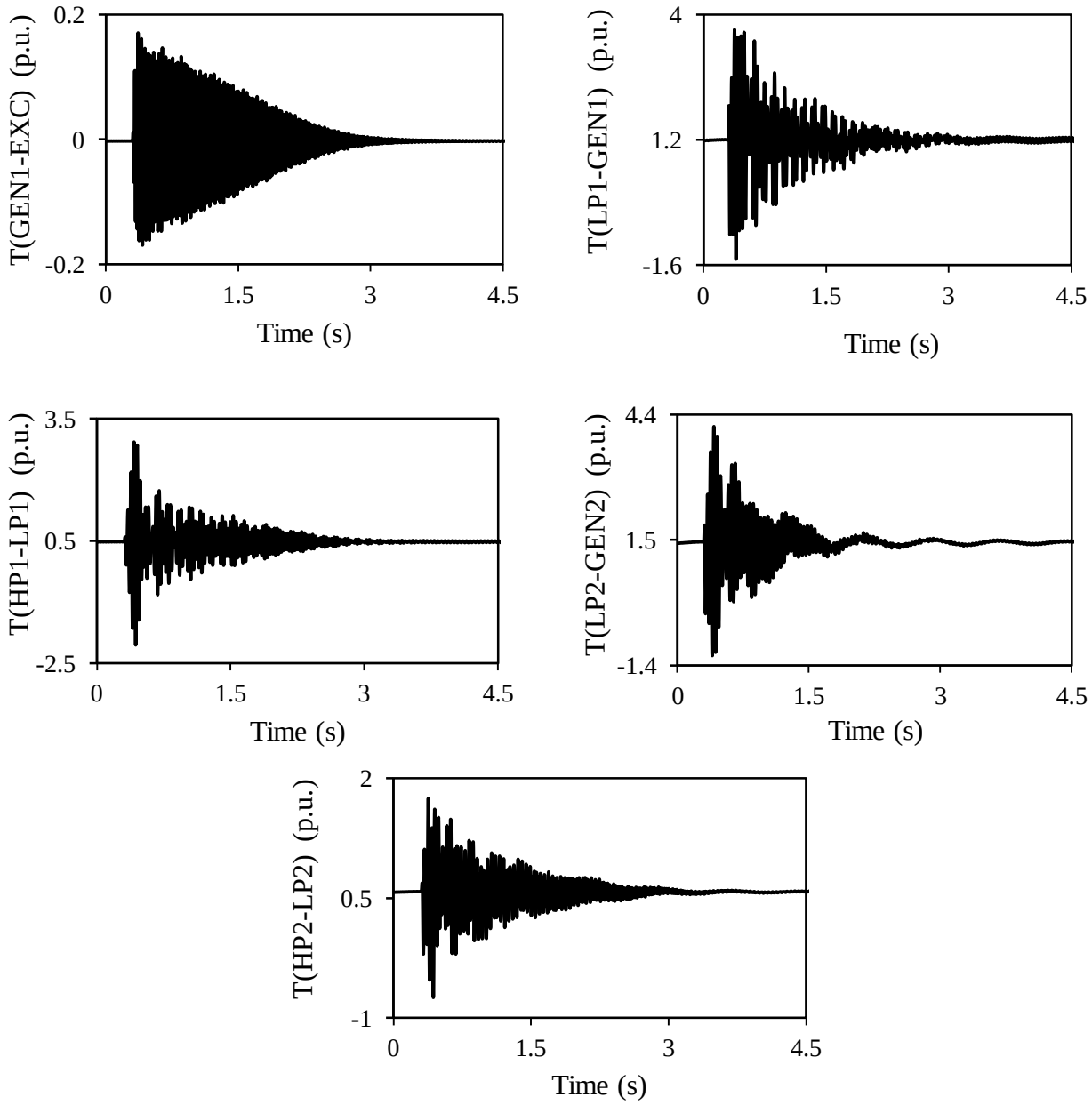

Figure 3.77: Turbine-generator shaft torsional torques during and after clearing a 3-cycle, three-phase fault on Line 5 (50% compensation degree, supplemental control II is activated).

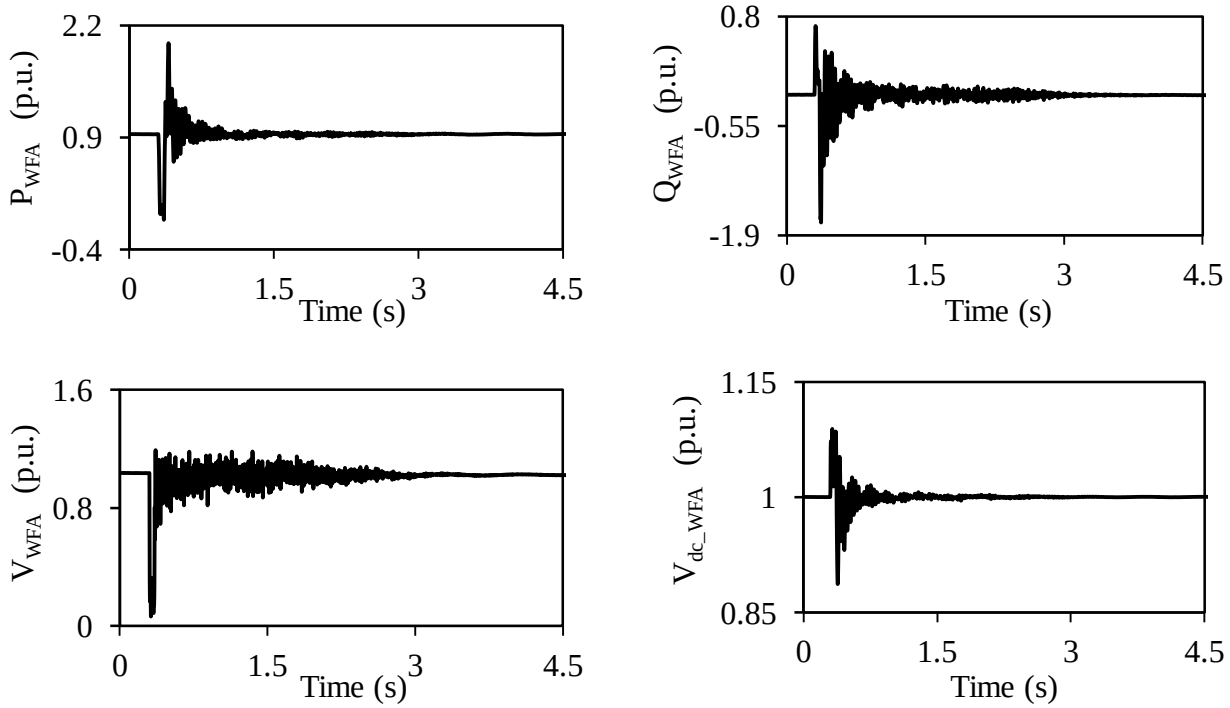

Figure 3.78: Wind farm A real and reactive powers, terminal voltage and dc capacitor voltage during and after clearing a 3-cycle, three-phase fault on Line 5 (50% compensation degree, supplemental control II is activated).

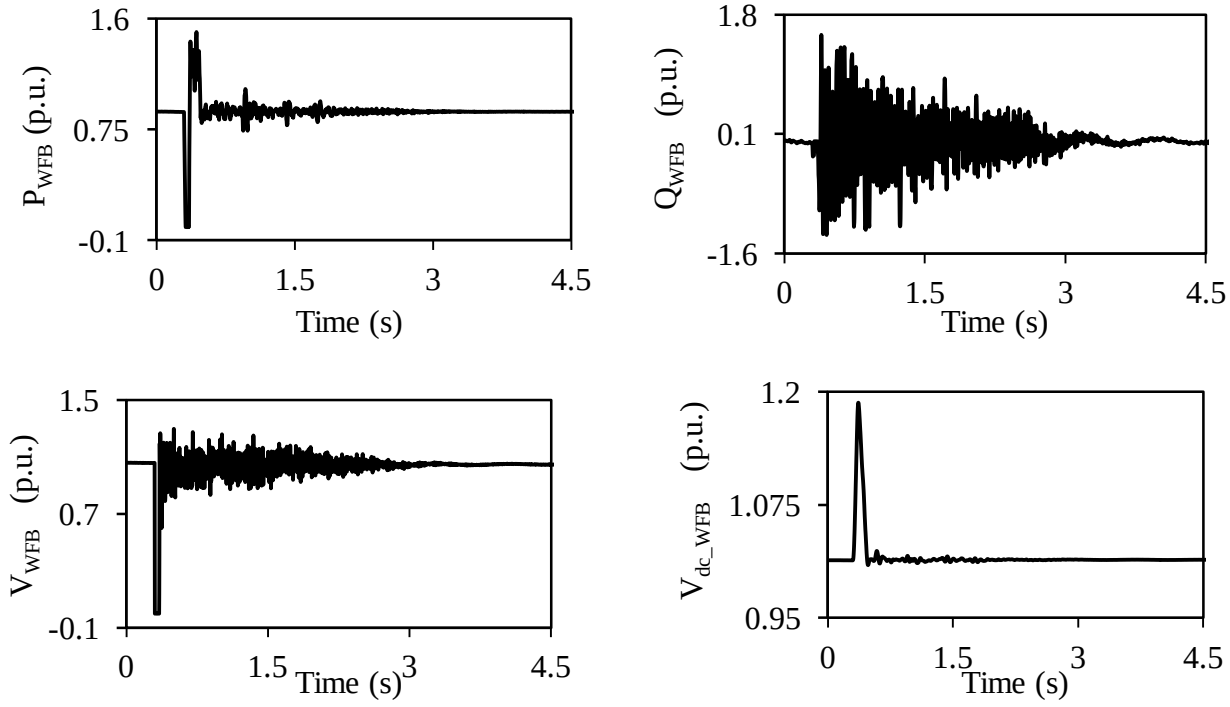

Figure 3.79: Wind farm B real and reactive powers, terminal voltage and dc capacitor voltage during and after clearing a 3-cycle, three-phase fault on Line 5 (50% compensation degree, supplemental control II is activated).

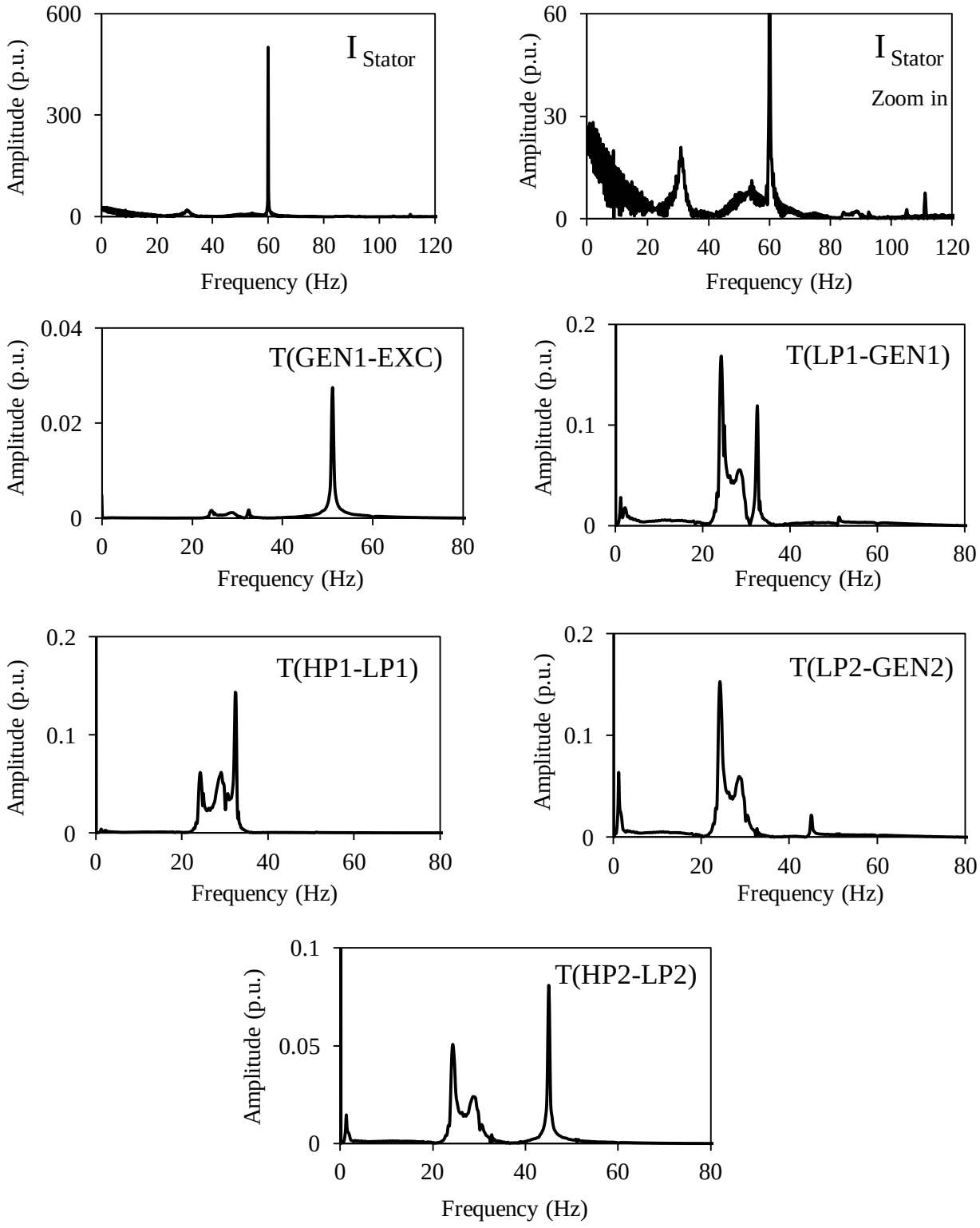

Figure 3.80: Frequency spectrums of the stator current of the DFIG wind turbine and the turbine-generator shaft torsional torques during and after clearing a 3-cycle, three-phase fault on Line 5 (50% compensation degree, supplemental control II is activated).

In each group, the turbine-generator shaft torsional torques, wind farms A and B active and reactive powers, terminal voltage and the BtB dc voltage as well as the frequency spectrums of the stator current of the DFIG wind turbines and the turbine-generator shaft torsional torques are shown. Moreover, the transfer functions of Supplemental control II in Group B are the same as those given in Table 3.2.

The comparison between Figures 3.5, 3.8 and Figures 3.73, 3.76 shows that changing the series capacitive compensation degrees results in changing the contributions of the torsional modes to the induced torsional torques in the different shaft sections of the turbine-generators. As it can be seen from Figure 3.73, the (GEN1-EXC), (LP2-GEN2) and (HP2-LP2) shaft torsional torques exhibit growing oscillations that indicate the presence of SSR. On the other hand, Figure 3.74 clearly shows the absence of SSI in wind farm A. Moreover, Figure 3.75 shows that the adverse impact of SSR is not extended to affect the performance of wind farm B. The comparison between the figures in Groups A and B demonstrates the effectiveness of supplemental control in mitigating SSR at the 50% compensation degree of Lines 1 and 2.

3.5 Summary

In this chapter, two supplemental controls of offshore and DFIG-based wind farms for mitigating SSR and SSI are presented. The effectiveness of these controllers are investigated through serveral case studies of time-domain simulations for different transmission line compensation degrees, fault types and locations as well as wind farm (OWF) ratings. The main conclusions drawn from the results of these studies are presented in the next chapter.

CHAPTER 4

SUMMARY AND CONCLUSIONS

4.1 Summary

Wind power plant ratings are relatively small compared to conventional power plants such as hydro, nuclear, natural gas or coal power plants. But with the continueous growth in wind energy technologies, large wind power plants (greater than 100 MW) are now in operation around the world. Integrating large wind power plants into existing power systems is always a difficult and capital intensive task for wind energy developers and transmission system providers.

Series capacitive compensation is the most economical way for increasing the transmission capacity and improving power system transient stability. However, subsynchronous resonance (SSR) is one of the major obstacles for the wide spread of high degrees (60% and higher) of series capacitor compensation. Recently, a new obstacle, namely subsynchronous interaction (SSI) has been added to the list after the Zorillo Gulf wind farm incident in Texas in October 2009. SSI is due to the interaction between large doubly-fed induction generator (DFIG)-based wind farms and series capacitor compensated transmission systems. In an integrated power system with high degree of series capacitive compensation and high penetration of wind energy convsersion systems, SSR and SSI could exist concurrently during some system contingencies and operating conditions.

Furthermore SSI mitigation has become part of the key technical requirements for integrating large wind power plants into transmission systems by the Federal Energy Regulatory Commission (FERC). Transmission system providers now make provisions to study SSI during system impact studies or full interconnection study phase of projects. These studies will be required in areas where series compensation is applied in the transmission system [40]. Therefore, mitigating SSR and SSI is an important area of research and development targeting at developing practical and effective countermeasures.

This thesis investigates the potential use of offshore and doubly-fed induction generator (DFIG)-based wind farms for simultaneous mitigation of SSR and SSI. SSR and SSI damping

is achieved by introducing supplemental control signals in the reactive power control loops of the HVDC onshore converter and the grid side converters of DFIG wind turbines of large wind farms.

Chapter 1 introduces some fundamental benefits of series capacitive compensation of transmission lines. Brief introductions to SSR and SSI are also presented. An overview of HVDC transmission and the objective of the research are also presented in this chapter.

In Chapter 2, the system used for the investigations conducted in this thesis is described and the detailed dynamic models of its individual components are also presented in this chapter. The results of the digital time-domain simulations of a case study for the system during a three-phase fault are presented at the end of this chapter.

Chapter 3 demonstrates the effectiveness of two supplemental controls in damping SSR and SSI oscillations through time-domain simulation studies. The supplemental controls performance at different system contingencies and operating conditions is also investigated.

4.2 Conclusions

The studies conducted in this thesis yield the following conclusions for the system under study.

1. The system under study is a typical example of a power system incorporating series capacitive transmission system and high penetration of wind energy conversion system. Subsynchronous resonance and subsynchronous interaction simultaneously exist at all cases of 60% compenstion degree. This is not the case at 50% compensation degree, where the existence of SSI was not observed.
2. The adverse effects of simultaneous existence of SSR and SSI extend their impact to the DFIG wind turbines of the offshore wind farm (Wind farm B). Although these turbines are “supposed” to be immune to SSI because the HVDC converters virtually isolate them from the system dynamics, induction generator effect (IGE) was observed in some case studies.
3. The turbine-generator shaft torsional torques are not sinusodial with a single frequency component, but contain contributions from all the torsional modes of the shaft system.

Moreover, the shaft section between the generators and the low-pressure stage turbines are subjected to the highest stresses.

4. Changing the series capacitive compensation degrees results in changing the contributions of the torsional modes to the torsional torques induced in the different shaft sections of the turbine-generators.
5. The electrical subsynchronous resonance frequency of the system (f_e) is a function of the capacitive reactances of Lines 1 and 2 and the equivalent inductive reactance of the system. The SSI mode is the complement of this frequency (60 - f_e). In all the reported cases in this thesis except for the interruption of Line 4, SSI mode is found to be 24.5 Hz. In the case of the interruption of Line 4, SSI mode is 30.5 Hz. This is due to the change of f_e from 35.5 Hz to 29.5 Hz.
6. The proposed supplemental controls, namely Supplemental controls I and II have shown to be effective in mitigating SSR and SSI at different series capacitive compensation degrees, fault types and locations as well as wind farm B (OWF) ratings. Supplemental control II is, however, more effective in mitigating SSR and SSI in the case of system faults on Line 4 followed by subsequent line interruption as this action virtually splits the system into two subsystems.

In general, the studies which have been documented in this thesis present a contribution to the understanding of simultaneous mitigation of subsynchronous resonance and subsynchronous interaction using wind energy conversion systems. Further research is needed in this area to bring the potential to when the damping capability of renewable energy systems can be sold as ancillary service. The ultimate objective is to combine wind farms with conventional power plants and Flexible AC Transmission Systems (FACTS [41]) controllers so that together they provide the real and reactive modulating powers in wide-area control of large power systems.

REFERENCES

[1] Global Wind Energy Council, "Global Wind Report Annual market update 2013", April 2014, http://www.gwec.net/wp-content/uploads/2014/04/GWEC-Global-Wind-Report_9-April-2014.pdf

[2] B. Fox, D. Flynn, L. Bryans, N. Jenkins, D. Milborrow, M. O'Malley, R. Watson and O. Anaya-Lara, " Wind Energy Integration: Connection and System Operational Aspects," IET Power and Energy Series 50, 2007.

[3] The European Wind Energy Association, "The European Offshore Wind Industry Key 2011 Trends and Statistics," online report, January 2012, http://www.ewea.org/fileadmin/ewea_documents/documents/publications/statistics/EWEA_stats_offshore_2011_01.pdf

[4] Renewable Energy World, "Offshore Wind Booming in Europe, " online report, January 20, 2011, http://www.renewableenergyworld.com/rea/news/article/2011/01/offshore-wind-booming-in-europe

[5] M. Henderson, D. Bertagnolli and D. Ramsey, "Planning HVDC and FACTS in New England," 2009 IEEE-PES Power System Conference and Exposition, Seattle, Washington, USA, March 15 – 18, 2009, pp. 1 – 3.

[6] Ercot System Planning, "Ercot CREZ Transmission Optimization Study," online report, April 2008, http://pbadupws.nrc.gov/docs/ML0914/ML091420467.pdf

[7] P.M. Anderson, B.L. Agrawal and J.E. Van Ness, *Subsynchronous Resonsance in Power Systems,* IEEE Press 1990.

[8] L. Fan, R. Kavasseri, Z. Lee Miao and C. Zhu, "Modeling of DFIG-Based Wind Farms for SSR Analysis," IEEE Transactions on Power Delivery, Vol. 25, No. 4, October 2010, pp. 2073 – 2082.

[9] A. Ostadi, A. Yazdani and R. Varma, "Modeling and Stability Analysis of a DFIG-Based Wind Power Generator Interfaced with a Series Compensated Line," IEEE Transactions on Power Delivery, Vol. 24, No. 3, July 2009, pp. 1504 – 1514.

[10] R. Gruenbaum, J. Rasmussen and Chun Li, "Series Capacitors for Increased Power Transmission Capacity of a 500 kV Grid Inertie," Proceedings of the 2012 IEEE - EPEC General Meeting, London, Ontario, Canada, October 10 – 12, 2012, pp. 164 – 169.

[11] J. Zhang, "Power System Dynamic Enhancement using Phase Imbalance Series Capacitive Compensation and Doubly Fed induction Generator-Based Wind Farms," M.Sc Thesis, University of Saskatchewan, Saskatoon, SK., Canada, April 2013.

[12] IEEE SSR Working Group, "Terms, Definitions and Symbols for Subsynchronous Oscillations," IEEE Transactions on Power Apparatus and Systems, Vol. PAS - 104, No. 6, June 1985, pp. 1326 – 1333.

[13] G.D. Irwin, A.K. Jindal and A.L. Isaacs, "Subsynchronous Control Interactions between Type 3 Wind Turbines and Series Compensated AC Transmission Systems," Proceedings of the 2011 IEEE-PES General Meeting, Detroit , MI, USA, July 24 – 28, 2011, pp. 1 – 6.

[14] J.W. Balance and S. Goldberg, "Subsynchronous Resonance in Series Compensated Transmission Lines," IEEE Transactions on Power Apparatus and Systems, Vol. PAS - 92, No. 5, September 1973, pp. 1649 – 1658.

[15] G. Tang, "Damping Subsynchronous Oscillations using a VSC-HVDC Back - to -Back System" M.Sc Thesis, University of Saskatchewan, Saskatoon, SK., Canada, July 2006.

[16] A.A.M. Shaltout "Subsynchronous Resonance in Large Turbo-Generators Connected to a Series Capacitor Compensated Power system," Ph.D Thesis, University of Saskatchewan, Saskatoon, SK., Canada, 1981.

[17] M. Bongiorno, A. Peterson and E. Agneholm, "The Impact of Wind Farm on Subsynchronous Resonance in Power Systems," online report, April 2011, http://elforsk.se/Global/Vindforsk/Rapporter%20VFIII/11_29_report.pdf

[18] P.M . Anderson and R. Farmer, *Series Compensation of Power System*, United States of America: PBLSH! Inc., 1996.

[19] G. Andersson, R. Atmuri, R. Rosenquist and S. Torseng, "Influence of Hydrounits' Generator-to-Turbine Inertia Ratio on Damping Subsynchronous Oscillations," IEEE Transactions on Power Apparatus and Systems, Vol. PAS - 103, No. 8, August 1984, pp. 2352 – 2361.

[20] L. Harnefors, M. Bongiorno and S. Lundberg, "Input - Admittance Calculations and Shaping for Controlled Voltage Source Converters," IEEE Transactions on Industrial Electronics, Vol. 54, No. 6, December 2007, pp. 3323 – 3334.

[21] IEEE Committee Rep., "Reader's Guide to Subsynchronous Resonance," IEEE Transactions on Power Systems Vol. 7, No.1, February 1992, pp. 150 – 157.

[22] G.D. Irwin, "Subsynchronous Interactions with Wind Turbine" Technical Conference - CREZ System Design and Operation, Taylor, Texas, USA, January 26, 2010.

[23] NERC, "Lesson Learned - Subsynchronous Interaction between Series Compensated Transmission Lines and Generation," online report, July 26, 2011, http://www.nerc.com/pa/rrm/ea/Lessons%20Learned%20Document%20Library/LL20110705_Sub-Synchronous_Interaction.pdf

[24] B. Badrzadeh and S. Saylors, "Susceptibility of Wind Turbine Generators to Subsynchronous Control and Torsional Interaction," IEEE-PES T&D Conference and Exposition, Orlando, FL., USA, May 7 – 10, 2012, pp. 1 – 8.

[25] L. Fan and Z. Miao, "Mitigating SSR using DFIG-Based Wind Generation," IEEE Transactions on Sustainable Energy, Vol. 3, No. 3, July 2012, pp. 349 – 358.

[26] B. Badrzadeh, M. Sahni, D. Muthumuni, Y. Zhou, and A. Gole, "Subsynchronous Interaction in Wind Power Plants – Part 1: Study Tools and Techniques," Proceedings of the 2012 IEEE-PES General Meeting, San Diego, CA, USA, July 22 – 26, 2012, pp. 1 – 9.

[27] J. Arrillaga, *High voltage Direct Current Transmission,* 2nd Edition, London, UK, Institution of Electrical Engineers, 1998.

[28] C. Feltes and I. Erlich, "Variable Frequency Operation of DFIG-Based Wind Farms Connected to the Grid through VSC-HVDC Link," Proceedings of the 2007 IEEE-PES General Meeting, Tampa, Florida, USA, June 24 – 28, 2007, pp. 1 – 7.

[29] A.K. Skytt and P. Holmberg "HVDC Light for Connection of Wind Farms," Presented at the 2nd International Workshop on Transmission Networks for Offshore Wind Farms, Royal Institute of Technology Stockholm, Sweden, March 29 – 30, 2001.

[30] J. Peralta, H. Saad, S. Dennetiere, J. Mahseredjian and S. Nguefeu, "Detailed and Averaged Models for a 401-Level MMC-HVDC System," IEEE Transactions on Power Delivery, Vol. 27, No.3, July 2012, pp. 1501 – 1508.

[31] W. Qiao, "Dynamic Modeling and Control of Doubly Fed Induction Generators Driven by Wind Turbines", Power Systems Conference and Exposition, PSCE '09, IEEE/PES, March 2009, pp. 1-8.

[32] E. Muljadi, C.P. Butterfield, A. Ellis, J. Mechenbier, J. Hochheimer, R. Young, N. Miller, R. Delmerico, R. Zavadil, and J.C. Smith, "Equivalencing the Collector System of a Large Wind Power Plant," in Proceedings of the 2006 IEEE PES General Meeting, Montreal, Quebec, Canada, June 18-22, 2006.

[33] P. Kundur, *Power System Stability and Control,* Newyork, McGraw-Hill, 1994.

[34] O. Anaya - Lara, N. Jenkins, J. Ekanayake, P. Cartwright and M. Hughes, *Wind Energy Generation : Modeling and Control,* Wiley, 2009, John Wiley and Sons, Ltd.

[35] S.O. Faried, I. Unal, D. Rai and J. Mahseredjian, "Utilizing DFIG-Based Wind Farms For Damping Subsynchronous Resonance in Nearby Turbine-Generators," IEEE Transactions on Power Systems, Vol. 28, No. 1, February 2013, pp. 452 – 459.

[36] H. Patel, V.K. Sood, "Modeling of Voltage Source Converter-based HVDC System in EMTP-RV," 2010 IEEE-EPEC Conference, Halifax, Nova Scotia, Canada, August 25 – 27, 2010, pp. 1 – 6.

[37] R.M. Hamouda, M.R. Iravani and R. Hackem, "Co-ordinated Static VAR Compensator and Power system Stabilizers for Damping Power System Oscillations," IEEE Transactions on Power Systems, Vol. 2, No. 4, November 1987, pp. 1059 – 1067.

[38] R.M. Hamouda, M.R. Iravani and R. Hackam, "Torsional Oscillations of Series Capacitor Compensated AC/DC System," IEEE Transactions on Power Systems, Vol. 4, No. 3, August 1989, pp. 889 – 896.

[39] J.H. Chow and S. Ghiocel, "An Adaptive Wide-Area Power System Damping Controller using Synchrophasor Data", a chapter in, "Control and Optimization Theory for Electric Smart Grids", Editors: Aranya Chakrabortty and Marija D. Ilić, Springer, 2012.

[40] D. Girard, E. Camm, Y. Lawando and J.K. Niemira, "Tutorials on Renewable Energy Plant Design and System Interconnection," 2013 IEEE-PES General Meeting, Vancouver, British Columbia, Canada, July 21 – 25, 2013.

[41] Y.H. Song and A.T. Johns, *Flexible AC Transmission Systems (FACTS),* London, Institution of Electrical Engineers, 1999.

APPENDIX A

DATA OF THE SYSTEM UNDER STUDY

A.1 Synchronous Generators

Table A.1 : Synchronous generator data

	G1	G2
Rating (MVA)	600	700
Rated Voltage (kV)	22	22
Armature Resistance, r_a (p.u.)	0.0045	0.0045
Leakage Reactance, x_l, (p.u.)	0.140	0.120
Direct - axis Transient Reactance, x_d, (p.u.)	1.650	1.540
Quadrature - axis Synchronous Reactance, x_q, (p.u.)	1.590	1.500
Direct - axis Transient Reactance, x'_d, (p.u.)	0.25	0.23
Quadrature - axis Transient Reactance, x'_q, (p.u.)	0.46	0.42
Direct - axis Sub-transient Reactance, x''_d, (p.u.)	0.20	0.18
Quadrature - axis Sub-transient Reactance, x''_q, (p.u.)	0.20	0.18
Direct-axis Transient open-circuit Time Constant, T'_{do}, (s)	4.50	3.70
Quadrature-axis Transient open-circuit Time Constant, T'_{qo}, (s)	0.67	0.43
Direct-axis Sub-transient open-circuit Time Constant, T''_{do}, (s)	0.04	0.04
Quadrature-axis Sub-transient open-circuit Time Constant, T''_{qo}, (s)	0.09	0.06
Zero Sequence Reactance, x_0 (p.u.)	0.42	0.36

A.2 Turbine - Generators Mechanical Shaft Data

Table A.2: Turbine-generator 1

Mass	Shaft Section	Inertia M (p.u.)	Damping D (p.u./p.u. speed)	Spring Constant k (p.u./rad)
EXC		5.1953028	0.001382	
	GEN1-EXC			3.7414773
GEN1		661.91839	0.176111	
	LP1-GEN1			83.497161
LP1		1167.2677	0.310564	
	HP1-LP1			42.7159
HP1		187.49671	0.04988	

Table A.3: Turbine-Generator 2

Mass	Shaft Section	Inertia M (p.u.)	Damping D (p.u./p.u. speed)	Spring Constant k (p.u./rad)
GEN2		1078.3791	0.0573	
	LP2-GEN2			114.03409
LP2		1192.9066	0.0634	
	HP2-LP2			145.15423
HP2		353.93443	0.0188	

A.3 Modal Speed Calculation Data

Turbine-Generator 1

$$\Delta\omega_m = (\Delta\omega_0 \quad \Delta\omega_1 \quad \Delta\omega_2 \quad \Delta\omega_3)^T$$

$$\Delta\omega = (\Delta\omega_{HP} \quad \Delta\omega_{LP} \quad \Delta\omega \quad \Delta\omega_{EXC})^T$$

$$Q_1 = \begin{bmatrix} 0.5 & -0.6306 & 0.8959 & -0.0005 \\ 0.5 & -0.1629 & -0.2514 & 0.0012 \\ 0.5 & 0.4611 & 0.1872 & -0.0097 \\ 0.5 & 0.6026 & 0.3148 & 1 \end{bmatrix}$$

Turbine-Generator 2

$$\Delta\omega_m = (\Delta\omega_0 \quad \Delta\omega_1 \quad \Delta\omega_2)^T$$

$$\Delta\omega = (\Delta\omega_{HP} \quad \Delta\omega_{LP} \quad \Delta\omega)^T$$

$$Q_2 = \begin{bmatrix} -0.9333 & -0.6592 & 0.5774 \\ 0.3499 & -0.3872 & 0.5774 \\ -0.0808 & 0.6446 & 0.5774 \end{bmatrix}$$

A.4 Wind Farm A (DFIG-Based Wind Farm) and Wind Farm B (Offshore Wind Farm)

Table A.4: Wind farms A and B parameters

	Wind Farm A	Wind Farm B
Number of Wind Turbine Generators	300	140
System Frequency (Hz)	60	60
Rated Capacity of each Wind Turbine Generator (MVA)	1.67	1.67
Generator Nominal Voltage (kV)	0.575	0.575
DC Nominal Voltage (V)	1150	1150
Average Wind Speed (m/s)	11	11
Number of Poles	6	6
Rated Capacity of Turbine (MW)	1.5	1.5

A.5 DFIG Data

1.5 MW, 0.575 kV, 60 Hz

R_s = 0.023 p.u., L_{ls} = 0.18 p.u., L_{md} = 2.9 p.u., L_{mq} = 2.9 p.u.,

R'_r = 0.016 p.u., L'_{lr} = 0.16 p.u., H_t = 4 sec, H_g = 0.71 sec, K_{shaft} = 1.2 $\frac{p.u.}{rad}$,

BtB dc capacitor = 0.01 F, dc voltage = 1.15 kV.

A.6 Transmission Line Parameters

All transmission lines have the same series impedance and shunt admittance per unit length.

$Z_{T.L.\ Series}$ = 0.0118 + j0.3244 Ω/km

$Y_{T.L.\ Shunt}$ = 5.0512 μs/km

Transmission Voltage = 500 kV

A.7 Transformers

Table A.5: Transformer data

	T 1 (Generator 1)	T 2 (Generator 2)	T3 (Wind farm B)	T4 (Wind farm A)
Rating, (MVA)	600	700	525	525
Rated Voltage (kV)	22/500	22/500	34.5/500	34.5/500
Resistance, r_T, (p.u)	0.0012	0.0028	0.005	0.005
Leakage Reactance, x_T, (p.u)	0.12	0.28	0.15	0.15

A.8 System Load

Total Load (L) = 300 MW + 150 MVAR

APPENDIX B

SUPPLEMENTAL CONTROL OUTPUT SIGNALS FOR THE CASE STUDIES

B.1 Supplemental Control I Output Signals

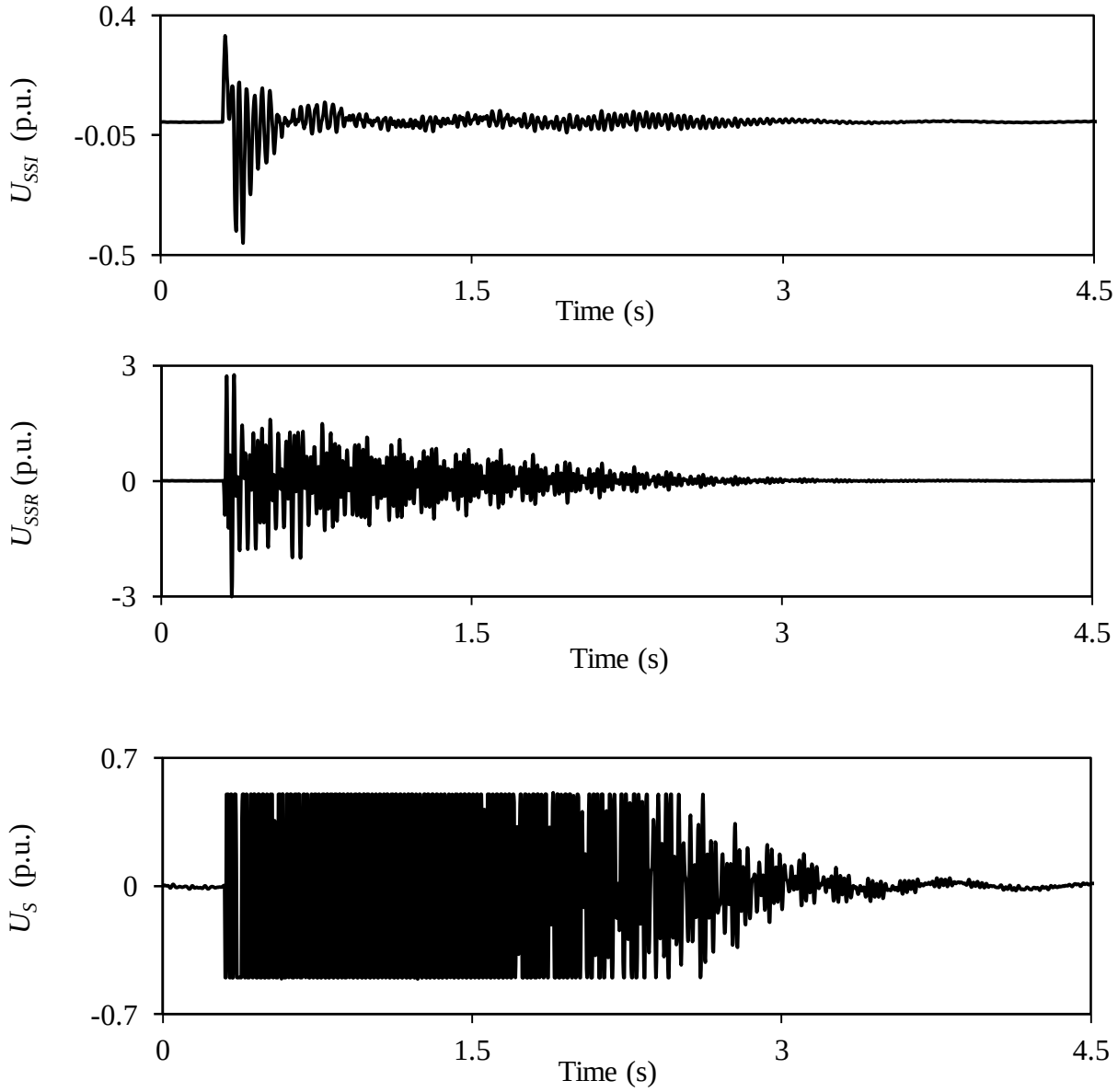

Figure B.1: Supplemental control I output signals during and after clearing a 3-cycle, three-phase fault on Line 5 (60% compensation degree, wind farm B rating = 210 MW).

B.2 Supplemental Control I Output Signals (Line 3 length = 50 km)

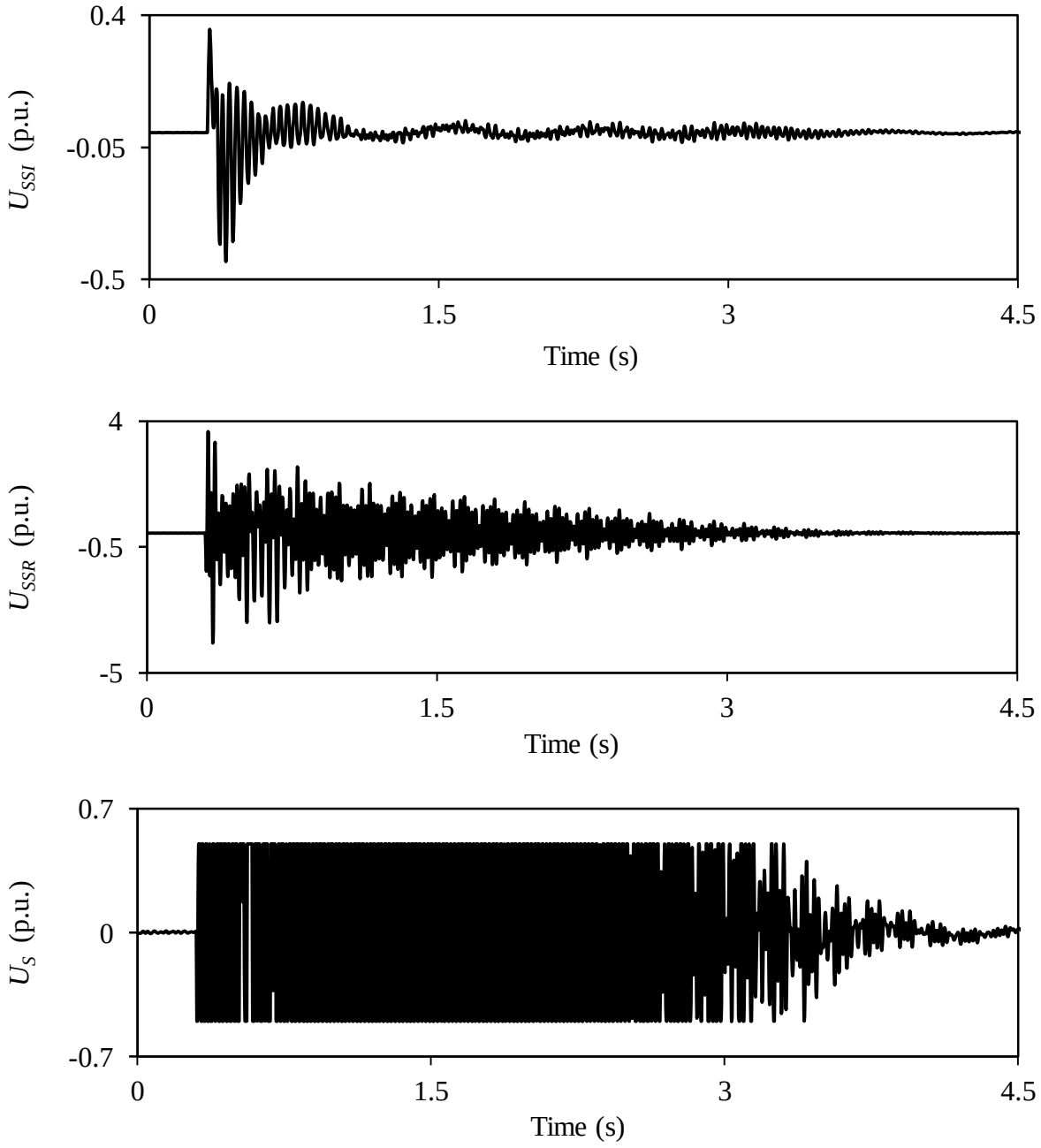

Figure B.2: Supplemental control I output signals during and after clearing a 3-cycle, three-phase fault on Line 5 (60% compensation degree, Line 3 length = 50 km).

B.3 Supplemental Control I Output Signals (Line 3 length = 100 km)

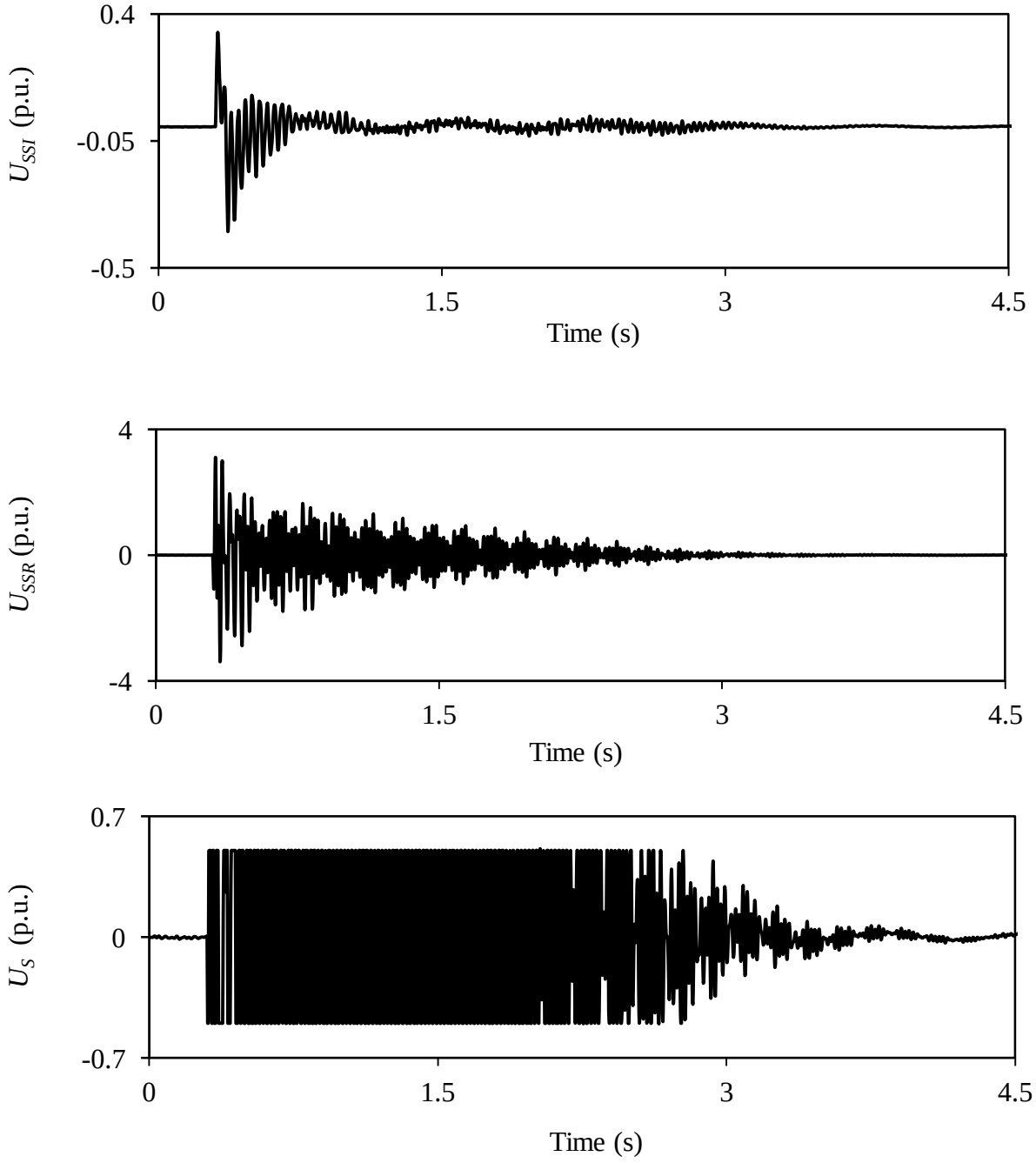

Figure B.3: Supplemental control I output signals during and after clearing a 3-cycle, three-phase fault on Line 5 (60% compensation degree, Line 3 length = 100 km).

B.4 Supplemental Control I Output Signals (Line3 length = 200 km)

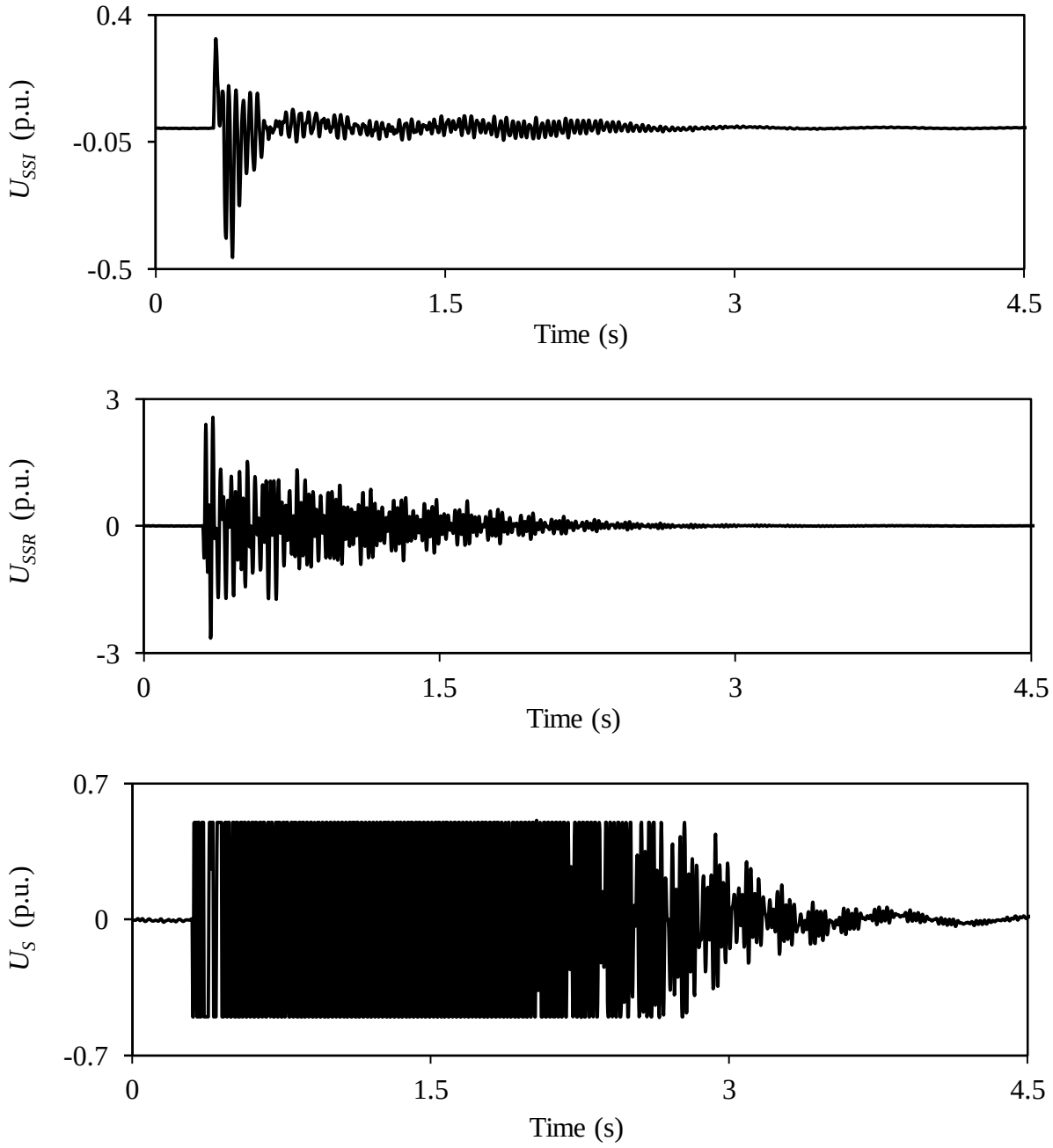

Figure B.4: Supplemental control I output signals during and after clearing a 3-cycle, three-phase fault on Line 5 (60% compensation degree, Line 3 length = 200 km).

B.5 Supplemental Control I Output Signals (Wind farm B rating = 150 MW)

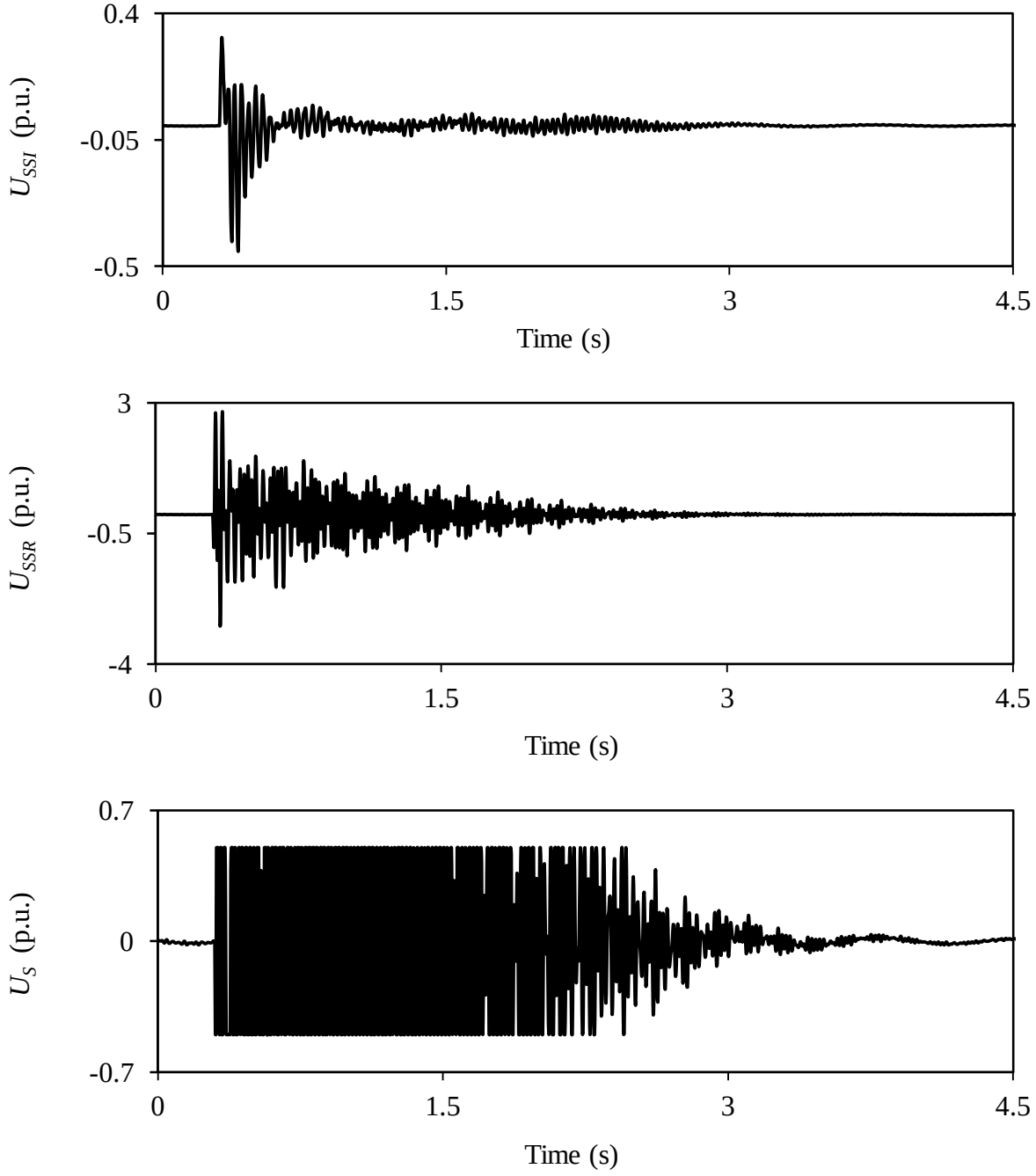

Figure B.5: Supplemental control I output signals during and after clearing a 3-cycle, three-phase fault on Line 5 (60% compensation degree, wind farm B rating = 150 MW).

B.6 Supplemental Control I Output Signals (Wind farm B rating = 300 MW)

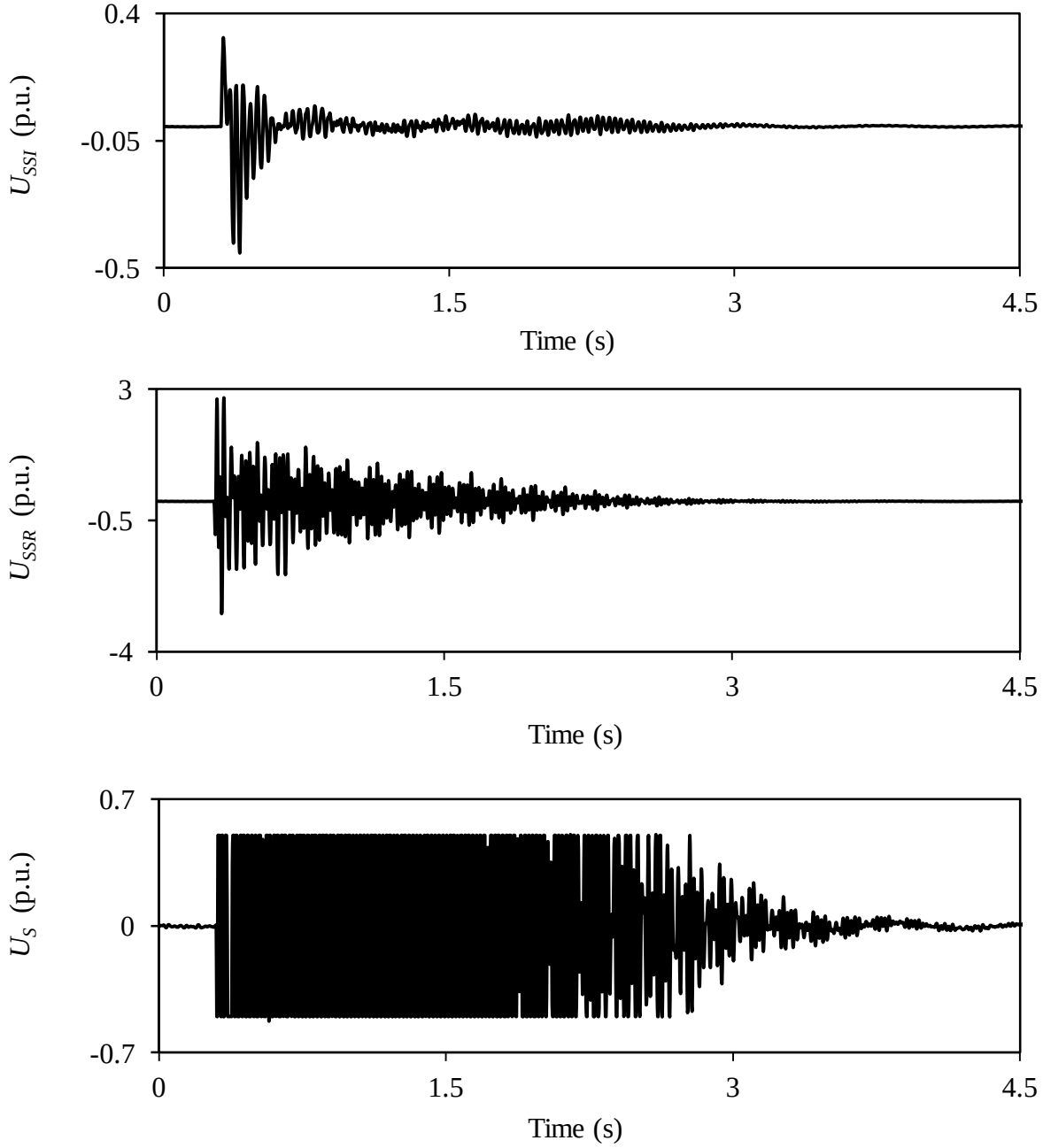

Figure B.6: Supplemental control I output signals during and after clearing a 3-cycle, three-phase fault on Line 5 (60% compensation degree, wind farm B rating = 300 MW).

B.7 Supplemental Control I Output Signals (Double Line-to-Ground Fault (L-L-G))

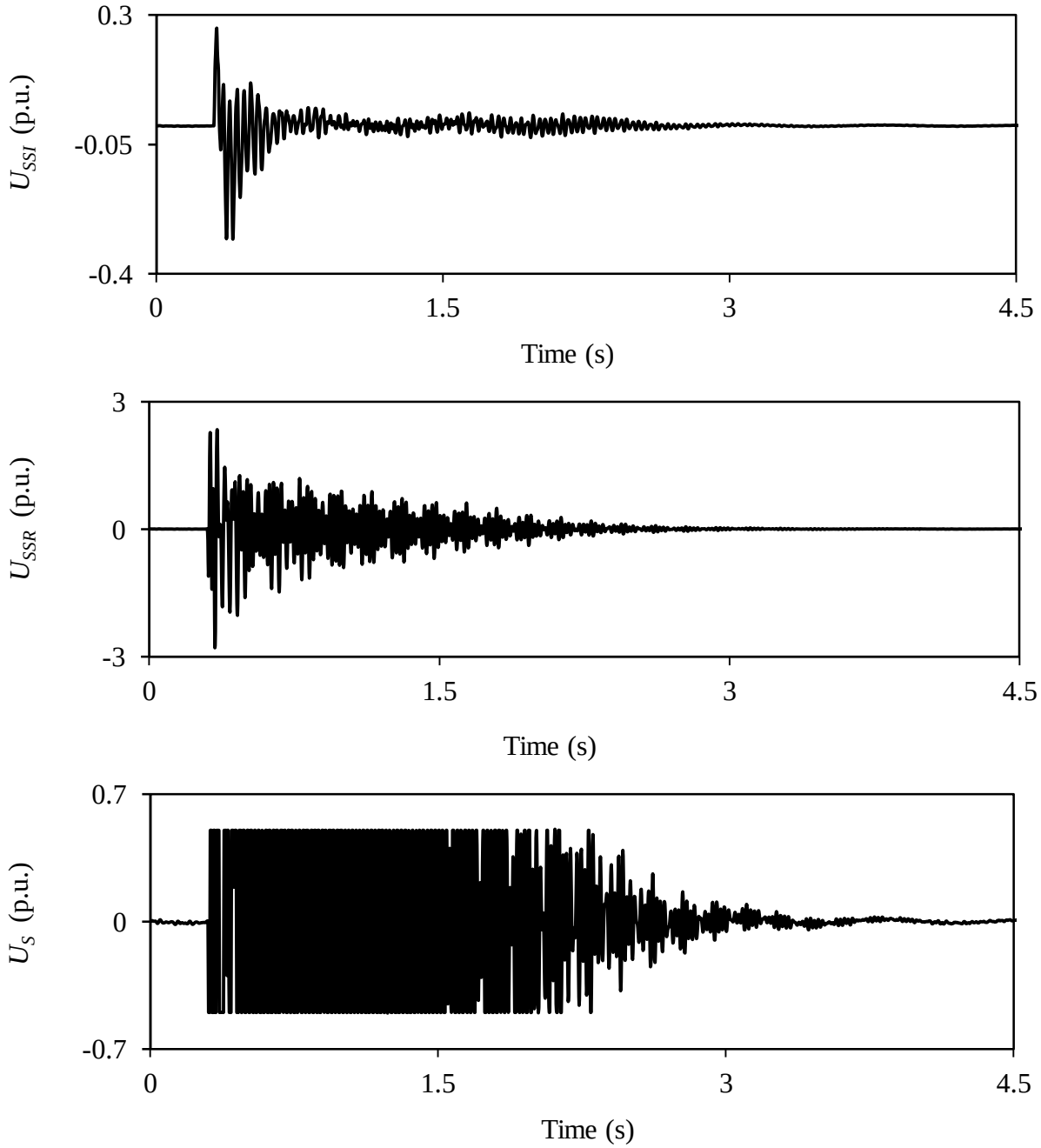

Figure B.7: Supplemental control I output signals during and after clearing a 3-cycle, L-L-G fault on Line 5 (60% compensation degree).

B.8 Supplemental Control II Output Signals

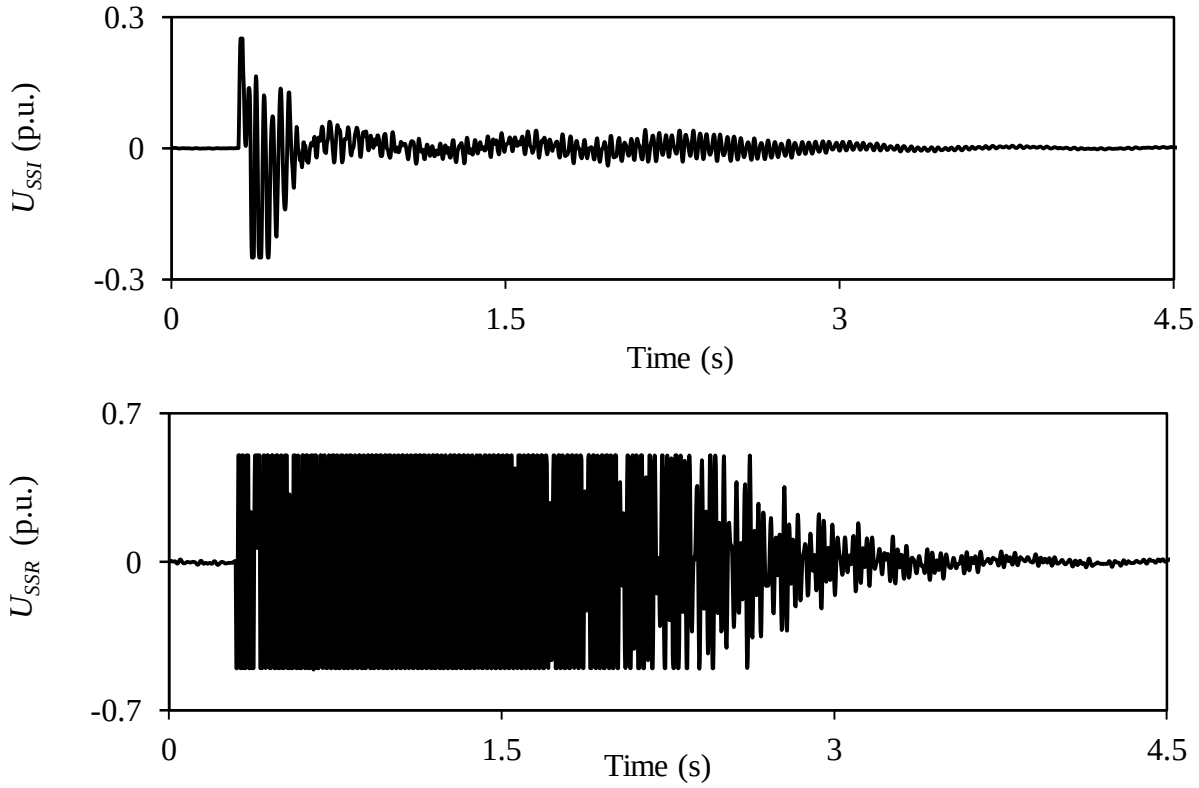

Figure B.8: Supplemental control II output signals during and after clearing a 3-cycle, three-phase fault on Line 5 (60% compensation degree).

B.9 Supplemental Control II Output Signals (Three-phase Fault on Line 4)

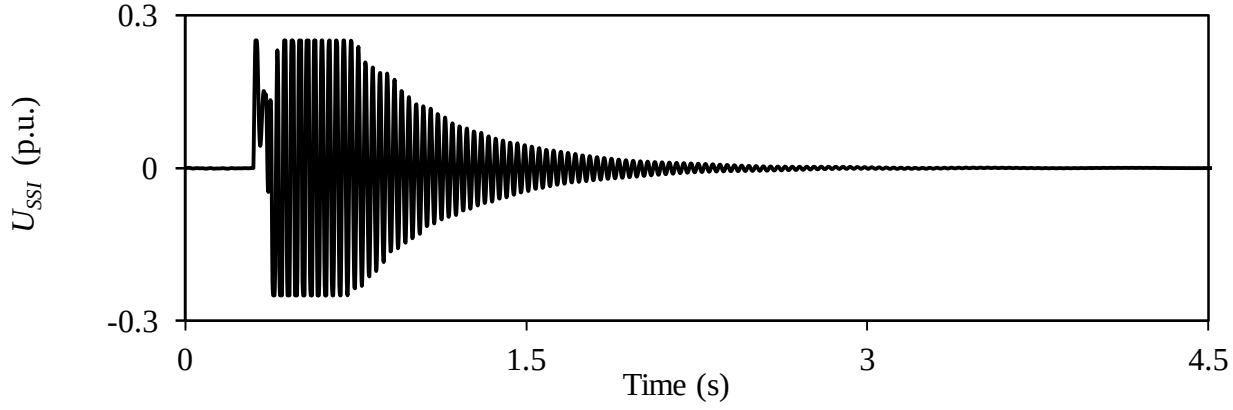

Figure B.9: Supplemental control II output signals during and after clearing a 3-cycle, three-phase fault on Line 4 (60% compensation degree).

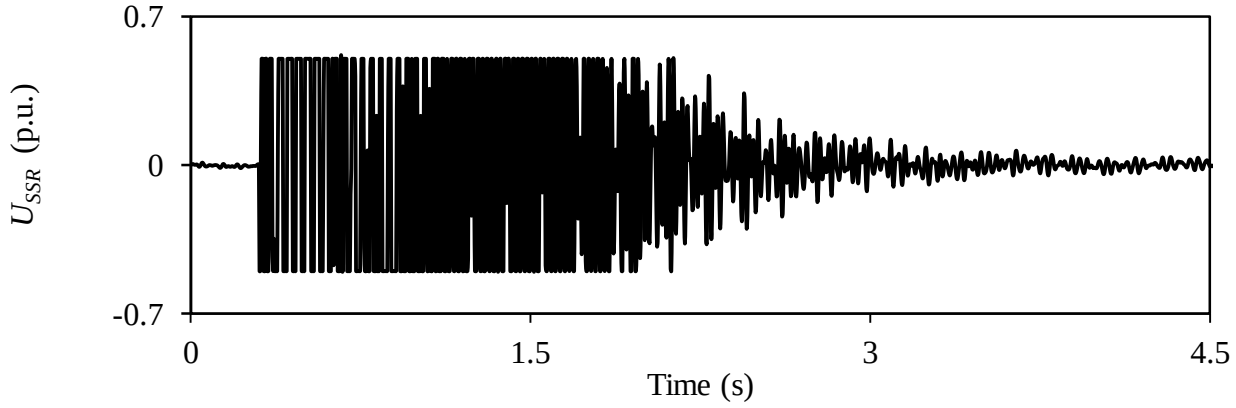

Figure B.9: continued.

B.10 Supplemental Control II Output Signals (50% Compensation Degree)

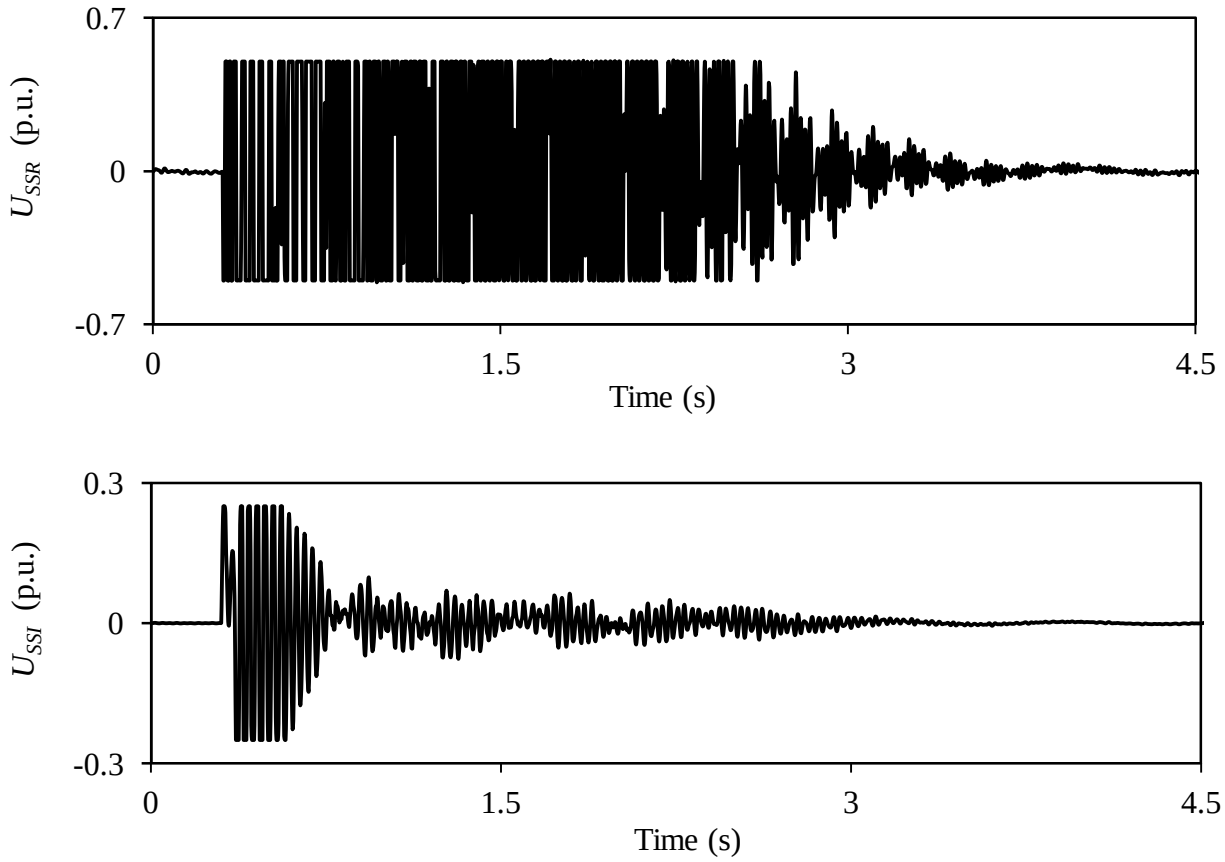

Figure B.10: Supplemental control II output signals during and after clearing a 3-cycle, three-phase fault on Line 5 (50% compensation degree).